

UNIVERSITY OF BIRMINGHAM | COLLEGE OF ENGINEERING AND PHYSICAL SCIENCES

TOWARDS THE DEVLOPMENT OF IMPRINTED NANOPARTICLES FOR GLYCAN DETECTION

by

LAURA MARIE BROOKS

A thesis submitted to the University of Birmingham for the degree of DOCTOR OF PHILOSOPHY

School of Chemical Engineering
College of Engineering and Physical sciences
University of Birmingham
January 2023

UNIVERSITY OF
BIRMINGHAM

University of Birmingham Research Archive

e-theses repository

This unpublished thesis/dissertation is copyright of the author and/or third parties. The intellectual property rights of the author or third parties in respect of this work are as defined by The Copyright Designs and Patents Act 1988 or as modified by any successor legislation.

Any use made of information contained in this thesis/dissertation must be in accordance with that legislation and must be properly acknowledged. Further distribution or reproduction in any format is prohibited without the permission of the copyright holder.

ABSTRACT

Recent advancements in glycomic profiling have led to the discovery of an extensive library of biomarkers which could be used in future diagnostic tools. The current significant barrier to producing new diagnostic technologies is the ability to engineer highly selective and sensitive synthetic systems for complex biomolecules. Some advances have been made via molecular imprinting (MI) in the field, but the systems are not easily translatable to clinical environments.

Molecular imprinting (MI) entails the formation of complementary spatial pockets using monomers that may bind to the target biomolecule covalently or non-covalently. For example, boronic acid derivatives are commonly used monomers for glycan recognition—often termed “synthetic lectins.” These functional monomers covalently bind to cis-diols to form pH-sensitive reversible esters with glycans. Thus, when boronic acids are used in MI, common issues such as template entrapment are overcome via pH modulation of the system to release the target.

MI systems have previously been reported for drug delivery, chromatography and biosensing systems. Many designed systems have shown excellent binding affinities for biosensing applications to their target glycans. However, few can bind to larger glycan structures and discriminate against specific glycosidic linkages (i.e., α-2,3 vs. α-2,6 glycosidic bonds).

In this thesis, we propose a method for glycan recognition through imprinted nanoparticles entailing boronic acids as the glycan binding monomer. The application of this study could

improve future diagnostic assays for glycan detection. The proposed method has not been conducted on nanoparticles before and could result in highly selective and sensitive molecularly imprinted nanoparticles (MINPs). This strategy entails self-assembling glycan boronate esters under anhydrous aprotic solvent conditions. The boronate ester template is imprinted onto nanoparticles by forming a polymeric matrix around the template. The resulting cavities on the nanoparticle's surface should possess multiple boronic acid receptors capable of forming covalent bonds with the target glycan. These functional monomers are spatially locked on the particle surface for a multivalent binding event. Fixing boronic acids in a specific spatial orientation should afford selective cavities to distinguish different glycosidic linkages and glycan motifs with different 3D shapes. The results of this research provide a starting point for the development of MINPs for selective glycan detection.

An overview of this thesis is provided below.

Chapter 1: Introduces background to the field with a focus on common glycan changes observed in cancer. Different glycan detection and identification methods are explored, leading to artificial receptors and the advancements of molecular imprinting on the nanoscale for glycan detection. The common trends and limitations of synthetic glycan detection systems are discussed.

Chapter 2: Highlights the PhD aims and the future applications of this work.

Chapter 3: Provides a brief explanation of the characterisation methods to clarify the work conducted in this thesis.

Chapter 4: Examines different nanoparticles for their applications as stable, water-soluble, pH-resistant supports for future MI works.

Chapter 5: Describes the synthesis of boronic receptors, the formation of glycan boronate-esters and their characterisation.

Chapter 6: Describes the optimisation and development of a protocol for MINPs.

Chapter 7: Conclusions and future work.

COVID-19 STATEMENT AND DECLARATION OF WORK

CONDUCTED BY THIRD-PARTY CONTRIBUTORS.

The global COVID-19 pandemic posed significant challenges to our research endeavours, particularly in accessing laboratories and essential consumables. Laboratory-based research was suspended between March 2020 and July 2020, disrupting our workflow. As university buildings gradually reopened, stringent campus regulations were implemented to ensure the safety of students and staff. Unfortunately, these regulations restricted researchers from engaging in collaborative projects with external schools, hindering multidisciplinary research. Consequently, technicians assumed a pivotal role in conducting chemical analyses and operating chromatography instruments previously managed by researchers. While their assistance was invaluable, reliance on third-party involvement occasionally led to delays in data acquisition, impacting the pace of our synthetic progress. Furthermore, limitations on laboratory occupancy and the implementation of rotating schedules further constrained our research activities. To provide clarity on the extent of external technical support required, Table 0-1 summarises instances where such assistance was necessary.

Table 0-1: Summary of work conducted by others owing to the time constraints inflicted by the pandemic.

Figure	Comments
Figure 4-47	Theresa Moris obtained some microscopy images for the reported averaged data sets.
Figure 5-4	Christopher Williams obtained the TOF-MS spectra for my synthesised product.
Figure 5-40	Christopher Williams obtained the TOF-MS spectra for my synthesised product.
Appendix 9-15	Christopher Williams obtained the TOF-MS spectra for my synthesised product.
Appendix 9-17	Christopher Williams obtained the TOF-MS spectra for my synthesised product.
Appendix 9-18	Christopher Williams obtained the TOF-MS spectra for my synthesised product.
Appendix 9-19	Christopher Williams obtained the TOF-MS spectra for my synthesised product.
Appendix 9-24	Christopher Williams obtained the TOF-MS spectra for my synthesised product.

Figure 5-41	**Christopher Williams obtained the TOF-MS spectra for my synthesised product.**
Appendix 9-25	**Christopher Williams obtained the TOF-MS spectra for my synthesised product.**
Appendix 9-26	**Christopher Williams obtained the TOF-MS spectra for my synthesised product.**
Figure 6-4	**Theresa Moris obtained the images for the nanoparticles.**
Figure 6-6	**Theresa moris obtained the images for the nanoparticles.**
Figure 6-14	**Synthesis of glass beads used in the preparation of MINPs.**

ACKNOWLEDGEMENTS

Firstly, I want to express my gratitude to my supervisors, Professor Mendes and Dr Fernandez-Villamarin. Your cheerful outlook and kind words of encouragement during my PhD journey have been invaluable. With your guidance, this thesis exists today.

Secondly, I want to acknowledge the unique individuals with whom I have had the pleasure of working with over the past four years. Thank you to Dr Tommasone, Dr Norman, Dr Ward, Dr Allabush, Dr Mahmoodi, Dr Gibson, Dr Vafaei, Dr Tabaei, Kamlesh, Yazmin, Pushpa, Alice, Barbara, Dario, Laura, Miguel, Charlie, Hannah, Daniel C, and Daniel K. Together, we have experienced the highs and lows of research, and it has been a privilege to share this journey with you all.

I am incredibly grateful to the staff at the University of Birmingham for their support during my time there. The brilliant staff at the chemical engineering department, including Helen, Lynn, Chris, Elaine, Ronnie, Angela, and Jackie, provided me with emotional support and guidance that made my experience unforgettable. I would also like to thank the technical staff in the chemistry department, including Cecile, Chi, and Chris, who were always available to offer advice. With their help, characterisation was possible, particularly during the COVID-19 restrictions. Once again, thank you to everyone who made my time at the university an unforgettable experience.

I would like to express my sincere gratitude to my dear friends and my beautiful partner for their constant emotional support during these challenging years. Scott, Harvey, Georgie, Kath,

Drew, and Debbie, you guys are amazing! I would also like to give a special shoutout to Tore - I mentioned your name, so enjoy it while it lasts, as I will always call you Vic.

I want to express my gratitude to my supportive family, who have always been there for me throughout my academic journey, motivating me never to lose hope. Special thanks to my mother and grandmother, who never lost faith in my abilities, even when I doubted myself. It is primarily due to their unwavering support that I continue to persevere and contribute to cancer research. Thus, I dedicate this thesis to my relatives who sadly lost their battle to this cancer.

To conclude, I want to remind myself to be kinder and more trusting towards myself.

CONTENTS

Chapter One 1

i. Introduction 1

ii. Glycans in biology 3

iii. Post-translational modifications (PTMs)..... 12

iv. Glycosylation 14

v. N-glycosylation 16

vi. Aberrant glycosylation and prostate cancer (PCa)..... 20

vii. Methods of glycan detection and analysis 24

viii. Lectin-based techniques for studying glycans. 25

ix. Use of lectins in tandem with mass spectrometry (MS)..... 30

x. Glycoblotting for glycan detection 34

xi. Limitations of lectins for glycan detection 38

xii. Synthetic receptors for glycan detection 40

xiii. Synthetic non-covalent receptors (SNCRs)..... 41

xiv. Covalent synthetic receptors 64

xv. Introduction to molecular imprinting(MI) 79

xvi. Molecular imprinting (MI) on a 2D surface 82

xvii. Molecularly imprinting on a 3D surface 89

xviii. Summary 101

Chapter Two 103

Chapter Three 107

ii. Techniques and methods 107

iii. Dynamic light scattering (DLS) and zeta potential (ZP) 107

iv. Transmission electron microscopy (TEM) 113

v. Isothermal titration calorimetry (ITC) 116

vi. Mass Spectrometry (MS) 122

vii. Matrix assisted laser desorption ionisation (MALDI) 126

viii. Electrospray ionisation (ESI) 127

ix. Atmospheric solid phase analysis probe (ASAP) Ionisation . 128

x. Mass analysers 129

xi. Time OF flight (TOF) analyser 129

xii. Quadrupole analyser 130

xiii. Quadrupole time-of-flight analyser (Q-TOF). 132

xiv. Liquid chromatography – mass spectrometry (LC-MS) 133

xv. nuclear magnetic resonance spectroscopy (NMR) 135

xvi. Ultraviolet-visible spectroscopy 142

xvii. Application of UV-vis for metallic nanoparticles..... 145

xviii. Fluorescence spectroscopy 147

Chapter Four 150

ii. Synthesis of gold nanoparticles 154

iii. Characterisation of gold nanoparticles 162

ii. Functionalisation of gold nanoparticles 168

iii. Functionalisation of gold nanoparticles with cysteamine hydrochloride (cys). 172

iv. Functionalisation of gold nanoparticles with 1,4-benzenedimethanethiol (BDMT). 178

v. Functionalisation of gold nanoparticles with the aid of additional surfactants 184

vi. Functionalisation of gold nanoparticles with 1,4-BDMT in the presence of Tween-20 186

vii. Functionalisation of gold nanoparticles with 11-mercaptoundecanoic acid (11-MUDA) and 4-mercaptobenzoic acid (4-MCA) in the presence of Tween-20 (T20). 193

viii. Gold nanoparticle summary 201

ix. Polymeric nanoparticles 203

x. Introduction to emulsion polymerisation. 204

xi. Synthesis of polyacrylamide nanoparticles (PAM) 208

xii. Functionalisation of polyacrylamide (PAM) nanoparticles with glycan receptors. 214

xiii. Investigating the stability of 3-acrylamidophenyl boronic acid polyacrylamide nanoparticles (APBA-PAM). 219

xiv. Summary of polyacrylamide (PAM) nanoparticles. 223

xv. Introduction to oil-in-water (O/W) emulsion polymerisation reactions. 225

xvi. Synthesis of polystyrene (PS) nanoparticles 227

xvii. Purification of polystyrene (PS) nanoparticles..... 233

xviii. Increasing the solubility of polystyrene (PS) nanoparticles . 234

xix. Investigating the stability of polystyrene (PS) nanoparticles. 244

xx. Functionalisation of polystyrene nanoparticles with glycan receptors 248

xxi. Optimisation of addition of benzoboroxole receptors onto polystyrene (PS) nanoparticles..... 256

xxii. Fluorescence spectroscopy studies with polystyrene nanoparticles 261

xxiii. Polystyrene nanoparticle summary..... 267

xxiv. Chapter summary..... 269

Chapter Five 271

i. Synthesis of the glycan boronate ester templates for molecular imprinting (271

ii. Synthesis of the synthetic boronate receptor..... 273

iii. NMR study of boronate-ester formation 282

iv. Synthesis of boronate-esters with neutral sugars..... 289

v. Indirect analysis of boronate-ester formation via MS methods. 300

vi. Study to evaluate the extent of boronate-ester formation with charged sugars 328

vii. The synthesis of Boronate esters with neuraminic acid derivatives. 332

viii. NMR study of boronate-ester formation with N-Acetyl-2-O-methyl-α-neuraminic acid 348

ix. Summary 355

Chapter Six 357

ii. Development of glycan imprints on nanoparticles. 359

iii. Incorporation of organic solvents for molecular imprinting . 368

iv. Purification of nanoparticles after molecular imprinting 370

v. ITC binding studies of polystyrene nanoparticles 373

vi. Application of solid-phase synthesis to polystyrene nanoparticles 387

vii. Preparation of glass beads for molecular imprinting 389

viii. Incorporation of functionalised glass beads to aid the development of MINPS 393

ix. Analysis of nanoparticles produced from solid-phase synthesis. 395

x. Summary 403

Chapter Seven 405

Chapter Eight 411

ii. Chemicals and materials 411

iii. Data analysis 411

iv. Dynamic light scattering (DLS) and zeta potential measurements (ZP) 412

v. Glassware cleaning 412

vi. Transmission electron microscopy (TEM) 413

vii. Isothermal titration calorimetry (ITC) 414

viii. UV-Vis spectroscopy measurements 415

ix. Preparation of LC-MS Samples 416

x. Preparation of MALDI matrixes 417

xi. The synthesis of gold nanoparticles 418

xii. Functionalisation with 1,4-benzenedimethanethiol or cysteamine hydrochloride 418

xiii. Functionalisation of gold nanoparticles with thiols in the presence of Tween-20. 419

xiv. Functionalisation with 11-mercaptoundecanoic acid or 4-mercaptobenzoic acid..... 419

xv. Synthesis of polyacrylamide (PAM) nanoparticles 420

xvi. Synthesis of functionalised polyacrylamide nanoparticles . 421

xvii. Synthesis of polystyrene (PS) nanoparticles 422

xviii. Synthesis of water-soluble polystyrene nanoparticles..... 423

xix. Synthesis of polystyrene nanoparticles functionalised with DHEBA and 3-acrylamidobenzoboroxole/ 3-acrylamidophenylboronic acid 424

xx. Synthesis of 5-acrylamide-2(hydroxmethyl)phenylboronic acid (AABOB) 425

xxi. Preparation of the glycan-boronate complex 426

xxii. Benzoylation of the complex sugar 427

xxiii. Development of polystyrene nanoparticles baring pocket imprints 428

xxvi. Functionalisation of glass beads with 3-aminopropyl-β-d-lactose for molecular imprinting. 430

xxvii. Hybrid approach to producing MINPs utilising glass beads. 431

Chapter Nine xlii

ii. Gold nanoparticle theoretical concentration based on LSPR peak xlviii

iii. theoretical concentration of bulk gold in the synthesis of gold nanoparticles calculated from reagent mass. xlix

iv. Polystyrene nanoparticles calculations.....lv

ABBREVIATIONS AND NOMENCLATURE

Acronym	Definition
AABOB	3-acrylamidobenzoboroxle
ACN	Acetonitrile
AOT	Dioctyl sulfosuccinate sodium salt
APBA	Acrylamido - phenylboronic acid
APS	Ammonium persulphate
APTMS	(3-aminopropyl)trimethoxysilane
ARS	Alizarin red S dye
ASAP	Atmospheric solid analysis probe
BDMT	1,4 - dibenzenemethanethiol
BIPY	Biphenyl
BOB	Benzoboroxole
BPH	Benign prostate hyperplasia
C18	Carbon - 18
CCS	Collision cross-section
CCD	Charged coupled device
CD_3OD	Deuterated methanol
COSY	Homonuclear correlation spectroscopy
CRC	Colorectal cancer
CTC	Circulating tumour cells
DCM	Dichloromethane
DFT	Density function theory
DHB	2,5-Dihydroxybenzoic acid
DHEBA	N, N'-(1,2-Dihydroxyethylene)-bis-acrylamide
DLS	Dynamic light scattering
DLVO	Derjaguin, Landau, Verwey and Overbeek theory
DMF	Dimethyl formamide
DMSO	Dimethyl sulfoxide
DVB	Divinyl benzene
EDC	1-Ethyl-3-[3-dimethylaminopropyl]-carbodiimide hydrochloride
ELISA	Enzyme-linked-immunoassays
ELLA	Enzyme-linked lectin assays
ES	Excited state

ESI	Electrospray ionisation
FDA	Food and Drug Administration
FITC	Fluorescein isothiocyanate
FUT8	Fucosyltransferase 8
HIV	Human immunodeficiency virus
HOMO	Highest occupied molecular orbital
HPLC	High-performance liquid chromatography
HRP	Horseradish peroxidase
IPA	Isopropyl alcohol
IR	Infrared
ITC	Isothermal titration calorimetry
K_B	Boltzmann constant (1.380649 E-23 J/K)
K_D	Dissociation constant (M)
KPS	Potassium persulphate
LC	Liquid chromatography
LCMS	Liquid chromatography-mass spectroscopy
LOMO	Lowest occupied molecular orbital
LSPR	Localised surface plasmon resonance
MALDI	Matrix-assisted laser desorption ionisation.
MCA	4-Mercaptobenzoic acid
MFI	Median fluorescence intensity
MI	Molecular imprinting
MINP	Molecularly imprinted nanoparticles
MIP	Molecularly imprinted polymers
MS	Mass spectroscopy
MUDA	11 - Mercaptoundecanoic acid
N_A	Avogadro's number (6.022 E23 = 1 mole)
NHS	N-Hydroxysuccinimide
NMR	Nuclear magnetic resonance spectroscopy
NP	Nanoparticle
PAA	Poly - acrylamide
PBA	Phenylboronic acid

PCa	Prostate cancer
PDI	Polydispersity index
PEG	Poly-ethylene glycol
PET	Photoinduced electron transfer
PS	Polystyrene
PSA	Prostate specific antigen
PTM	Post-translation modifications
RPM	Revolutions per minute
SAM	Self-assembled monolayer
SD	Standard deviation
SDS	Sodium dodecyl sulphate
SIGN	Dendritic cell-specific intercellular adhesion molecule-3-grabbing non-integrin lectin
SPR	Surface plasmon resonance
T20	Tween - 20
TEM,	Transmission electron microscopy
TEMED	Tetramethylethylenediamine
THF	Tetrahydrofuran
TLC,	Thin layer chromatography
TOF	Time of flight
TRF	Transferrin
UEA	Ulex europaeus agglutinin-1 lectin
UV	Ultra - visible
WGA	wheat germ agglutinin lectin
XRD	X-ray diffraction spectroscopy
ZP	Zeta potential

CHAPTER ONE

I. INTRODUCTION

Cancer is one of the UK's biggest killers, with around 375,000 new cases each year, with only 50% of those patients surviving beyond ten years.[1] Thus, there is a demand for better diagnostics and therapeutics. This thesis focuses on improving cancer diagnostic platforms to provide earlier detection and improve patient prognosis. Key to diagnostic tests are the biological markers or biomarkers; an example is glycoproteins. Many FDA-approved cancer biomarkers are glycoproteins or glycan antigens.[2]

Glycoproteins are used in the present diagnostic test for prostate cancer (PCa). The biomarker is called the prostate-specific antigen, or PSA for short.[3] This can be found in the blood in one of two forms – bound to proteins or as free PSA (*f*PSA). The standard diagnostic test in the UK looks at the total prostate-specific antigen (PSA) amount. According to the present methodology, those under four ng/mL do not have PCa; those reading four ng/mL and above are considered for further testing.[4] However, elevated PSA levels are not always indicative of cancerous growth. Prior literature reports PSA levels as 'inherently variable.' Explanations for these variations may be active lifestyles, medication, size of the prostate, or variances in analytical processing (e.g., assay performance, sample handling and laboratory processing).[5] Furthermore, those with elevated PSA levels may have prostatitis or benign prostate

hyperplasia (BPH); these are not cancerous. Therefore, some patients may receive a false-positive PSA result. False readings are because the prostate is the dominant site of benign and malignant growth. The methodology mentioned above is unspecific, leading to unnecessary examinations and biopsy procedures, damaging not only to patients but also at an economical cost to the UK's health department.[6] Conversely, those patients with aggressive PCa (Gleason score of 8 or greater [7]) are not being diagnosed efficiently, with 33 deaths per day due to PCa in the UK.[8] With over 52,000 men diagnosed with PCa each year, there is a need to differentiate between prostatitis, benign hyperplasia (BPH), and indolent and aggressive cancers. [9–13] Therefore, there is a need for a new diagnostic tool which can provide exceptional accuracy for aggressive PCa glycoforms. Advancements in glycomic profiling have identified key trends in glycan structures and linkages of glycoproteins.[14] Tracking and detecting these glycan motifs could provide new methodologies facilitating discrimination of indolent and aggressive cancers.[15]

The chapter will briefly introduce what are glycans and the vast array of structures they can adopt, in addition to the previously reported methods for glycan detection via natural and synthetic receptors. After this introductory chapter, the aims of this thesis will be discussed, followed by the research attempting to address the gap in the field.

II. GLYCANS IN BIOLOGY

In humans and living systems, glycans comprise simple monosaccharides, as illustrated in figure 1-1.[16] Monosaccharides are the most basic form of sugars, all with the same general formula - (CH2O)n. They are classified as either aldehydes (aldoses) or ketones (ketoses). [17] A combination of many saccharide units through condensation reactions forms a polysaccharide. table 1-1 summarises the classifications.

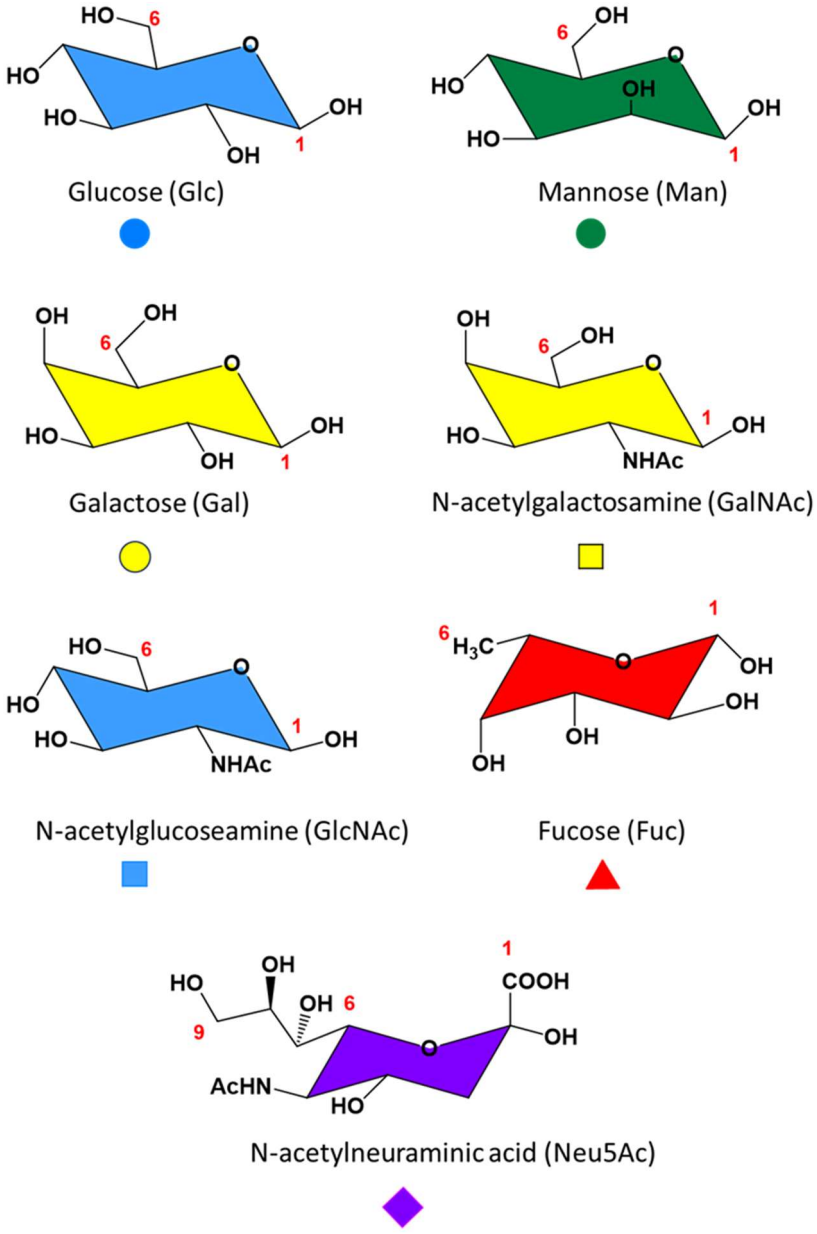


Figure 1-1: Common monosaccharides present in glycans. Shorthand notation for each sugar unit represents a colour and symbol as per symbol nomenclature for glycans (SNFG).

[18]

Table 1-1: Classification of monosaccharides

Classification	Description	Example
Mono-saccharide	1 sugar monomer	Glucose
Di-saccharide	2 sugar monomers linked by glycosidic bond	Lactose
Tetra-saccharide	4 sugar monomers linked by glycosidic bonds	Stachyose
Oligo-saccharide	2 – 10 monomer units	Raffinose
Poly-saccharide	>10 saccharide monomers linked together by glycosidic bonds	Starch

Sugars can adopt linear and cyclic structures; the formation of the cyclic structures is shown in figure 1-2. The reducing end of a sugar (aldehyde/ketone carbonyl is attacked by another hydroxyl group within the sugar and hence is denoted intramolecular nucleophilic attack. The reducing ends may attack different hydroxyl groups, forming different-sized rings.

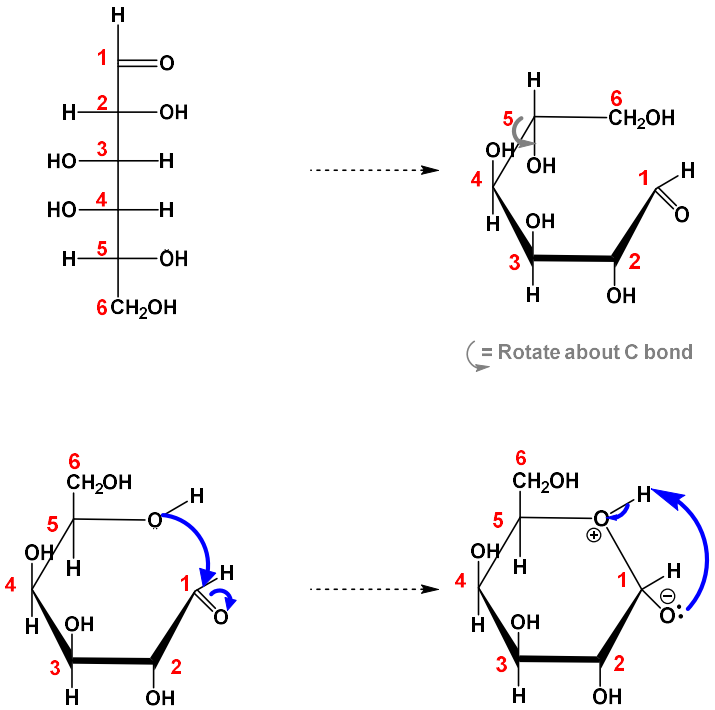


Figure 1-2: Intramolecular nucleophilic attack to form cyclic structures of D-Galactose with new stereocentres.

The number of carbon atoms and the spatial orientation of the hydroxyl group at the furthest chiral carbon from the carbonyl group determines the identity of sugars in their linear forms. For instance, in D-galactose, the hydroxyl group on the chiral C-5 carbon furthest away from the carbonyl group is located on the right-hand side, as demonstrated in figure 1-2. While in L-galactose, it is on the left-hand side.

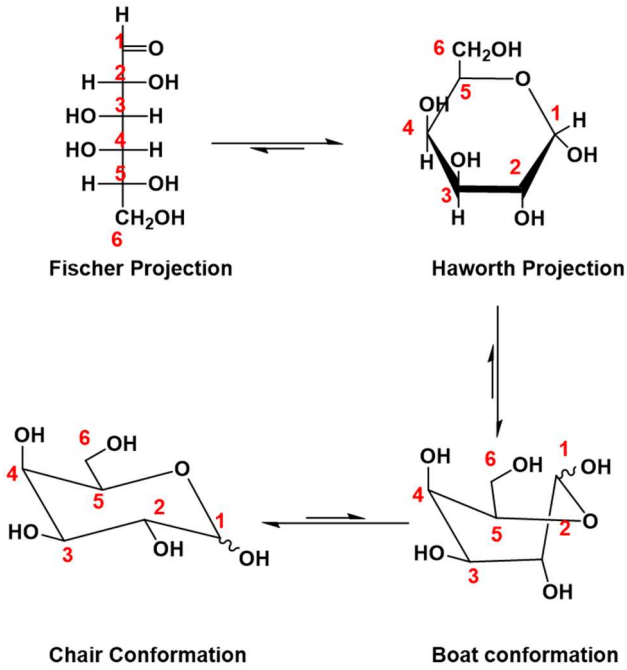


Figure 1-3: D-galactose tautomer's are present in the solution in dynamic equilibrium. The hydroxyl group orientation at the anomeric carbon (C_1) defines whether it is α or β .

Sugars can also take on additional stereoisomers denoted alpha (α) and beta (β) conformations due to the cyclic structure (figure 1-3). The orientation of the hydroxyl group at the anomeric centre and the CH_2OH substituents determine these conformations. When the hydroxyl group and the CH_2OH substituents are on opposite faces of the ring, the sugar is marked as α. On the other hand, when they are on the same face of the ring, the sugar is said to be in the β configuration.

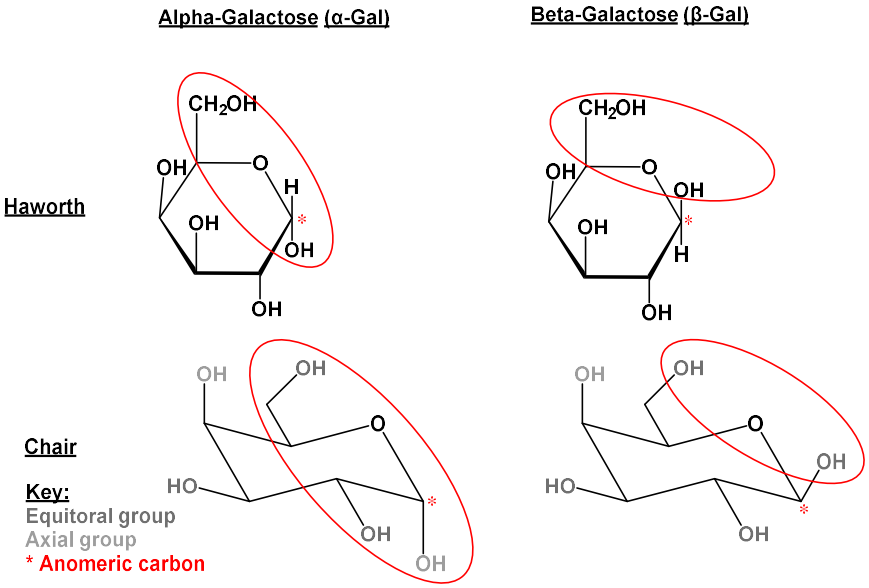


Figure 1-4: α-galactose and β-galactose depicted both in Haworth and chair conformations, showing the relative orientations of the hydroxyl groups at the anomeric centre concerning the CH_2OH substituents.

The rotation of carbon bonds within the cyclic sugars leads to additional structures, such as 'boat' and 'chair.' The ring substituents can adopt different spatial conformations known as axial and equatorial, which are highlighted in figure 1-4. The 'chair' structure is often the most stable owing to the hydroxy or bulkier R groups situated further apart. In solution, many structures often occur in equilibrium, creating a complex mixture of structures. The exact percentage for each form is specific for each monosaccharide for a given set of conditions. For example, fructose (figure 1-5) is known to adopt the β-D-fructopyranose conformation dominantly under aqueous conditions at 20 ºC.[19]

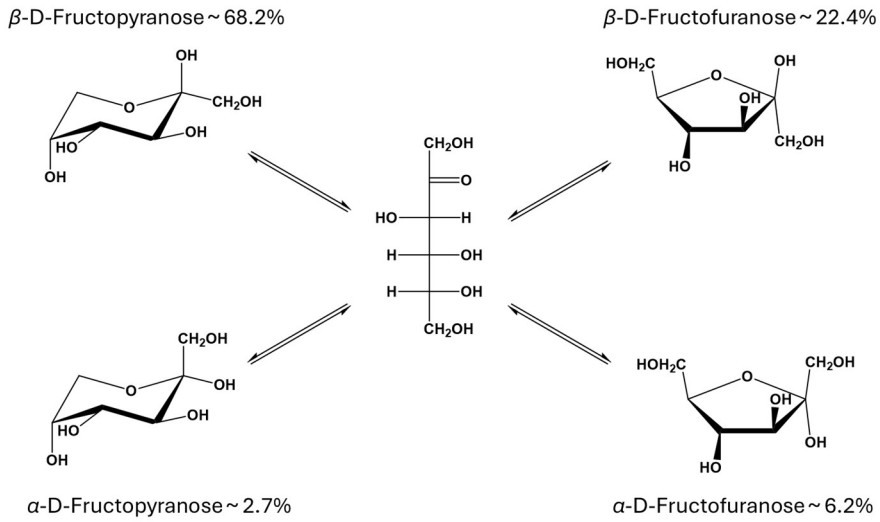


Figure 1-5: Tautomer's of keto-D-fructose exist in dynamic equilibrium in an aqueous solution with relative proportions concerning one another. Diagram recreated from literature.[19]

In biology, glycan motifs comprise many cyclic monosaccharides linked together via glycosidic bonds. In nature, cyclic chair conformations are more likely to form over other tautomer's. The cyclic forms reduce ring strain, allowing larger ring substituents to be spaced further apart.

Six-membered rings are the most thermodynamically favoured among all ring sizes due to the tetrahedral angles providing zero ring strain. The glycosidic bonds form between the anomeric carbon of one sugar and any of the unmodified hydroxyl groups of another, creating a diverse range of structures. For instance, combining four identical glucopyranose units can result in 1792 different isomers. [20] This complexity is compounded when different monosaccharides are involved, each capable of forming glycosidic linkages at different hydroxyl groups. Glycans are biomolecules that contain crucial information and participate in almost every biological process owing to the vast

amount of structures they can form. For instance, six glycan monomers can combine to form over a trillion oligomeric structures, significantly more than the 4,096 forms produced by DNA nucleotides and the 60 million structures produced by peptides. [21] Glycans can exist freely, as part of the cell membrane, or as part of other biological molecules such as proteins. Some of their roles include intercellular signalling, enhancing the solubility of macromolecules, promoting glycoprotein folding, protecting against proteases, storing nutrients, protecting against immune recognition, promoting intracellular glycoprotein folding, and participating in the trafficking and degradation of glycoproteins. [15,21–23]

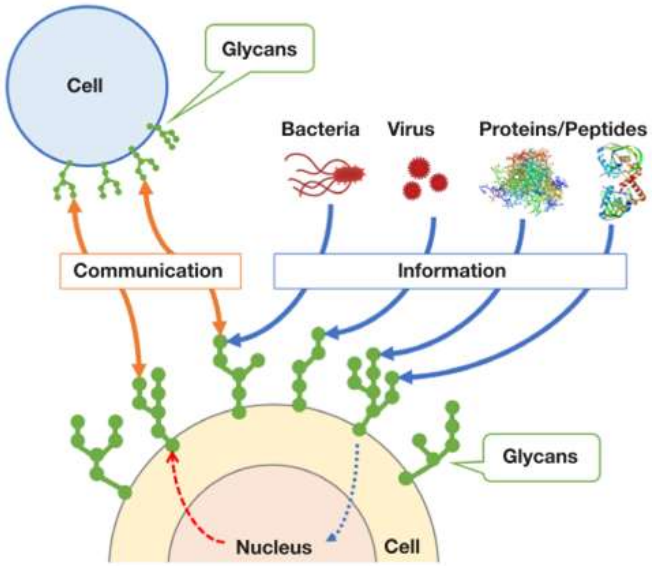


Figure 1-6: Diagram displaying some of the roles glycans participate in taken from literature.[15]

Targeting entire glycan motifs is difficult since the human glycome is still largely unknown.[24] Currently, the field focuses on small known motifs correlated with diseases such as rheumatoid arthritis, diabetes [25], and various cancers[15,16,22,25] In the case of prostate cancer, an increase in core fucosylation, sialylation, and N-acetyl galactosamine proportions is closely related to aggressive PCa. These factors are monitored and tracked in the patient's serum. [10,26–29].

III. POST-TRANSLATIONAL MODIFICATIONS (PTMS).

Proteins are intricate biomolecules that perform vital roles in numerous bodily processes, including protection against infections and coordination of biological processes between cells and tissues. These molecules comprise four structures: primary, secondary, tertiary, and quaternary. The primary structure is an amino acid sequence, with local intramolecular forces determining secondary structures. Tertiary structures result from further polypeptide folding due to intra- and intermolecular forces. In contrast, quaternary structures are formed when multiple polypeptide units combine to create the final three-dimensional protein structure. Any alteration to the amino acid sequence can cause a momentous change in the protein's 3D shape, which is crucial to its function. Modifications that occur after ribosomes synthesise proteins, known as post-translation modifications (PTMs), are also essential to regulate cellular activity and aid in cell signalling. [30] PTMs can sometimes occur at other stages in the proteins' life cycle; enzymes may mediate these, or they may occur spontaneously. Erroneous PTM processes can interfere with normal cell biology and pathogenesis, making it critical to identify and understand PTMs when studying disease treatment and prevention. These PTMs include phosphorylation, glycosylation, methylation, acetylation, lipidation, and proteolysis, with this chapter exploring only glycosylation and are summarised below - table 1-2.

Table 1-2: Summary of the common PTMs that may occur to a protein.

Name	Type of modification
Acetylation	Addition of acetyl groups to nitrogen atoms of amino acid residues
Methylation	Addition of methyl groups to an amino acid residue
Phosphorylation	Phosphorylation of amino acid residues..
Lipidation	Addition of lipid group to a protein.
Proteolysis	Enzymatic cleavage of a protein into smaller fragments.
Glycosylation	Addition of glycans to amino acid residues.

IV. GLYCOSYLATION

Glycosylation is a post-translation modification occurring in the cell's endoplasmic reticulum (ER) and golgi apparatus. This process is enzyme catalysed. Half of all proteins typically expressed within a cell undergo this process. Glycosylation aids cellular functions such as antigen recognition, gene expression, protein folding and cellular communications. [31] Errors during this post-translational modification have resulted in many human diseases – diabetes, cancer, and neurodegenerative diseases [32,33] This modification entails the addition of oligosaccharides (glycans) to an amino acid residue of the polypeptide chain; there are five known types of glycosylation: N-glycosylation, O-glycosylation, C-glycosylation, glypiation and phosphogylcosylation. [34] Only those frequent to eukaryotes are summarised in table 1-3.

Table 1-3: Types of post-translational modifications of proteins common to eukaryotes.

Name	Type of modification
N-glycosylation	Glycan attached to the amide group of Asn.
O-glycosylation	Glycan attached to the hydroxyl group of ser, threonine (Thr) or tyrosine (Tyr).
C-glycosylation	Glycan attached to the C2 atom of tryptophan (Trp) through a C-C bond.
Glypiation	Glycan acts as a bridge to connect the protein to a membrane bound anchor.

The primary peptide sequence determines the number and locations of potential glycosylation sites. N-glycosylation is the most common; the N denotes that the glycans are covalently binding to the nitrogen atom of asparagine of the polypeptide chain. In contrast, O-glycosylation is due to the covalent binding of the polypeptide's serine and threonine hydroxyl residues (figure 1-7).

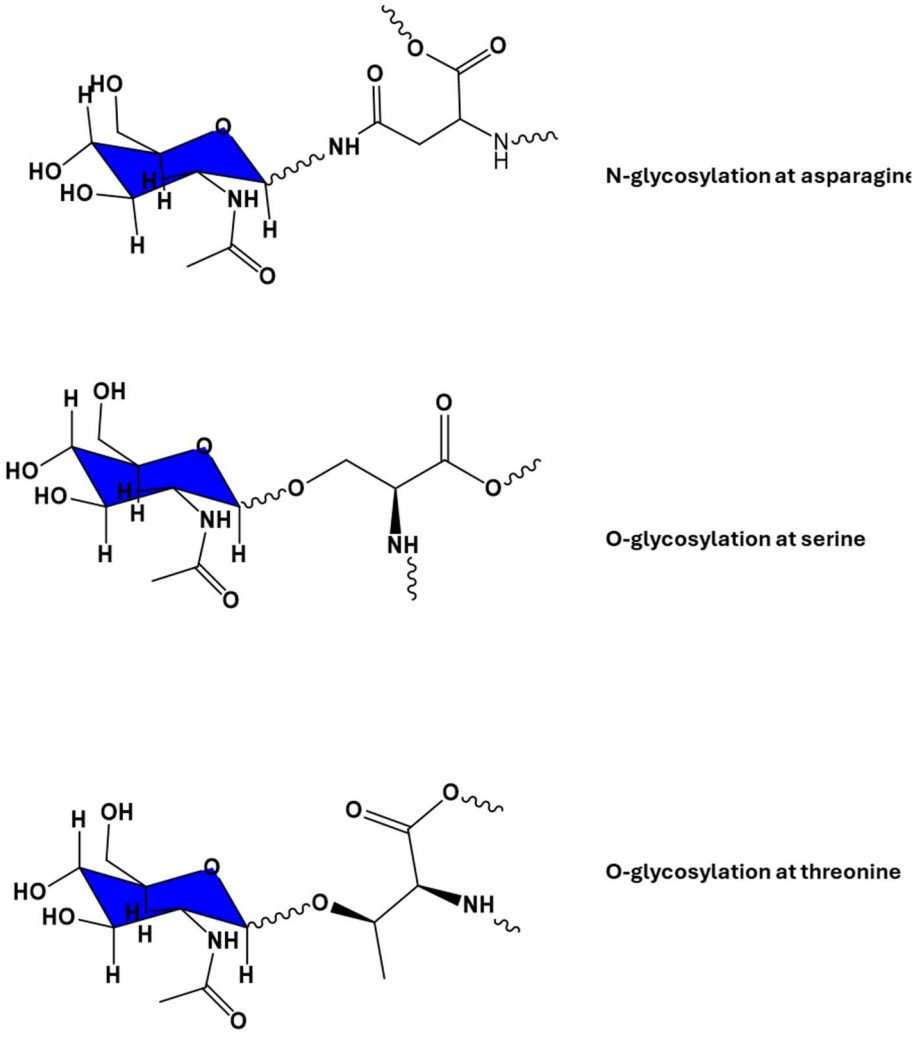


Figure 1-7: N-linked and O-linked N-acetylglucosamine residues.

N-glycans will be the focus of this thesis since the single N-glycosylation site of PSA has varying glycan motifs in literature.[17]

V. N-GLYCOSYLATION

N-glycosylation is the most common and complex post-translational protein modification, which affects 90% of glycoproteins. [35] This leads to adding glycans via covalent bonds to the nitrogen atom of asparagine or arginine side chains of the polypeptide sequence (figure 1-7). N-glycosylation occurs in the endoplasmic reticulum (ER) by glycosyltransferase enzymes that recognise specific amino acid motifs. It is at these motifs that the N-glycosylation takes place. For N-glycosylation in eukaryotes, only Asparagine (Asn) is glycosylated, providing there are the following sequences adjacent: -Asn-X-Thr or -Asn-X-Ser whereby X can be any amino acid except proline.[36,37] The presence of proline a bend in the peptide, resulting in a β-turn and a 180-degree bend in the peptide sequence. This can hinder glycosylation, prevent post-translation modifications, and impede protein function (figure 1-8). [38,39]

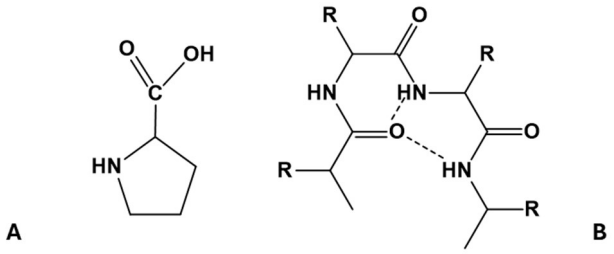


Figure 1-8: A) Proline the amino acid. B) Schematic of beta turns in a polypeptide sequence inducing almost 180-degree turns. Dotted lines depict the hydrogen bonds that stabilise the structural motif commonly observed in proteins.

This sequence alone does not guarantee glycosylation; it depends on the number of glycosylation sites in a protein and the expression of glycosylation enzymes within the cells. [15] The protein's secondary structure will influence if the Asn unit is spatially available for glycosylation.

The beginning oligosaccharide produced in the ER is universal to all N-glycans at the beginning of their life cycle. The starting 14 sugar precursor is depicted below (figure 1-9). The process begins with the formation of a glycosidic bond between the asparagine residue of the -Asn-X-Thr or -Asn-X-Ser sequence (figure 1-7) and the first sugar units (GlcNAc, Figure 1-1).The formation of this first bond to the protein initiates enzymes known as glycosidases. These remove 3 Glc and 1 Man (figure 1-1) unit from the Glc3Man9GlcNac2 precursor.

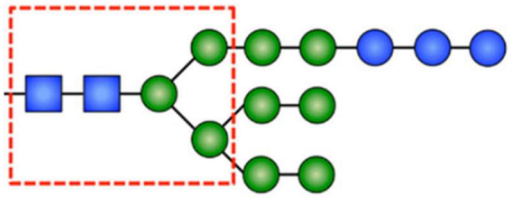


Figure 1-9: $Glc_3Man_9GlcNac_2$ starting glycan precursor for N-glycosylation of proteins in the endoplasmic reticulum. The "core" glycan structure for N-glycans is highlighted in the red box. Image reproduced from literature. [40]

This process signals and aids protein folding by enhancing protein solubility and signalling lectin-based chaperones - calnexin and calreticulin. [40,41] The lectin-chaperones catalyse disulphide bond formation, which aids the formation of the native conformation.

Once achieved, vesicles transfer the newly synthesised glycoprotein to the golgi apparatus for further PTMs, such as removing further Man units or adding other sugars such as fucose, sialic acid and galactose.

In the golgi apparatus, further modifications occur to the polypeptide strand. The golgi apparatus comprises many spherical sacs that function independently with their different enzymes. At the end of the processing in the golgi apparatus, three general glycan structures arise: high mannose, hybrid, and complex N-glycans (Figure 1-10) [40]

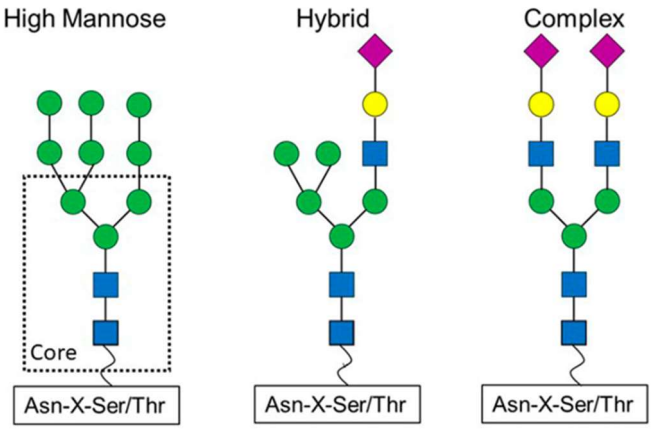


Figure 1-10: Types of N-glycans produced following glycosylation within the golgi apparatus.

The protein will have different glycan structures at each available glycosylation site since not all processes will occur uniformly. The final processed glycoproteins are transported from the golgi apparatus in secretory vesicles to their required site, such as the cell membrane. Glycan structures on the cell surface often provide detailed information on the cell state. Glycan structures in healthy cells will differ considerably from those in diseased cells. One such example is the increasing number of branched N-glycans in cancerous entities, as opposed to healthy cells and tissues.[42] In recent years, aberrant N-linked glycosylation has been linked to many diseases: rheumatoid arthritis, type-1 diabetes, Crohn's disease, and several cancers.[2,16,43–50]

VI. ABERRANT GLYCOSYLATION AND PROSTATE CANCER (PCA).

Aberrant glycosylation occurs when cellular changes in glycosylation may arise from altered expressions of the enzymes which mediate the addition of saccharides to proteins and lipids. Aberrant glycosylation may lead to the production of glycoproteins with specific cancer-associated aberrations in glycan structures. As previously emphasised, the configuration and composition of the attached glycans affect the biological activities of the proteins. For example, if during the protein folding process as previously described, the protein fails to assume its native conformation and prematurely departs the ER, this could have severe consequences, such as the onset of neurodegenerative diseases, cancers, and diabetes. [51] The standard procedure, if the correct conformation is not obtained, entails the addition of the removed residues. Thus, reforming the original 14-sugar precursor glycan previously shown in figure 1-9. The presence of this precursor glycan signals the incompletion of the folding process and initiates the folding to begin again with the protein. Repetition of the protein folding procedure via the addition and removal of glucose units occurs until the protein is ready for transport. Failure to attain its native conformation via folding activates enzymes to break down the faulty protein. The unfolded protein is transported out of the ER for degradation. Erroneous glycosylation processes are deemed a hallmark of cancer.[52]

Previous glycan studies show that N-glycans of malignant cells are more branched like the complex glycans depicted in figure

1-10 compared to their regular counterparts.[53] This increases the number of glycan termini available for enzymes to modify. A common modification is the sialyation of these branches by Sialyltransferases. [42,48] Sialyltransferase enzymes add sialic acid units (figure 1-11) to glycans. These units are nine carbon backbone sugars, which can be present in various forms; predominantly, the β form is present in aqueous solution, whilst the α form dominates in glycan structures in nature. The cyclic structures account for around 98% of the species in water, with the remaining 2% being the linear forms.[54] These sialic acids are known markers for various receptors involved in the trafficking of cells.

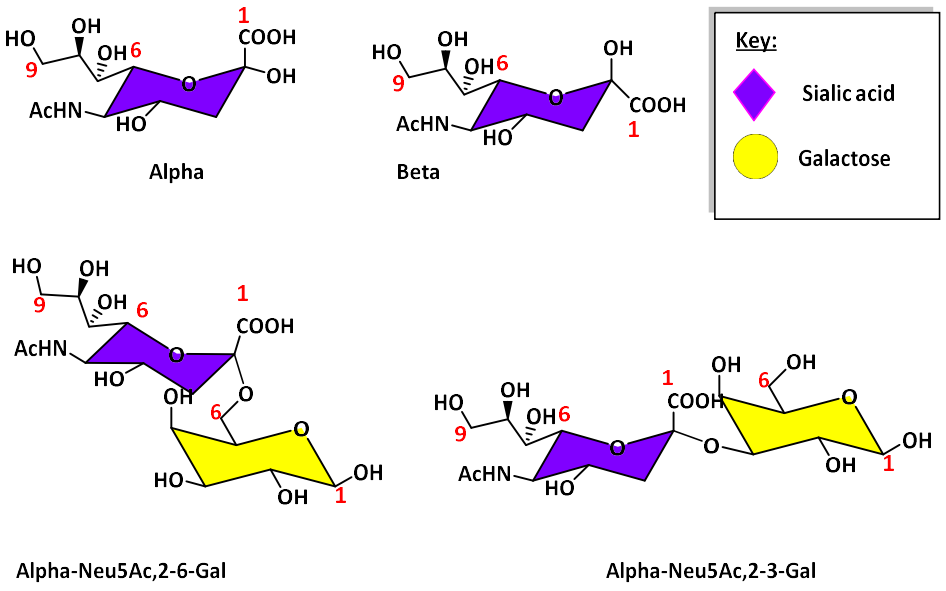
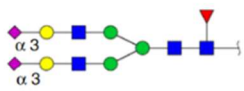
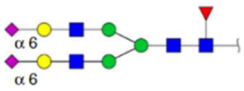
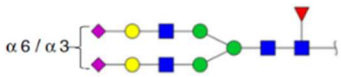


Figure 1-11: Epimers of sialic acid and the dominant alpha form present in glycans with the commonly observed, α2-6-Gal and α2-3-Gal linked glycan motifs.

In the late 80s, many researchers found the over-expression of sialic acids indicative of metastatic cancer. Tracking sialic acid expression changes via lectin binding studies displayed critical

differences in the glycan structures of PCa tissues compared to BPH tissues. More recent lectin-binding studies by Gratacós-Mulleras and co-workers. identified terminal sialic acid glycoform trends for aggressive PCa serum samples.[55] The serum of aggressive prostate cancer (PCa) patients predominantly contains biantennary glycans that are terminated in α-2,3-linked sialic acids, as displayed in Table 1-4. However, the lectin study revealed a decrease in the number of di-sialylated terminal glycans that end in an α-2,6/α-2,6 linkage on both ends and end in a mixed α-2,6/α-2,3 fashion.[55]

Table 1-4: Summary of Gratacós-Mulleras and co-workers. findings.

#	Glycan Structure	Description	Changes observed for PCa
1		Biantennary α-2,3 sialic acid terminated N-glycan.	Proportions increased in aggressive PCa serum.
2		Biantennary α-2,6 sialic acid terminated N-glycan.	Proportions decreased in aggressive PCa serum.
3		Mixed biantennary α-2,3/α-2,6 sialic acid terminated N-glycan.	Proportions decreased in aggressive PCa serum.

Additionally, high-grade prostate cancers commonly exhibit increased core fucosylation, which is an aberrant process driven by fucosyltransferase 8 (FUT8).[3,26] FUT8 catalyses the addition of a fucose residue to the core glycan structure (highlighted in the red box in Figure 1-9) at the innermost GlcNAc residue of N-glycans (as shown in Table 1-4) via the red triangles

to form an α-1,6 glycosidic linkage.[56] The upregulation of FUT8 in some cancers is crucial in the immune evasion process and the regulation of various immune-related proteins, contributing to disease progression.[55,57,58]

Slight changes in glycan structures can have a tremendous impact on cellular health and the progression of diseases. Tracking these changes requires knowledge of the complete glycome, which is still largely unknown.[24] However, researchers in the field are progressing by focusing on smaller, known glycan motifs, such as changes in sialic acid and fucose expression. These deviations in structural motifs positively correlate with disease and its progression. These glycan motifs can be specifically targeted with lectins, offering new disease treatment possibilities.

VII. METHODS OF GLYCAN DETECTION AND ANALYSIS

The human system has four fundamental molecules: glycans, nucleic acids, proteins, and lipids. However, the field of glycomics is still in its infancy compared to the advances in genomics and proteomics. [59] Deciphering glycan structures is challenging as glycan biosynthesis is not template-driven and involves a diverse range of enzyme-mediated steps. [22] Conversely, proteins and nucleic acids are template-driven, making their structure prediction easier. Therefore, there is a pressing need for a unified process to capture and analyse glycans, which can aid in developing new diagnostic tools for diseases such as prostate cancer. Lectin-based techniques and mass spectrometry are the current standard methods for detecting and analysing glycan structures. [4,54,55,60].

VIII. LECTIN-BASED TECHNIQUES FOR STUDYING GLYCANS.

Lectins are proteins that naturally bind to specific glycans through non-covalent interactions, including hydrogen bonding, hydrophobic CH-π, and electrostatic interactions. [61] Their specificity for glycan targets depends on the lectin's geometric features and the residues' physicochemical properties within the binding site. Naturally occurring lectins are vital in various human diseases and pathological events, including inflammation, immune responses, protein trafficking, cell adhesion, and cancer. [21,62,63]

In research and medicine, lectins identify abnormal cells and disease biomarkers by detecting glycans on cell surfaces or free sugars in serum. [64] They can also help enrich and purify glycoproteins and their glycan structures, which would otherwise be difficult to isolate. Lectins are commonly utilised in enzyme-linked lectin assays (ELLAs).

In ELLAs, the lectins are immobilised onto a solid surface to capture the target biomolecules. For example, if the target molecule of interest was fucosylated glycans, a suitable lectin used for their capture may be Ulex europaeus agglutinin-1 (UEA-1) lectin.[65] These microplate assays may be visualised via the schematic below.

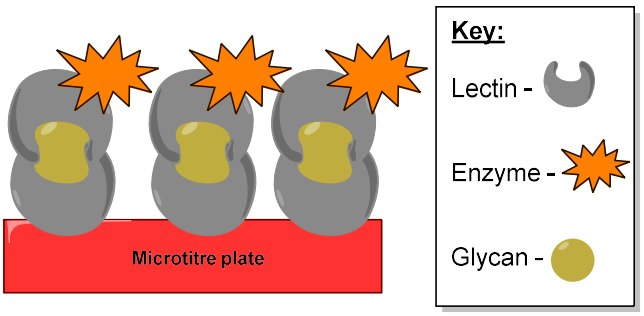


Figure 1-12: Schematic of ELLA (Enzyme-linked lectin assays) plate assays for glycan detection.

Following glycan capturing, a second lectins which is conjugated to a detection molecule such as biotin are added to form the "sandwich," much alike the traditional ELISA (enzyme linked immunoassays). The lectins are traditionally linked to specific enzymes to form an enzyme-lectin conjugate to detect specific carbohydrates on the surface of cells or glycoproteins. The extent of activity of the enzyme-lectin conjugate is proportional to the amount of the specific glycan motif present, permitting relative quantification via the enzymes.

Naturally, these detection methods are limited due to enzymes' expensive nature, short shelf life and sensitivity. However, ELLAs are still used since they are accessible and quick, making them highly convenient for high-throughput analysis. [65] One such example, is their use in tracking fucosylation levels of PSA in patients' serum, to compare the difference between PCa and BPH patients.[65,66] However, they are not without drawbacks; these assays are often associated with issues providing appropriate blocking solutions to prevent nonspecific binding with the microplate surfaces used.

Lectins may also be incorporated onto nanoparticle surfaces to identify glycans on cellular surfaces, or free in serum. For

example, circulating tumour cells (CTCs) often overexpress specific glycan motifs.[67] The lectin-functionalised nanoparticles can identify these specific glycan motifs. For ease of isolation, the nanoparticles may possess a magnetic core to avoid cumbersome isolation methods. This technique has been exploited in literature and a schematic illustrating the process is provided in Figure 1-13.

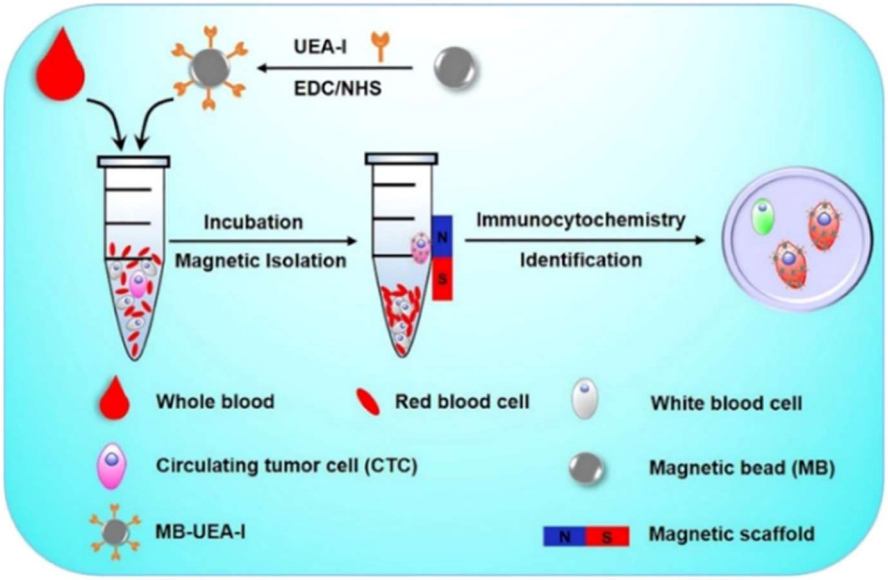


Figure 1-13: Schematic was taken from literature [67] – illustrates the use of lectin functionalised fluorescent magnetic nanoparticles (MB-UEA-I) for enriching circulating tumour cells (CTC) present in serum samples.

Consequently, lectin-decorated magnetic nanoparticles are employed in glycan studies. Prior studies showed the ability to detect CTCs from colorectal cancer specimens owing to the specificity of the lectin for α,1-2-fucose motifs, which are commonly overexpressed in the serum of colorectal cancer patients. [67,68]

Alternative methods of detecting aberrant glycosylation have been conducted in literature for the detection in-vivo. [69–73] For example, nanoscale diagnostic imaging systems have been created to target over-expressed glycan motifs affiliated with cancers such as colorectal cancer. [68]

These nanosystem comprises fluorescently labelled nanoparticles bearing the relevant glycans for their targets. Chen and coworkers created FITC (Fluorescein isothiocyanate)-labelled silica nanoparticles decorated with lectins (Ulex europaeus Agglutinin-1 (UEA-1)).[68] Thus, nanoparticles accumulated at sites with a significant presence of α,1-2-fucose (i.e., colorectal polyps) as demonstrated via Figure 1-14.

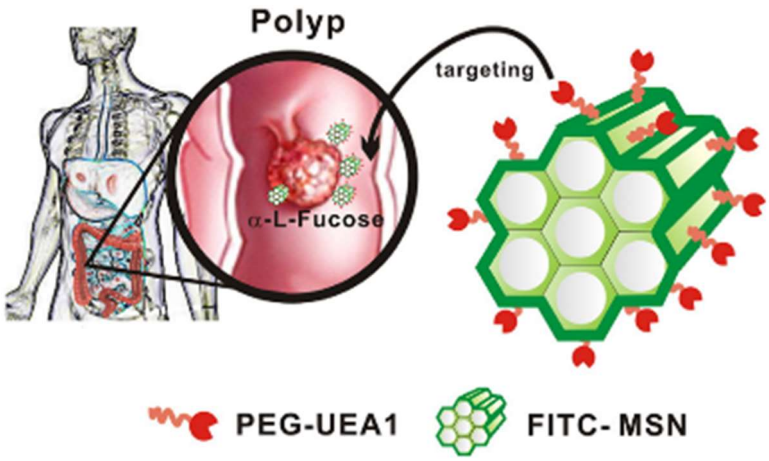


Figure 1-14: – Fluorescent mesoporous silica nanoparticles labelled with the UEA lectin, which targets α,1-2-fucose motifs overly expressed on CRC polyps. Schematic taken from literature.[68]

The study found the nanoparticles preferentially accumulated at carcinomas and adenomas. A probable reason may be

glycosylation patterns of these cells result in the terminal fucose motifs more spatially accessible for a binding.[74]

The methods using lectins mentioned earlier can only offer an approximation of a few specific glycoforms. Furthermore, they may not accurately reflect the true nature of glycan interaction in living organisms for the examples provided where glycans were cleaved from their parent biomolecules. [25] In addition, the glycans are often present in tiny amounts, therefore enrichment is carried out.

Enzymes are used to digest glycoproteins from cells, organs, and serum to isolate glycans from crude sample mixtures. However, these samples usually contain significant impurities, including peptides, lipids, DNA/RNA, and salts, which could introduce impurities or alter the glycan structures during the enrichment process. Finally, the proteins may be impacted by environmental changes and exposure to different buffers and enzymes, which could cause conformational changes that damage the structural information that researchers are seeking. Even if the purification process does not contaminate or alter the glycan structural information, the interactions being studied are weak. Lectin-glycan interactions are considered weak binding events, with values typically in the Ka ≈ 10^6 -10^7 mM^{-1} range. [75]

Other limitations of using lectins include poor selectivity, limited resistance to heat and pH changes, and high production costs. [62,64,76] These restraints make it challenging to use lectins in widespread clinical applications.

Alternative methodologies used to study glycans entail the use of lectin-based affinity chromatography. This methodology is more quantitative and specific, separating and enriching the glycan motifs first. It is often the first step before conducting mass spectroscopy (MS) for structural analysis. This will next be discussed.

IX. USE OF LECTINS IN TANDEM WITH MASS SPECTROMETRY (MS).

The analysis of glycans is a multifaceted process that often involves several techniques, including enzymatic sequencing, lectin enrichment, NMR, MS, and computational studies.

Mass spectrometry (MS) is a sensitive and efficient technique that can provide structural information on complex macromolecules. While it is commonly used for proteomic studies, analysing glycans using MS alone can be conducted, although difficult, due to their low abundance, microheterogeneity, and poor ionisation efficiency in the presence of other biomolecules like peptides. [14] As a result, additional techniques are necessary to enrich the abundance of glycans by removing other biomolecules from the solution.

The enrichment and isolation of glycoproteins may be achieved through techniques such as lectin-affinity chromatography and lectin micro-assays. Lectin based sandwich assays have been previously discussed (Figure 1-12).

In lectin-affinity chromatography, lectins are affixed to a solid support, such as a chromatography column. The sample, containing glycoproteins, is passed through this support, the

glycan motifs of interest bind to chromatography column. Non-target biomolecules are washed away using a buffer, leaving only the bound target molecules. Bound target molecules are eluted from the column via the use of an elution buffer, interrupting the interactions between the bound targets and the stationary phase.

The analysis of eluted biomolecules is conducted via MS methods. To reduce the destruction of the sample during MS analysis, soft ionisation techniques such as electrospray ionisation (ESI) and matrix-assisted laser desorption ionisation (MALDI) are commonly employed. The aim of these softer ionisation methods is to reduce the likelihood of fragmentation and simplify the obtained spectra.

The produced signals (m/z peaks) can be compared with data from search engines to infer the structural motifs present. Several glycan search engines are available, including GPFinder 3.0, Glycopeptide search, MAGIC, I-GPA, Byonic, and PGlyco 2.0. [35] These search engines contain information on the possible theoretical fragments that can form from the N-glycoproteins and provide statistical analysis on how closely the experimental data matches the expected theoretical fragments.

Lectin affinity chromatography is a valuable tool in conjunction with MS for studying glycans. However, it does have limitations related to lectins. One of the challenges is distinguishing between different isomers of glycans and other biomolecules with similar structures and masses. Additionally, the lectins used in this technique may modify glycan motifs during interaction with the affinity column, and they are both unstable and expensive. Eluting the glycans from the lectin columns

often requires harsh conditions, such as high salt levels and pH changes, which can lead to degradation and reduced accuracy of glycan characterization downstream. Nonetheless, when used in combination with mass spectrometry (MS), lectins can provide valuable structural information on captured glycan motifs. [77]

Ion mobility-mass spectroscopy (IM-MS) is a technique that may be used more commonly in the future. It can differentiate between sugars connected by various glycosidic linkages with varying ion shapes. [78] The technique separates gas-phase glycan ions based on their interaction with a collision gas and their corresponding masses. Firstly, the ions are separated by their mobility through a buffer gas on a millisecond timescale using an ion mobility spectrometer. Then, their mass-to-charge ratio is determined using a mass analyser. The process relies on the "drift times" of ions in the collision gas, which provide information on the ion's shape and size. The IM-MS technique converts the ion's "drift times" into a rotationally averaged collision cross-section (CCS). These CCS values are unique to a specific ion in a specific drift gas and can be stored in a database to identify different isomers of the same m/z. A database of different glycan motifs' CCS values can be published to detect glycans in biological samples more efficiently. However, there is yet to be a conclusive database containing this information. Moreover, the technique requires a competent scientist to enrich glycans from their parent biomolecules, a complex process. [78]

Present glycan analysis conducted routinely is moving towards an automated processing system which reduces the analysis

and enrichment/isolation time vastly to facilitate its use in a clinical environment for diagnostic purposes. [15,79]

X. GLYCOBLOTTING FOR GLYCAN DETECTION

Until the 1980s the determination of glycan sequences was rarely attempted outside of Japan as the task could take up to one year to achieve owing to the difficulty of glycan purification and enrichment.[80] Present technology has advanced significantly over the last 30 years permitting easier analysis of glycan structures. Majority of the early sequencing attempts were conducted by Akira Kobata and colleagues. [81]

A popular research method is '*glycoblotting*.' Briefly, the "blotting" process entails the isolation of the glycans via enzymatically or chemically cleaving them from their proteins, like previously discussed. The final isolated glycan mixture is separated by use of gel electrophoresis prior to the glycoblotting procedure.[80] The procedure results in the separation of glycans on a gel membrane and individual signals occurring for each glycan type.

More recent advancements have saw the "*blotting*" procedures become automated, with the production of a commercialised automated instrument - '*SweetBlot™*'.[59,80,82–84] The research protocol was originally proposed by Nishimura and co-workers.[83] The advantages of automating the "blotting" include increased efficiency, reproducibility, and increased throughput.[85] With up to 96 glycan samples being able to be simultaneously processed without any specialised training. [85]

Furthermore, MS may be used in tandem with such blotting methods . [15,82,85–88] This method involves the use of beads

("BlotGlyco") to capture and isolate the glycans from other biomolecules before MS structural analysis. This differs from the well-known gel membranes traditionally used for "blotting" as described above. The general workflow for this is outlined in the below illustration. [89]

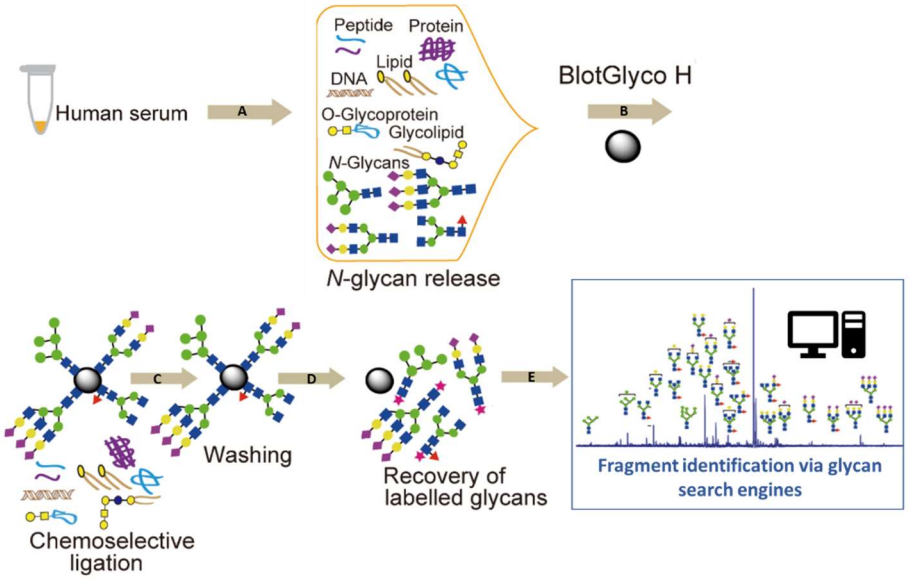


Figure 1-15: Schematic workflow of glycoblotting-assisted MALDI-TOF/MS analysis of glycans in serum recreated from literature. [89] Steps A-D are conducted by an automated "SweetBlot" instrument and is used in tandem with MALDI-TOF/MS. A) Enzymatic cleaving of N-glycans from proteins to produce a complex mixture conducted manually B) Automated process of attachment of N-glycans to hydrazide-functionalised 'BlotGlyco beads' C) washing to remove impurities D) Recovery of the captured glycans for structural analysis.

The “SweetBlot” instrument conducts steps A-E automatically.[88] First, the process begins as always with the release of the glycans from their biomolecules. Next, the targeting and isolation of the glycans can be conducted via the use of “BlotGlyco” beads. “BlotGlyco” beads are coated with hydrazide functional groups which enables them to participate in chemoselective reactions with the reducing end (aldehyde/ketone functional groups). of glycans. The resulting hydrazone bond permits the use of vigorous washing steps eliminating other impurities which are non-specifically bound. Finally, the glycans are released from the beads for MALDI-TOF-MS analysis. The resulting fragmentation patterns may be cross-referenced to glycome databases for glycan identification. Through this protocol, over 300 cancer patients' N-glycan structures were analysed and identified, with the glycomic database providing matches for patients' samples based on their recorded aberrant glycosylation patterns. [82]

The advantages of using “BlotGlyco” beads over traditional gel membranes in glycoblotting are improved signal-to-noise ratio, recovery, chemoselective glycan enrichment, more streamlined processes.[90–92] Furthermore, the beads may offer enhanced efficiency due to the beads possessing specific functional groups for capturing and isolating glycans, such as hydrazide or boronic acid groups.[83] The formation of these covalent bonds thus reduces the non-specific interactions as unbound molecules are washed away. Additionally, glycobeads may exhibit higher binding capabilities and lower nonspecific binding compared to traditional gel membranes. These properties reduce the risk of sample loss and increase the

recovery of glycans, leading to more reliable and reproducible results.

To conclude, automated glycan purification such as '*SweetBlot™*' (System Instruments, Hachijo, Japan)[93] is a highly efficient alternative to manual methods that require skilled scientists for enrichment.

However, this method is not without its drawbacks for analysing glycans. The implementation of sweetblot into clinical environments is presently limited due to incomplete glycomic libraries and high instrumentation costs. [15]

XI. LIMITATIONS OF LECTINS FOR GLYCAN DETECTION

Thus far, the techniques within this chapter have been focused on the use of lectins and enzymes for the release and subsequent capturing of glycan motifs from their parent biomolecules. Therefore, all these techniques inherently have similar drawbacks. Some of these drawbacks are their instability, short shelf-life, and susceptibility to degradation.[64,76,94] Furthermore, the use of such enzymes to cleave the glycans from the parent and the subsequent processing (i.e. glycoblotting) the glycans undergo may increase the chances of altering the natural morphology of these carbohydrates, leading to unreliable analysis.

A further consideration, these methods rely on the Glycomics database, to identify structural fragmentation patterns produced via MS methods. The obtaining of the MS spectra is reliant on known lectins for targeting the biomarkers. Since, the human glycome is incomplete and there is a finite range of lectins, this limits the ability to identify all aberrant glycan motifs.[24]

The lectin-based methods lack specificity in discriminating different glycosidic linkages such as α-2,3 and α-2,6 linkages (Figure 1-11) previously discussed.[95] These factors preclude the use of “Sweetblot” in tandem with MS translation for clinical diagnostic purposes.

Alternative, methodologies such as the IM-MS are currently being developed to overcome this but are reliant on glycomic

databased also. Thus, there is still a major barrier to translating these techniques to clinical environments.

XII. SYNTHETIC RECEPTORS FOR GLYCAN DETECTION

When targeting natural biomolecules like glycans, the most effective approach is to emulate nature's processes biological recognition events. Therefore, creating new glycan receptors that replicate natural lectin-glycan interactions is crucial. The desired synthetic glycan receptors must provide greater binding affinities – naturally occurring lectin binding are remarkably weak for biological molecular recognition ($<10^7$ M^{-1}).[96]

Successful synthetic receptors offer several benefits, such as increased stability and resilience to external environmental changes (like temperature and pH). Furthermore, easy modification is advantageous, including the use of fluorescent probes for visualisation or quantification without the need for expensive, complicated and expensive analytical equipment like mass spectrometers. Synthetic lectins have a wide range of applications, including diagnostics, therapeutics, and research. Synthetic receptors can operate via covalent or non-covalent interactions.

XIII. SYNTHETIC NON-COVALENT RECEPTORS (SNCRS)

During the process of engineering synthetic receptors researchers commonly refer to the crystal structures of the native lectin-glycan complex for inspiration and hence interact similarly to lectins. [97,98] Important non-covalent interactions of interest include: π-π, H-Bonding and CH- π interactions and are highlighted below in

Figure 1-16. The H-bonding may occur between polar functional groups of the target and receptor. The CH- π interactions may occur between the CH of sugar rings (pyranose/furanose) with aromatic rings of the synthetic receptors. [99,100]

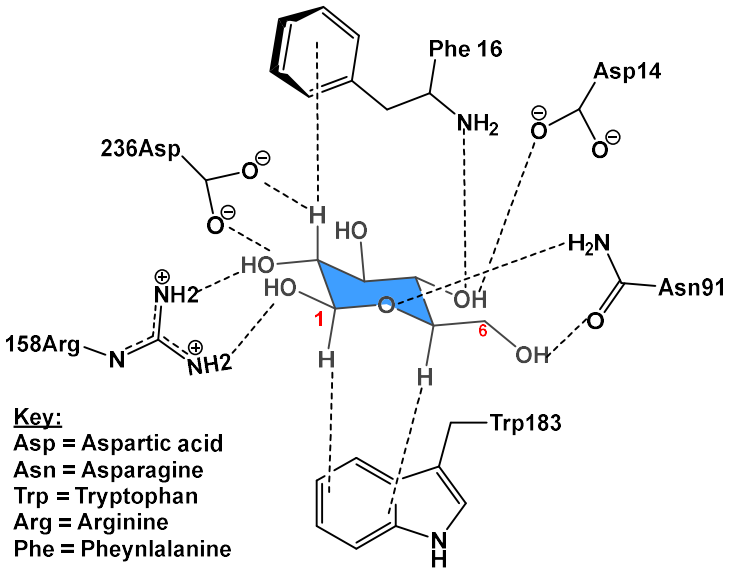


Figure 1-16: Diagram depicting the common intermolecular interactions occurring between synthetic receptors and glycan units. [101]

Binding a synthetic receptor to its target in aqueous media poses numerous challenges. To be considered an excellent synthetic receptor, it must be able to function effectively in aqueous conditions, outperform natural biological receptors, and maximise the number of interactions with the glycan to promote high selectivity and affinity. These interactions include hydrophobic interactions (for -CH groups), polar interactions (for -OH groups), and electrostatic interactions (for charged groups such as $-COO^-$). One of the most significant barriers a receptor must overcome is distinguishing between the hydroxyl groups of the glycans and the almost identical hydroxyl groups of the aqueous media, as depicted in Figure 1-17. [63,102–106]

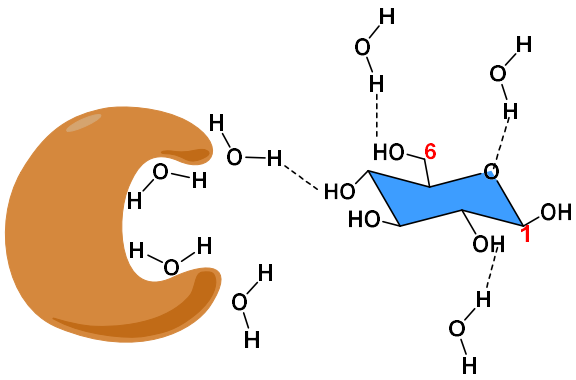


Figure 1-17: Schematic to illustrate the sugars solvation and the challenge a lectin faces when trying to differentiate between hydroxyls of water and sugar.

To interact with the sugar in aqueous media, a lectin must also overcome the solvation of the glycan itself and displace a water molecule (Figure 1-17). Although this process is almost isoenergetic, when non-polar CH groups of the sugar encounter non-polar regions of the receptor, this interaction is much more thermodynamically favoured.[107] This interaction displaces higher energy water molecules from both the sugar and

receptor, allowing them to move freely into the bulk of the solvent, thereby reducing the system's free energy. This compensates for the isoenergetic polar interactions. Furthermore, the lack of functional groups that target hydroxyl groups further exacerbates the challenge of designing synthetic carbohydrate receptors.[107]

Most early work on synthetic receptors was trailed in organic media such chloroform, acetonitrile, and acetonitrile: methanol mixtures. [108] The receptors often including some of the following moieties – imidazole, pyrrole, pyridine, or biphenyl (BIPY) rings incorporated into the framework, these all permitted the mimicry of the vital CH-π, π-π and H-bonding interactions. [109–113] Receptors which operate on mimicry of protein-carbohydrate interactions are termed biomimetic synthetic receptors. Several types of macrocyclic structures have been developed by Aoyama[114] and Davies[115] , whilst acyclic structures have been studied by Mazik[63,102–106] and Francesconi.[116–119]

Typically, the design of artificial receptors is guided by Cram's principles of complementarity and preorganisation. Complementarity states "hosts must have binding sites which can simultaneously contact and attract the binding sites of the guests without generating internal strains or strong nonbonded repulsions."[120] Preorganisation states "*the more highly hosts and guests are organised for binding and low solvation prior to their complexation, the more stable will be their complexes*."[120]

The common initial systems arising in the early 1990s were large macrocycles which were highly organised for binding to sugars with both polar and non-polar complementary functionality. A

commonly referenced system is that of Davis and co-workers developed in 1998 and is shown in Figure 1-18.[114]

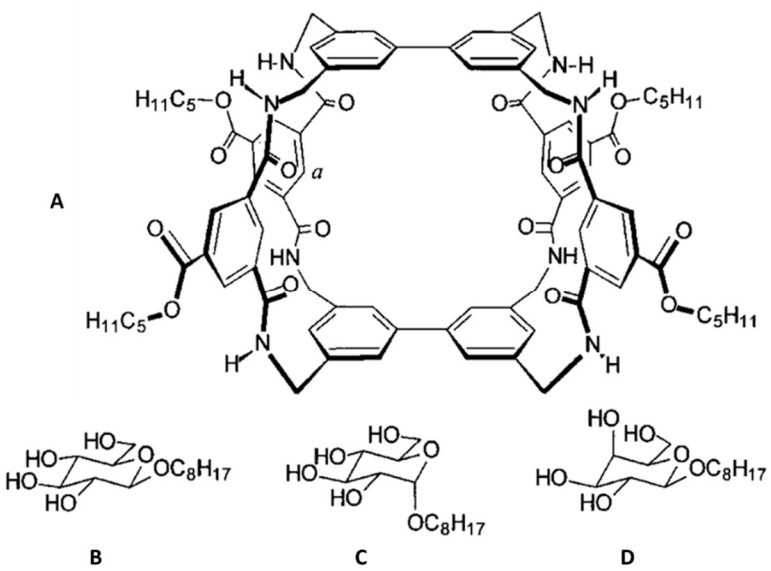


Figure 1-18: Diagram recreated from literature[115] for the structures of Octalam (A) and its glucopyranose derivatives (A-C) used in the NMR binding study ($CDCl_3$/MeOD).

The octalum structure illustrated above was assessed in a non-polar, aprotic solvent to ensure solvent molecules did not compete with the receptor for non-covalent interactions (I.e. hydrogen bonding). Following the addition of the glucose derivatives (Figure 1-18) the NMR spectra displayed clear peak shifts for the BIPY protons, indicating binding. However, the NMR peaks were broad and poorly resolved due to the limited solubility of octalum in pure chloroform.[115] Thus, a fluorescence titration was carried out to obtain the following association constants (Ka) were observed in chloroform: 1.3×10^4 M^{-1}(α-anomer) and 3×10^5 M^{-1} (β-anomer).[121] When octalum is excited with a wavelength of 285 nm (λ_{exc}), it emits a fluorescent signal

(λ_{MAX}) at 387 nm. Upon octalum interacting with the glycosides the fluorescent intensity was observed to be reduced. [115]

In the presence of methanol (8%) an NMR binding study was able to be conducted ($CDCl_3/CD_3OD$ 92:8) to obtain association constant values of 980 M^{-1}(β-anomer) and 20 M^{-1} (α-anomer) for the glucose derivatives. Thus, both NMR and fluorescent studies displayed a preference for the β-D-glucoside over the α-anomer. The interactions between octalum and the sugars may be explained by considering how lectins interact in nature.

From crystallographic studies of lectins interacting with sugars it is known aromatic amino acids can provide positive intermolecular interactions such as hydrophobic CH-π by situating above the plane of the sugar ring. As previously shown in

Figure 1-16. This was the inspiration for the placement of biphenyl (BIPY) rings at the top and bottom of the macrocycle, to provide structures known as “temples.” The “temples” always consist of apolar aromatic roofs and floors, whilst the pillars are always polar. Thus, the aromatic rings are situated above and below the plane of the sugars and may interact with axial substituents of the sugar (Figure 1-18-B/C) via CH-π interactions. The equatorial groups of the pyranose sugar may interact with the polar side groups connecting to the BIPY rings via hydrogen bonding (H-bonds). [96]

The significant increase in the binding affinity for the fluorescent study may be rationalised by the removal of the competing solvent.[122] Despite, the observed binding, the octalum structure had several issues with solubility and synthetic yield. The

receptor system was later modified in the early 2000's to incorporate more hydrophilic side chains to improve its solubility. [107] The improved structure is illustrated below -Figure 1-19. The greater solubility in aqueous solvent systems permits ease of structural analysis (i.e. NMR) in a more biologically relevant solvent without the need of functionalised monosaccharides.

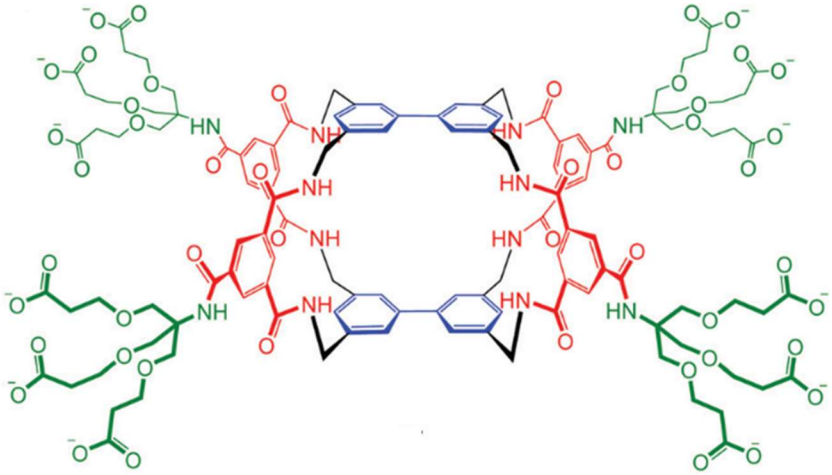


Figure 1-19: Diagram taken from literature[107] for the first water-soluble temple receptor designed by Davis and coworkers in 2005.

Thus, the above structure can be studied with a racemic mixture of naturally occurring glucose in aqueous medium via NMR or fluorescence titrations. The racemic mixture of glucose (α/β = 40:60 was added to the new synthetic receptor to provide an association constant of 9 M^{-1}(fluorescence titration). [123] Thus, this revised ocatulum structure in the presence of water produced a significantly lower binding constant. Highlighting the challenge of targeting monosaccharides in water owing to solvation competition when binding non-covalently. Furthermore, the selectivity of the newer water-soluble temple

remained the same (I.e. β anomer >> α anomer). The system was also trialled with other monosaccharides, and binding was observed, displaying the system was not exclusive for glucose only. Rather, these "temple" structures were found to bind more significantly to all equatorial saccharides. [123] The sugar with the highest binding constants was found to be methyl β-D-glucoside (Ka = 32 M^{-1}) followed by D-glucose (Ka = 9 M^{-1}). [96]

The synthesis process for temple-based structures was lengthy, resulting in low yields of less than 2% and a preference for equatorial saccharides. However, researchers led by Ke have developed a simpler system that produces higher yields.[124]

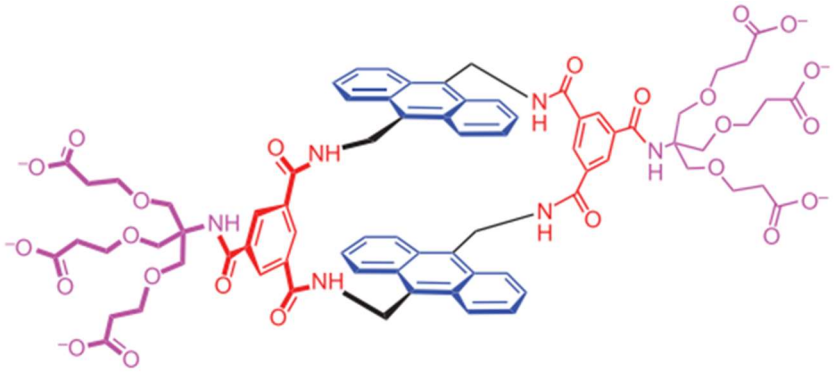


Figure 1-20: Diagram recreated from literature [124] to depict a simpler anthracene biomimetic receptor inspired by octalum. ^{1}H NMR (D_2O) studies with glucose and methyl β-D-glucoside produced binding constants (Ka) of 56 M^{-1} and 96 M^{-1} respectively.

When studied via fluorescence titrations analogous to those conducted for octalum, the system was found to bind more tightly to glucose, with a binding of (Ka) 56 M^{-1}. Despite its simplicity the anthracene-based receptor was observed to be highly selective for glucose over other sugars and hence more

practical for real-world applications - glucose sensing. However, like octalum (Figure 1-18-A & Figure 1-19), this system also binds to all equatorial sugars. [124]

Subsequent modifications to the octalum temple-based receptors were conducted via Barwells and coworkers [125] They aimed to improve on the original binding to glucose in water and improve the selectivity of the receptor. Modifications were only made at positions that would not affect the core conformation of the temple. Thus, the 4,4 positions of the BIPY ligands were altered. These positions are indicated in green below by the “R” substituent on the BIPY ring.

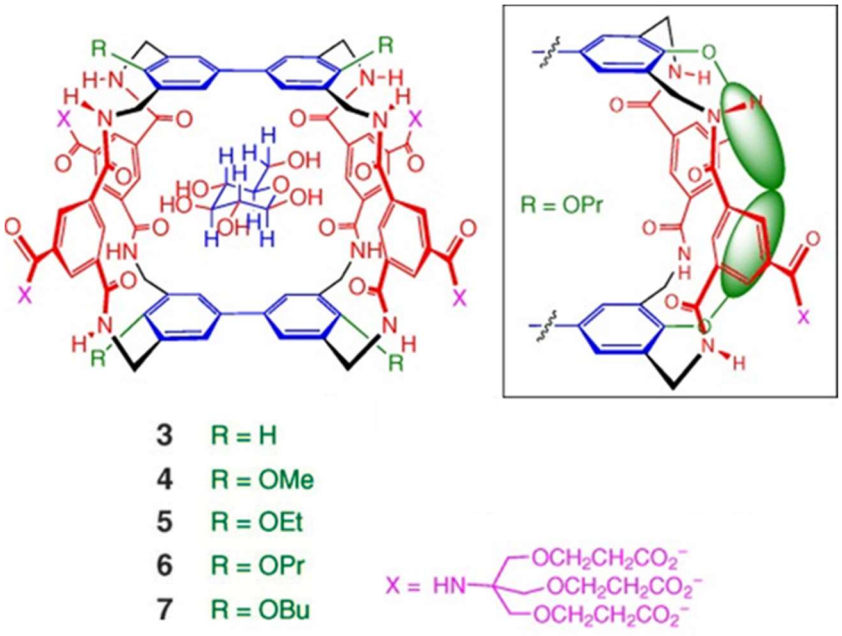


Figure 1-21: Diagram recreated from literature[126] illustrating the effect of substituting octalum at the 4,4' positions of the BIPY ring to provide additional hydrophobic interactions for sugar binding events resulting in significantly improved binding affinity and selectivity towards the targeted sugars.

They observed increasing the alkyl chain length from methyl to propyl ester linkages (R3 – R6, Figure 1-21) resulted in an increased binding for glucose. The propyl ester substituted receptor (receptor 6, R6 - Figure 1-21) displayed the best binding (Ka = 60 M^{-1}). Furthermore, the selectivity of this derivative of octalum was found to be enhanced in comparison to the other derivatives of octalum (Figure 1-18, Figure 1-19). Remarkably receptor 6 was found to be more selective than the natural lectins used for this motif – *concanalin A, lens culinaris agglutinin and psium sativum agglutinin*.[127] These lectins are known to bind both mannose and glucose. The rational of the increased binding as the alkyl length is increased may be rationalised by considering the hydrophobic interactions available to the sugar. [126] However, despite these increase in hydrophobic interactions with the sugar, the association constant was not an improvement over the simpler anthracene structure developed by Ke and coworkers (Figure 1-20).

To increase the hydrophobic interactions of these temple-based receptors, the BIPY rings were substituted for larger aromatic rings to view if the binding could be enhanced. The corresponding new octalum based structures are depicted below (Figure 1-22).

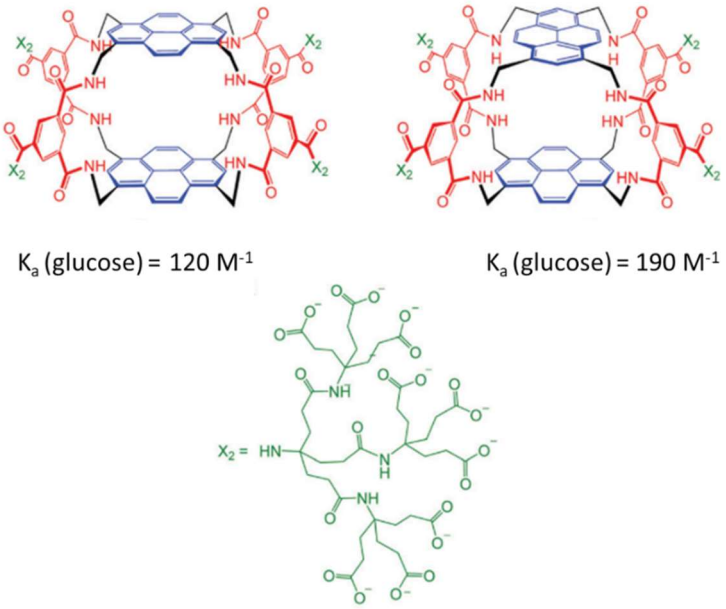


Figure 1-22: Diagram recreated from literature[107] to show the two isomers created when substituting the BIPY ring for pyrene ring of the octalum based temple. The corresponding binding constants were determined via ITC.[128]

The increase in the cavity area resulted in stronger binding affinities for all tested saccharides overall when compared to the previously tested octalum based receptors. [123,124,126]

Thus, the increase in availability of hydrophobic interactions for the saccharides was highly favoured for sugar recognition.[124,129] For example, the glucose affinity increased significantly upon changing to a more extensive aromatic system, as shown in Figure 1-22.[128] Furthermore, the system was found to outperform the natural wheat germ agglutinin (WGA) lectin (Ka = 730 M^{-1}) when binding N-acetyl galactosamine(Ka = 1.8x10^4 M^{-1}).[107]

It may seem counterintuitive that adding extra space for sugar molecules to move would enhance their binding to octalum

temples. However, adding a larger aromatic floor provides more freedom of movement, which increases the hydrophobic surface area and allows for a greater number of complementary hydrophobic interactions. This, in turn, reduces the overall entropic loss in the system. [129] The increased hydrophobic "floor" also helps to displace more water molecules during the binding interaction, further reducing the entropic loss. The enhancements in the binding constants highlight the importance of hydrophobic interactions.

In addition, the larger cavities resulted in a change in the binding modes. Previously, these systems displayed a preference for all equatorial neutral sugars. These newer temples display stronger affinities for axial sugars (e.g. D-mannosamine Ka = $3.12x10^3$ M^{-1}). [129]

The pyrene ring's planar structure enables it to preferentially bind to axial groups in sugars compared to the non-planar BIPY ring. The BIPY ring's ortho protons create a non-planar system, causing steric hindrance for the axial protons or other substituents of the sugars. More steric hindrance exists in the BIPY-based octalum structures' cavity for all axial sugars, which reduces hydrophobic interactions between the sugar and the BIPY ring. Replacing BIPY with anthracene removes steric hindrance and allows better interaction between axial components of sugars.

It was hypothesised that the pyrene-based receptor (Figure 1-22), which bound cationic sugars, could be altered to better attract sialic acid (Figure 1-11). Sialic acid is a negatively charged sugar which is difficult to target and detect and is often associated with cancer.[130] To achieve this, guanidine motifs

were incorporated into the system, as they have been found to bind well to sialic acids in a non-covalent manner.[104,131]

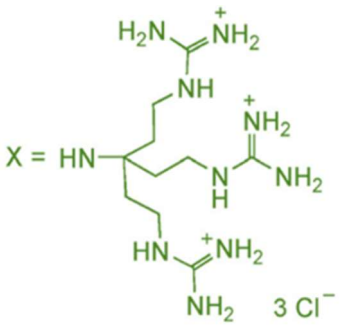


Figure 1-23: Guanidinium motifs added to the side arms of the pillars of the octalum derivative to modify the receptors affinity towards negatively charged sugars such as sialic acid.

By incorporating positively charged guanidinium motifs (Figure 1-23) into the pillars of the "temples" the cavity of the receptors became more conducive to interacting with the negatively charged sugars. The new octalam based biomimetic receptor was impressively shown to bind α-methyl neuraminic acid (methyl sialic acid) with a 1:2 binding stoichiometry (host: guest) with an association constant of 1.3×10^3 and 5.7×10^2 M^{-1}.[129] Thus, a great improvement towards creating biomimetic receptors capable of interacting in a multivalent manner for the detection of an array of sugars in a biological medium. The synthesis of these receptors were complex procedures, and isolating of the isomers was highly challenging task with a yield below 30%.[129]

Elsewhere, less elaborate systems have been explored which have the advantage of simpler synthetic routes with higher yields. Hamilton et al[132], showed complex macrocycles are not

necessary to obtain modest binding (Ka = 2.6 x 10^4 M^{-1}) to saccharides (1-O-octyl-β-D-glucopyranoside) (Figure 1-18-B) in organic aprotic solvents (Figure 1-24). However, due to the solvents they operate in they have limited translation to biological applications.

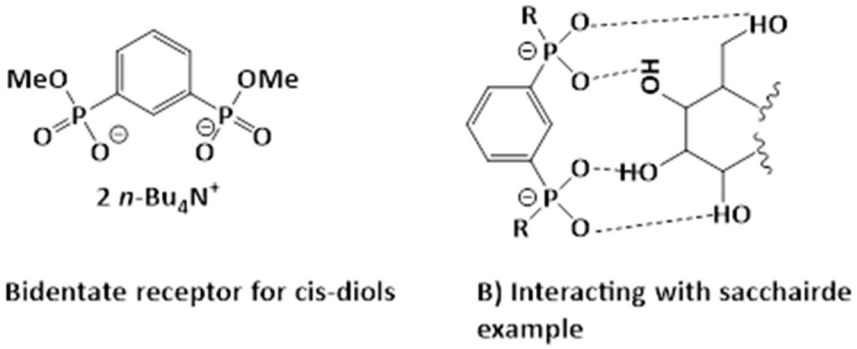


Figure 1-24: Schematic of simple carbohydrate receptor capable of binding 1-O-octyl-β-D-glucopyranoside proposed by Hamilton and co-workers to obtain modest binding (Ka) of 26, 000 M-1in aprotic organic solvents such as acetonitrile.

Elsewhere, advances were made in the field to create systems capable of binding multiple sugars which would improve on the octalum based receptors. Francesconi[117] explored molecular tweezer-based systems (Figure 1-25) using bridges of varying sizes to examine selectivity and binding towards mannosides.

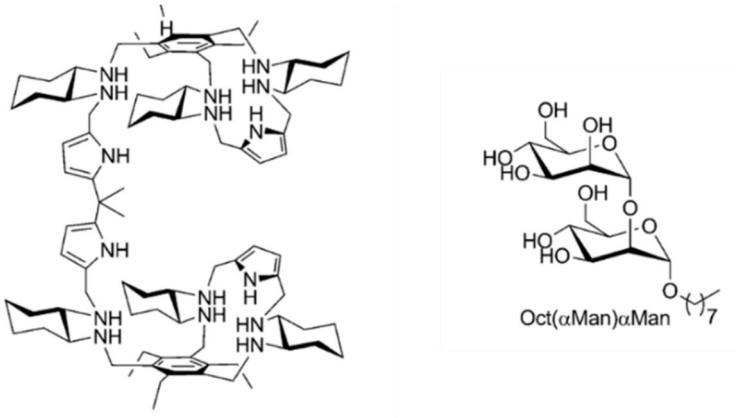


Figure 1-25: Diagram of anti-infective diaminopyrolic receptor for selective recognition of mannosides designed by Francesconi and Roelens.[117]**.**

Francesconi and Roelens system was found to bind oligo-mannosides, these are of interest when designing artificial receptors, particularly for therapeutic purposes. For example, the interaction between the DC-SIGN lectin found on dendritic cells within the immune system and the viral glycoprotein gp120, present on the HIV (human immunodeficiency virus) envelope, facilitates the infection of human cells by HIV. This interaction underscores the importance of recognising mannose residues. Specifically, the mannose alpha (1-2) mannose dimannoside motif, which constitutes the smallest fragment of the Man9 epitope within the viral gp120 glycans, is crucial for recognition by immune system lectins (DC-SIGN). [118]

The designed receptor was thus able to bind larger oligosaccharides in organic media, which is an improvement over octalum based receptors that only bound smaller saccharide units. Despite its limited solvent medium, recognising the Man a(1-2)Man motif is an improvement. XRD, NMR, and computational modelling confirmed the interactions

with the mannosides, indicating that the hydrophobic rings could have CH-π interactions with the mannosides, which are the driving force behind the binding events. [116,117,119,133,134] These interactions have been elsewhere studied via XRD, NMR and computational modelling and are viewed as the driving force for recognition. [119,135]

Mazik and his colleagues have been at the forefront of research into synthetic carbohydrate receptors since 2000. [63,98,102,104–106,109,136–142] They have created a series of acyclic receptors, consisting of three recognition units linked by phenyl spacers, which are used to recognise glycans through multiple interactions. The core central recognition unit which was substituted throughout the works is provided below.

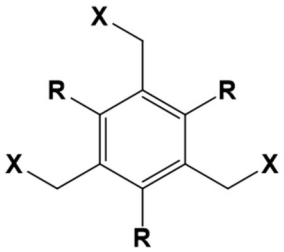


Figure 1-26: Core structural unit used in Maziks and coworkers research to develop multivalent non-covalent receptors for pyranose sugars.

The design of these structures with flexible side arms was inspired by the crystal structures of the 2:1 receptor: glucopyranoside complex discovered in nature.[101] To evaluate the binding towards sugars, Mazik varied the connecting units and the nature of the recognition units (Figure 1-26). Their efforts have resulted in noteworthy progress in developing non-covalent synthetic receptors that exhibit similar multivalent

behaviour to naturally occurring lectins. Through a series of iterative studies, they altered the heterocyclic ring structures, sizes, and substituents.

A general trend was observed in the binding affinity and selectivity of pyridine-based receptors when aromatic nitrogen experienced decreased sterics.[143]. An illustration of these series of receptors is depicted below.

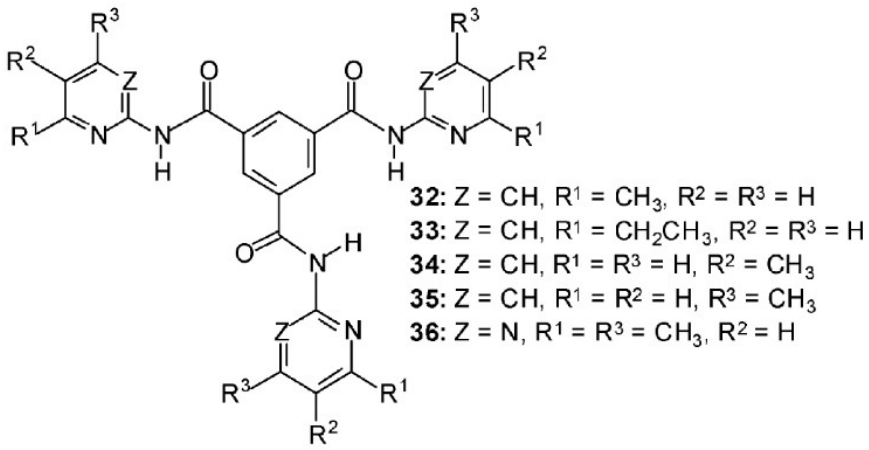


Figure 1-27: Diagram recreated from literature[143] depicting early acyclic receptors developed by Mazik and coworkers for binding glucopyranosides in organic solvent systems.

The modification of the R groups of the pyridine ring resulted in changes in the binding affinity and selectivity measured values. A reduction of the steric at the pyridine nitrogen increased the binding affinities. This increase was observed for receptors 34 and 35 in addition to different selectivity towards the α-glucopyranosides (Figure 1-27).[102]

In contrast, receptor 32 had lower binding constants and preferred the β-sugar. The differences in receptor behaviour can

be explained by considering the spatial orientation of the C_1-OR group of the sugars. (Figure 1-18-A & Figure 1-18B).

In the α-anomer, the C_1-OR group is spatially accessible to form hydrogen bonds with the C_2-OH groups. Thus, the synthetic receptor is hindered from interacting intermolecularly with these groups. In contrast, the β-anomers C_1-OR group is less available for intramolecular interactions (C_2-OR) and thus interacts more strongly with its synthetic receptors. Hence, most of the receptors favour β-glucopyranosides (Figure 1-18-B) over the α forms. [102] With receptors 34 and 35 possessing more significant binding towards the α-anomer, it suggests the intermolecular receptor-glycan interactions were able to out compete with the intramolecular hydrogen bonding within the sugar.

Furthermore, steric constraints were found to also influence the binding affinity. Substitution of the receptor's amide groups (side arms) for amino groups were trialled to assess increased flexibility of the receptor. (Figure 1-28).

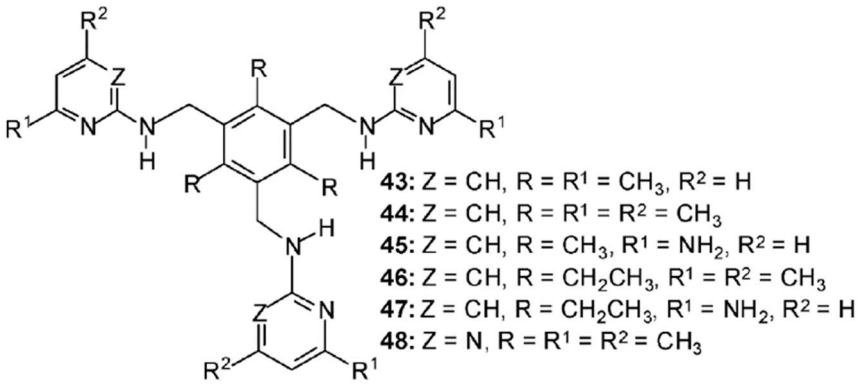


Figure 1-28: Maziks synthetic receptor with more flexible amino side arms capable of binding cooperatively to glucose in organic media. Diagram recreated from literature.[102]

The amino groups increased the available rotation within the arms around the core phenyl ring. Thereby permitting preorganisation and accommodation for the target glycans. The acrylamide-linked acyclic receptor 36 was found to bind the β-anomer tightly (Ka = 1.37 x 10^4 M^{-1}) in a 1:1 binding.[102]

However, when the amide is substituted for amino groups, the binding was found to further increase providing a 1:2 interaction between guest: host. (Figure 1-29).

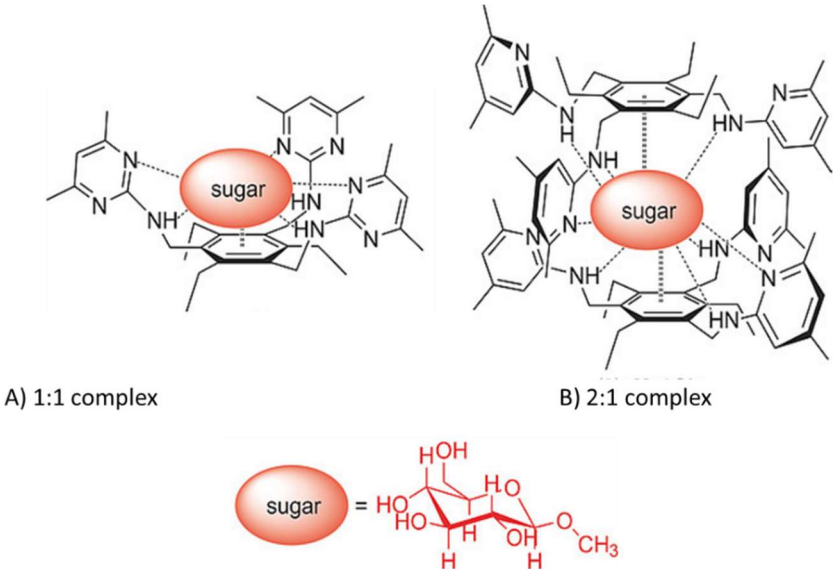


Figure 1-29: Diagram recreated from literature [98] for the Binding motifs observed from the crystallographic studies of the synthetic receptors designed in 2004. These receptors commonly used the 2-amino-4,6-dimethyl-pyridine motifs to bind to glucopyranosides in a 1:2 or 2:1 manner.

The increased binding constants (Ka_1=1.258 x 10^5 M-1 and Ka_2= 6.98 10^3 M^{-1}, β(Ka_1 x Ka_2) = 8.78 x 10^8 M^{-2})[102] observed are due to the ability to make more spatial accommodations for the sugar within the cavity (Figure 1-29), thereby increasing the intermolecular interactions and the observed binding constant. Computational and crystallographic studies show that the cavity can hold two sugars, better resembling natural multivalent interactions with lectins. [98]

Other publications included substituting the pyridine motif (c.f. Figure 1-29) for alternative structures (Figure 1-30)such as 5-imidazole[106], 3-indole[106], isobutyl amino[144], isopropyl amino[144], guanidinium[104], and quinolinium[105].

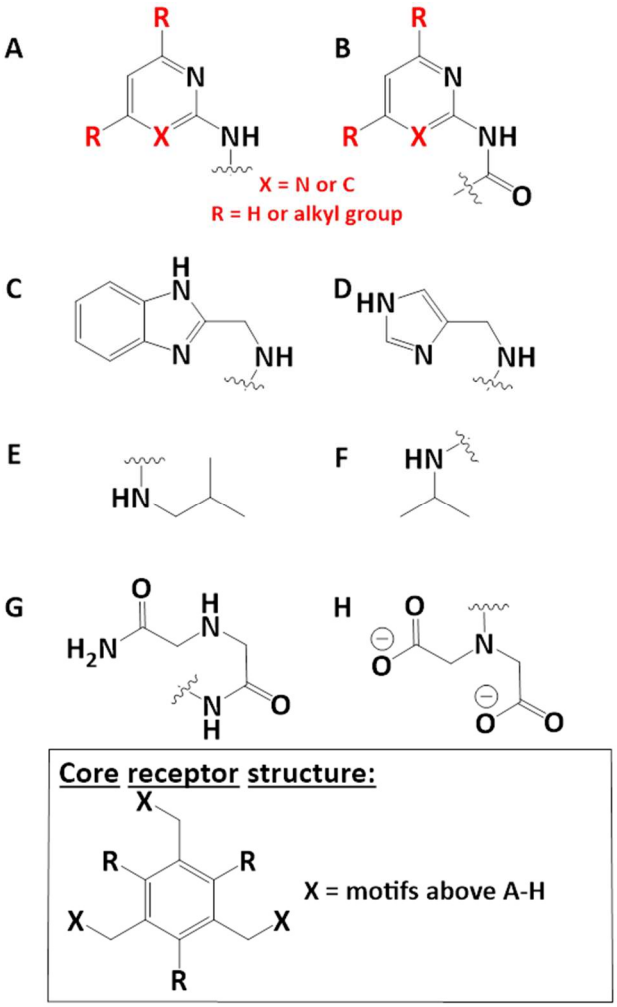


Figure 1-30:Common motifs (A-H) substituted onto the main core receptor structure by Mazik and coworkers. [102,137]

Mazik found that substitution of the 2-amino-4,6-dimethyl-pyridine motifs (Figure 1-30-A & Figure 1-29) altered the selectivity of the SCR's developed. [104] Of most significance the guanidinium SCR's (Figure 1-30-C) were selective towards the negatively charged sialic acid-based pyranose sugars (Figure 1-1) which are of key importance for cancer diagnostics. The guanidinium based receptors were a significant improvement over the previous models owing to the increased ability to operate in aquatic environments, these studies were carried out in 10% water to provide enhanced binding strengths ($Ka_1 = 2x10^5$

M^{-1}, $Ka_2 = 6.1x10^4\ M^{-1}$, $Ka_3 = 1.2x10^4\ M^{-1}$ or $\beta = >13x10^{13}\ M^{-3}$, where $\beta=K_1 \times K_2 \times K_3$).[102,104] The systems developed by Maziks were a significant improvement over those previously developed in the early 2000's. (Figure 1-18, Figure 1-19, Figure 1-21 & Figure 1-22). They not only provided tighter binding constants but were also able to perform in 10% water providing a multivalent cooperative approach analogous to that observed in natural lectins where the initial association of a sugar induces conformational changes enhancing the binding of a subsequential site.[120] Synthesising synthetic receptors is an often a complex task that requires many steps, often producing low yields. In contrast these series of acyclic receptors were significantly simpler in comparison to the previous macrocycles (Figure 1-18). These receptors can be achieved in under five steps with a yield of over 50%.[98]

To conclude, developing water-soluble receptors that exhibit high selectivity and good yields is a high challenging, yet essential to advance diagnostic technologies. The discussed literature mostly operated in organic solvents and were not capable of binding larger oligosaccharides. Furthermore, the receptors often exhibited the capacity to bind to multiple sugars and thus were not highly specific. The reasons thus pose a significant hurdle to these macrocycles and acyclic receptors use in clinical applications.

Most studies have centred on non-covalent interactions in aprotic organic solvents to avoid solvation complications. Targeting sugars with synthetic carbohydrate receptors is particularly difficult due to the structural complexity of carbohydrates and the strong solvation shells surrounding

glycan biomolecules. In contrast to proteomics, glycoproteomic, and glycomics, which are less established fields, with only a partial library of all known glycan structures. Therefore, limiting researchers' understanding of common glycan motifs.[24]

Fortunately, simpler systems such as boronic acid-based synthetic receptors are better suited for studying glycans in water. In addition, they are easier to synthesise and functionalise thus may become easier to be incorporated into a future diagnostic. These will next be discussed.

XIV. COVALENT SYNTHETIC RECEPTORS

Covalent synthetic receptors for glycans are chemically engineered molecules that can bind to specific carbohydrate structures through covalent bonds. These receptors can be designed to recognise a wide variety of glycans, making them highly versatile. They offer several advantages over non-covalent synthetic receptors.

Firstly, the covalent bonds formed by these receptors with glycans are stronger and more stable than non-covalent interactions. This property is particularly useful in applications where strong and enduring interactions are required. Secondly, covalent synthetic receptors can be designed to form specific covalent bonds with target glycans, allowing for highly selective recognition of specific motifs. In complex biological systems where many similar glycans may be present, this selectivity is crucial. Finally, covalent synthetic receptors overcome the needs to distinguish the hydroxyl groups of solvent molecules and its glycan target since they preferentially bind to cis diols.[115]

Boronic acids are commonly incorporated into synthetic covalent receptors for glycans and other Lewis base-containing compounds. These acids have an incomplete shell in their neutral form, causing the boron atom to readily react with nucleophiles known as Lewis bases to reach the stable octet form (Figure 1-31).

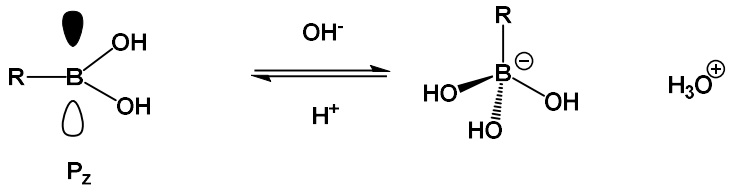


Figure 1-31: Formation of the anionic boronate anion which readily occurs in aqueous conditions to complete boron's octet.

This electronic property enables boronic acids to form strong reversible complexes with 1,2- and 1,3-substituted Lewis base donors such as hydroxyl, amino and carboxylate groups as depicted. [145] Thus, boronic acids can target amino acid and glycan motifs of interest. The advantage of boronic acids are they are dynamic receptors which can reversibly bond to the glycan target when certain conditions are satisfied as depicted via Figure 1-32.

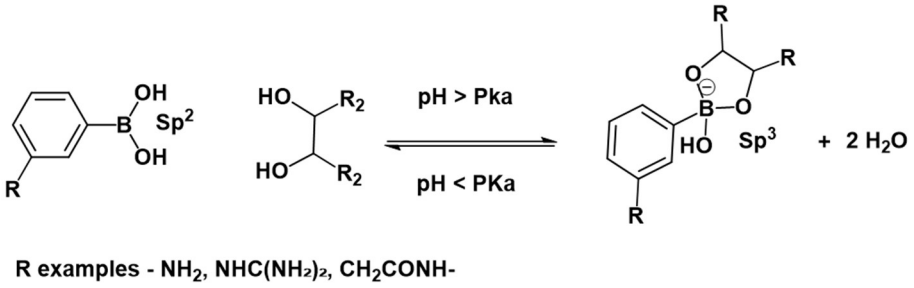


Figure 1-32: Reaction of phenylboronic acids (PBA) with cis-diols to form the cyclic boronate esters.

The optimal pH for binding is often between the pKa values of the boronic acid and the diol (glycan) as shown in Equation 1 . The pKa values however are known to vary with solvent, pH, temperature and sterics. [145]

$$pH = \frac{pka\ receptor + pka\ ligand}{2}$$ **Equation 1**

Phenylboronic acid (PBA) is known to bind to sugars preferentially at alkaline pH. At alkaline pH, the electronic structure changes to form a negative tetrahedral boronate anion. Whilst, at lower pH below the pKa of the boronic acid the boron adopts a sp^2 neutral trigonal form. Trigonal neutral boronate esters are more unstable than the starting boronic acid due to the ring strain and is, therefore more easily hydrolysed back to the starting phenylboronic acid and cis-diol. [146] The dynamic equilibrium between these boronic acids and cis-diols is depicted below (Figure 1-33).[147]

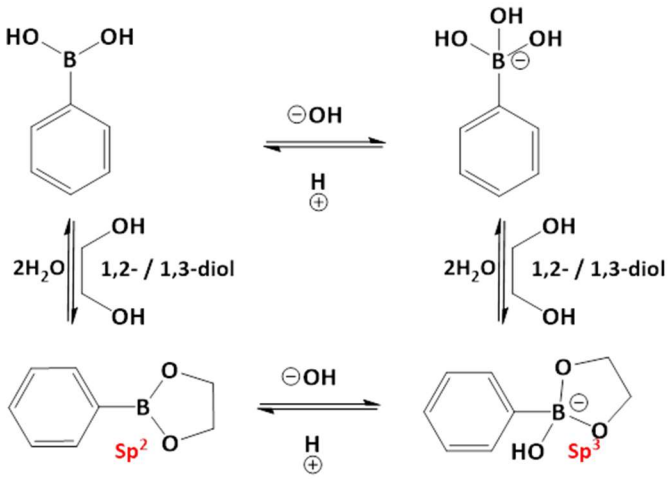


Figure 1-33: Dynamic equilibrium of PBA in water with cis-diols.

Conversely, the charged tetrahedral boronate esters are more stable and less susceptible to degrading. If the boronic esters are formed in organic aprotic solvent they are relatively stable in this medium and aren't hydrolysed, thus the trigonal sp^3 neutral boronate esters are more commonly formed in organic

solvents.[147] Since the pKa > physiological pH for PBA, these molecules have limited potential for biomedical applications, due to the weak binding nature physiologically relevant pH.

The binding affinity at physiological pH can be manipulated via the modification of the electronic properties of the boron centre. Upon adding electron withdrawing groups (EWG) on the aromatic ring, the electron deficiency of the boron centre increases, increasing the Lewis acidity. For example, in PBA the addition of a nitro group at the *meta* position was previously reported in literature to lower the pKa from ~8 to ~7.[148] This structure is illustrated in Figure 1-34.

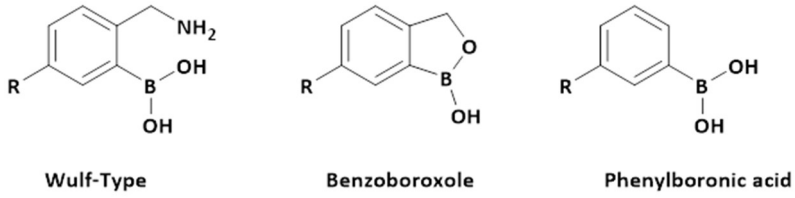


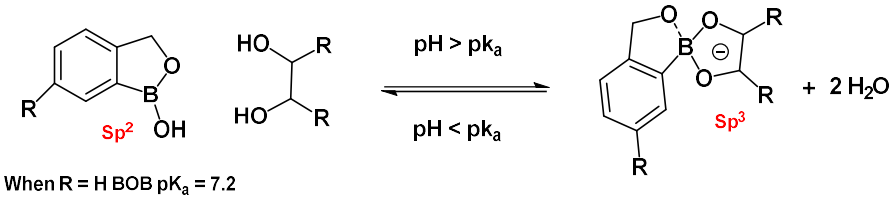
Figure 1-34: Structures based on the commonly known phenylboronic acid motifs. Modification at the meta position as denoted by R can enhance the binding properties. Wulf-type boronic acids contain intramolecularly coordinated B-N or B-O bonds which facilitate the formation of the sp^3 boronate anion. [149]

Furthermore, the acidity of the boron centre may also be increased by introducing an amine in the ortho position as depicted by the Wulff-type boronic acid displayed in Figure 1-34. The boronate ester formed is stabilised via intramolecular B-N interactions between the ammonium anion and the negatively charged boron centre.[150] The stabilisation of the boron reduces the pKa, the sp^3 centre can remain stable even

under neutral conditions unlike traditional PBA molecules. Wulff-type have been previously reported to have pKa values as low as 5.2.[149] Thus, are more advantageous for biological applications.

Alternatively, benzoboroxoles (BOB) may also be employed for sensing applications owing to their lower pKa values (pKa = 7.2)[130] in comparison to PBA type molecules. Upon benzoboroxoles (Figure 1-34) reacting with a cis-diol a five membered ring is broken, releasing the BOB ring strain. This favourable release promotes boronate-ester formation resulting in a lower pKa for these BOB systems.[151]

The PBA species are less favoured in sensing applications in comparison to the BOB and Wulff-type boronic due to them possessing a higher pKa and preferring furanose sugars.[152] Since the majority of naturally occurring saccharides in glycoproteins are in the pyranose form, PBA molecules are less compatible for glycan sensing. Furthermore, at physiological conditions PBA are less likely to form the negatively charged boronate species (sp^3 hybridised form) which is known to form more stable adducts. Conversely, under these conditions BOB derivatives readily form the stable sp^3 anionic centre (Figure 1-35) and have a greater preference for hexapyranose sugars.[61,153,154]



When R = H BOB pK_a = 7.2

Figure 1-35: Dynamic equilibrium for BOB type molecules with cis-diols in aqueous medium.

The versatility of these boronic motifs is evident by the vast variety of publications and reported applications. Common themes reported were the use of boronic acid functionalised hydrogels, peptides, and polymeric nanoparticles for a variety of uses such as drug delivery and sensing. [155–162] The most pertinent to this thesis is their application for saccharide detection. [20,95,145,152,160–170]

Boronic acids have a vast number of applications as evidenced by the broad array of publications entailing their use as chromatography systems, anticancer drugs (Bortezomib), catalysts, and in dynamic combinatorial chemistry.[152,153,171–175] Boronic acids are most known for their participation in Suzuki cross-coupling reactions (Figure 1-36), permitting the formation of new C-C bonds, as most recently exploited for the use of functionalizing gold-palladium alloy nanoparticles with new C-C bonds.[172]

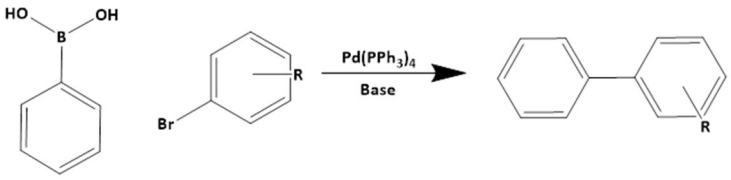


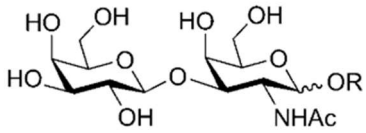
Figure 1-36: Schematic for boronic acids role in Suzuki cross coupling reactions widely used in catalysis.

One of the earliest examples of sugar detection with boronic moieties was reported by Shinkai et al in 1991. [176] The boronic acid group transferred the sugar target into the organic phase via formation of the boronate-ester. This is analogous to the performance of the first octalum sensor previously described which was capable of transferring glucose from water into chloroform (Figure 1-18).

In addition to glycan recognition, boronic acids have been used for biomolecule recognition for any molecules with adjacent hydroxyl groups (or nucleophilic groups). They have been reported to bind to many diverse types of molecules such as diamines, dopamine, nucleosides, and amino acids. These binding interactions are discussed elsewhere. [95]

Since 1991, boronic acids have been used in solid phase synthesis to make functionalised peptides. The peptide chains facilitate the selective delivery of the boronic receptors to the site of interest. Peptides can be designed to recognise and bind to biomolecules expressed on cell surfaces or tissues of interest. Peptides also improve the solubility of boronic acids and hence the receptors stability in biological mediums. Thus, the combining of peptides and boronic acids results in a combined covalent and non-covalent receptor. Boronic acid functionalised peptides have been reported for sensing a variety

of sugars such as sialic acid and fructose (Figure 1-1). Perhaps the most pertinent example thus far was the identification of the Thomsen-Friedenreich antigen (TF-antigen), which is widely accepted as a hallmark of cancer, with virtually all cancers expressing this marker (Figure 1-37).[2,29,177] The disaccharide antigen plays an important role in cell adhesion and cancer biology.



TF antigen (Gal-β-1,3-GalNAc)
R = lipid or protein

Figure 1-37: Thomsen-Friedenreich antigen glycan motif composed of N-acetyl galactosamine and galactose.

The TF-antigen is composed of cis-diols capable of forming boronate-esters with boronic acids via covalent bonds. In addition, if the boronic acid is incorporated into the peptide backbone as shown in Figure 1-38, additional non-covalent interactions may enhance the binding (Ka = 2 mM^{-1}).[178]

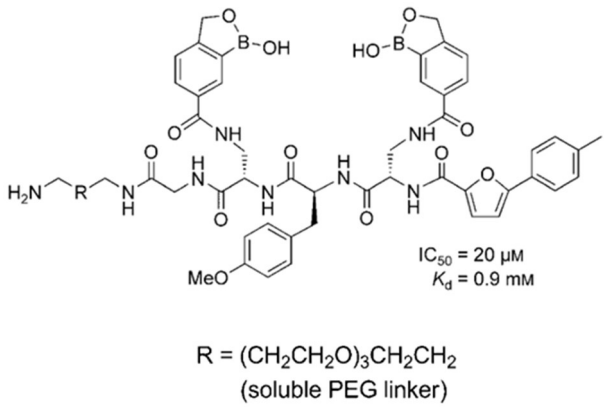


Figure 1-38: Figure recreated from literature [177] for the first boronic functionalised peptide capable of targeting the glycan motif ((Gal-β-1,3-GalNAc) of the TF-antigen to provide a measured association constant of 2 mM^{-1}.

The β-peptide bundles spontaneously self-assemble to form supramolecular helical complexes denoted foldamers. The use of boronic acid functionalised peptide helical structures have elsewhere been employed for the detection of other molecules with adjacent nucleophilic groups such as dopamine (Ka = 8.14 x 10^2 M^{-1}) and sorbitol (Ka =44 M^{-1}) in aqueous conditions.[179] However, the observed binding of these systems was weak and non-selective in nature.

Improvements were reported by Schepartz et al.[179] , they reported the detection of fructose in water at physiological conditions (Ka = 663 M^{-1}). The binding was thought to be assisted by the peptide's cationic amino acid side chains. These may enhance the solubility of the boronic acid functionalised receptor in solution in addition to providing key additional electrostatic interactions with the target fructose molecule.

Elsewhere boronic acids have also been incorporated into systems for biosensing such as photoinduced electron transfer (PET) systems. A typical PET sensor entails the excitation of a molecule which is intermolecularly quenched by another functional group via Van der Waals interactions, transient collisions, or formation of π-stacked complexes. These non-covalent interactions prevent traditional radiative decay processes such as fluorescence and hence leads to "dynamic quenching." This process is followed by a change in the fluorescence signal due to target binding. This mechanism can be better explained via one of the first PET boronic acid sensors produced by Shinkai and co-workers in

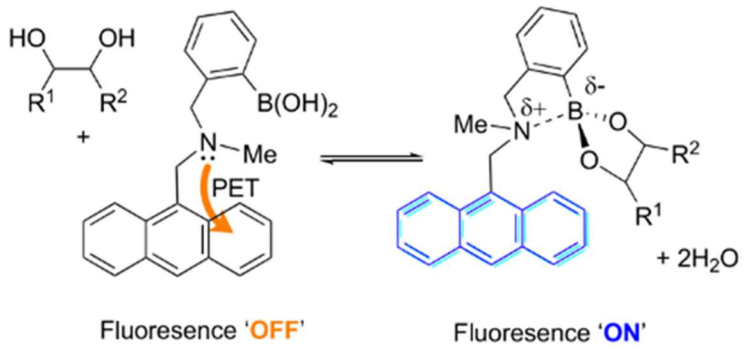


Figure 1-39.[180]

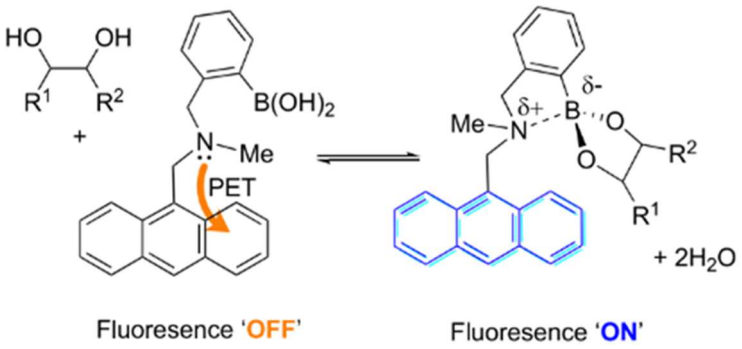


Figure 1-39: Image recreated from literature depicting [180] boronic acid PET sensor produced in 1994 by Shinkai and coworkers showing selectivity for D-Fructose (K_a = 1000 M^{-1}) over D-Glucose (K_a = 63 M^{-1}).

The anthracene-based receptor when bound to glucose resulted in an increase in the fluorescent signal. In the absence of a monosaccharide the fluorescence signal was quenched due to intermolecular transfer of a lone pair of electrons. This is depicted above via the orange arow denoting the transfer of nitrogen lone pair to the conjugated anthracene system. The transfer prevents a radiative decay process from occurring for the anthracene. However, when a cis diol is in proximity, the boron centre is believed to interact with this lone pair of electrons on the nitrogen as depicted above via the dotted line. This interaction is driven by the Lewis acidity of the boron centre. Thus, reducing the diminishing the quenching and an increase in the fluorescence.

The system Shinkai and his colleagues [20] created showed selectivity for D-fructose (Ka = 1000 M-1) over D-glucose (Ka = 63 M^{-1}).[20] This selectivity is typical of receptors based on mono-boronic acid derivatives.[152] These receptors are known to favour the furanose form over the pyranose sugars. Thus, sugars which

form a higher proportion of furanose tautomer's under equilibrium will form tighter binding. The proportion of fructose tautomer's was previously established (Figure 1-5). To conclude under physiological conditions, fructofuranose provides a higher proportion of the *syn*-peri planer pair of hydroxyl groups for binding to the boronic acid. Despite glucose having syn-periplanar-1,2, -diol motifs, there is less propensity for the furanose (~ 0.14%) forms under these conditions.[181]

However, when additional boronic acids is added, the binding constant was found to significantly increase. Since glucose possess two diol motifs a multivalent receptor increases the possibility of a stronger interaction with glucose.

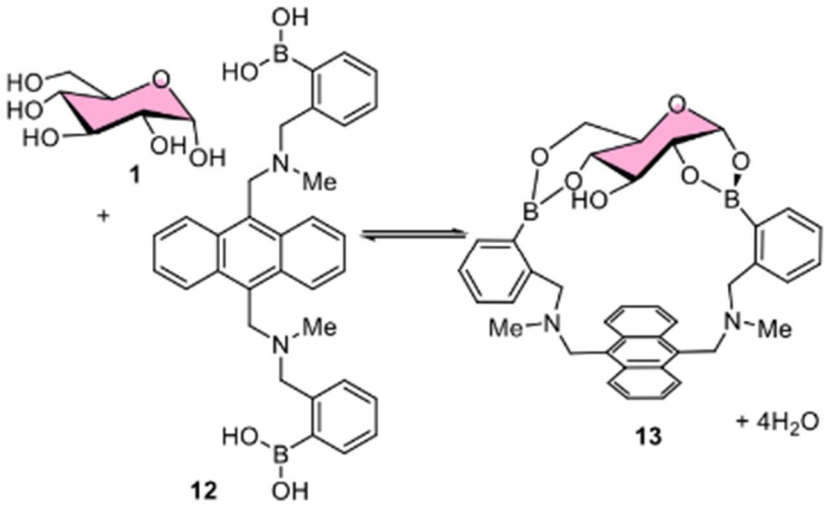


Figure 1-40: Illustration of the multivalent PET boronic system developed by James and coworkers taken from literature. [182] **Selectivity was observed to be modified towards different pyranose sugars when modifications were made to the arms of the aromatic system.**

The ditopic anthracene-based sensor was observed to significantly favour glucose (Ka = 3.981 x 10^3 M^{-1}) now over fructose (Ka = 3.16 x 10^2 M^{-1}), with the binding constant more than tripling for glucose. [20,182] These sensors are thus capable of binding to glucose in serum. The use of these systems as glucose sensors are highly dependent on the concentration of the target in solution (i.e. glucose). For example, if blood glucose levels are below 10 mM and the receptors association constant is 4 mM^{-1}, the corresponding dissociation constant is thus 0.25 mM. Therefore, the dissociation constant is lower than the blood glucose level, this suggests these receptors would be capable of binding glucose at these concentration levels efficiently. [181] The enhanced efficiency of these receptors

following the addition of a second boronic acid, may be explained by the concept of preorganisation. The boronic acids were spaced effectively apart by the anthracene centre thus spatially orientating towards glucose cis diols in the pyranose form.

James et al[182]. demonstrated that modification of the linker length between the two boronic acid groups significantly changes the selectivity of these receptors. It was originally thought it was the increased Lewis acidity of boron that drives the fluorescence on state. [180] However, more recent density functional theory (DFT) and XRD studies have suggested the mechanism is not a PET one but something else such as proton insertion or a disaggregation mechanisms.[183–187] The mechanism of action is not yet fully agreed by all researchers, but this has not reduced their uses in biomedical applications such as - electrochemical sensors, responsive hydrogels/polymers, controlled drug release and imaging to name a few. [164,174,188–190]

Whilst these systems have reported moderate binding constants (Ka) such as those shown above, they have only been applied to simple saccharides and have limited solubilities owing to their large fluorescent aromatic systems. Furthermore, boronic acids are known to bind to all cis-diols and thus are not selective to only glycans. Thus, their transition to a clinical environment is limited, without further modification. The use of covalent receptors will be further covered in more detail for their applied use in molecular imprinting (MI). In MI systems the boronic acids are spatially locked in position for an interaction

which increases their selectivity towards specific shapes and hence glycan motifs.

XV. INTRODUCTION TO MOLECULAR IMPRINTING(MI)

Molecular imprinting (MI) is a way to achieve specific recognition on a 2D or 3D surface via the use of various forms of interactions such as – hydrogen bonding, electrostatic interactions, hydrophobic interactions, weak metal coordination and dynamic covalent bonds. Using these interactions permits the systems to recognise their targets and bind them selectively when they are present amongst a complex mixture. These artificial systems are more stable than their biological competitors (lectins/antibodies).

MI is an established method with well over 15,000 publications covering a wide range of applications such as – diagnostics, drug delivery, responsive hydrogels, in-vivo imaging and enrichment of glycoproteins. [13,191–204]

Molecularly imprinted polymers (MIPs) can be split into two main categories depending on how the template interacts with the cavity - covalent and non-covalent or semi-covalent (boronic acid / saccharide etc.). The advantages of covalent imprinting leads to more uniform imprints and enhanced selectivity. However, the drawbacks of this method are slower binding and release of the template owing to the breaking of a stronger bond. Non-covalent imprinting relies on the same interactions as the synthetic receptors previously described and hence will require milder conditions for template removal. The advantages of non-covalent methods are faster removal of template and hence faster binding kinetics than covalent

approaches. Consequently, non-covalent imprinting is more commonly used. [197]

MI entails forming a polymer matrix around a given template of interest such as a protein to form a mould around the target. The removal of the target yields cavities with a favourable three-dimensional arrangement for future target binding. The selection of cross-linking molecules, the solvent, and the polymerisation agents are key factors to consider when designing a pocket.

The solvent and the cross-linking molecules should not compete, or negatively affect the formation of the imprint. The selected monomers should complement the functionality of the template molecule to enhance interactions in addition, to forming the polymeric matrix around the template target. [205] Furthermore, the selection of the polymerisation agents (initiator) needs to be considered based on the functional groups that are available for cross-linking events. For free radical polymerisation reactions common initiators include: azobisisobutyronitrile (AIBN), ammonium persulfate (APS) and tetramethylethylenediamine (TEMED) for free radical polymerisation reactions.

The use of MI can result in the formation of complexes which would not naturally occur owing to the removal of the entropic and enthalpic barriers via preorganization of the template molecule, which can be explained due to preorganisation.[120] A good MI should be selective for its target and exhibit low affinities for non-template molecules.

MIPs have limited use in real world applications such as diagnostics due to issues such as template leakage, mass transfer issues, limited solvent systems and binding site heterogeneity.[204,206] MI on the nanoscale has become increasingly popular to mitigate some of these issues. Molecularly imprinted nanoparticles (MINPs) can resolve the drawbacks of bulk MI (MIPs) as they provide a larger surface/mass ratio, more accessible pockets, better solubilities, and lower heterogeneities. [198]

The use of surface imprinting on nanoparticles often entails the immobilisation of the template to a solid support like beads. Functional monomers such as boronic acids and crosslinkers are added which bind to the target adhered to the beads. The use of solid supports permits imprinting of templates that would otherwise be insoluble in the polymerisation mixtures. Additionally, the use of solid supports in tandem with boronic acids mitigates template entrapment issues. The removal of the imprinted particle can be easily obtained via modulation of the pH, resulting in the glass beads with the template and the MINPs in solution for collection. However, these particles are still susceptible to cavity deformation if the cross-linking density of the pocket is not optimised.

The first use of boronic acids for molecular imprinting was conducted by G. Wulff and Sarhan in 1972. [195,197] The use of MI has immensely increased since the 70s due to its wide range of applications in drug delivery, biosensors, biological assays, and separation techniques. For this thesis, the focus will be on their use in biological assays and biosensors entailing the use of glycans as targets.

XVI. MOLECULAR IMPRINTING (MI) ON A 2D SURFACE

The concept of MI on a 2D surface was first reported by Gunter Wulff over 30 years ago.[204] Wulff is recognised by many as the "father of molecular imprinting" emphasising his contribution to the field.[207]His works began on organic polymers in 1972. The work began on His research which has most significance for this project is that of his covalent imprinting with boronic functional groups.[195,208] Wulffs research provided a starting point for glycan detection via molecularly imprinted materials. Since, polymer imprinting methodologies has been explored in numerous application settings.

The application of MI for 2D surfaces has previously been explored for imprinting of proteins. Protein imprinting has become more common owing to the increasing need to sense proteinaceous biomarkers for medical diagnostics and improve drug delivery systems.[205] MI of whole proteins is not without its challenges due to the large template size, their complexity, and poor solubility in organic solvents. When imprinting these targets, typically a broad variety (heterogeneity) of pockets are produced, with different affinities and specificities because of the proteins ability to change to non-native conformations.[206] Some of these conformation changes can be mitigated by imprinting under physiological conditions. The issue is many of the monomers and initiators used for MI traditionally have limited solubilities in these conditions.

The biomarker for prostate cancer (PSA) has previously been used for molecular imprinting on a 2D gold surface. [202] The

glycoprotein was imprinted onto a surface via boronic based receptors to highlight the capacity for MI to be used in future diagnostic tools. The resulting surfaces produced were found to discriminate between glycosylated and non-glycosylated forms of the same glycoprotein.

The imprinted pocket produced was found to not bind significantly to other glycoproteins, even those with a greater degree of glycosylation (i.e. more hydroxyl groups for boronic acid to bind). Thus, the pocket displayed selective binding. In addition. smaller glycoproteins (i.e. in comparison to the imprinted template (PSA)) which could fit inside the pocket were also evaluated and no significant binding signal was produced. The pocket was deemed to be sensitive to its target PSA. The surface plasmon resonance (SPR) binding experiments produced a high binding constant (Ka), which translated to a dissociation constant (Kd) of 1.8 μM.[209] When studying natural immunological complexes the dissociation values are used to depict how strongly the molecules interact, these values are generally in the nanomolar (nM) to micromolar (μM) range.[210] Since PSA naturally occurs in serum in the nM - μM range, these surfaces were capable of capturing PSA in a clinically relevant concentration. [209] However, despite these pockets being highly specific, their dissociation constants (μM range) are not applicable for most biomarkers which are present in serum at much lower concentrations (i.e. nM). For example, the PSA biomarker is present in the blood at low quantities: of the order of nanomolar range.

Alternative surface imprints of glycan motifs entailed the use of different chemistry such as via copper-azide click chemistry as demonstrated via Figure 1-41

Figure 1-41 .[175]

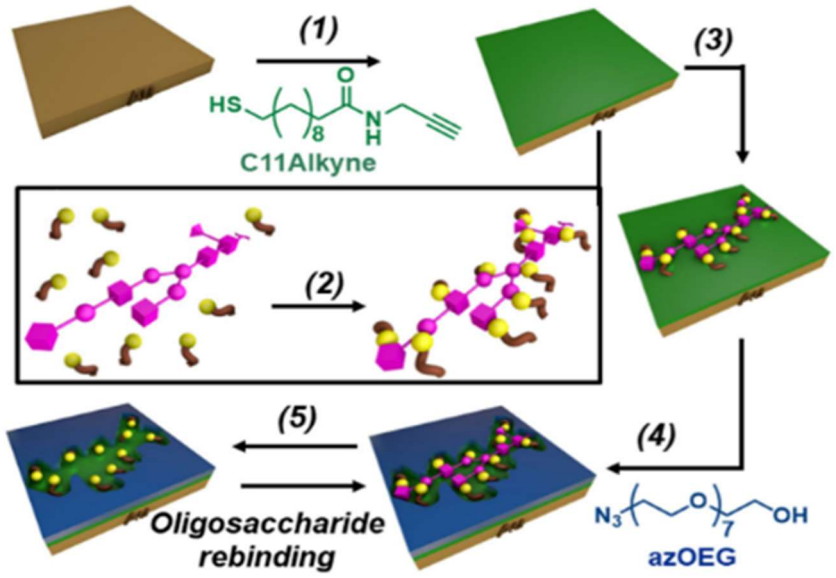


Figure 1-41: Diagram taken from literature [175] to illustrate a molecularly imprinted gold surface via the use of copper – azide click chemistry to form specific spatial cavities capable of sensing stachyose (Ka = 0.09 mM-1 / Kd = 11 mM).

The aromatic triazole and hydrophobic alkane moiety could permit hydrophobic non-covalent interactions with the sugars if the spatial orientation permitted. For these studies, the imprinted surface was compared to a control. The control surface possessed the boronic acids in the correct orientation fixed to the surface as denoted by step 3 above. However, step 4 whereby the molecular scaffold around the boronate-ester template was not conducted. This permits a greater degree of movement for the boronic acids which are fixed to the surface.

An interesting observation arose, with the imprinted surface and control surface (no polymer layer) nearly having the same Kd values for stachyose. Thus, the capacity to bind to the target was unaffected. The matrix formed around the scaffolding may have been too small to have influenced the overall binding or the cross-linker used may not have been rigid enough to affect the properties of the binding site. This highlights the importance of controlling the polymer matrix layer to enhance the binding. As expected, the surface lacking the molecular scaffolding resulted in a reduction in selectivity of the pocket. This was previously observed for Francesconi et al[117] system with the linkers for 'molecular tweezers' whereby increasing the flexibility and hence size of the linkers led to a decrease in selectivity (Figure 1-25).It is well known that benzoboroxole (BOB) moieties can outperform their boronic acids (BA) as glycan receptors as previously discussed in Covalent synthetic receptors. Consequently, BOB monomers are commonly utilised in MI over phenylboronic acids.

Prior Mendes research was conducted on the use of BOB moieties on a gold surface to enhance the compare the difference in the observed binding for stachyose. Prior works with phenylboronic acids obtained dissociation constants in the mM range

Figure 1-41). A schematic for the formation of the gold imprinted surfaces with BOB moieties is provided below - Figure 1-42.

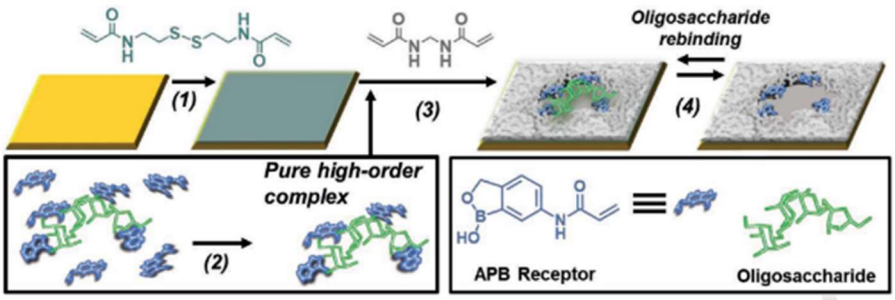


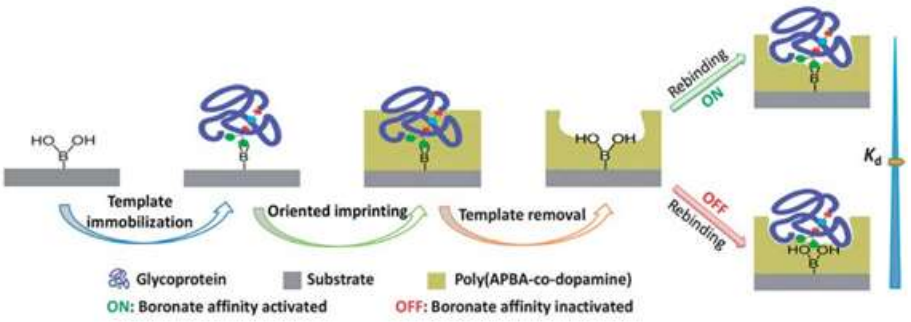
Figure 1-42: Illustration taken from literature [203] for the formation of SAM on gold surfaces utilising free radical polymerisation chemistry to obtain a selective pocket capable of binding stachyose (Ka = 1.205 x 10^3 M^{-1}/ Kd = 0.83 x 10^{-3}M)

When using the BOB type receptors, the binding was observed to increase (Ka = 1.205 x 10^3 mM^{-1}) in comparison to the acrylamido - phenylboronic acid (APBA) imprinted surface (

Figure 1-41). The protocol was repeated with different saccharides to view if the established methodology was applicable. When nystose was selected as a template the imprinted surface provided a binding constant of 1.538 x 10^3 M^{-1} (Kd = 0.65 x 10^{-3} M) [203] Thus, highlighting the application of this method to create selective pockets for a range of saccharides. Furthermore, the extent of selectivity this pocket afforded was excellent with no binding observed via SPR for other sugars.

MI of oligosaccharides has elsewhere been reported on alternative surfaces such monolithic columns and glass slides using different co-monomers. [211] Such as the use of a boronic acid terminated surface to adhere the sugar of interest to the surface. The subsequent imprint entailed the use of a mixture of

both dopamine and boronic acids (poly (acrylamidophenyl boronic acid (APBA)-co—dopamine (DOPA)) polymer). A schematic of this is illustrated below.



pH	K_d (M)	R^2	k_{on} (M^{-1} s^{-1})	k_{off} (s^{-1})
3.0	2.7×10^{-7}	0.973	2.4×10^{3}	6.6×10^{-4}
5.5	1.3×10^{-8}	0.985	1.2×10^{4}	1.5×10^{-4}
7.4	1.2×10^{-9}	0.960	1.5×10^{4}	1.7×10^{-5}
9.0	6.6×10^{-9}	0.983	9.2×10^{3}	6.1×10^{-5}

Figure 1-43: Illustration adapted from literature [211] to depict the use of boronic acid functionalised surfaces to capture the target glycan of interest. The subsequent imprinted cavity was produced via the use of a poly (acrylamido phenyl boronic acid (APBA)-co—dopamine (DOPA)) polymer matrix.

The formation of the copolymer matrix around the sugar template was controlled via time-controlled reactions, much like the above works on a 2D surface (Figure 1-42). The use of both dopamine and boronic acid permits a molecular imprint which has two binding modes depending on the environment conditions. The advantage of this surface is the ability to bind to its targets at lower pH values if needed via the use of the dopamine moieties which provided an outstanding binding association of 3.7 x 10^6 M^{-1} (Kd at pH 3).[211] When combining both

dopamine and boronic acids, the binding constants were greater than the previous works outlined on a 2D surface outlining the benefits of combining both covalent and non-covalent interactions. These surfaces produced a dissociation constant (Kd) in the nM region for horseradish peroxidase (HRP). The imprinting methodology was reproduced on alternative surfaces such as porous columns and glass slides emphasising the versatility. The drawbacks of this method were it lacked selectivity, with the column also capturing RNase B (Kd ~ 25 μM)[212], due to the co-polymer matrix used which will interact strongly with all other hydroxyl groups available non-specifically. The polymer matrix thus should be composed of molecules which do not strongly interact with other similar structures to the target in addition to providing a rigid scaffold to maintain the pockets shape.

The works on 2D surfaces over the past decade highlight the potential for MI in a diagnostic tool with dissociation constants reported in clinically relevant ranges. When benzoboroxole molecules were incorporated a significant increase was reported for these imprints in their selectivity and affinity. These covalent systems overall improve upon the non-covalent systems owing to their ease of use in biologically relevant media. Thus, MI on solid supports when coupled with covalent receptors such as boronic acid functional monomers can result in highly selective pockets for their target structures with competitive binding constants.

XVII. MOLECULARLY IMPRINTING ON A 3D SURFACE

More recently, MI has become more popularly used on the nanoscale to form molecularly imprinted nanoparticles (MINPs). Sensing biological targets using nanoparticles and hence on the nanoscale attempts to mimic lectin properties. MI on nanoscale leads to greater mass transfer in comparison to using bulk materials. [198,205]

MINPs have previously been reported for drug delivery, biosensors, and *in-vivo* cancer imaging studies to be able to obtain Kd values in the nM and pM ranges. [198,213–217] These affinities are superior to the previous 2D (~μM – nM range) imprints owing to the advantages of imprinting on a smaller surface which is more biologically comparable to their natural receptors.

The ability to mimic natural receptors on the nanoscale has been well demonstrated by Yan Zhao and co-workers, the receptors produced have been applied for separation, catalysis, and various other biological functions such as artificial enzymes.[218–225]

A common theme is the application of molecularly imprinted water-soluble micelles, created via dynamic assembly of amphiphilic molecules such as surfactants. Their nanoscale, hydrophilic exterior and hydrophobic interior permits their use as a capsulation device for drug molecules and peptides owing to their mimicry of water-soluble proteins and enzymes. [212] The choice of surfactants can be carefully selected to ensure the

nanoparticles sizes are of the correct magnitude for the intended application - ionic surfactants baring single hydrocarbon chains can form micelles under 10 nm.[226] Furthermore, the ionic surfactants also impart stability to the charged boronate esters formed on the surface of the micelles. The micelle formation (Figure 1-44) was conducted in the presence of the template, cross-linkers (divinyl benzene (DVB) functional monomers (vinyl-Benzoboroxole (*V*- BOB)/ vinyl-phenylboronic acid (V – PBA)) and a photoinitiator (2,2-dimethoxy-2- phenyl acetophenone (DMPA))

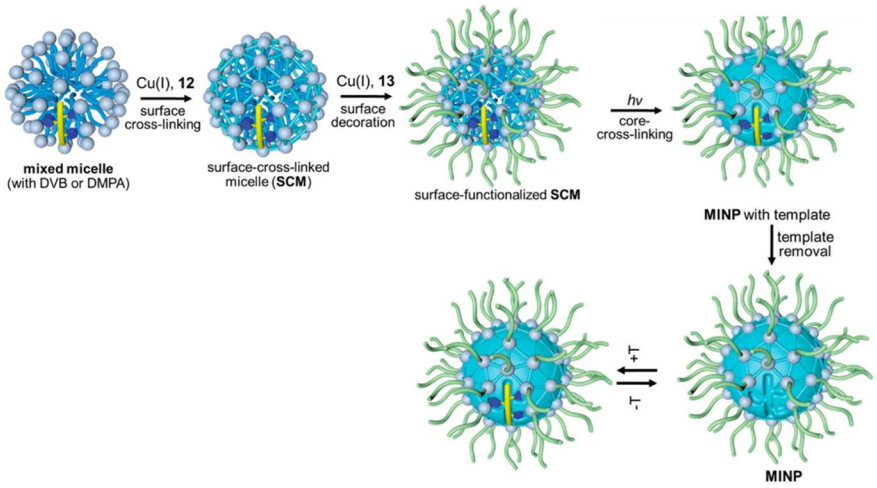


Figure 1-44: Image adapted from literature[212] to depict the formation of molecularly imprinted micelles created by Zhao and coworkers.

Zhao and co-workers commonly utilised alkyne functionality in the micelles to take advantage of click-chemistry which was previously observed for the works conducted on a 2D gold surface.[175] The micelles were imprinted for a variety of different glycan motifs, some of which are depicted below.

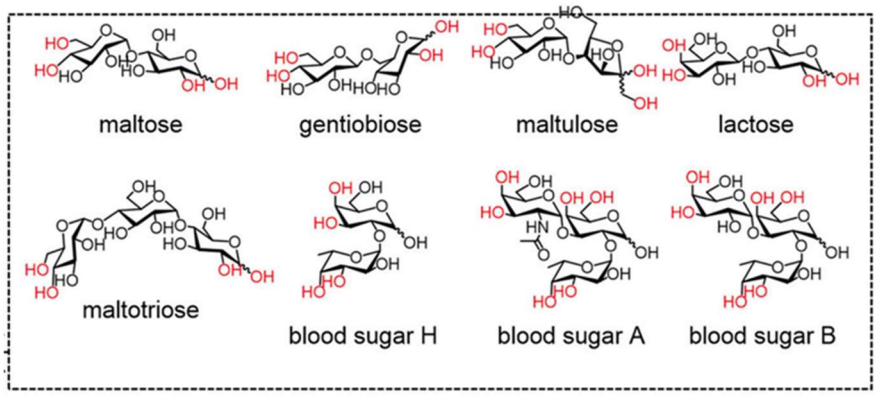


Figure 1-45: variety of glycan motifs trialled for the micelles imprinting by Zhao and coworkers. The highlighted cis-1,2-diol, cis-3,4-diol and trans-4,6-diol motifs are commonly bound by phenylboronic acids and benzoboroxole functional monomers to form boronate esters.

The micelles were able to bind to the glycans via the cis-diol motifs as highlighted in Figure 1-45 via the use of vinyl-phenylboronic acid (*V*-APBA). The pockets thus possess boronic acid covalent receptors set up in a specific spatial orientation for a subsequent binding interaction as depicted below. This is analogous to the 2D works conducted by Norman et al [175] which saw binding constants for stachyose of the mM range (Ka = 0.09 mM-1 / Kd = 11 mM). The micelles bared a hydrophilic outer surface, but a hydrophobic pocket because of the aromatic crosslinkers and aromatic functional monomers (APBA or BOB, Figure 1-46). The pocket was observed to have the greatest binding over the pH range 6.5-8.5 owing to the formation of the negatively charged sp^3 boronate ion (Covalent synthetic receptors). When phenylboronic acids are substituted for benzoboroxole motifs the resulting negatively charged boronate ester complexes were stabilised in the pocket via the positively charged surfactants of the micelles.

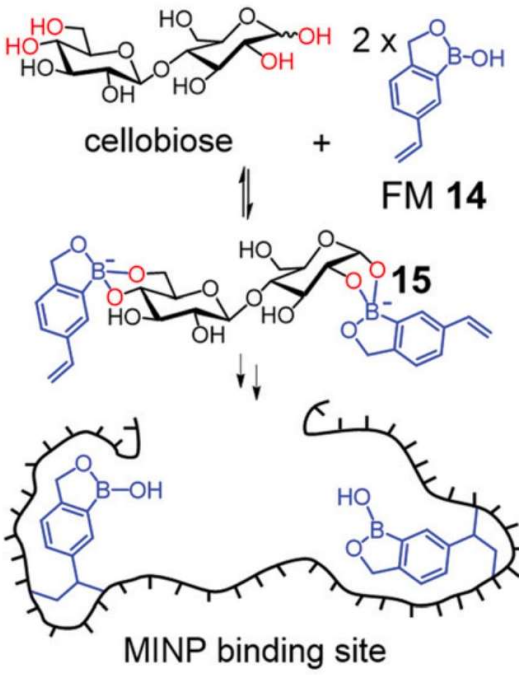


Figure 1-46: Schematic of the pockets formed on the surface of the micelles image adapted from literature[212].

It was observed that the benzoboroxole boronate esters produced higher binding constants (Ka) than their phenyl boronic counter parts. Since the boronate ester product is anionic and amphiphilic it is easily solubilised and enters micelle pockets with ease. In contrast, the phenylboronic acid boronate ester is less easily solubilised owing to the formation of a neutral sp^2 neutral ester when the pH <<pKa. Furthermore, the phenylboronic acid boronate ester is harder to synthesise than the boronate ester. [212,227,228] Enhanced binding was also previously observed for the 2D gold surfaces which possessed benzoboroxoles over boronic acid motifs as receptors. [203]Thus, BOB receptors outperform boronic acid-based receptors when used in molecular imprinting.

Most pertinent to this thesis was the works conducted by Gunasekara and colleagues with the imprinting of

oligosaccharides.[228] A significant barrier most systems are that they target simple sugars such as fructose and glucose which have limited translational applications. However, Gunasekara began work imprinting larger motifs such as blood sugar H, A and B which were previously illustrated in Figure 1-45. The works advanced on the water-soluble micelle structures developed by Zhao utilising benzoboroxole molecules as the receptors. Isothermal titration calorimetry studies (ITC) found that when sugar H was imprinted the binding constant was 35.6 x 10^3 M^{-1}. Remarkably, their micelles did not bind appreciably via ITC to sugar A or B. Thus, the system was highly selective for its target oligosaccharides and could detect its target in the μM range (Kd = 28 μM).[228]

The driving force for the formation of these binding sites and the consequent binding motifs depicted above may be explained by considering the free energy of the system. For example, when a glycan such as glucose enters a binding site (i.e. lectin such as hexokinase), the binding interactions result in > 65 water molecules to be released from both the glycan and the pocket itself. The release of free solvent molecules into the bulk results in an increase in entropy and hence can provide a large driving force in glycan binding.[229] Therefore, reducing the thermodynamic barrier correlated with the solvation of the hydroxyl groups involved in the binding interaction. Thereby, mimicking proteins and enzymes morphology on the nanoscale giving rise to their nickname of artificial enzymes. [230]

Elsewhere artificial enzymes have been used in plate-based assays, which are important for clinical analysis. An example of one is the enzyme-linked immunosorbent assay or more

commonly referred to as ELISA. This is the most common method to quantify complex biological samples via the use of natural antibodies and enzymes. Since they use natural biological receptors, they have the usual drawbacks of limited There has long been a desire in research to develop rapid, robust, and more sensitive assays as previously described in the introduction to this section.

The future of diagnostics could see the use of MINPs often referred to as synthetic antibodies in the traditional microplate (ELISA) assays. There are already several efforts been published highlighting the possibility of one day these being commonly utilised in a clinical setting for diagnostics. [216,231,232] Some examples are the use of MINPs incorporated into a standard ELISA based assay for the detection of drugs (cocaine)[216] and glycopeptides (Vancomyci) [231,232]. These reports used the solid-phase synthesis approach (Figure 1-47) to produce highly selective pockets on the nanoparticles surface which could outperform their competitor (standard antibody ELISA format).

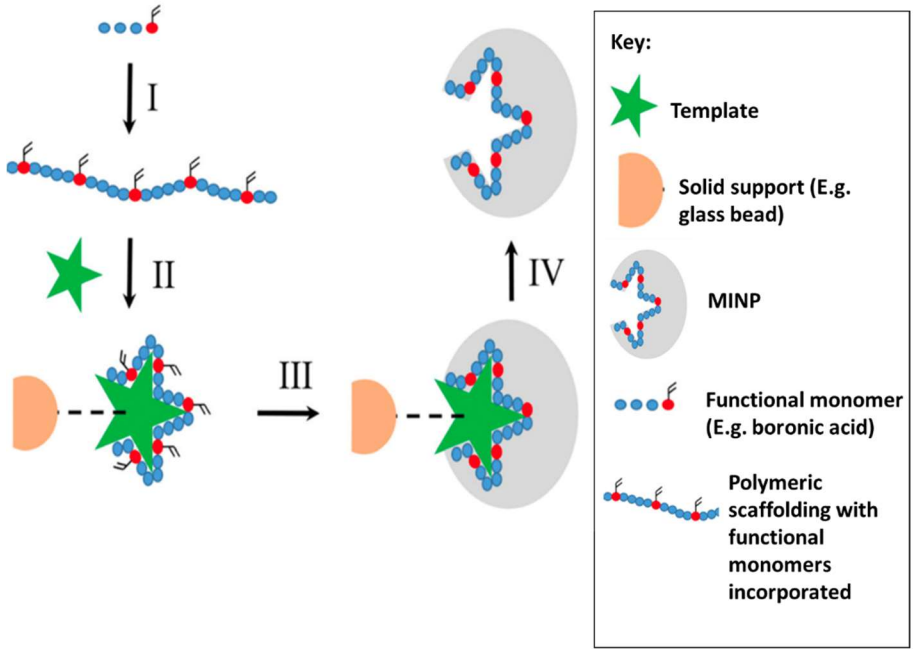


Figure 1-47: Adapted illustration[232,233] for the formation of molecularly imprinted nanoparticles via the use of solid phase synthesis. Stage 1 depicts the formation of the polymeric scaffolding. Stage 2 depicts the formation of the complex requiring imprinting and the fixation of this to a solid phase such as a glass bead. Stage 3 depicts the formation of a polymeric matrix around the template complex. Followed by finally the removal of the template sugar via heat to reveal polymeric molecularly imprinted nanoparticles.

Nanoparticles prepared by solid phase synthesis methods overcome the challenge affiliated with nanoparticle purification and template extraction. This is due to the last step (stage 4) being an affinity purification step, the particles are collected in stages based on their affinity to the support. Those particles which are bound non-specifically are washed away first. The particulates which are more strongly bound will be

subsequently washed away as the temperature of the system is raised. [232,233] Therefore, particles formed via this method possess high affinity and specificity towards their targets making them excellently suited for mobilisation onto the surface of microplate wells for pseudo-ELISA assays.

Elsewhere researchers have attempted to imprint the tri-saccharide motif: Gal-α-1,3(Fuc-α-1,2) Gal. The MI was conducted onto metallic nanoparticles to be used to coat microplate wells. Thus, if the target template is present in solution, these come anchored to the well walls via the MINP. The advantages of utilising magnetic particles enable easier isolation and hence enrichment of targets from complex biological media. This is a common disadvantage for MINPs synthesised in solution (i.e., emulsion polymerisation). Thus, MI is commonly conducted on solid surface to overcome the challenges traditionally associated with nanoparticle purification. The application of imprinting the type B trisaccharide motif (Gal-α-1,3(Fuc-α-1,2) Gal). enables a quick identification of the target by eye as demonstrated in Figure 1-48. [234]

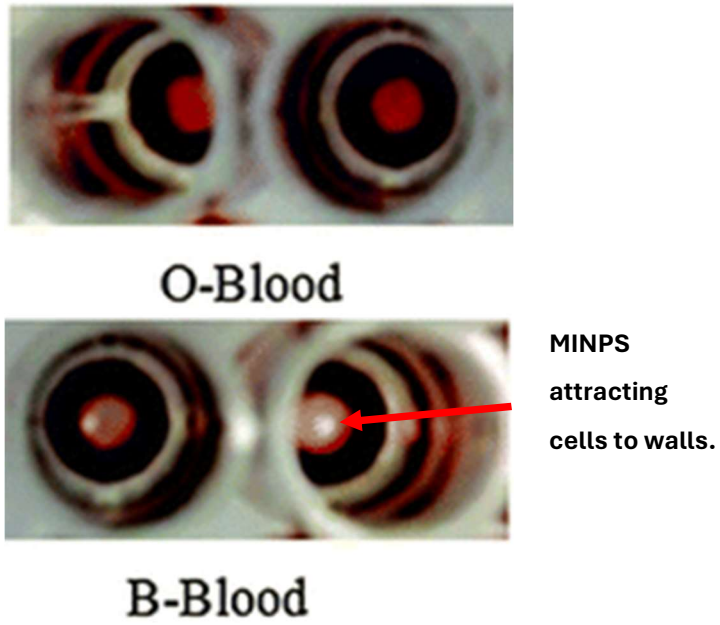


Figure 1-48: Image adapted from literature[234] displaying the presence of MINPs for the detection of blood antigens for development of antibody free blood type detection.

The presence of the target motif in the wells results in the serum becoming clear owing to the movement of the red blood cells to adhere to the nanoparticles on the well walls. When the target was not present the serum remained a red colour. [234]

The MINP examples provided were able to provide limits of detection (LODs) of their biomarkers in the μ-pM range. Thus, illustrating the potential for MINPs to be applied for use in a plate-based assay qualitatively.

More recently attempts have been made to imprint more challenging structures, such as whole glycoforms onto the surface of magnetic nanoparticles. [235] Bie et al. have shown its possible to achieve whole glycoprotein selectivity, while only targeting the surface glycan structures. [157,236]

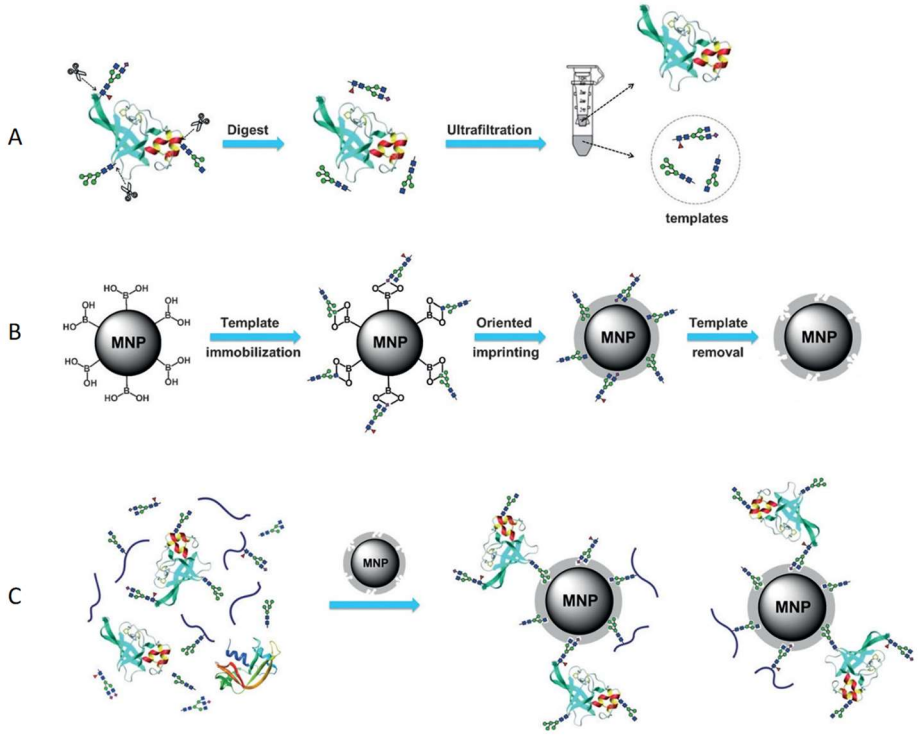


Figure 1-49: Image adapted from literature to depict the 3 main steps to forming MINPs.[157] First, in step A The glycan template is isolated. Second in step B the glycan template is attached to the surface of a nanoparticle (NP) for imprinting. Finally in step C the particles are evaluated by incubating them with a biological sample to test its affinity and selectivity towards its target.

The desired glycan was imprinted onto the surface of magnetic nanoparticles, using boronic acid groups as shown in Figure 1-49. This resulted in the boronic acid targeting one single cis diol of the target structural motif. To create selectivity towards this capture species, a polymer scaffold was created around the glycoform on the nanoparticle surface. The removal of the glycan from the surface thus resulted in a specific 3D cavity complementary to its template. The thickness of the silica layer

forming the polymer matrix was controlled, by adjusting the polymerisation time, ensuring enough glycan was sufficiently covered but still able to detach efficiently. Once the layer was formed, the glycan was removed by acid washes to cleave the ester bond. Afterwards, studies were conducted to determine the binding affinity.

The MINPs could differentiate between RNase A (control) and RNase B (MI template). The imprinted particles exhibited a desirable dissociation constant of 25 μM (Ka = 0.04 μM^{-1}) towards its template (RNase B), the amount of RNase B extracted and hence affinity was several orders of magnitude higher for RNase B over RNase A (control). RNase A provides a control since the polypeptide chain is the same however, it is not a glycosylated protein unlike RNase B. Other glycosylated proteins with a different polypeptide chain were also assessed to confirm the selectivity of the imprint such as HRP (horseradish peroxidase) and transferrin (TRF, two glycosylation sites). The imprinted particles were observed. When imprinted with TRF the MINPs only extracted TRF glycoprotein. Thus, demonstrating recognition of an intact glycoprotein via its glycan chain albeit

However, a caveat to these imprints formed are the reusability of the cavities. Often MINPs displaying tight binding (I.e. low dissociation values) suffer from template entrapment and hence have limited reusability. Thus, limiting their translation to clinical applications.

Like the works of Bie et al. (Figure 1-49) [236], Li and co-workers [237] demonstrated a similar imprinting methodology can be applied to silica nanoparticles as demonstrated via Figure 1-50. [237]

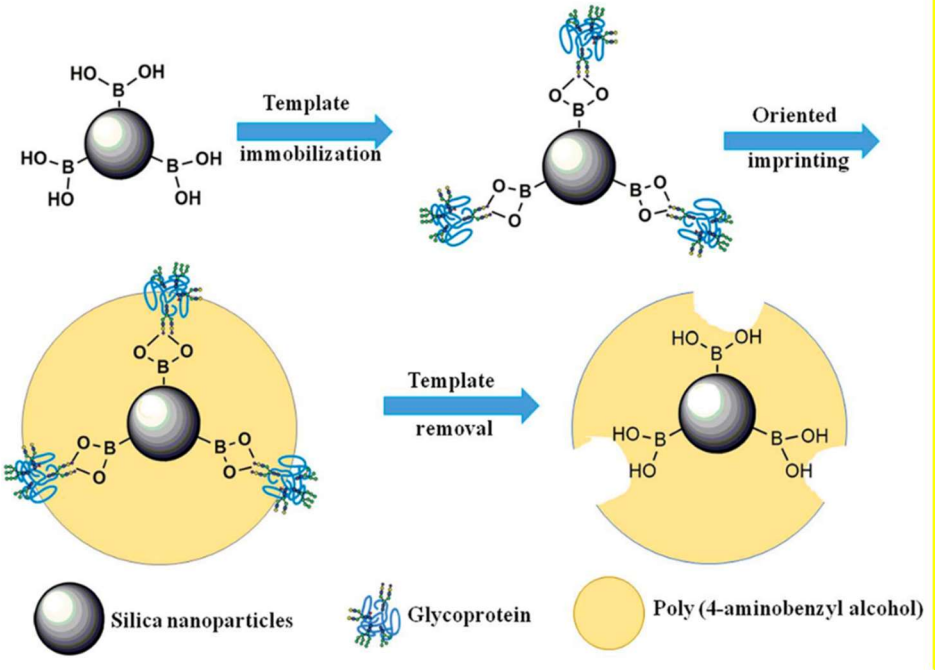


Figure 1-50:Schematic overview for the preparation of magnetic silica MINPs taken from a prior report.[237] The imprinted particles were reported to have similar affinity (Ka = 141 x 107 M^{-1}/ Kd = 0.71 x 10-7 M). to that of real antibodies (Kd ~ 10-7 – 10-9 M) for the imprinted target (TRF). [237]

The formation of the imprint resulted with pockets with comparable dissociation constants to prior works conducted by Bie and coworkers. (Figure 1-49). However, in contrast these particles were unable to differentiate between different glycoproteins of interest (i.e. RNase B, TRF and HRP). The main different between the two works discussed are the polymeric scaffold used. Thus, emphasising the impact on the polymeric scaffold in boosting selectivity. This was also previously observed for the works conducted on a gold 2D surface.

XVIII.SUMMARY

The wide variety of carbohydrate structures makes discrimination between closely related isomers difficult. This difficultly is shown in the lack of publications currently available for glycan detection with high specificity and high affinities. [61] The ability to selectively target glycan motifs can lead to earlier diagnosis for diseases leading to enhanced qualities of lives via earlier intervention. Consequently, research into the identification of glycan biomarkers has been extensively conducted in recent years. Thus, a growing library of glycan motifs is emerging. Researchers have explored the use of different functionality and interactions to form selective and high affinity imprints on both 2D and 3D surfaces. However, many of these works faced a variety of challenges. Some of these challenges include, poor solubility of systems, poor selectivity, poor affinity, template entrapment, template rearrangement, cavity deformation, poor reusability, and challenging synthetic protocols. [192]

Some of the challenges may be overcome via the use of nanoparticles and glass beads. The advantages of molecular imprinting on magnetic particles or glass beads allows quick purification of the imprinted particles from the bulk polymerisation solution. This is a common disadvantage for MINPs synthesised in solution (i.e., emulsion polymerisation). Thus, MI is commonly conducted on solid surface to overcome the challenges traditionally associated with nanoparticle purification. Furthermore, the use of these supports for placement and hence fixation of covalent receptors enhanced the observed binding affinity (Ka) of the receptor towards its

target. A common trend for the use of nanoparticles described entailed the use of boronic acids fixated to a surface to bind to a cis-diol present on the target. The selectivity of the system relied on the use of formation of a suitable polymeric scaffold around the target.

In comparison, the works previously discussed on a 2D surface often entailed the use of a multivalent interaction to trap the template. [203] These pockets contained more than one boronic acid fixed onto the surface. Thus, it is postulated if such a method could be used with a nanoparticle. Although the reusability of the 2D imprinted surfaces was not discussed in these works. The reusability of MI might be possible, owing to the reversible nature of the boronic employed, providing the scaffolding is rigid and robust. [238]

The future a multivalent imprinted pocket on the nanoscale could provide high affinity and high selectivity towards its target with applications to be incorporated into microplate assays. The work within this thesis thus is targeted towards the formation of high order boronate ester complexes to be imprinted onto nanoparticles surface. This will be explained in greater detail next.

CHAPTER TWO

I. PROJECT AIMS & APPLICATION

This PhD thesis focuses on the development of nanoparticles capable of binding to desired glycan targets selectively.

The first objective of this PhD is to identify a suitable nanoparticle material that can undergo MI. Suitable nanoparticles should meet the following criteria: spherical shape with low PDI, ability to be functionalised easily under mild conditions, resuspend ability in aqueous media, ability to withstand changes in the solvent system such as pH changes.

The next objective is the synthesis of the glycan boronate-esters (Figure 2-1) of interest.

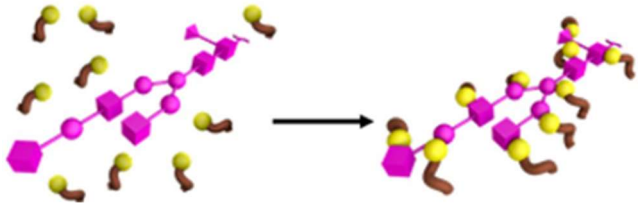


Figure 2-1: Schematic illustration for the binding of boronic acid receptors to glycan targets.

Followed by their purification and characterisation. The control of the orientation of the boronic based receptors is key to forming reproducible and highly selective molecular imprints. Majority of work conducted in literature relies heavily on the polymeric scaffold to impart selectivity which can be

challenging to control. Thus, the use of multiple boronic moieties fixed in a complementary position eases this burden. The formation of the boronate-ester complex was previously optimised and developed by the Mendes group.[203]

Finally, the template (Figure 2-1, glycan boronate ester) requires fixing to the surface to the nanoparticles. To enhance further the selectivity the template will be surrounded by a polymeric scaffold. The resulting cavities on the nanoparticles surface as illustrated below along with the overall PhD aims - Figure 2-2.

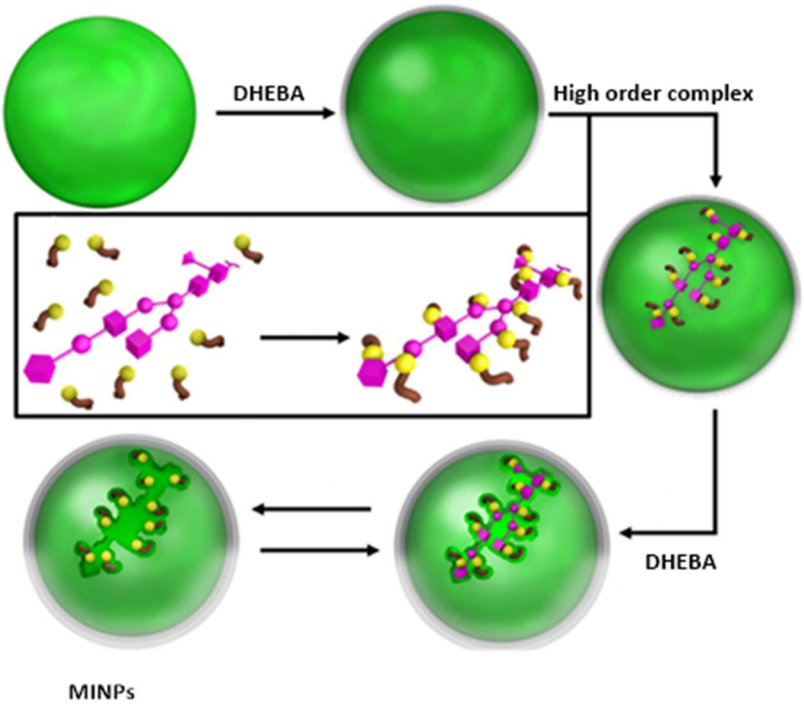


Figure 2-2: Illustration of PhD aims to develop nanoparticles baring surface pockets which are selective for the glycan templates.

The application of this research is towards the use of MINPs in a diagnostic assay. For example, the use of MINPs for the

selection of specific glycoforms affiliated with aggressive prostate cancer. The nanoparticles could be incorporated into a clinical assay to provide quantitative signals to indicate the amount and presence of specific glycoforms. This is presented below.

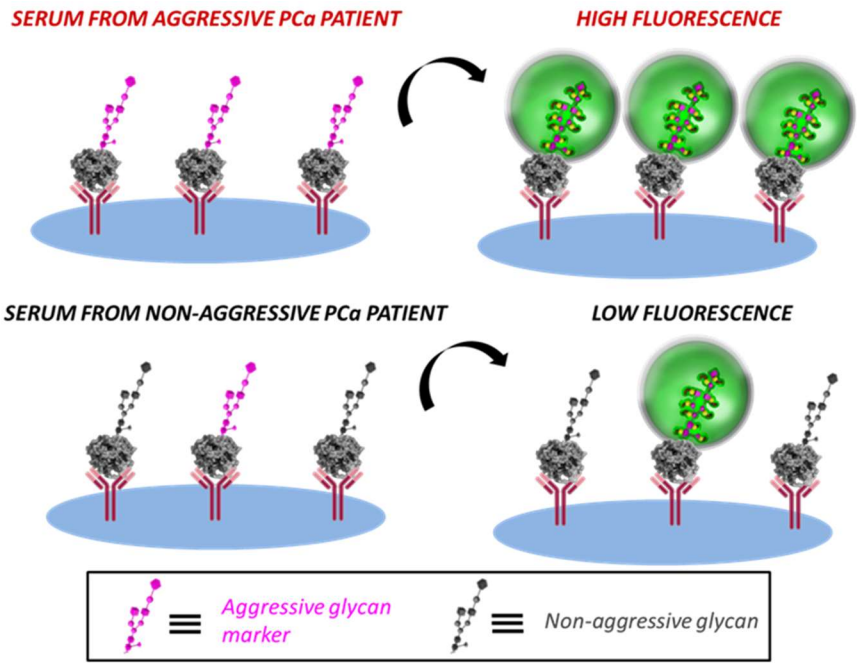


Figure 2-3: Illustration of the potential use of MINPS in a microplate assay to provide a quantitative fluorescent diagnostic tool for the corresponding biomarker of interest.

For nanoparticles to be used in such an assay there are specific qualities the nanoparticles should possess. They should have homogenous pockets and be of comparable size to the biological target (i.e. PSA). The PSA biomarker has an estimated footprint of ~ 4.4 X 4.1 X 5.1 nm.[202] Therefore, the nanoparticle produced should be of the same magnitude of size to best mimic the naturally occurring interaction between the PSA antigen and antibody. Furthermore, the nanoparticles require a

high degree of stability and hence a long shelf-life to permit their use in a diagnostic tool which may require the nanoparticles to be used multiple times on a surface. Finally, the nanoparticles should be simple to synthesise and functionalise under mild conditions and have excellent reproducibility in terms to size and the polydispersity. Some of the characterisation methods for analysing the nanoparticles will next be discussed to provide the necessary knowledge for the following research chapters.

CHAPTER THREE

II. TECHNIQUES AND METHODS

In the forthcoming techniques and methods section, comprehensive details of the analytical techniques employed through this research are outlined. This section is designed to provide a clear and thorough understanding of the methodologies used.

III. DYNAMIC LIGHT SCATTERING (DLS) AND ZETA POTENTIAL (ZP)

Particles or colloidal suspensions in solution can interact with incoming electromagnetic radiation, generating scattered light that can be analysed to obtain information about them. The described technique is more commonly known as dynamic light scattering (DLS). It is helpful to yield information on molecular weights and size distributions. The method is highly popular for analysing proteins, nucleic acids, and viruses, which describes changes in the hydrodynamic diameter of biomolecules and the aggregation of the biomolecules in solution.[239]

In detail, particles dispersed in a liquid will move under Brownian motion. Thus, upon incident light being shone through a dispersion, the movement of particles induces scattering. The fluctuations in the intensity of the collected light can yield information on the particle's sizes. Larger particles will scatter light more than smaller particles, resulting in fewer fluctuations

over time. Conversely, smaller particles will produce more significant light intensity fluctuations over time. Graphically this may be visualised below (Figure 3-1).[239]

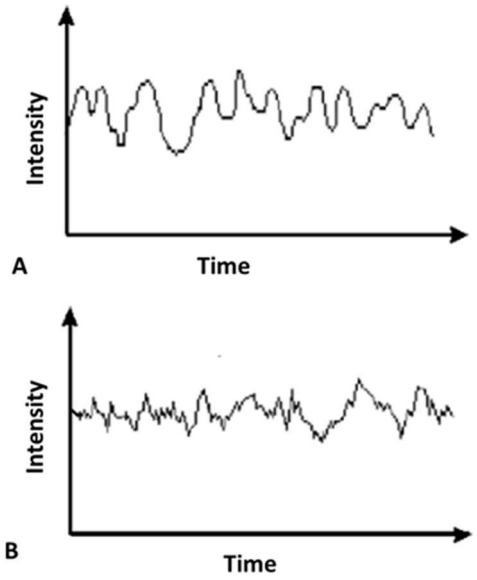


Figure 3-1: Light fluctuations over time due to A) Larger particles & B) Smaller particles.

Owing to the greater speed of the particles and hence a greater probability of colliding with the light in each period. The speed (D, translational diffusion coefficient, m^2/s) in which particles move through the solution can be calculated from the graph (Figure 3-1) of light intensity over time. The speed of the particles (D) is important as it provides information on the hydrodynamic radius (R_H) of the particles. The relationship between the two is expressed via Equation 2.

$$D = \frac{K_B T}{6\pi\eta R_H}$$ **Equation 2**

This is known as the Stokes-Einstein equation and is used by DLS instruments to estimate the average particulate size. This equation provides an inverse relationship between the size (hydrodynamic diameter, R_H) and the speed (D) of the particles. Since all other parameters - K_B, (Boltzmann constant, m_2 kg K^{-1} s^2), T (temperature, K), and η, (viscosity, kg m^{-1} s) are physical constants, one can quickly obtain an estimation of particulate size.

The estimated sizes calculated from this method deviate from microscopy methods. This is due to the DLS measurements include the layer of ions and water molecules that move with the particle. The ion layer thickness is known to vary depending on external factors such as – ionic strength of the medium. The ionic strength of the medium affects the amount of charge that is felt by nearby particles, which can classically be described by DLVO (Derjaguin, Landau, Verwey and Overbeek) theory.[240]

DLVO theory describes the stabilisation of colloidal dispersions by the relationship between van der Waals (VDW) and electrostatic forces. [240] These two forced and independent and opposite in nature and can be modulated by control of the chemical composition of the system. Briefly, at low ionic strength, there is a small concentration of counter-ions surrounding the particulate in solution. Therefore, the particles are said to be weakly “shielded” or “screened” and have large Deye length. In this scenario, the electrostatic repulsion forces are dominant relative to the VDW forces. In contrast, mediums containing a high proportion of charges (higher ionic strength), will be able to “shield” the charges on a particle's surface, a reduction in the Debye length and a reduction in electrostatic

repulsion forces. [240] Since DLS measures the particles and the layer of ions around it, particulates suspended in high ionic strength mediums are more likely to be highly shielded thus leading to higher hydrodynamic diameters (RH). The Debye length will be explained below concerning obtaining zeta potential measurements.

Furthermore, DLS also provides insights into the dispersion of colloids in solution. The dispersion of colloids is known as polydispersity index value (PDI). The PDI is calculated from the mathematical fitting functions applied to calculate the translation diffusion coefficient (D). Briefly, the PDI value represents how well the sample fits the mathematical model. For example, suppose the sample deviates from the mathematic model significantly. In that case, more than one single population of sizes are said to be present. The greater the number of deviations, the greater the PDI and the greater the dispersity. One challenge associated with nanoparticle synthesis is the ability to produce a monodisperse sample. PDI values range from 0 to 1, where samples with values closer to 1 are said to be highly heterogenous (polydisperse), and those close to 0 indicate a homogenous (monodisperse) population.[241]

Furthermore, DLS instruments also provide insights into the charge of the particulates, the instrumentation provides this information in the form of zeta potential values. Thus, it is commonly denoted zeta potential measurements in literature. These values predicted by the DLS instrument are again related to DLVO theory. To provide an illustration of how the particles charge is calculated it is first necessary to view how charges

form on a particles surface, this may be visualised via the below depiction.

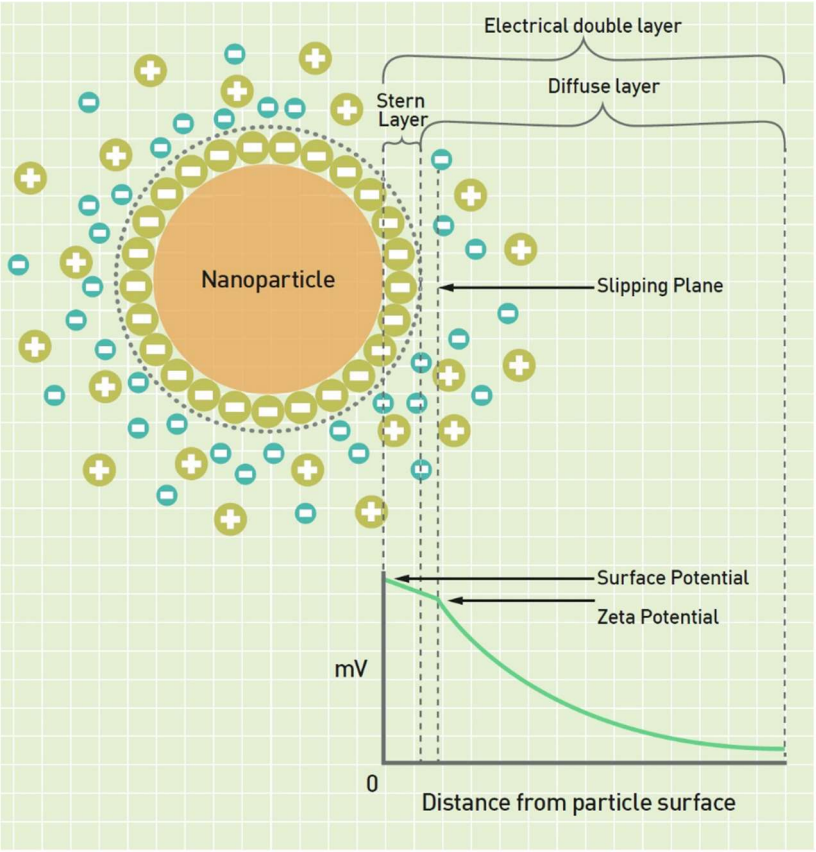


Figure 3-2: Schematic representation of the accumulated charges at the nanoparticle interface and the liquid medium. Image taken from literature. [242]

The layer of ions on a particle's surface is known as the stern layer, as shown in Figure 3-2. Previously the Debye length was discussed in relation to the size of the particles. As depicted by the above diagram the Debye layer (electric double layer) is composed of the intensely bound ions on the particle surface (stern layer) and the loosely associated counter-ions (diffuse layer). Any ions within the electrical double layer will move with

the nanoparticle in the solution. This region is known as the hydrodynamic diameter. For these reasons, DLS size measurements are always greater than other methods, such as electron microscopy.[232,243,244]The electric potential (mV) at the slipping pane region provides the zeta potential value (mV) produced by DLS instruments.

The potential varies depending on the distance from the particle surface. This value indicates the stability of the colloidal suspension. The greater the magnitude, the greater the colloidal stability. Particles with more significant charges repel each other more effectively and are less likely to flocculate. Generally, nanoparticles with zeta potential values greater than +/- 30 mV are considered to have a reasonable degree of stability.[241] For the data to be of suitable quality, criteria must be met; the sample must be of suitable concentration to efficiently scatter the light, have low salt concentration, and be well dispersed in a polar solvent.[241] A dilute colloidal suspension may result in insufficient light scattering events; conversely, too highly concentrated samples may diminish the intensity of scattered light. Thus, the observed results are highly dependent on the concentration of the sample. Consequently, these criteria are not easy to obtain, often leading to misinterpretation and poor-quality zeta potentials. A further caveat of zeta potential is that its values are pH dependent, and the pH of the solution itself varies with temperature and concentration. The combination of the above issues often means that reproducing zeta potential values can be difficult due to dilution errors, temperature, concentration, and pH variances. DLS and Zeta values can only be used as a rough guide for stability and size.[245]

IV. TRANSMISSION ELECTRON MICROSCOPY (TEM)

Electron microscopy is a technique used to capture images of objects that are smaller than the limit of traditional microscopy. It provides information on the dispersity of nanoparticle samples and tracks the size increments during reactions. The technique involves directing high-energy electrons produced from a tungsten filament towards a copper grid (sample) under vacuum conditions (Figure 3-3).

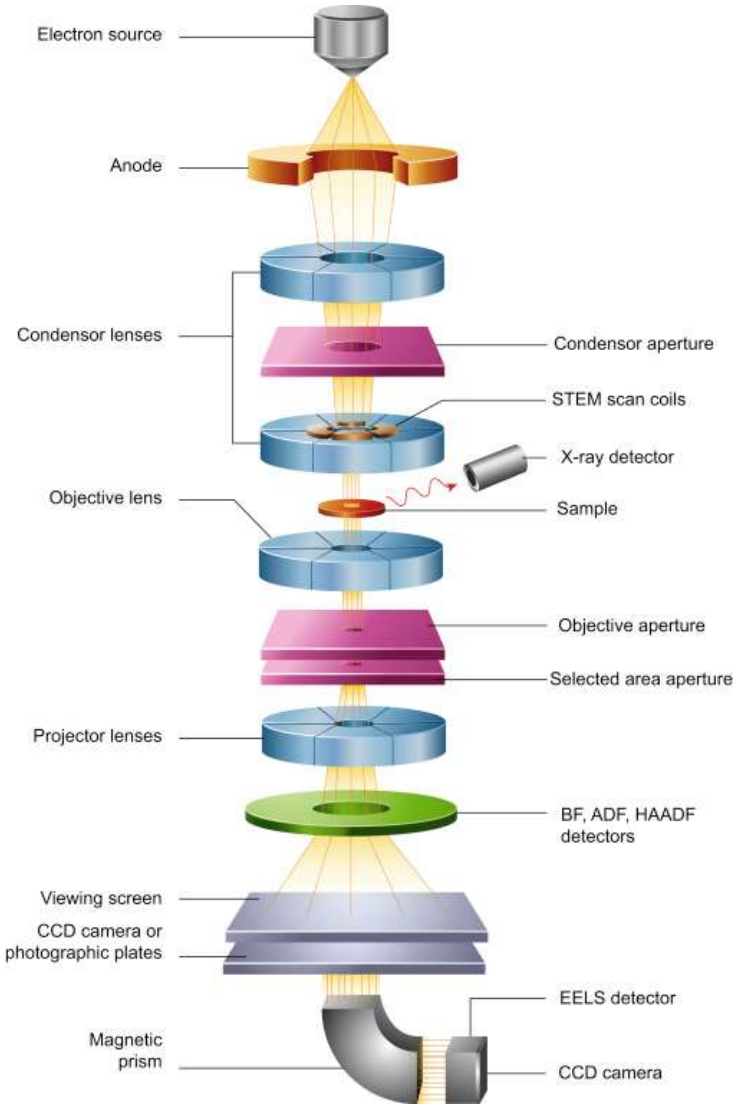


Figure 3-3: TEM schematic - Image taken from literature[246]

Electromagnetic lenses guide the electrons onto the sample, where they scatter upon interacting with the atoms in the sample. The scattering patterns produce dark and bright spots on the fluorescent screen, which is then converted into an image via a charge-coupled device (CCD). The image produced can be viewed on a computer screen (Figure 3-4).

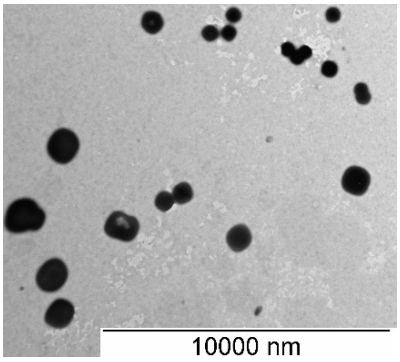


Figure 3-4: Example of a TEM image displaying dark spots are produced from scattered electrons leading to "shadows" of nanoparticles.

To obtain electron scattering and hence the produced images, there are some requirements of the sample. Since electron scattering is proportional to atom density, light organic particulates are less dense and hence do not scatter the electrons efficiently to produce an image. Therefore, for these lighter samples they must first undergo a staining procedure. For heavier atoms such as those in metallic nanoparticles no staining is required and hence TEM is well suited for these samples.

Although TEM provides detailed data, it is not without its drawbacks. Some of the drawbacks are sample preparation may result in changed surface morphology, the dried particulates are prone to aggregation, the use of high energy electron beams can result in sample destruction, polymeric particles often flatten to form “pancakes” on the TEM grids, thus leading to erroneous diameter values recorded which are not representative of the particles in solution. Thus, TEM is often used in tandem with other techniques to provide insights into nanoparticle morphology, dispersity, and functionalisation progress.

V. ISOTHERMAL TITRATION CALORIMETRY (ITC)

Isothermal titration calorimetry (ITC) is a label-free technique that measures the heat generated (exothermic reaction) or absorbed (endothermic reaction) when a binding event occurs between a ligand (L) and receptor (R) (Equation 3).

$$\boldsymbol{R + L \rightleftharpoons RL} \qquad \textbf{Equation 3}$$

ITC is the gold standard for studying intermolecular interactions because no sample modifications are required. It is the only technique capable of determining binding affinity (Ka) in a single experiment, [247] which makes it a popular choice in literature for studying nanoparticle interactions, as well as biomolecules such as DNA and proteins. [248]

$$\boldsymbol{Ka = \frac{1}{Kd}} \qquad \textbf{Equation 4}$$

From the interaction between the receptor and the ligand the measured heats in the system can be translated into binding constants (Ka) which can mathematically be depicted by Equation 4 and Equation 5.Binding constants explain how strongly the receptor ([R]) and ligand ([L]) interact with one another.

$$\boldsymbol{Ka = \frac{[RL]}{[R][L]}} \qquad \textbf{Equation 5}$$

The rate at which the receptor and ligan bind and dissociate is provided by the equilibrium dissociation constant: KD (Equation 6). The equilibrium dissociation constant (KD) is thus inherently

related by the association (Ka) and dissociation (Kd) constants above provided. The relationship between these three are provided by Equation 6.

$$\mathbf{K_D} = \frac{Ka}{Kd} \; or \; \frac{K\,on}{K\,off} \qquad \textbf{Equation 6}$$

Where the dissociation constant (Kd) is the reciprocal of the binding constant (Ka). The association binding constant is a function of the concentration of the receptor ([R]), ligand ([L]) and new complex ([RL]). Knowledge of the binding constant provides thermodynamic information to be deduced for a given reaction. Thus, the Gibbs free energy may be calculated via:

$$\Delta G = -RT \; ln\, Ka \qquad \textbf{Equation 7}$$

$$\Delta G = \Delta H - T\,\Delta S \qquad \textbf{Equation 8}$$

Where R is the gas constant being 1.978 Cal $mol^{-1}K^{-1}$ and T is the absolute temperature measured in Kelvins (K). All other thermodynamic parameters can be calculated by fitting to an appropriate binding model of the ITC experimental data.

The ITC instrument comprises two cells, as illustrated in Figure 3-5. One cell serves as the reference cell, containing only the blank solvent, while the other is the sample cell, containing the sample in the same solvent as the reference cell. The injection of the ligand through the loading syringe into the sample cell initiates small temperature changes within the sample cell. These changes are then subtracted from the temperature of the reference cell to produce the raw data, representing the heat of interaction between the receptor and the biomolecule (Q).

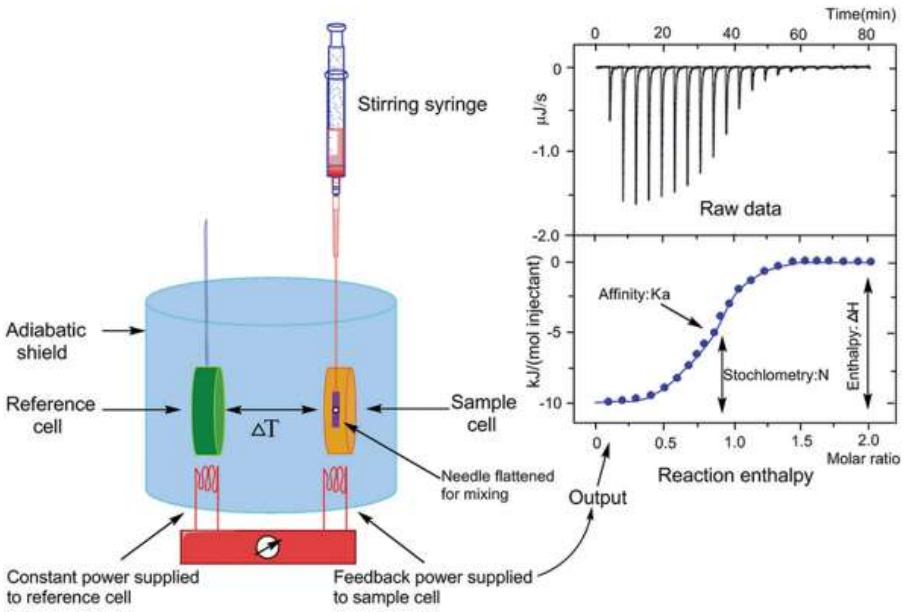


Figure 3-5: Schematic diagram of ITC instrument with its raw isotherm and processed isotherm. Diagram taken from literature. [249]

This heat arises from both non-covalent and covalent interactions between the receptor and the ligand, as well as the interaction of the solvent with the molecules. The heat evolved per injection is proportional to the amount of ligand that interacts with the receptor. As the titration experiment continues the available receptor concentration decreases, resulting in a decrease in the heat changes as the titration progresses towards saturation, in which no more heat changes are detected. This graphically is shown in Figure 3-5.

To derive useful information from the raw data, processing is required. Integrating the individual injection peaks plotted against the molar ratio of the ligand to the molecule of interest (Figure 3-5) provides a range of kinetic and thermodynamic

parameters, such as binding constants (Ka), reaction stoichiometry (n), enthalpy (ΔH), entropy (ΔS), and Gibbs free energy (ΔG). To be precise, the enthalpy (ΔH) of the binding interaction can be directly calculated from the global heat associated with the binding interaction (Q) using the equation below. [250]

$$\boldsymbol{Q = [RL].Vo.\Delta H} \qquad \textbf{Equation 9}$$

Where V_o is the volume of the ITC sample cell, and [RL] is the final concentration of the produced complex in the ITC cell, of units dm^{-3} and mol $dm^{3,}$ respectively. Using Equation 9, it is evident that an appropriate concentration must be used to get appreciable heat signals, to permit correct determination of thermodynamic parameters. If insufficient concentrations and hence heats occur, this will result in a shallower increase with no clear point of inflection of the isotherm. This dependency on curve shape (c.f. Figure 3-6) and concentrations of ligand and receptors is often a limitation of ITC. [251,252]Often with increasing the concentration of the ligand/receptor is not possible due to solubility limitations. Equation 10 provides a mathematical description for the C-Value (Figure 3-6) or the Wiseman parameter, which serves as a reference for ideal values between 10 and 500, as depicted by the isotherms presented in Figure 3-6. [252]

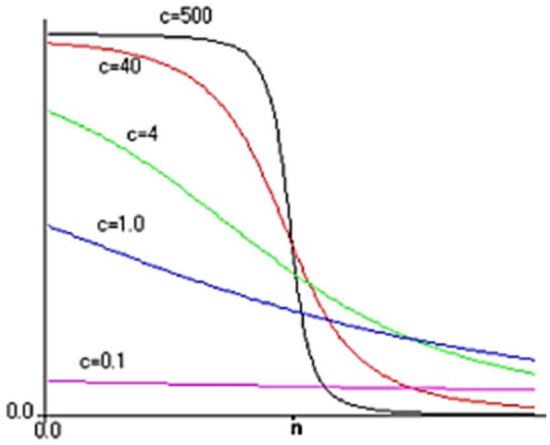


Figure 3-6: Graph to show the relationship between the Wiseman parameter and the shape of the ITC processed data.

$$C = n\frac{[R]}{Kd} \text{ or } C = n\,Ka\,[R] \qquad \textbf{Equation 10}$$

Therefore, systems with exceedingly high or low affinities (Ka) are difficult to study via ITC as the titration peaks in the raw data appear with the same intensity. Thus, the integration produces a flat curve, leading to no clear inflection point for accurate determination of the thermodynamic parameters. However, altering the concentration of the receptor may result in concentration below the limit of detection or may be impractical to alter the concentration of the receptor due to solubility or aggregation issues. In the case of high affinity reactions, these may be studied via displacement studies.[253]

For low affinity systems (Ka < 10^4 M^{-1}), the concentration required for a C value > 10 are usually impractical. One must fix the n value if the reaction's stoichiometry is known. [251,252] This approach is considered a viable method for exploring weak interactions (i.e., C<10) to determine the binding constant (Ka), as previously reported in literature.[254] Despite ITC being

denoted a gold standard technique it is not without its drawbacks, it is a low throughput system only capable of studying one ligand at a time, with a single experiment taking around 60-180 minutes, excluding the instrumentation cleaning procedures. Furthermore, only binding interactions within a narrow range of binding affinities can be studied.[253]

VI. MASS SPECTROMETRY (MS)

Mass spectrometry (MS) is a powerful analytical technique that helps determine the structural composition of a compound. It comprises five essential parts: an ion source, a mass analyser, a detector, a vacuum system, and a data recording system, as shown in Figure 3-7. Samples are typically placed in a volatile solvent and can be introduced directly or via a chromatography device after purification.

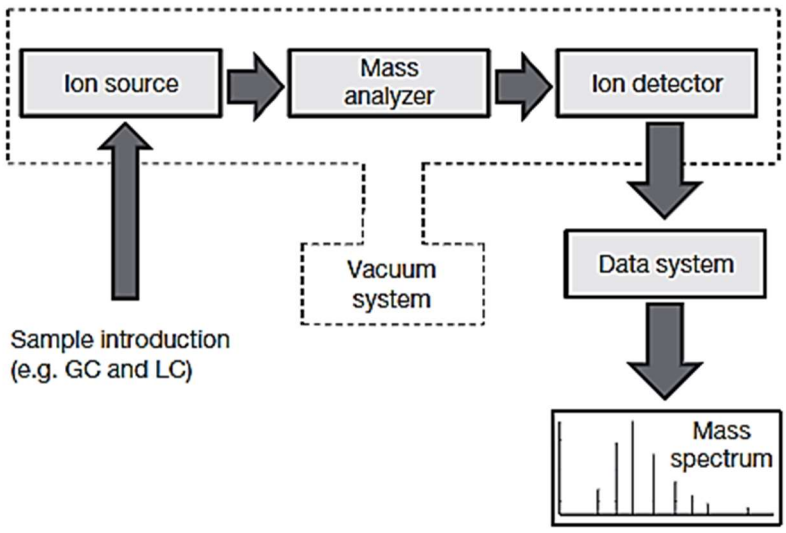


Figure 3-7: Schematic representation of a mass spectrometer taken from literature.[255]

In brief, MS involves ionising the samples to create gaseous ions, which are then accelerated under vacuum through magnetic/electric fields towards the mass detector.

The ions can be generated using various methods such as electrospray ionisation (ESI) and matrix-assisted laser desorption ionisation (MALDI). The mass-to-charge (m/z) ratios

are usually given as the mass of the compound with or without a proton ([M+H] or [M-H]), depending on whether the sample was run in positive (+) or negative mode (-). The resulting mass spectrum has the relative abundance (%) on the y-axis and m/z on the x-axis. An illustration of what MS data looks like is provided in Figure 3-8 for an organic molecule with a mass of 142. The most abundant ion is usually referred to as the base peak and is set to be 100% abundant, while other peaks are normalized to this value.

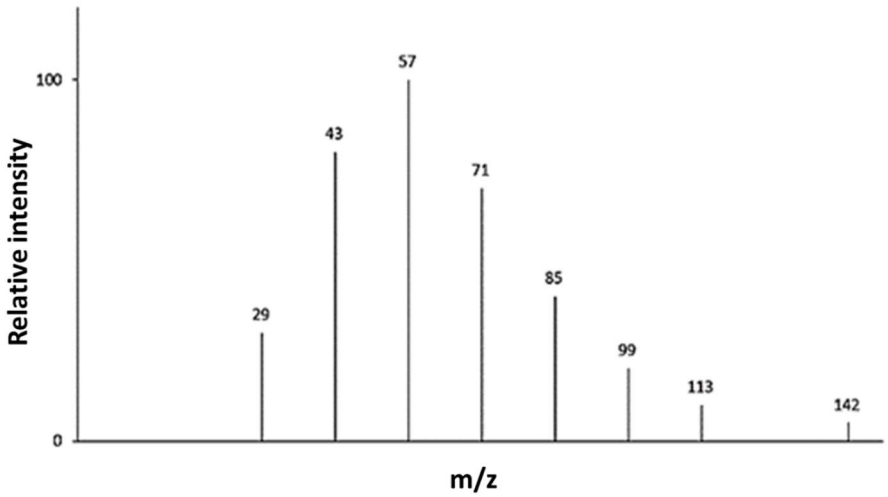


Figure 3-8: Example of a MS spectra. Showing ions produced from an organic molecule with a mass of 142.

The spectra show a series of ions at 43, 57, 71 and 85 all differing by 14 corresponding to the loss of CH_2 units. These peaks arise due to the parent ion at 142 m/z units fragmenting during the high energy ionisation process into smaller molecules. Large molecules of greater mass can sometimes be difficult to

analyse if they heavily fragment during the ionisation process. The ionisation method should therefore be considered before MS analysis.

The data produced from MS can help identify elements with different isotopes, as these isotopes produce a characteristic pattern for that atom. The peak heights from the pattern are indicative of the relative proportions between them. Characteristic isotopic patterns are commonly observed for compounds containing Br, Cl, or B. Thus, if your compound contains any of these elements, the MS spectra peaks should display the expected characteristic isotopic pattern.

Furthermore, when deducing unknown compounds from a reaction there are some rules that can help such as the "*nitrogen rule - If the mass is an odd number, the compound is said to have an odd number of nitrogen atoms*".[256] Conversely, if a compound doesn't contain a nitrogen atom, or has an even number of nitrogen, the molecular ion has an even mass according to the "*nitrogen rule*". Knowing the chemical formula of the compound of interest hence can help predict the expected masses.

However, one should be aware that the most stable ions created during ionisation appear with the highest intensity, while less stable ions appear with less intensity, irrespective of concentration. Therefore, analysis of reaction completion can be complicated via MS. This is further exacerbated in cases where the precursor ion is more stable than the product ion. Thus, it is frequent practice to combine chromatography techniques with MS (i.e., liquid chromatography – mass spectroscopy (LC-MS)) to remove these precursors first.

MS is highly advantageous for structure analysis owing to the small amount of product required for full structural analysis. This method is extremely sensitive and requires less than 1 mg mL-1 of sample for compound analysis, making it far more sensitive than NMR.

VII. MATRIX ASSISTED LASER DESORPTION IONISATION (MALDI)

There are many methods for ionisation however, only the ones relevant for this thesis will be outlined here. A common ionisation method for large molecules is matrix assisted laser desorption ionisation (MALDI). In MALDI a matrix solution is added to the sample, the purpose of the employed matrix absorbs a short laser pulse, which energy is then transferred over to the sample allowing it to become ionised. The ionised molecule can then pass through the electric field to the detector to be analysed. Due to the matrix being ionised rather than the macromolecule, this makes it a softer technique reducing the amount of fragmentation of the molecule. A common "gold standard" matrix that is often used for analysing biological samples such as polysaccharides and peptides are composed of 2,5-dihydroxybenzoic acid (DHB) and a suitable solvent of choice for the biomolecule. [257]

VIII. ELECTROSPRAY IONISATION (ESI)

The electrospray ionisation (ESI) technique is a gentle method of ionisation that is used to study a variety of molecules. In ESI, the sample is dissolved in a volatile solvent, which is then introduced to an electric field in the MS instrument through a charged needle. This process results in the formation of droplets that are transported in a high vacuum towards the detector. As the solvent evaporates, only the charged macromolecules are detected and measured for their m/z value. ESI is especially effective for the study of large molecules, as it allows for the identification of intact macromolecules without fragmentation.

IX. ATMOSPHERIC SOLID PHASE ANALYSIS PROBE (ASAP) IONISATION

Atmospheric solid analysis probe (ASAP) is a method sometimes used to ionise a solid sample for MS detection. ASAP is commonly used for low polarity complex samples that cannot be separated by chromatographic methods, ionized by other methods, or solubilized easily. The ionisation method entails the use of a probe in which the sample is placed on, the sample is vapourised by heating gas such as nitrogen, followed by applying an electric field to produce gaseous ions (corona discharge). Common solvent molecules are readily ionised and are available to collide with the gaseous sample molecules which are not easily ionised. Thus, producing molecular ions such as [M+H]+, this method is commonly used for LC-MS analysis along with electrospray ionisation. [258]

X. MASS ANALYSERS

There are several types of analysers that are commonly used to analyse the m/z ratio of ions created in the spectrometers such as - time-of-flight (TOF) and quadrupole analysers.

XI. TIME OF FLIGHT (TOF) ANALYSER

TOF is the most basic and commonly used analyser, it applies the use of an electric field to accelerate charged ions through an electrical potential via magnets. As the name suggests its records the time taken to fly to the detector through the electric field, ions of larger mass taking longer to fly to the detector than those of smaller masses bearing the same charge. Ions with larger charges will have different speeds as they will be more strongly deflected by the applied field and hence will have greater velocity. This analyser can measure an extensive range of ions arriving at the detector all at once, therefore no information is lost due to their non-filtering nature. Therefore, the advantage of these analysers is that they can cover a wide mass range, making them suitable for analysing large biomolecules such as proteins and oligosaccharides which will often fragment a lot providing a wide spread of ions. In addition, TOF analysers are known for their high sensitivity and high resolution, permitting fast acquisition times.

XII. QUADRUPOLE ANALYSER

The quadrupole analyser is composed of four rods arranged around a central axis, which each rod having a potential, rods opposite one another have the same applied potential as demonstrated via Figure 3-9.

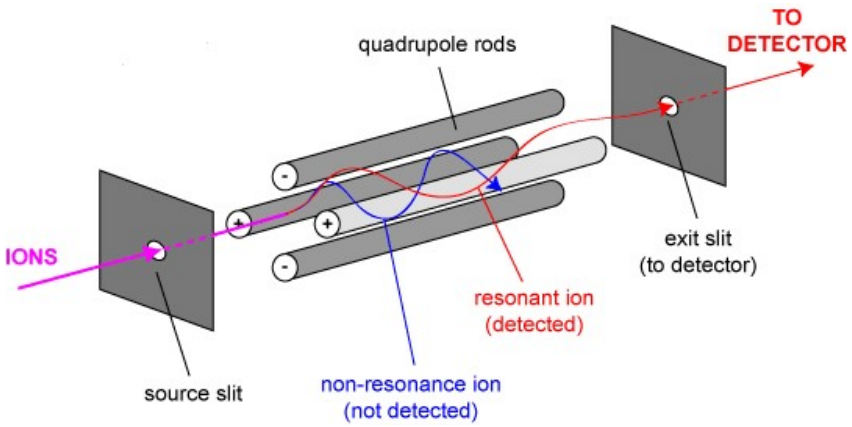


Figure 3-9: Schematic diagram representing the four rods which influence an ions path due to their applied potential which limits the number of ions which can reaches the detector at any given time.

The field applied down the rods is alternated over time, which produces an oscillating electric field. The ions' ability to pass through the oscillating field created is dependent on the m/z ratio of the ions, the oscillating field can be manipulated so that only one ion is stable enough to pass down the length of the quadrupole to reach the detector, this is depicted via the red oscillating path of Figure 3-9. Ions baring different m/z ratios will not be able to pass down the quadrupole which is depicted by the blue oscillating wave on the schematic above (Figure 3-9).

As the voltages are increased other ions of different m/z ratios can be detected over time.

Quadrupole analysers therefore only detect single m/z ratios at a time; therefore, this scanning nature limits the acquisition rate and leads to spectral bias. This scanning nature makes them highly suitable for complex sample analysis where you know your expected ion of interest and thus you can filter for this ion (m/z) only. Thus, quadrupole analysers are routinely used for analytical applications. Although these analysers can be set to scan a wider range of ions, they cover smaller ranges and have lower sensitivity and resolution to TOF analysers previously discussed.

XIII. QUADRUPOLE TIME-OF-FLIGHT ANALYSER (Q-TOF).

In research, quadrupole time-of-flight (Q-TOF) analyser are commonly used. This analyser uses TOF to measure the ion flight times to determine their m/z rations, whilst the quadrupole aspect uses the radio frequencies and the voltages to selectively filter ions of interest based on their m/z ratios. Thus, this technique takes advantage of the high selectivity of the quadrupole analyser for specific ions and the high resolution and acquisition times of TOF to produce a highly detailed and accurate MS spectrum.

XIV. LIQUID CHROMATOGRAPHY – MASS SPECTROMETRY (LC-MS)

Liquid chromatography -mass spectrometry (LC-MS) is a highly regarded analytical technique used to separate a mixture of species, which are then quickly analysed via MS. The separation of complex mixtures is achieved through manipulation of the species' affinity to the solid stationary phase support or the mobile phase (solvent system). Various stationary phase columns can be used to interact with distinct functionalities. Accordingly, depending on the strength of the compounds' interaction with the stationary phase, they will detach at various times during solvent passing through the column. The mobile phase's passage is obtained by operating under pressure, and the desorption of different compounds from the stationary phase can be achieved through the manipulation of the mobile phase (solvent system). For example, a more polar mobile phase is required to elute more polar compounds from the column, while less polar compounds will desorb from the stationary phase as the polarity of the mobile phase decreases, owing to a stronger affinity to the less polar mobile phase.

Researchers can use different stationary phase columns, each having different functional groups. The C-18 column is the most used non-polar reverse-phase column. Reverse-phase columns are used to separate polar species that would otherwise strongly interact with the stationary phase. To enhance separation, a hydrophobic C-18 column is usually combined with a polar mobile phase composed of a mixture of solvents, such as water/acetonitrile or acetonitrile/methanol,

depending on the solubility of the analytes. Normal-phase columns are used for less polar compounds that can be easily removed from the column by increasing the eluent's polarity over time. These columns are commonly used in combination with MS instruments. The compounds eluting from the column are directly injected into the ionisation chamber of the MS instrument, ionising each species one by one, provided the proper eluent gradient is applied. An incorrect column gradient and composition can result in multiple species eluting simultaneously, leading to complicated observed MS data. Therefore, LC-MS is a robust technique for analysing complex mixtures of species.

XV. NUCLEAR MAGNETIC RESONANCE SPECTROSCOPY (NMR)

Chemists and biologists use nuclear magnetic resonance (NMR) spectroscopy to obtain structural information on organic molecules. NMR spectrometers exploits the magnetic properties of specific atomic nuclei to provide details information about the structure, the chemical environment of molecules and the progression of reactions. More specifically, this technique occurs due to atomic nuclei. possessing intrinsic quantised angular momentum. This can be picturised by a spinning top toy which spins about an axis as displayed in Figure 3-10.

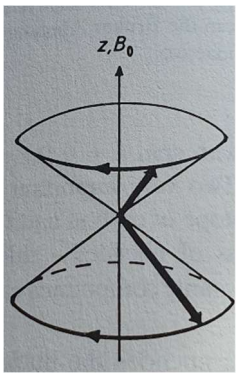


Figure 3-10: Image recreated from literature illustrating the precession of nuclides about an axis analogous to a spinning toy. [259]

This spinning motion (S = nuclear spin) can also be described by Equation 11 - where I represent the overall nuclear spin which is intrinsic to each isotope and can be predicted and h is Planck's constant.

$$S = \frac{h}{2\pi}\sqrt{I\,(I+1)} \qquad \textbf{Equation 11}$$

Since the nuclei contain charged particles, they can be envisioned as tiny magnets, thus when they are spinning about an axis, they will possess an associated magnetic moment (μm), as described by Equation 12.

$$\mu_m = \gamma S \qquad \textbf{Equation 12}$$

Therefore, the spinning nucleotides will respond to an applied magnetic field (B_0) enabling the existence of NMR spectra. However, not all species will produce an NMR signal, and therefore not all species are NMR active. Species which do not produce an NMR signal are said to have a null magnetic moment (μ_m=0) and is therefore unable to respond to the applied magnetic field (B_0).Overall the nuclear spin (I) is calculated as the number of unpaired protons plus unpaired neutrons multiplied by ½. Only those possessing whole integer I values lead to NMR activity (Equation 13), commonly studied nucleotides are summarised in Table 3-1

$$\mathrm{I} = (\#\ \text{of unpaired protons} + \text{unpaired neutrons})(0.5) \qquad \textbf{Equation 13}$$

Table 3-1: Physical properties of common nucleotides and their natural abundances.

Nucleotide	Nuclear Spin (I)	Natural Abundance	NMR active
^{1}H	1/2	99.9885%	Yes
^{2}H	1	0.0115%	Yes
^{12}C	0	98.9000%	No
^{13}C	1/2	1.0700%	Yes

When a nuclide possessing a nuclear spin (I) of 0.5 is placed in a static magnetic field (B_0), it induces a change in the nucleotides. The nucleotides spins become split, this results into the splitting of spins into discrete quantised levels. The values the levels (m) can take are expressed via Equation 14.

$$M = -I, (-I + 1), (-I + 2) \ldots\ldots +I \quad (m = -I \text{ to } +I). \qquad \textbf{Equation 14}$$

For example, a nucleus with an odd number of neutrons and protons will produce a nuclear spin (I) value of 0.5 (Equation 13). Therefore, when these nucleotides are placed in a magnetic field (B_0) their spins will be split according to Equation 14. Therefore, there will be two levels of m = - ½ and m = ½. These levels are no longer of the same energy because of the applied magnetic field (B0) splitting. This process is visually illustrated below - Figure 3-11.

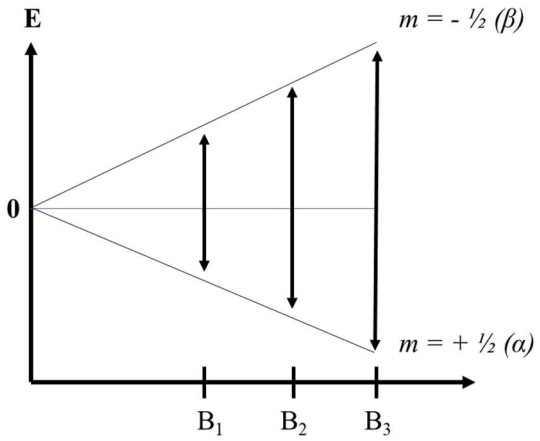


Figure 3-11: Diagram to depict the nuclear spin splitting in the presence of an applied magnetic field, creating new energy levels denoted: m = -1/2 and + 1/2 for I = 1/2.

The difference between these two states, is called the energy gap (ΔE) and may be mathematically described via the below equation. Whereby, B_0 (applied magnet field) and $\boldsymbol{\gamma}$ (gyromagnetic ratio) are both constants. The gyromagnetic ratio is a physical property of the nucleus being studied. All other variables were defined earlier. The greater the applied magnetic field (B0) the larger the splitting (Figure 3-11). [260]

$$\boldsymbol{h\nu} = \Delta \boldsymbol{E} = \boldsymbol{\gamma} \frac{\boldsymbol{h}}{\boldsymbol{2\pi}} \boldsymbol{B_0} \qquad \textbf{Equation 15}$$

Simplified to

$$\boldsymbol{\upsilon} = \frac{\boldsymbol{\gamma}}{\boldsymbol{2\pi}} \boldsymbol{B_0} \qquad \textbf{Equation 16}$$

Following being subjected to the applied magnetic field ($\boldsymbol{B_0}$), the nuclei begin to relax, emitting a frequency denoted as the resonant frequency (Equation 17). This relaxation phenomenon is responsible for the production of an NMR signal known as a

chemical shift ($\boldsymbol{\delta}$). Therefore, each active nuclei (I > 0) relaxing will produce a chemical shift.[259]

$$\boldsymbol{\delta}\ (\boldsymbol{ppm}) = \frac{(\boldsymbol{\upsilon_i} - \boldsymbol{\upsilon_R})}{\boldsymbol{\upsilon_0}} \qquad \textbf{Equation 17}$$

The NMR signals produced ($\boldsymbol{\delta}$) are a measure of the influence of the chemical environment on the resonant frequency of a specific nucleus (Hz), which will vary depending on the frequency of the nucleus ($\boldsymbol{\upsilon_i}$), a reference frequency ($\boldsymbol{\upsilon_R}$) and the frequency (MHz) of the NMR machine ($\boldsymbol{\upsilon_0}$). The relationship between which is expressed in Equation 17 and expressed in ppm.

Furthermore, changes in the nuclei environment will cause changes in the resonant frequency of the nucleus and hence its apparent chemical shift in the NMR spectrum. The chemical environment a nucleus resides in can lead to a reduced effect of the magnetic field due to a term called 'shielding.' The level of shielding a nucleus experience is related to the number of electrons near a nucleus which can provide an opposing magnetic field to the applied magnetic field ($\boldsymbol{B_0}$) which reduces the magnetic field felt by the nuclei resulting in a lower resonant frequency.

In addition to the chemical shift, and hence the position of the signal, its multiplicity (splitting) and integration will need to be considered for structural determination. The signals can appear as more than one line, the number of lines refers to the splitting patterns. These splitting patterns and hence number of lines follow Pascal's triangle (Figure 3-12) only when dealing with equivalent adjacent nuclei. Equivalent nuclei are ones who sit

in the same chemical environment and feel the same effect of the magnetic field.

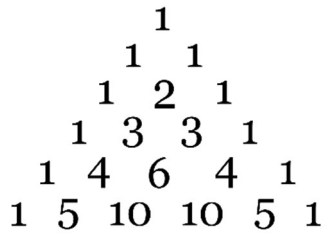


Figure 3-12: Pascal's triangle - can be used to determine the splitting pattern observed in NMR for number of equivalent nuclei.

For example, a nucleus next to two other equivalent neighbouring nuclei will produce a signal ($\boldsymbol{\delta}$) which is split into three lines as depicted via Pascals triangle. The lines will have an intensity ratio of 1:2:1 ratio and are called a triplet signal. When dealing with non-equivalent nuclei the splitting of the NMR signal and the multiplicity can be predicted via Equation 18.

NMR signal multiplicity rule = $2\boldsymbol{nI} + \mathbf{1}$ **Equation 18**

Therefore, in proton NMR (^{1}H), a doublet peak (Figure 3-13 B) provides information on the adjacent protons. This peak infers the nucleus is adjacent to an equivalent proton. Thus, from proton NMR you can gain insights into the structure of the organic molecule.

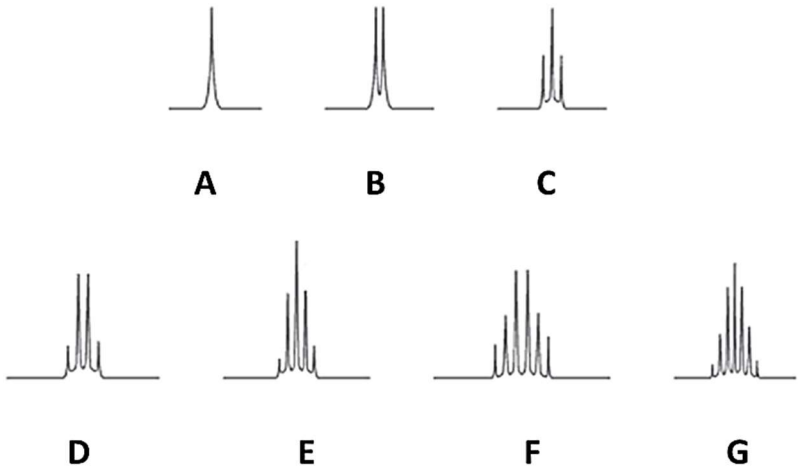


Figure 3-13: Image recreated from literature [261] for the common splitting patterns observed in proton NMR spectra.

Finally, the NMR signals (Figure 3-13) are integrated to provide a numerical value corresponding to the number of protons (nucleus') responsible for producing that signal. Therefore, NMR is commonly used to verify if the corresponding product and hence structure was synthesised.

XVI. ULTRAVIOLET-VISIBLE SPECTROSCOPY

UV-vis spectroscopy (UV) is commonly used to determine compounds based on the intensity of light absorbed in the ultraviolet and visible regions. The technique entails the use of electromagnetic radiation which is directed into the sample via the used of mirrors as depicted via Figure 3-14.

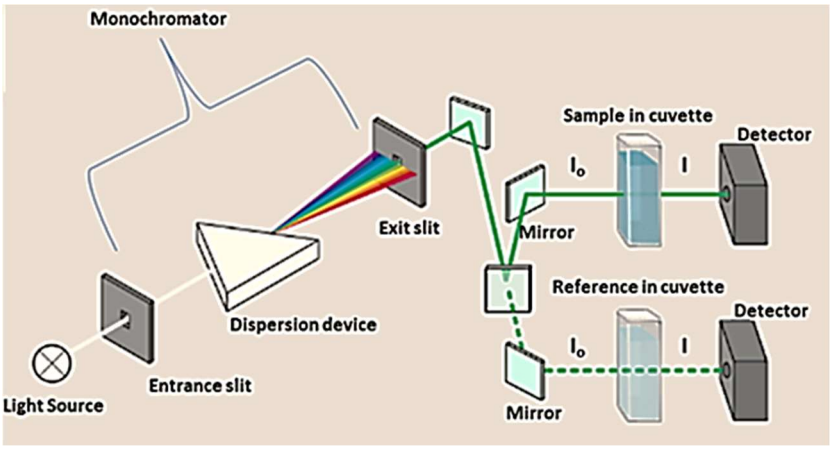


Figure 3-14: Internal components of a common UV-visible (UV-Vis) spectrophotometer which measures the amount of light a sample absorbs.

After light passes through the sample, the resulting light intensity (I, Figure 3-14) is subtracted from the intensity of light applied to the sample (Io, Figure 3-14) to produce an absorbance value. The relationship between absorbance and the intensity of light before and after interacting with the sample is provide below in Equation 19.

$$Absorbance = log\ 10\ \frac{Io}{I} \qquad \textbf{Equation 19}$$

Since the solvent, the sample is dispersed in will also interact with the emitted light it important to conduct a background subtraction. This is conducted by measuring the absorbance of the solvent only (reference). This is depicted above in Figure 3-14 where the UV-Vis instrument measures both the sample and the reference simultaneously and subtracts the absorption from the sample.

For a sample to absorb the light certain conditions must be satisfied. The condition is the energy of the photon must correspond to the energy of the energy gap (ΔE). The energy gap (ΔE) refers to the space between two different electronic states – the HOMO and the LUMO. Therefore, the absorption of the photon provides the energy to excite an electron to be promoted to the lowest unoccupied molecular orbital (LUMO) from the highest occupied molecular orbital (HOMO). The relationship between the wavelength of light absorbed and the energy difference between the HOMO and LOMO are described in Equation 20. Species which are known to strongly absorb UV-visible light are known as chromophores. These molecules possess double bonds in which the delocalisation of π-electrons over the several bonds causes a decrease in the energy gap between the HOMO and LOMO.[238] Therefore, not all molecules produce an absorption spectrum because their energy gaps are too large.

$$\boldsymbol{\Delta E = h\upsilon = \frac{hc}{\lambda}} \qquad \textbf{Equation 20}$$

Where the absorbance values produced by UV-Vis are specific to each wavelength of light the sample is probed with. Usually, a spectral scan is conducted for a sample which records the absorption of light at a range of wavelengths commonly ranging

from 200 – 800 nm. The resulting spectra produced looks like Figure 3-15.

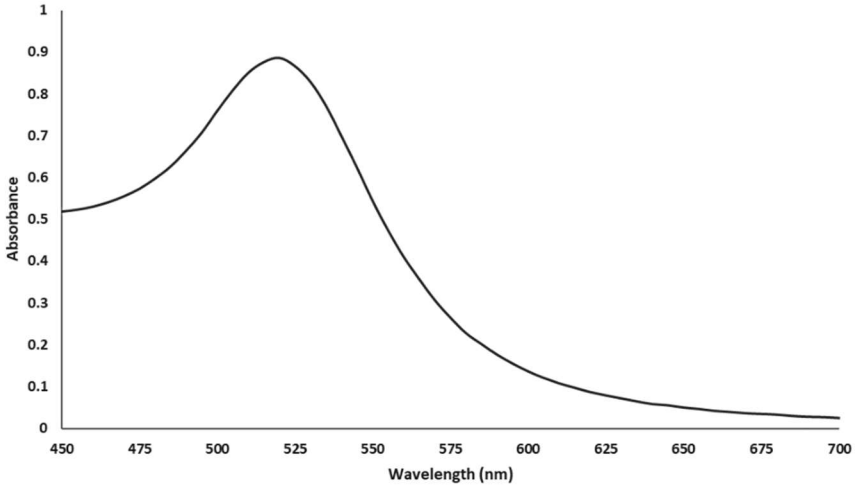


Figure 3-15: Example of PC read out from UV-vis spectrophotometers depicting the absorbance of the sample across a variety of wavelengths.

From the spectral scans produced via UV researchers can gain information about the concentration of an absorbing species from the absorbance. The relationship between concentration and absorbance is described by the "Beer-Lamberts Law" - Equation 21.

$$A = \varepsilon C L \qquad \textbf{Equation 21}$$

"Beers Law" holds true when the concentration is sufficiently low enough, for these conditions to be satisfied it is agreed the absorbance must remain below 1 for the relationship to remain linear. Beyond this, deviations from linearity may occur due to phenomena such as the reabsorption of light, changes in the refractive index, or other chemical interactions.

XVII. APPLICATION OF UV-VIS FOR METALLIC NANOPARTICLES

The way metallic nanoparticles interact with UV-vis photons is unique, resulting in an absorption spectrum Mie theory that explains this occurrence. Local surface plasmon resonance also accounts for the strong absorption bands found at specific wavelengths for noble metal nanoparticles. [262] Instead of an absorption peak, the UV-Vis spectrum displays an LSPR peak. This is due to the electromagnetic field interaction with delocalised free electrons and the excitement of delocalised electrons in the metal's conductance band, which causes electron cloud displacement, as illustrated in Figure 3-16. . [263]

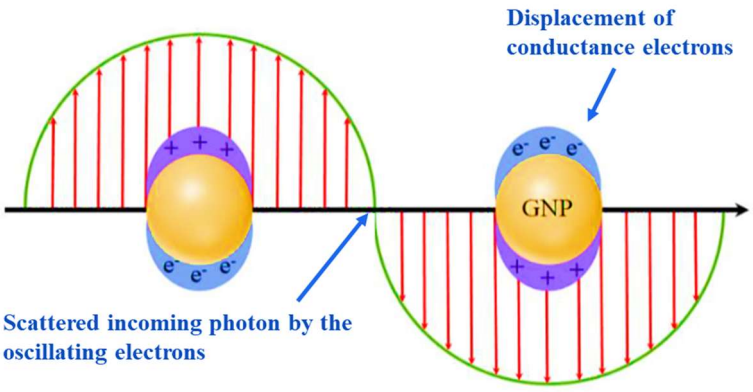


Figure 3-16: Illustration of the light scattering phenomenon leading to the LSPR bands in UV-vis spectra of gold nanoparticles.

This displacement can lead to the scattering of electromagnetic radiation when specific conditions are met, such as when the incident photon and electron oscillation frequency (surface plasmon) are identical as described by Equation 22.

$$\lambda = \frac{c}{v}$$ **Equation *22***

Gold nanoparticles, for example, absorb light in the green region of the visible spectrum, while scattering red light thus appearing as a ruby-red colloidal suspension. [264] Mie's theory suggests that the UV spectrum undergoes a bathochromic shift as particle size increases, which holds for particles up to 100nm. [265–268] This theory makes nanoparticle size tracking and controlled synthesis easier. The bathochromic shifts in the UV-Vis spectrum can be visually monitored to determine the reaction progress, and the reaction can be stopped once the desired colour is achieved. [269] Additionally, the Beer-Lamberts' law can be applied to the UV spectra to obtain insights into the concentration of metallic colloidal suspensions as shown in Equation 23.

$$A = \varepsilon C L$$ **Equation 23**

XVIII. FLUORESCENCE SPECTROSCOPY

A typical fluorometer passes a light source through a monochromator to focus the light to pass through the entrance and exit slits onto the sample as depicted earlier via Figure 3-14. The monochromator only permits a single wavelength of light to pass through at any given time. The emitted light intensity is measured by a detector. The main difference to a UV-vis spectrophotometer is the detector location. The detector is rotated 90 degrees with respect the incident light axis. This allows the collection of the light emitted from the sample that is not from the incident light.

Normally for fluorescence spectroscopy, one wavelength of light is used to excite the sample. A wavelength in which the sample absorbs the greatest number of photons is usually chosen. This wavelength is referred to as λ_{max}, if it is not known it can be deduced by conducting measuring its absorption via UV-visible spectroscopy. UV-vis produces an absorption profile as previously shown in Figure 3-15.

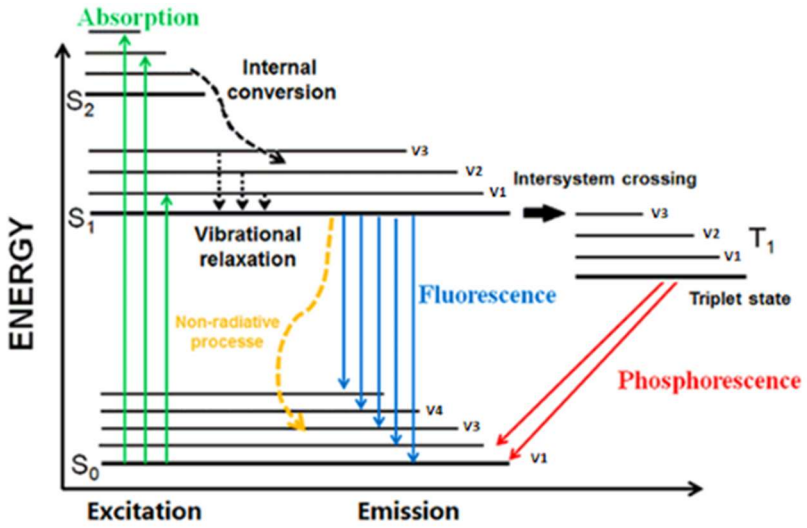


Figure 3-17: A Jablonski diagram to summarise the allowed transition permitting the sample to fluoresce.

Fluorescence spectroscopy, therefore, promotes electronic transitions from one state to another, shown by the green absorption lines. Following the promotion of an electron to a higher electronic state (S_2), the excited electron relaxes and emits a photon of light which is measured by the detector. The energy of the excited electron may be dissipated via vibrational relaxation, intersystem crossing (forbidden singlet to triplet transition resulting in phosphorescence shown in red (Figure 3-17.)

The energy of the photon emitted from a fluorescent sample is always lower in energy than that absorbed. The energy loss is due to vibrational relaxation whilst in the ES which is shown in Figure 3-17. Vibrational relaxation occurs on a much faster timescale than electronic relaxations. Since fluorescence cannot occur without the initial absorption phenomenon, the intensity of fluorescence is therefore proportional to the amount of light absorbed via Equation 24**.**

$$\boldsymbol{Fluorescent\ intensity}\ (\boldsymbol{I_f}) = \qquad \textbf{Equation 24}$$

$$\boldsymbol{k\, I_o\, \Phi \left[1 - \left(10^{-\varepsilon bc}\right)\right]}$$

Where $\boldsymbol{\phi}$ is the quantum yield (Equation 24), $\boldsymbol{\varepsilon}$ is the molar absorptivity, $\boldsymbol{b}$ is the path length, K is a constant based on instrument geometry, and $\boldsymbol{c}$ is the concentration of the fluorophore.

$$\boldsymbol{\phi} = \frac{\boldsymbol{Number\ of\ emitted\ photons}}{\boldsymbol{Number\ of\ absorbed\ photons}} \qquad \textbf{Equation 25}$$

The fluorescent intensity ($\boldsymbol{I_f}$) is proportional to the number of photons absorbed at sufficiently low concentrations (***Equation 26***), much alike UV-vis. At much higher concentrations, the correlation between intensity and concentration is no longer linear. Thus, fluorescent measurements are recorded at very low concentrations to facilitate this mathematical approximation in the linear regime.

$$\boldsymbol{I_f = K\, I_o\, \Phi\, [\varepsilon bc]} \qquad \textbf{Equation 26}$$

However, not all molecules can fluoresce, to fluoresce a sample must absorb light at one wavelength and emit light at a different wavelength. Therefore, all samples which fluoresce also produce a UV spectrum. Furthermore, for a sample to absorb incoming light, the photons wavelength (λ) must be proportional to the energy gap as previously described (Equation 20). Fluorescence therefore detects a smaller number of compounds than UV-Vis.

CHAPTER FOUR

I. INTRODUCTION TO GOLD NANOPARTICLES

Popularly explored to produce specific recognition sites for biomedical applications is molecular imprinting (MI). These recognition sites are commonly labelled "biomimetic receptors." Mimicry of natural biological receptors such as lectins permits the identification of disease biomarkers. Thus, MI is vital to future diagnostic works. Molecular imprints on polymer surfaces have been employed for various works, such as anti-doping, artificial antibodies, and biosensors.[270] However, they are not without challenges and issues, including template conformation changes, imprint collapse following template removal, and reusability of the imprints. [271] Furthermore, MI on the nanoscale level makes it the perfect size for detecting proteins and specific cell surface moieties of the nanoscale. Our research themes wish to exploit this to develop molecularly imprinted nanoparticles that selectively target specific glycan motifs on protein surfaces.

In a previous report, the Mendes group discussed how oligosaccharides can be selectively recognised via MI surfaces. [272,273] Gold surfaces were used to conduct the MI, and the key to its success was incorporating boronic acid receptors, which had previously been called synthetic lectins in other publications.[61,170,274] An advantage of using boronic acids is the reversible nature of the boronate-ester bond and it's controlled

on and off binding via manipulation of the pH. The most recent publication within the group displayed selective binding through a multivalent approach, this is illustrated in Figure 4-1.

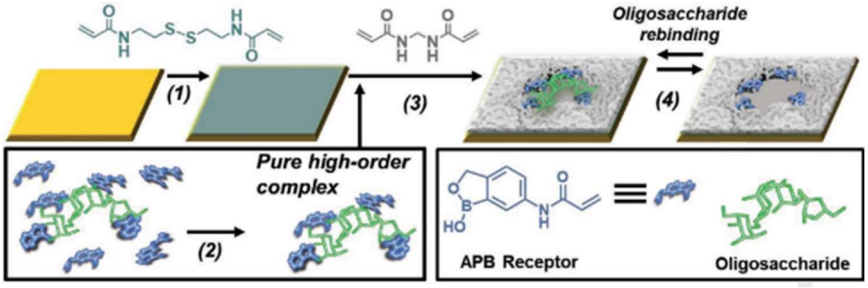


Figure 4-1: 2D surfaces with selective pockets for oligosaccharides previously created in the Mendes group via molecular imprinting methods. Diagram taken from previously reported literature. [203]

The 2D surfaces were created by forming self-assembled monolayers (SAMs) on the gold surface with an amide-terminated thiol linker. The SAMs provided free terminal amides for free radical polymerisation reactions. The glycan boronate-ester template was incorporated onto the surfaces via polymerisation reactions. Finally, the imprint achieved was produced by using a bis-acrylamide crosslinker to react with remaining surface acrylamides, which created a pocket with a shape that complemented the glycan of interest. [203]

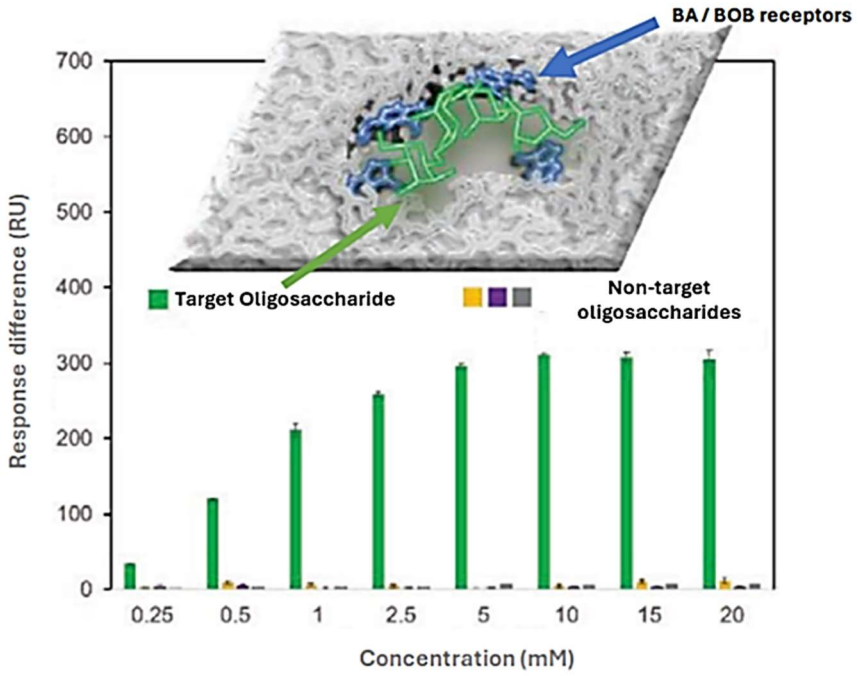


Figure 4-2: Image recreated from literature depicting selective binding scaffolds for specific oligosaccharides using MI methods [203]

Binding studies of these surfaces (Figure 4-2) revealed selectivity for the desired imprinted oligosaccharide, with very little to almost negligible binding displayed for other non-target oligosaccharides, even when comparing saccharides similar in unit length and sugar monomers. Thus, to advance research and target clinically relevant glycan structures, we aim to replicate this work on a 3D nanoparticle surface to yield higher binding affinities.

The nanoparticles synthesised should have homogeneous pockets and be of comparable size to the biological target. The target would be a glycan chain on a glycoprotein such as PSA.

Previous reports have estimated the size of PSA to be around 4.4 X 4.1 X 5.1 nm.[202] Therefore, the nanoparticle produced should be of the same magnitude of size to best mimic the naturally occurring interaction between the PSA antigen and antibody.

In addition, the nanoparticles need to be able to remain stable for a lengthy period if they are to have any potential for a future use in a diagnostic tool. Changes in the core particle's structure could in the future lead to template collapsing on the surface.

Finally, the nanoparticles should be simple to synthesise and functionalise under mild conditions and have excellent reproducibility in terms to size and the polydispersity. Following identification of the nanoparticle material, the focus will be directed to the functionalisation of the particles with glycan receptors in the subsequent sections.

II. SYNTHESIS OF GOLD NANOPARTICLES

Based on the previous d works in the group (Figure 4-1) conducted on gold surfaces, gold nanoparticles were the first type trailed.

Gold nanoparticles are commonly studied for biomedical applications, such as detecting proteins, DNA, and sensor technology.[275–278] In addition to their widespread use in biomedical applications, they have many advantages - ease of synthesis, ease of functionalisation and excellent optical properties. [277,279–282] The optical properties of gold nanoparticles have been described elsewhere in this thesis (Application of UV-vis for metallic nanoparticles).

As demonstrated in previous research, gold nanoparticle properties make them suitable for diagnostic assays. [283] In these studies, gold nanoparticles were combined with ELISA to enhance the detection limits and improve the control of antibody orientation on the exposed surfaces of the ELISA wells. Specifically, we aim to improve on previously reported 2D surfaces by replicating a gold surface with a SAM layer on a 3D surface. [175,203,209,284]

The synthesis of gold nanoparticles involved heating gold tetrachloride with citrate, which resulted in a ruby-red solution after 15 minutes. This synthesis is called the Turkevich reaction and occurs through redox and disproportionation. Briefly, sodium citrate reduces Au^{3+} ($HAuCl_4$) to Au^{+1}(AuCl). Then Au^{+1} (AuCl) is further reduced to Au ^{0}, and AuCl (+3) is oxidised to

AuCl4 (-1) by citrate. The reaction process is illustrated in Figure 4-3. [285]

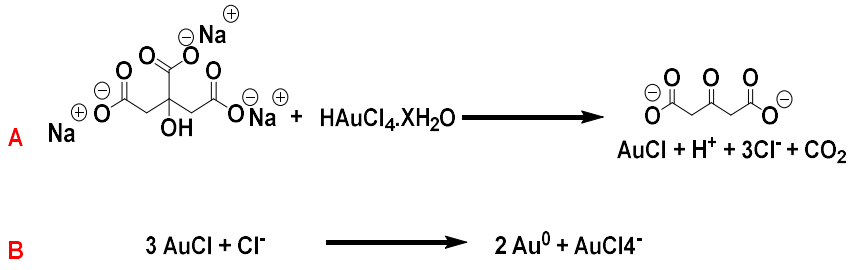


Figure 4-3: An accepted stepwise mechanism for the Turkevich [285] method showing the reduction of gold tetrachloride by sodium citrate. A) displays the initial redox reaction and B) the disproportionation reaction.

The sodium citrate stabilises the gold nanoparticles due to its negative charge, which provides electrostatic repulsions between gold spheres, preventing flocculation. The citrate ligands can also be substituted later for an alternative ligand, such as thiols. Both citrate concentration and the reaction media's pH can control the nanoparticles' size. The greater the concentration of citrate present, the faster the nucleation rate, leading to a more significant population of smaller particles due to faster nucleation rates.

Conversely, slower nucleation leads to lower nuclei concentration composed from the same concentration of precursors, resulting in fewer larger particles. Manipulation of pH changes the proportions of reactive gold precursors. A more significant amount of $[AuCl4]^{-1}$ is present at lower pHs, which has been shown to increase the reaction rate. Confirming $[AuCl4]^{-1}$ the most reactive gold precursor. [286,287]

Well-established literature confirmed the relationship between the molar ratio of gold tetrachloride and sodium citrate and its effect on the size of citrate-capped nanoparticles produced.[288] Equation 27 obtained from literature was used to calculate the fractional concentration (Equation 28) of citrate needed to make any size of gold particles from previously trialled experiments.[287]

$$\text{Diameter (nm)} = (-147.06)[\text{Fractional concentration of citrate}]+122.3$$ **Equation 27**

$$\text{Fractional Concentration (mM)} = [\text{Sodium Citrate}] \div ([\text{Sodium Citrate}] + [\text{HAuCl4}])$$ **Equation 28**

A range of values for the fractional concentration was selected to obtain a list of diameters for gold nanoparticles. The study was conducted to validate previous literature. Three different batches of nanoparticles were synthesised using the amounts calculated (Table 4-1). The reaction process is illustrated in Figure 4-4.

Table 4-1: Proportion of reagents used for the three reactions to produce gold nanoparticles of differing diameters according to well-reported literature.[287]

Theoretical diameter predicted (nm)	10.5	23.0	34.1
Volume of 1% $HAuCl_4$ stock (mL)	0.5	0.5	0.5
Fractional citrate concentration (mol dm^{-3})	0.8	0.7	0.6
Theoretical volume of 34 mM Citrate stock (mL)	1.2	0.8	0.6
Actual volume of citrate stock used (µL)	1200.0	750.0	550.0

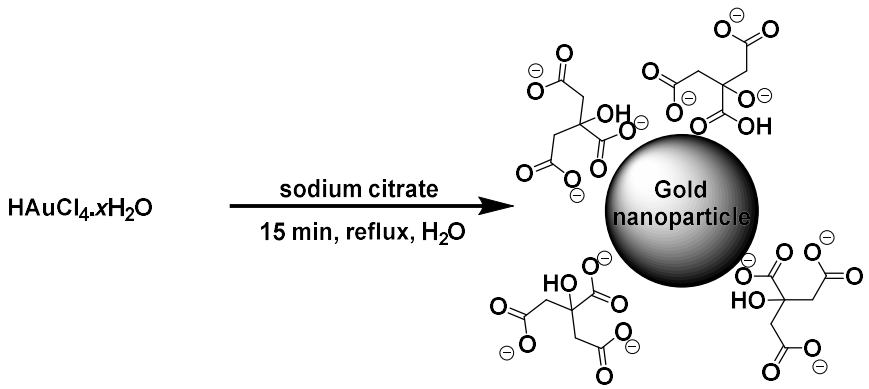


Figure 4-4: Synthesis of gold nanoparticles.

The gold tetrachloride stock (25 mM, 500 µL) was diluted in 50 mL water and refluxed whilst stirring. A warm sodium citrate solution was added upon refluxing the gold solution. The reducing agent volume varied depending upon the size of particles desired; three volumes were trialled in these studies and are tabulated above (Table 4-1) The resulting solution was left to reflux whilst stirring until a ruby red solution was obtained, which usually resulted within 5 minutes (Figure 4-5). As soon as the colour change was observed, the heating was turned off, and the reaction was left for 15 minutes to ensure it had been completed.



Figure 4-5: Ruby-red colloidal suspension of gold nanoparticles produced.

Upon cooling, the ruby-red suspensions were analysed by TEM to compare their sizes to the expected literature sizes (Table 4-1).

For TEM, the nanoparticles were first dried on mesh copper grids before viewing; for full methodology, refer to Transmission electron microscopy (TEM). The captured particle images were processed via Image J software.[289] The averaged diameter was calculated for all three reactions (figure 4-6). The study was

conducted to validate previous literature. Three different batches of nanoparticles were synthesised using the amounts calculated (Table 4-1). The spherical shape and size distributions of the particles synthesised are displayed in Figure 4-6. It was noted that the observed dimensions of the nanoparticles exhibited minor disparities from the theoretically reported sizes in the literature. These deviations could be attributed to variabilities inherent in the production of stock solutions. Furthermore, the theoretical diameters and the fractional concentrations (Table 4-1) were approximated to a single significant figure, thereby unavoidably introducing variability in the size determinations. During the microscopy image processing phase, nanoparticles were randomly selected from the entirety of the grid. Thus, it is conceivable that inherent biases may have influenced the outcome, potentially favouring specific spheres or grid regions. Hence, it is postulated that the above factors contributed to the observed deviations. To mitigate sampling bias, it is best to count and image over 200 nanoparticles to reduce these factors and ensure the sample size representitive.[290] Thus, the subsequent diameters recorded where possible were an average of over 200 particles.

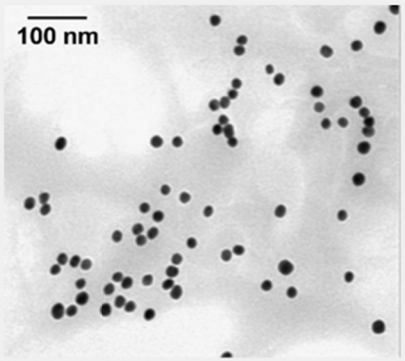
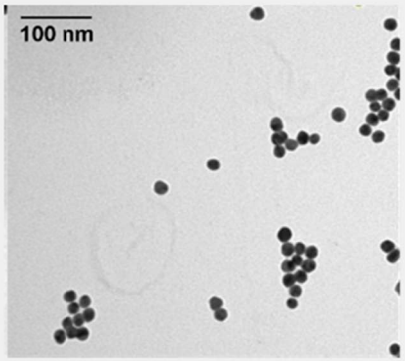
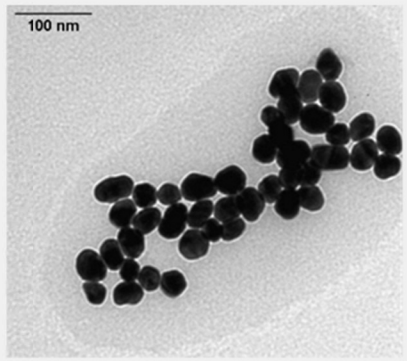
Theoretical diameter	11 nm	23 nm	34 nm
Measured TEM diameter	17 ± 1 nm Population = 32 particles	23 ± 4 nm Population = 33 particles	32 ± 4 nm Population = 112 particles
Microscopy images			

Figure 4-6: Comparison of expected literature sizes and actual experimental sizes of gold nanoparticles synthesised.

To summarise, the synthesis of 10-34 nm nanoparticles was successfully obtained as per previously reported literature.[287] This confirmed that the selected methodology could be used for future synthesis of other sizes. The conditions for obtaining the 17 nm gold nanoparticles were used for the subsequent experiments within this section.

III. CHARACTERISATION OF GOLD NANOPARTICLES

The synthesis was repeated after obtaining a reputable synthetic protocol for gold nanoparticles to assess its reproducibility.[287]

Briefly, 0.8 M fractional citrate was used to reduce the gold tetrachloride stock (Table 4-1) and refluxed to produce a ruby red solution (Figure 4-5). Complete characterisation of the particles was conducted using DLS, ZP, TEM and UV/vis spectroscopy techniques. For a full synthetic protocol refer to The synthesis of gold nanoparticles.

The DLS measurement approximated the nanoparticles to have an average hydrodynamic diameter of 34 nm (Figure 4-7) with a polydispersity index of 0.18. PDI values for nanoparticles vary from 0 to 1; those closer to 0 are monodisperse, and those with values tending more towards one are said to be more polydisperse.[241] The gold nanoparticles with a value of 0.18 are very well dispersed with little size variations.

Next, the zeta potential was measured by applying a potential to the nanoparticles to produce an averaged zeta potential value of -31.6 mV. The zeta potential value indicates these particles have excellent stability. Previously reported literature states that zeta potential values less than -/+ 25 mV are unstable, values exceeding -/+ 25 mV have intermediate stability and finally, values exceeding -/+ 30 mV are said to be very stable.[239,241]

TEM can also verify the above claimed dispersity, in addition to their size when dried on a mesh copper formvar grid. The particles when dried on a 2D surface provided spherical looking particles as shown in Figure 4-7.

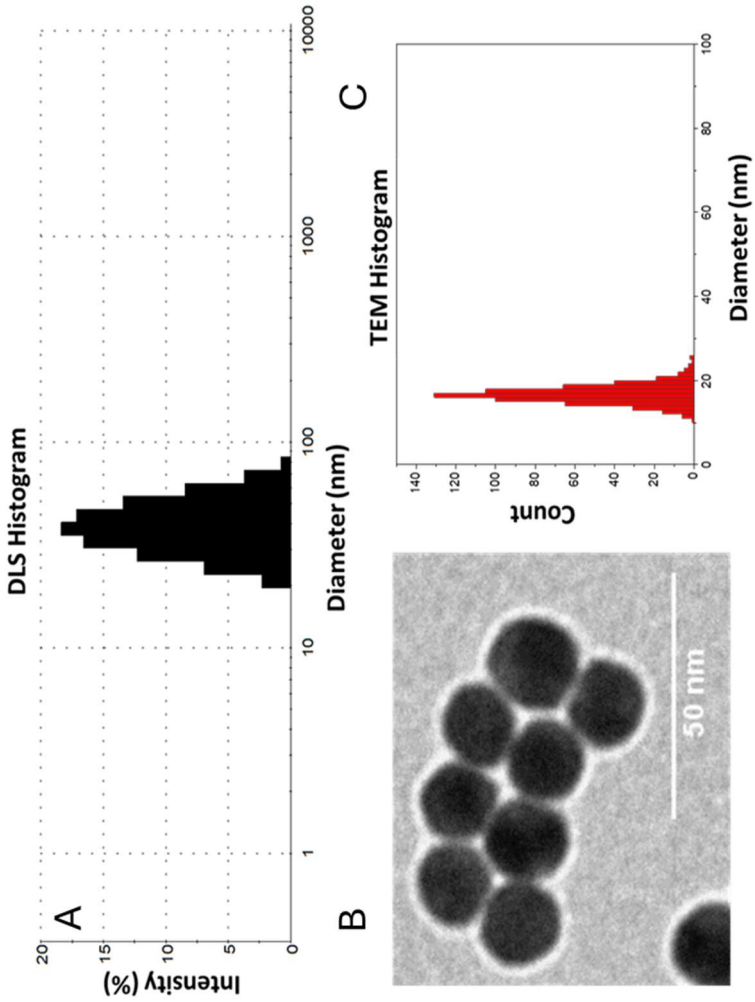


Figure 4-7: Characterisation of citrate-capped gold nanoparticles. A) DLS histogram showing an average size of 34 nm B) TEM image for gold nanoparticles (17 nm, SD ± 1 nm) C) TEM Histogram showing an average size of 17 nm and a narrow size distribution

The TEM images showed equally sized spherical nanoparticles well dispersed on the grid. To obtain information on the distributions of sizes present at least 200 particles were measured. The average particle size was found to be 17 ± 1 nm (population size 598).[290]

DLS and TEM are two popular methods used to measure the average particle. However, they often yield varying results due to their different methodologies. TEM directly measures particles on a 2D surface, which may be considered more precise. In contrast, DLS measures the translational diffusion coefficient (Equation 2). Thus, the DLS particle size is approximated via application of the Stokes-Einstein equation. This equation considers factors such as concentration, temperature, and solvent, which can result in highly variable measurements. [239] Therefore, when interpreting DLS size data, it is recommended to consider the correlation function data, the average hydrodynamic diameter, the PDI (polydispersity index), and the primary peak percentage with caution.[244]

Furthermore, DLS tends to produce larger diameters than TEM because it is an intensity-based technique.[232,243,244] The size discrepancies in publications range drastically from a few nanometres up to several hundred nanometres.[244] The scattering intensity is proportional to the sixth power of the particulate radius. Thus, larger particles mask the presence of smaller particles, even when the concentration of large particulates is extremely low. This results in a higher distribution towards larger diameters.[232] While it is possible to produce hydrodynamic diameters from DLS comparable in size to those made by TEM, this requires a perfectly uniform sample, which

can be challenging due to imperfections in samples. Therefore, comparing the number (TEM) and intensity (DLS) distribution results does not make sense. For clarity, Figure 4-8 visualises the intensity-based technique flaw.

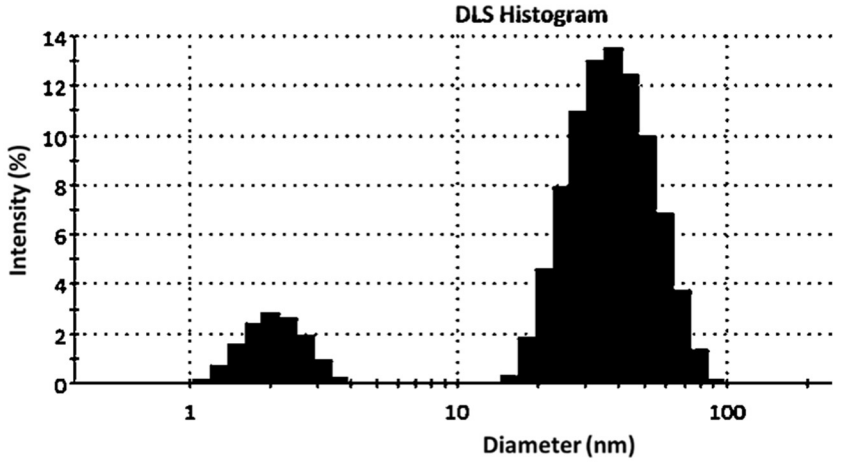


Figure 4-8: DLS measurement of a sample found to produce a hydrodynamic diameter of 21 nm despite over 80% of the particles being measured as 39 nm. Thus, additional nanoparticle populations may deviate from the results. Hence, DLS is most accurate when the sample is monodispersed.

Here, two distinct populations of nanoparticles exist with sizes of 2 nm and 40 nm. The presence of the smaller population significantly reduces the calculated average diameter, which would cause the hydrodynamic diameter to vary from the measured TEM microscopy diameter.

Thus, the discrepancies between DLS and TEM were confirmed acceptable and the summarised data in Figure 4-7 confirmed the chosen literature synthetic protocol was reproducible.

UV-vis spectroscopy was also conducted to complement the size analysis conducted above. UV-vis for gold nanoparticles is quick and convenient, providing insights into the polydispersity of the sample and particulate sizes. [291]

Gold nanoparticles exhibit localised surface plasmon resonances (LSPR), resulting in a strong absorbance band in the visible region of the UV-vis spectrum. The absorbance observed is denoted by as the "*LSPR peak*" after the collective oscillation of the free electrons at the particle surface (localised surface plasmon resonances), which are responsible for the phenomenon. The LSPR peak depends on the size and shape of the gold nanoparticles.[292] The UV-vis spectrum will show a single sharp peak corresponding to the particles' LSPR for a monodispersed sample of gold nanoparticles in solution. However, when several different particle sizes exist in solution, their LSPR peaks overlap. Thus, the UV-vis spectrum shows a broadened peak with a full width at half maximum that increases with increasing polydispersity. This is because the LSPR peak shifts bathochromically, as particle size increases (c.f. Application of UV-vis for metallic nanoparticles). Therefore, one can gain insights into the polydispersity of the gold nanoparticles by analysing the position and shape of the LSPR peak for the synthesised nanoparticles.

For these synthesised gold nanoparticles, the corresponding LSPR peak was observed at 520 nm, as shown below (figure 4-9).

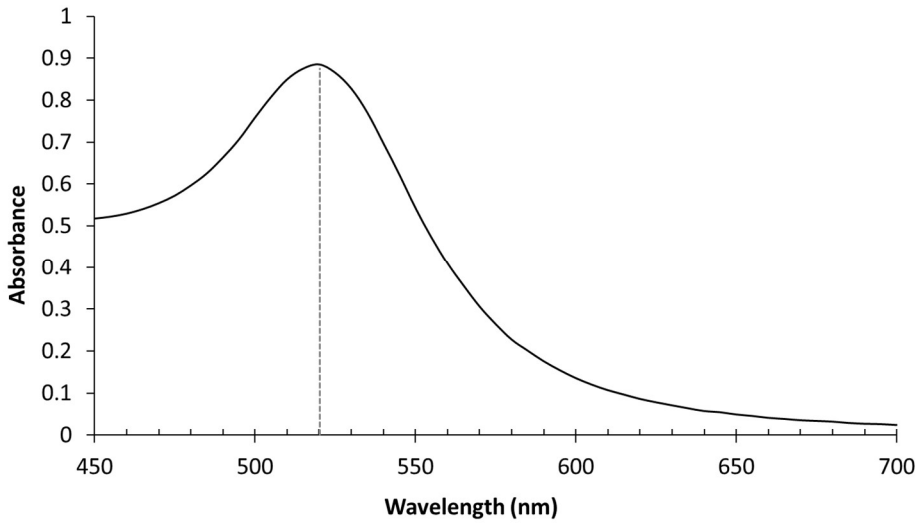


Figure 4-9: UV-Vis spectrum for gold nanoparticles displaying a LSPR peak at 520 nm (λ_{MAX} = 520 nm, Abs = 0.89).

The UV-vis spectrum above provides a basis for comparison of future gold nanoparticles. UV-vis is a very quick technique, providing insights into changes in nanoparticles surfaces. Thus, future batches after functionalisation are expected to yield different LSPR peak positions.

To conclude, from the DLS and TEM data, the particulates were found to be 34 nm and 17 nm, respectively. The subsequent replicates (

Appendix 9-1) of the synthesis provided nanoparticles measuring diameters of around 17 nm via TEM, and thus, the reported literature was confirmed reproducible and acceptable.[287] Further works will focus on the functionalisation of these nanoparticles to provide a starting point for molecular imprinting.

IV. FUNCTIONALISATION OF GOLD NANOPARTICLES

Gold nanoparticles were synthesised, and their compatibility with various thiol ligands as alternatives to citrate capping agents was explored. This approach presents the benefit of enhanced stability and possibilities for further particle customisation. Thiol ligands are especially well-suited for this application due to their strong affinity to gold, which leads to exceptional colloidal stability (with a bond strength of 40-50 kcal mol-1). [293] Thiol ligands were selected based on their ability to participate in high-efficiency coupling reactions, such as "*EDC-NHS*" and "click reactions", known for their high yield and capacity to form pH-resistant stable bonds.[294] These traits make them an excellent choice for molecular imprinting.

The "EDC-NHS" coupling reaction is commonly reported in literature for obtaining functionalised gold nanoparticles from citrate-capped nanoparticles.[291] The reaction entails a water-soluble crosslinker agent (EDC), which enables the formation of the new carbon bond (C-N) between a carboxylic acid carbonyl moiety and an amine group of another monomer. The general reaction scheme is outlined in Figure 4-10.

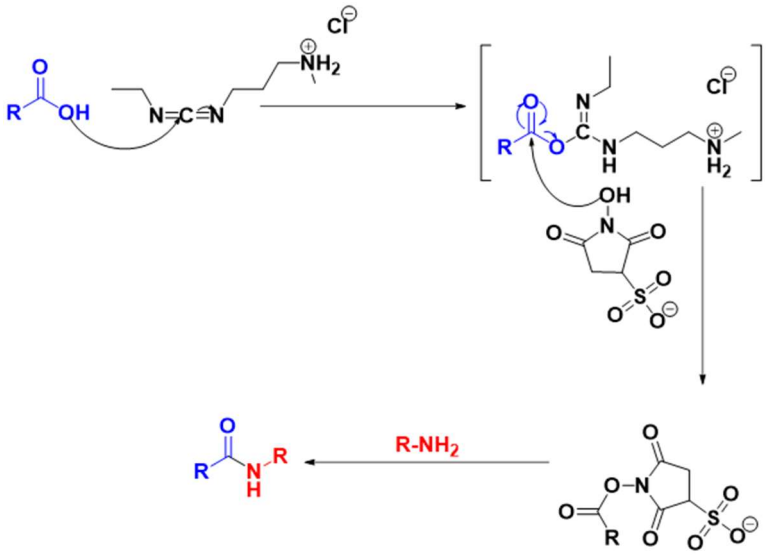


Figure 4-10: Reaction scheme for EDC-NHS coupling reactions to form a new stable amide.

Alternatively, "*thiol-ene click chemistry*" is also highly efficient and dependable for synthesising functionalised gold nanoparticles bearing stable C-S bonds with high yields [295]. It is extensively studied in nanoparticle surface modifications. [294,296] The reaction is commonly conducted via radical polymerisation and proceeds through a typical chain process consisting of initiation, propagation, and termination steps, as shown in figure 4-11.

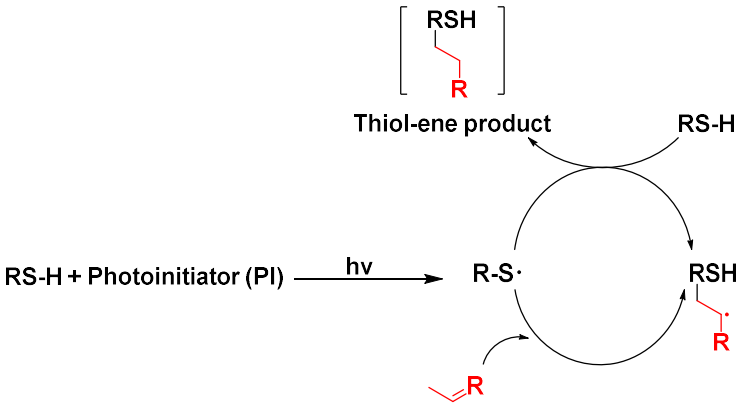
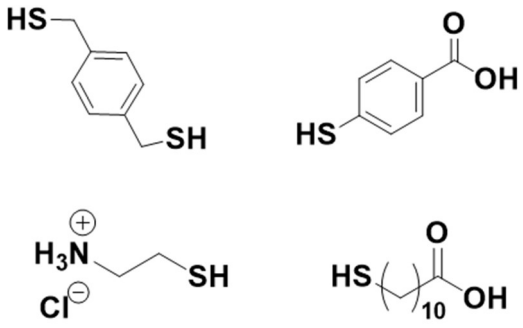


Figure 4-11: Example of thiol-ene chemistry polymerisation scheme producing the stable carbon thiol bond in the anti-Markovnikov product.

The thiol ligands investigated in this section are shown below in

.

figure 4-12 and vary in backbone length and the terminal



functional group.

Figure 4-12: Thiols selected for the functionalisation of gold nanoparticles from top left to bottom right – 1,4-benzenedimethanethiol (BDMT), 4-mercaptobenzoic acid (MCA), cysteamine hydrochloride (Cys) and 11-mercaptoundecanoic acid (MUDA).

Self-assembled monolayers (SAM) consisting of shorter thiol ligands were thought to provide a better rigid base for MI. [203] However, it is believed that shorter ligands may lead to unstable particle suspensions owing to the lack of electrostatic repulsion. Therefore, there is a need to compromise between what is best for the imprinting base and what is best for the nanoparticle's stability.

This section investigates the stability of gold nanoparticles when functionalised with the above ligands. The resulting suspensions will be analysed by UV-vis spectroscopy to provide information on the LSPR peak position, concentration of nanoparticles, changes in nanoparticle size, and monodispersity of the sample. [290,297,298]

V. FUNCTIONALISATION OF GOLD NANOPARTICLES WITH CYSTEAMINE HYDROCHLORIDE (CYS).

The water-soluble cysteamine hydrochloride (Cys) ligand (figure 4-13) was chosen for its amine functionality, providing a positive charge for electrostatic repulsions.[299] In addition, the short backbone was thought to give a rigid SAM for MI. The Cys ligand is an excellent choice for MI, providing amine-terminated surfaces that can be further modified through "EDC-NHS" reactions. [300]

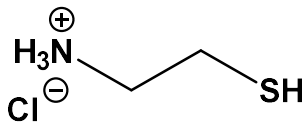


Figure 4-13: Cysteamine hydrochloride (Cys) ligand used to functionalise citrate-capped gold nanoparticles via ligand exchange reactions at room temperature.

Previously synthesised gold nanoparticles (C.f. ***The synthesis of gold nanoparticles***) first underwent centrifugation to eliminate unreacted reagents. The resulting pellets were then resuspended in water and analysed via UV-vis to obtain their LSPR peak. The spectra obtained is provided below for the purified nanoparticles (Figure 4-14).

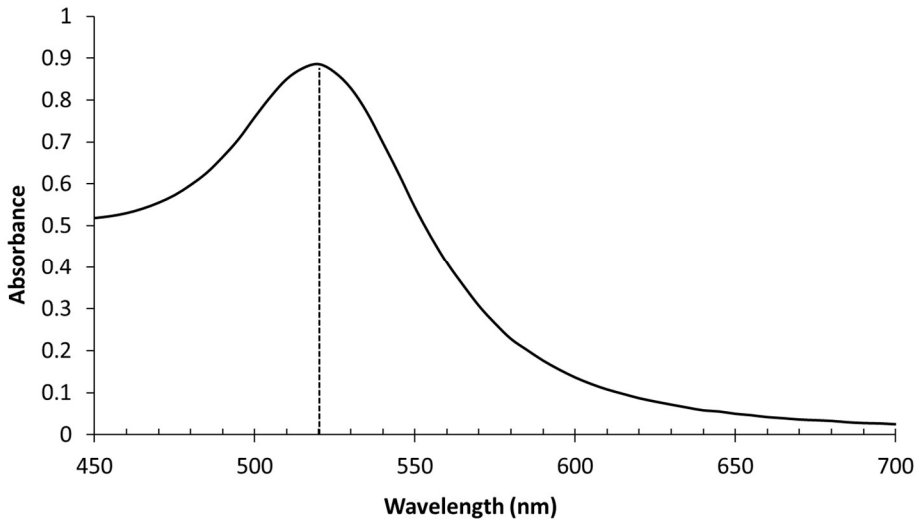


Figure 4-14: UV-vis spectrum of purified gold nanoparticles displaying their LSPR peak (λ_{MAX} = 520 nm, Abs = 0.62). of citrate-capped nanoparticles following purification to remove excess citrate

Following the purification of the gold nanoparticles, a decrease in the absorbance was observed via UV-vis from 0.89 to 0.62. This is a well-known phenomenon in the literature when using this method to purify nanoparticles. It can be attributed to not all nanoparticles settling and forming a pellet, as no process can be entirely effective. [301–303]

The above data demonstrates that the LSPR peak position (520 nm) remained unchanged, indicating no alterations in size.

The newly purified nanoparticles (166-500 µL) were treated with the Cys ligand (1 mM) at room temperature and allowed to react for four hours, as illustrated in Figure 4-15.

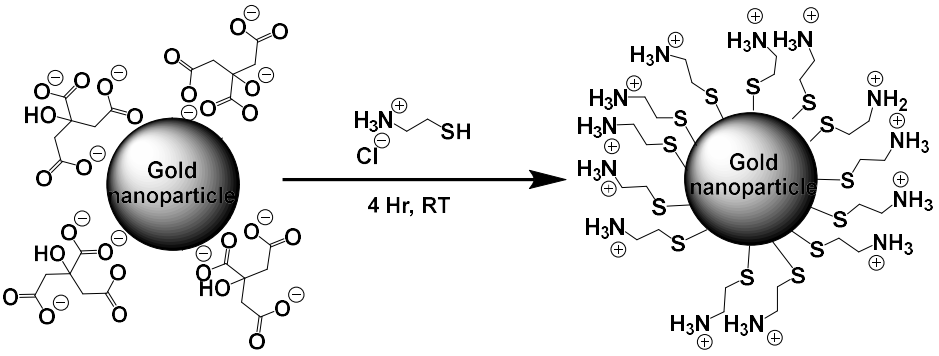


Figure 4-15: Ligand substitution reaction for citrate-capped gold nanoparticles to produce positively charged cysteamine hydrochloride (Cys) functionalised nanoparticles.

For this series of reactions, the concentration of gold nanoparticles was approximated (theoretical concentration of bulk gold in the synthesis of gold nanoparticles calculated from reagent mass.) by calculating the amount of bulk gold precursor added during nanoparticle synthesis and assuming no nanoparticles were lost during the purification process. A tabulated summary of the functionalisation reactions is provided below in table 4-2.

Table 4-2: Conditions trialled during the functionalisation of pure gold nanoparticles with thiol ligands. The reported concentrations of the gold nanoparticles were approximated from the bulk gold concentration used during the synthesis of the particles.

Ratio	Volume of purified gold nanoparticles	Volume of thiol 2 mM stock
1:1	500 µL, ($1.23x10^{-1}$ mM in reaction)	500 µL, (1 mM in reaction)
1:2	333 µL, ($8.18x10^{-2}$ mM in reaction)	666 µL, (1 mM in reaction)
1:3	250 µL, ($6.14x10^{-2}$ mM in reaction)	750 µL, (1 mM in reaction)
1:4	200 µL, ($4.91x10^{-2}$ mM in reaction)	800 µL, (1 mM in reaction)
1:5	166 µL, ($4.08x10^{-2}$ mM in reaction)	833 µL, (1 mM in reaction)

The Cys (thiol) concentration remained constant at 1 mM throughout these reactions. An excess of thiol was used to ensure complete coverage of the gold particles during substitution reactions. [282] The volume of gold nanoparticles added was varied to provide varying ratios of gold: thiol. To ensure the gold particles stability was maintained during these reactions, the dilutions of the purified nanoparticles were conducted utilising sodium citrate (34 mM).

All five reactions with the Cys ligand led to a clear solution within 24 hours, the colour change over 24 hours is provided below (figure 4-16). The colour of the nanoparticles turned purple within two hours, followed by the formation of black precipitates and a transparent solution.

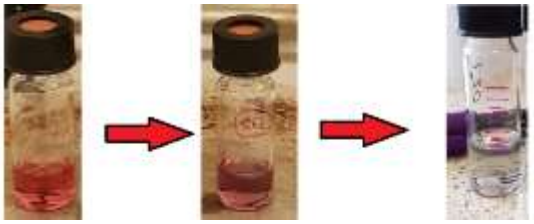


Figure 4-16: Progression of colour during cysteamine (Cys) functionalisation reaction – time zero, two hours and twenty-four hours.

The visible change in colour is indicative of a change in the nanoparticles surface. [304] This can be confirmed via a quick validation study by considering changes in the LSPR peak. The obtained UV-Vis spectra (Appendix 9-3).did not exhibit a distinctive LSPR peak. Thus, it was confirmed there was a lack of gold nanoparticles present in solution.

The presence of the black precipitate after 24 hours was assumed to be due to gold nanoparticle aggregation. [299] The precipitation is a result of nanoparticles forming clusters to reduce their high surface energy, which is not a favourable state thermodynamically. [305] This clustering is more likely to happen when the ligand backbone is short, as it increases the chances of nanoparticles coming into proximity with each other. Despite Cys having amine groups with a positive charge (pKa = 10.75) [306], it was insufficient to stabilise the nanoparticles electrostatically. During the formation of a covalent thiol bond with the gold sphere, the surface of the nanoparticles is temporarily de-shielded, which could result in aggregation to decrease the surface energy. [307] This process may occur in a shorter time frame than the formation of a covalent bond.

To summarise, our experimentation with the Cys ligand consistently led to a clear solution with black precipitation (figure 4-16). Alternative ligands were next investigated with longer backbones.

VI. FUNCTIONALISATION OF GOLD NANOPARTICLES WITH 1,4-BENZENEDIMETHANETHIOL (BDMT).

During functionalisation the purified gold nanoparticles, other ligands were also trialled such as 1,4-benzenedimethanethiol (BDMT - Figure 4-17). BDMT was selected for its advantageous properties, such as an extended carbon backbone, aromatic structure, and di-thiol functionality. The aromatic functionality packs well and forms complementary π-π interactions on the surface. Furthermore, the thiol group provides a strong anchor to the gold surface with a bond strength of 40 - 50 Kcal mol^{-1}. [293] Finally, the second thiol group participates in thiol-ene click chemistry reactions.

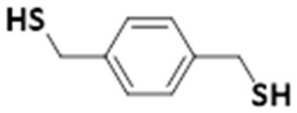


Figure 4-17: 1,4-benzenedimethanethiol (BDMT) ligand.

To analyse the responses of cysteamine hydrochloride (Cys), a comparative synthesis was conducted with the BDMT ligand (Functionalisation with 1,4-benzenedimethanethiol or cysteamine hydrochloride). To solubilise the BDMT ethanol was employed for these experiments, all other variables remained

consistent with the prior ligand substitution reactions with the Cys ligand (table 4-2).

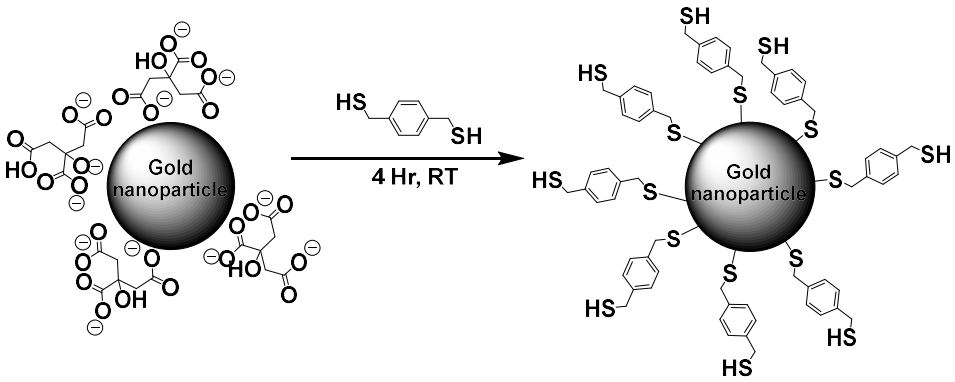


Figure 4-18: Synthetic protocol adapted from literature [282] for the synthesis of BDMT functionalised gold nanoparticles.

Briefly, purified nanoparticles previously synthesised were added to a vial of the thiol ligand, as previously conducted for the Cys ligand study (table 4-2). The solution was left stirring for four hours yielding pink colloidal suspensions, as shown in figure 4-19.

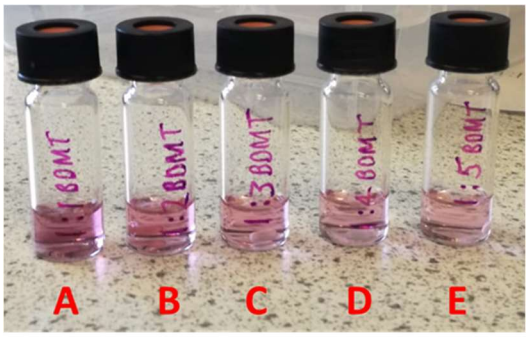


Figure 4-19: Pink solutions produced during the functionalisation of gold nanoparticles of varying concentrations (1.23x10-1 mM to 4.08x10-2 mM). in the presence of 1 mM of 1,4-benzenedimethanethiol (BDMT).

The absence of a transparent solution with precipitation was an improvement over the cysteamine (Cys) reaction series. After four hours of incubating with the BDMT ligand, UV-vis spectroscopy was conducted, and a summary is displayed in Figure 4-20.

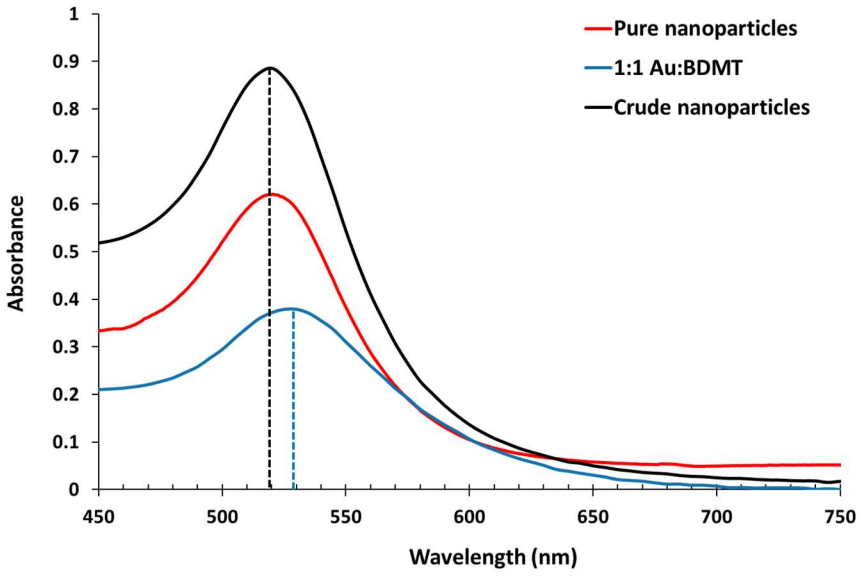


Figure 4-20: UV-vis spectra displaying the UV spectra for crude (impure) citrate-capped gold nanoparticles in black overlayed with these particles following their purification (red spectra). The LSPR peak change is displayed by the dotted lines following the pure nanoparticles incubation with the BDMT thiol (blue spectra).

The absorption values obtained from the spectrophotometer were normalised to consider differences in gold concentration between the reactions. This can be seen visually from figure 4-19, in which the solutions have distinct colours. To confirm if a change had occurred on the surface of the gold nanoparticles the LSPR peak positions were compared.

The previously synthesised citrate-gold nanoparticles (figure 4-9) displayed a LSPR peak around 520 nm, following the centrifugation of these particles (red spectrum, figure 4-20) the LSPR peak remained the same positioned at around 520 nm. Following these particles being incubated with the BDMT ligands a shift in the LSPR peak was observed, which is depicted

above via the blue spectrum (λ_{max} = 530 nm). In addition, to the bathochromic peak shift (10 nm shift), there was a notable change in peak height and peak width. These changes following functionalisation with the thiol ligand suggest a change on the nanoparticles' surface either due to nanoparticle coalescence, the addition of a thiol, or both.[264] The broadening of the LSPR peak with an accompanying absorbance reduction is indicative of an increase in particle size which may indicate functionalisation had taken place.

Nanoparticle coalescence was also considered, this may have occurred due to the use of the di-thiol BDMT ligand. This could have led to the formation of a cross-linked BDMT 3D network of gold nanoparticles. The cross-linking of nanoparticles results in an increase in molecular weight of this highly networked system thereby, resulting in the gradual precipitation. This phenomenon may also be responsible for the broadened peak observed. When multiple different sized particles or clusters are present in solution, their LSPR bands overlap and merge to form a broadened peak.

Since, the BDMT ligand is UV active, the absorption of this ligand was considered. The ligand is known to absorb strongly with a maximum absorption situated around 224 nm (λ_{MAX} = ~ 224 nm)[282]. Since the particles LSPR peaks do not coincide in this region, the changes observed are not attributed to the absorption of this ligand alone. Therefore, concluding the change observed was due to a change in the surface of the gold nanoparticles.[282]

Since, there was an observed change shift of 10 nm in the LSPR band following incubation with the BDMT ligand, the next step

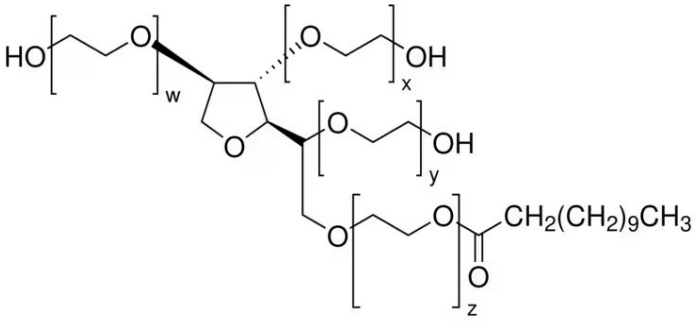
was to purify the nanoparticles, to remove any excess reagents. The nanoparticles were purified through centrifugal washes to remove excess citrate and thiol (1,4-BDMT). Following the formation of a pellet and removal of the supernatant, resuspension was attempted. The resuspension of the pellets was trialled in both water and ethanol. Attempts to reform a stable nanoparticle suspension failed, indicating that they had irreversibly aggregated.

Charged surfactants and longer alkane chains were next considered and added to prevent nanoparticles from coming close together during centrifugation processes resulting in irreversible aggregation.[308]

VII. FUNCTIONALISATION OF GOLD NANOPARTICLES WITH THE AID OF ADDITIONAL SURFACTANTS

The previous studies conducted with both Cys and BDMT were conducted in the absence of surfactants. It was next considered if the stability of the nanoparticles produced could be greater enhanced via the incorporation of a long-charged surfactant. During the chemisorption of the thiol, temporary stabilisation may be necessary during the nanoparticle surface rearrangement of ligands. [308]

Surfactants work by physisorption to the surface of the nanoparticles. The adsorption of surfactants onto the surface reduces the particle surface energy, leading to enhanced colloidal stability. When surfactant molecules possess long chains or charged species can provide either a steric or electrostatic repulsions between particles preventing them from flocculating in solution. For instance, Tween-20 (T20), an extended PEG-type surfactant (figure 4-21), is commonly used to stabilise gold nanoparticles through both steric and electrostatic repulsions.



W, X, Y & Z = 20

Figure 4-21: Structure of Tween-20 (T20) anionic surfactant commonly used to stabilise gold nanoparticles via steric and electrostatic repulsions.

Following the functionalisation, any excess T20 can be removed via centrifugation as usual. This route was next explored to see if the addition of tween-20 could aid the colloidal suspension stability.

VIII. FUNCTIONALISATION OF GOLD NANOPARTICLES WITH 1,4-BDMT IN THE PRESENCE OF TWEEN-20

A previous literature study reported that greater colloidal stability could be achieved using anionic surfactants and longer alkanethiols at pH 5-7. [301] The proposed mechanism of stabilising gold nanoparticles is outlined in figure 4-22.[308]

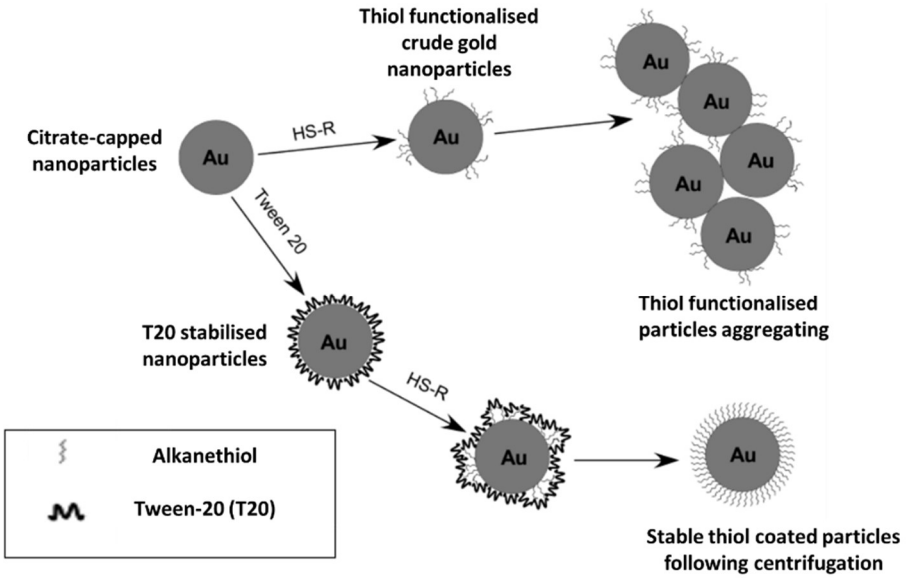


Figure 4-22: Diagram recreated from literature [301] to show the proposed role of Tween-20 in the chemisorption of thiols onto gold nanoparticles.

First the citrate-capped nanoparticles are incubated with a surfactant to coat their surfaces. The thiol is next added to the colloidal suspensions for the ligand exchange reactions to occur. Since gold forms strong covalent bonds with thiols this is preferential over the non-covalent interactions with the citrate/surfactant molecules. During this substitution process of the thiols replacing the citrate, the long, charged alkyl surfactant molecules provide a barrier permitting other nanoparticles coming into proximity in solution. The net result is the formation of stable thiol coated particles following centrifugation and removal of the excess long, charged alky surfactants. This process is summarised above in figure 4-22.

The previous study with BDMT was repeated in the presence of Tween-20 (T20, 3 mg/mL in reaction, Functionalisation of gold nanoparticles with 1,4-benzenedimethanethiol (BDMT).). The aim of the study was to verify if the particles can be prevented from agglomeration. An overview of the synthetic procedure adopted is shown below in figure 4-23 (Functionalisation of gold nanoparticles with thiols in the presence of Tween-20.).

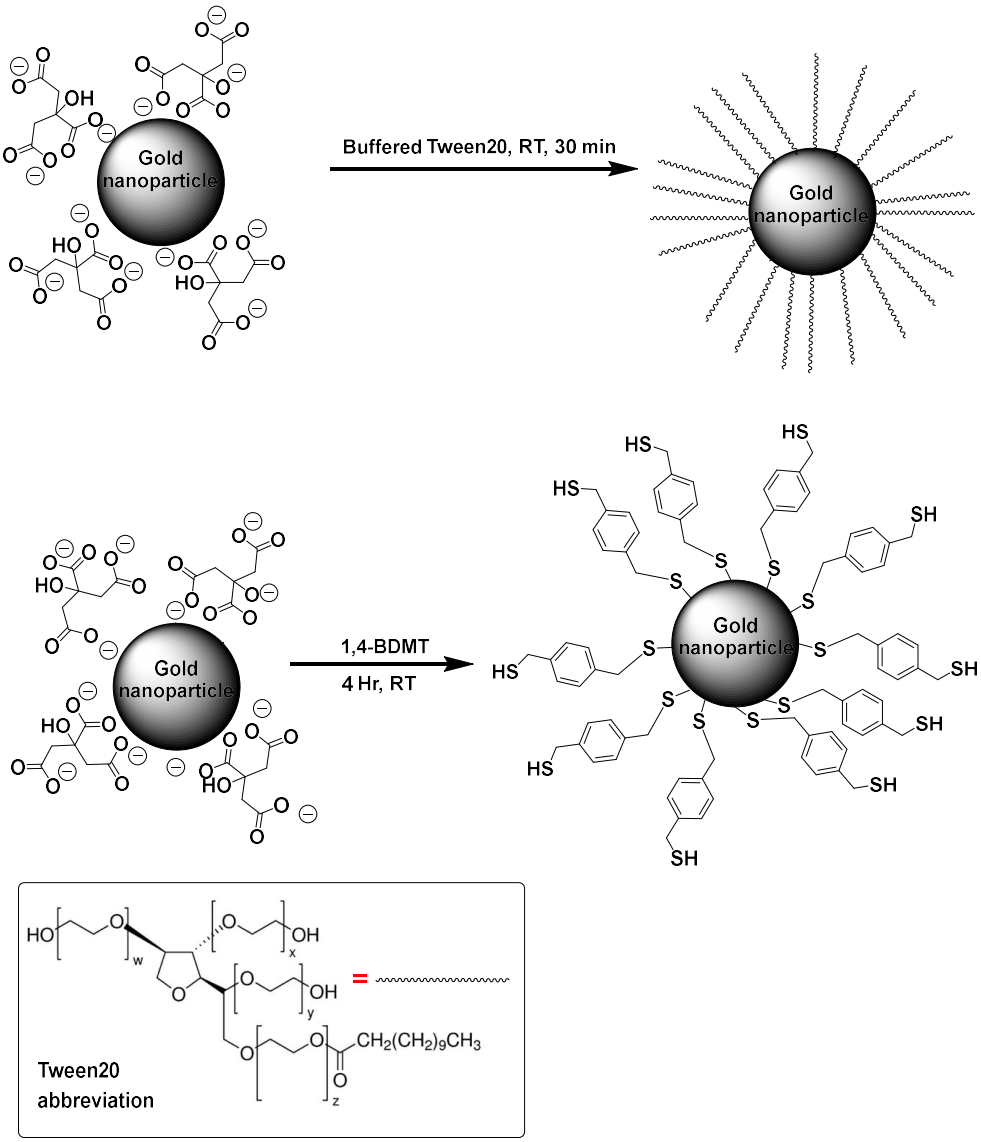


Figure 4-23: Synthetic scheme for the functionalisation of citrate-capped nanoparticles with 1,4-benzenedimethanethiol (BDMT) ligand in the presence of charged surfactant molecules such as Tween-20 (T20).

The colloidal suspension was pink at hour zero, which slowly turned purple over four hours, which was previously observed during the functionalisation of gold nanoparticles with the Cys ligand prior to the particles completely precipitating out of solution (figure 4-16).The LSPR peak of the purple solution obtained after four hours displayed below in change in Figure 4-24.

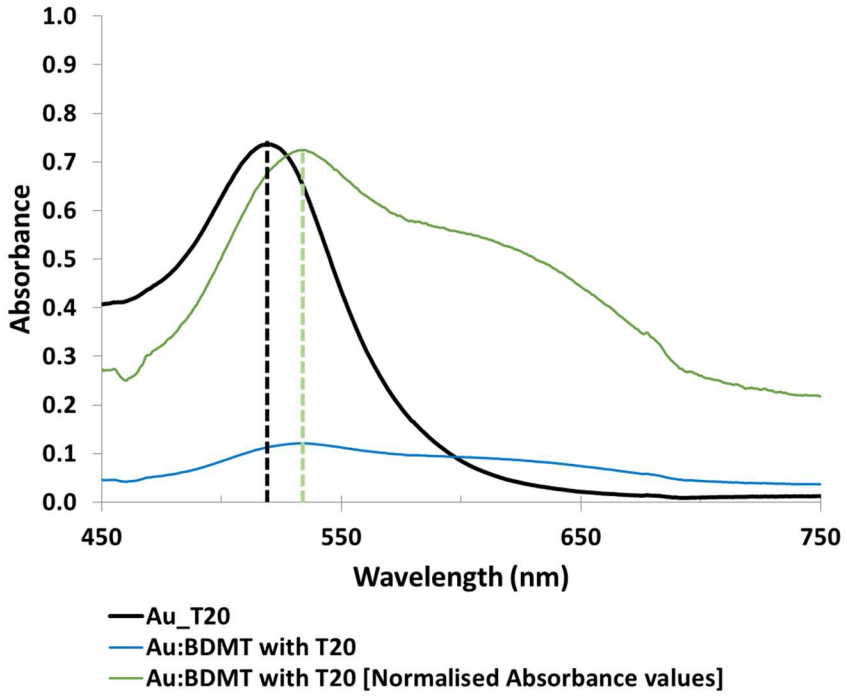


Figure 4-24: UV-Vis spectra of the gold nanoparticles before (black, λ MAX = 520 nm) and after (blue, λ MAX = 530 nm) functionalisation with BDMT in the presence of surfactant (T20). For ease of viewing LSPR peaks the absorbance values were scaled up according to the dilution factor (green spectrum).

The nanoparticles following incubation with BDMT and T20 produced a LSPR peak around 530 nm. This agreed with the previous study with gold nanoparticles with BDMT (Figure 4-24). However, the shape of the peak produced was dissimilar to that of the gold nanoparticles only incubated with T20 surfactant (figure 4-20, control, black spectrum).

Previous, reactions with BDMT always led to broadened LSPR peaks (Figure 4-20), the incorporation of surfactant was hoped to increase the stability of the colloids leading to sharper LSPR peaks.

The spectra above (Figure 4-24) can be explained via Mie's theory [268] The frequency at which electrons oscillate in the conduction band of gold determines the LSPR peak, which varies with the mass of the gold particles. As the mass of the particles increases, the oscillation frequency decreases, leading to a shift of the LSPR peak towards longer wavelengths. [308] [287] This explains the shift from ~520 nm to ~530 nm upon functionalisation with BDMT. In the presence of multiple particles of varied sizes, their LSPR bands may merge and appear as a single, broad peak. Thus, the broadened appearance in Figure 4-24 might be due to the di-thiol nature of the BDMT ligand. A gold nanoparticle may be covalently linked to many others, forming di-thiol bridges, and leading to a polydisperse sample, as illustrated below**.** The formation of 3D gold nanoparticle networks with di-thiols has elsewhere been discussed.[307]

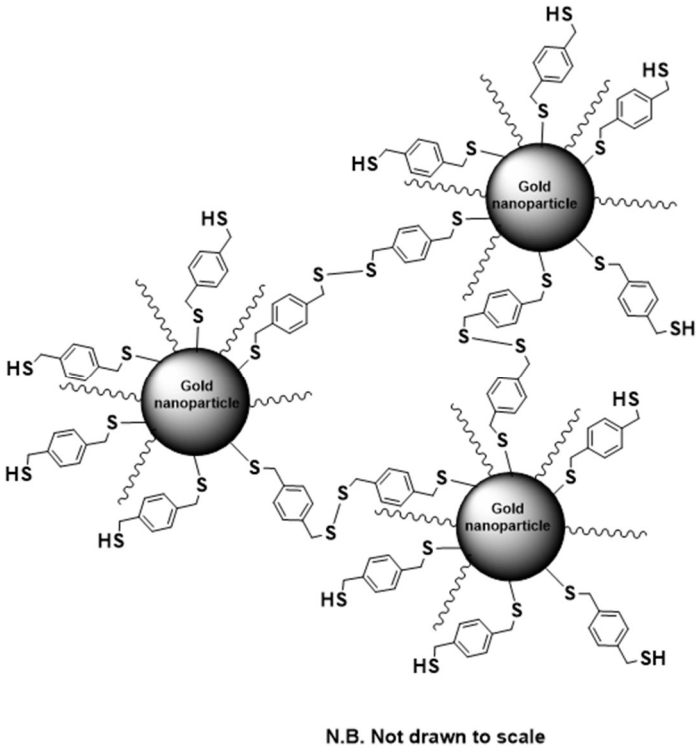


Figure 4-25: A hypothetical 3D network that may have been forming in solution when gold nanoparticles were functionalised with the BDMT ligands, owing to the di-thiol nature of the ligand. The increased molecular weight of the 3D network may have been responsible for the presence of precipitation in the suspensions and the broadened LSPR peaks observed.

Developing stable and evenly dispersed gold nanoparticles that can resist agglomeration in solution is crucial for successful MI. However, the tendency of gold nanoparticles to agglomerate during ligand exchange reactions presents a significant challenge. To address this issue, two studies were conducted, one with T20 and one without it. Both reactions resulted in purple solutions, even with an excess of surfactant present, indicating that the nanoparticles had agglomerated within four

hours. This study concludes that the broadened LSPR peaks were not due to a lack of steric and electrostatic repulsion in the solution between the nanoparticles but rather due to the unsuitability of BDMT as a ligand for producing stable and evenly dispersed gold nanoparticles. The covalent bond between the gold particle and thiol group was more favourable than the ionic interactions of T20. To prevent agglomeration, alternative mono-thiol ligands were explored to produce smaller nanoparticles that resist forming extensive 3D networks in the solution, leading to polydisperse suspensions.

IX. FUNCTIONALISATION OF GOLD NANOPARTICLES WITH 11-MERCAPTOUNDECANOIC ACID (11-MUDA) AND 4-MERCAPTOBENZOIC ACID (4-MCA) IN THE PRESENCE OF TWEEN-20 (T20).

Mono-thiolated ligands of varying backbone lengths were next trialled and are depicted in figure 4-26. The decision was made to compare the stability and LSPR peaks of gold nanoparticles functionalised with 11-mercaptoundecanoic acid (11-MUDA) and 4-mercaptobenzoic acid (4-MCA) while incorporating T20. Both ligands have thiol and carboxylic acid functional groups, but 11-MUDA has a more extended backbone than the other. These ligands have readily ionisable groups making them advantageous for providing electrostatic repulsions, much alike the presence of citrate ligands on the surface of citrate-capped nanoparticles.

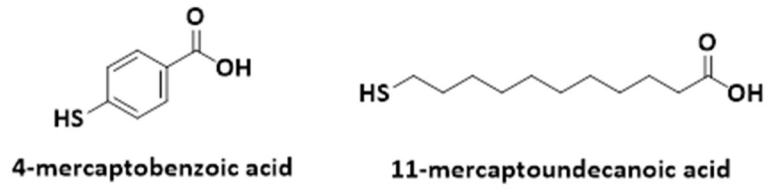


Figure 4-26: Mono-thiolated ligands used in the ligand exchange reactions to produce thiol functionalised gold nanoparticles.

The functionalisation of gold nanoparticles with 11-MUDA to form stable nanoparticles was previously reported in the literature.[308] Therefore, as a starting point, these conditions and methods were applied and are described in full in section functionalisation with 11-mercaptoundecanoic acid or 4-mercaptobenzoic acid.

Briefly, previously synthesised citrate capped gold nanoparticles were first diluted using sodium citrate to obtain a colloidal suspension of gold particles with a concentration (Gold nanoparticle theoretical concentration based on LSPR peak [290]) of 0.8 nM as per previously reported literature.[308] A buffered solution of Tween-20 was added to the diluted nanoparticles and was left to stir at room temperature for thirty minutes. In contrast to the prior studies, the thiol concentration was reduced to 0.5 mM (500 µL, 4-MCA/11-MUDA,) for these series of reactions, as per the literature protocol.[308]The desired thiol was added and was left to react for four hours at room temperature. The resulting colloidal suspensions were visually compared before and after, and the UV-vis spectra was obtained to track changes in the LSPR peaks displayed in Figure 4-27.

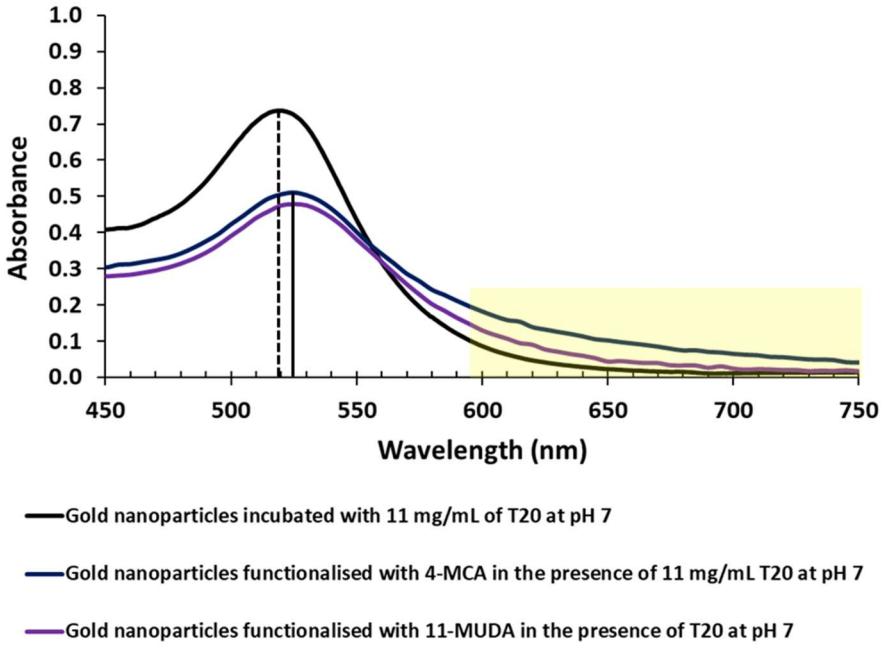


Figure 4-27: UV-Vis spectra illustrating differences in LSPR peaks between gold nanoparticles functionalised with 11-MUDA (represented by the purple line with λ_{MAX} = 524 nm and Abs = 0.479) and 4-MCA (represented by the blue line with λ_{MAX} = 525 nm and Abs = 0.51). The yellow highlighted areas indicate the key points of interest, and the dotted and solid lines mark the changes in λ_{MAX} compared to the control nanoparticles.

After thiol addition, both exhibited a slight bathochromic shift of around 5 nm, which is displayed via the dotted and solid line in Figure 4-27. In addition, some peak broadening was observed, which is highlighted in yellow. These changes could indicate the presence of another size population, which may suggest that flocculation is slowly occurring.[290]

The nanoparticle's capacity to remain stable in different pH solutions was examined due to the presence of an ionisable

group. When used for MI, nanoparticles' stability is critical, as a wide range of pH buffers may be required.

Qualitatively, colloidal stability can be evaluated via colour changes from red to violet/blue, followed by precipitation out of solution as previously observed for the cysteamine ligand (Figure 4-16). Quantitatively, the stability is measured via tracking changes in the LSPR peaks.[308]

Gold nanoparticles have a characteristic peak within the range of 520-550 nm, which can vary depending on their size. This peak is clearly visible in black in Figure 4-27. If the LSPR peak exceeds values greater than 600 nm, it may indicate that the nanoparticles have started to flocculate. This flocculation can be quantified mathematically by measuring the area under the curve between 600-800 nm, which is highlighted in yellow in Figure 4-27. The “Beer-Lambert Law” states that the absorbance of gold nanoparticles is directly proportional to their concentration, and this can be represented by Equation 23.

The nanoparticles underwent a full wavelength scan, and the area between 600 and 800 nm was measured to determine the "flocculation parameter".[309,310] This parameter was calculated for both ligands at different pH levels and surfactant concentrations to study the stability of the particles following functionalisation. The data obtained was plotted on graphs, which are presented in Figure 4-28 and Figure 4-29.

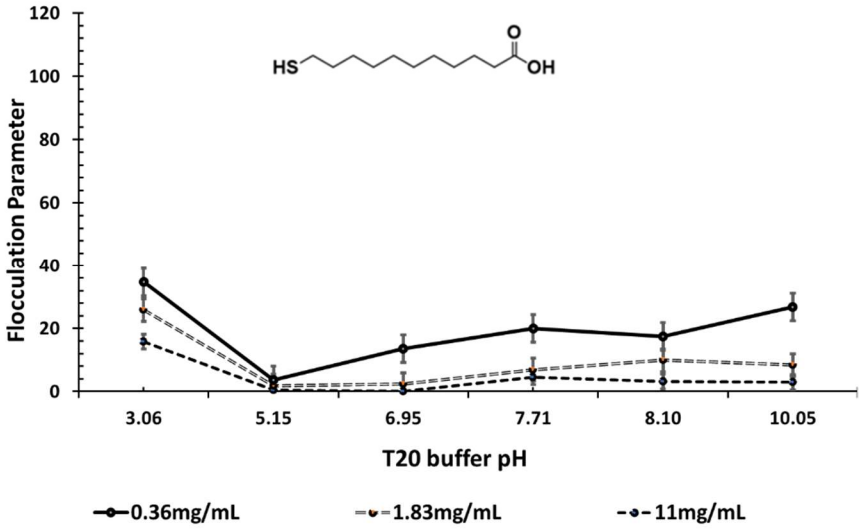


Figure 4-28: Summary of the calculated flocculation parameter values for 11-MUDA functionalised nanoparticles in the presence of different T20 concentrations and pH buffers.

Increasing the concentration of T20 reduces the flocculation of both 4-MCA and 11-MUDA, leading to improved stability of the gold nanoparticles in the solution. This is in agreement with prior literature.[301] The findings indicate that T20 plays a vital role in creating a steric repulsion effect among the gold nanoparticles, which is critical in producing functionalised gold nanoparticles with higher stability.

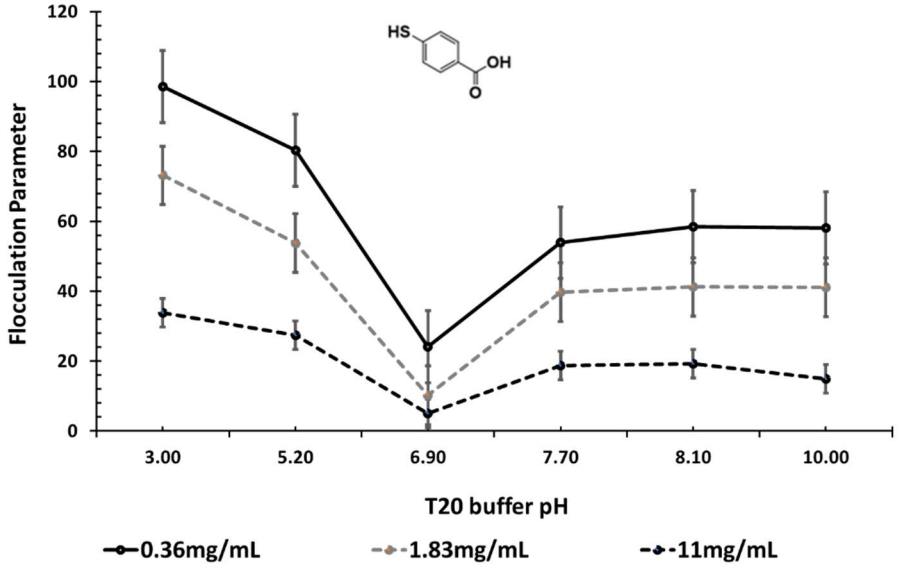


Figure 4-29: Summary of the calculated flocculation parameter values for 4-MCA functionalised nanoparticles in the presence of different T20 concentrations and pH buffers.

Both ligands have an optimal pH range between 5 and 7, where their flocculation is minimal. This is due to the ionisable carboxylic acid groups present at the end of the ligands that have a pKa of four to five.[311] At a pH higher than four, the deprotonated conjugate base form is produced, resulting in a negatively charged moiety. When the pH is increased beyond pH 7, the solution's ionic strength increases, leading to an increase in flocculation. This is because the number of ions present in the solution increases, making it more likely for the negatively charged carboxyl groups to be shielded, thereby reducing the electrostatic repulsions.[240,312,313] Consequently, there is a higher probability of gold nanoparticles coming closer in proximity and aggregating in the solution. The described scenario is denoted the critical coagulation concentration.

Ideal ligands for molecular imprinting (MI) should form tightly packed self-assembled monolayers (SAMs). It has been suggested that 4-MCA would be a better ligand for MI due to its ability to increase the organized packing on a gold surface through π-π interactions, providing a rigid support for molecular imprinting. This has been reported in previous studies on gold 2D surfaces. [314,315] However, on 3D surfaces, it resulted in less stable particles with minimum flocculation at higher pH values than 11-MUDA. This contradicts the theory since 4-MCA should have a lower pKa than 11-MUDA due to delocalisation through the aromatic ring. [311]

In contrast to the theory, the flocculation data suggests that the pKa value of 4-MCA on the gold nanoparticle is higher than that of 11-MUDA. This deviation suggests that the pKa of the free ligands is not the same as the pKa of the ligand bound to nanoparticles and that the pKa is dependent on the environment and spatial distribution of charges on the nanoparticles. [311,316] This may have caused the exacerbated flocculation between pH 3-5 for 4-MCA owing to the lack of charges on the surfaces to reduce the surface energy.

It appears that for the 4-MCA ligand, there is a penalty for tightly packing the ligands on the surface. This results in higher flocculation parameters, regardless of the pH and T20 values. The negatively charged carboxylic acid groups may not all ionise, or they may opt for a spatial configuration that provides less repulsion. As a result, there is incomplete surface coverage of the gold nanoparticles, which reduces the surface charge and decreases electrostatic stabilisation in the solution. Thus, 4-MCA is not an ideal ligand for this project's applications.

In summary, stable gold nanoparticles can be produced within the pH range of 5 to 7. The 11-MUDA thiol outperformed the 4-MCA thiol, producing more stable suspensions and, hence, lower flocculation parameters. The stability was due to greater ligand flexibility to orientate negatively charged carboxyl terminals optimally on the surface.[314] However, at higher pH, the ionic strength of the environment leads to increased charge screening and decreased particle stability. Furthermore, the systems displayed a high degree of variability, as shown by the error bars, which raises concerns about the reproducibility, stability, and feasibility of these systems for molecular imprinting of glycans. Thus, the systems have limited application for MI.

X. GOLD NANOPARTICLE SUMMARY

To summarise, nanoparticles that have been functionalised with thiol groups were produced using the 1,4-BDMT, 4-MCA, and 11-MUDA ligands. However, the stability of cysteamine hydrochloride and 1,4-BDMT was limited. Surfactants were used to attempt to improve the gold nanoparticles stability, but they were not successful for either 1,4-BDMT nor Cys reactions. It was believed that the di-thiol nature of the 1,4-BDMT ligand may have been forming 3D networks in solution increasing the mass of these particulates overtime leading to their coalescence out of solution. To reduce this long-charged surfactants were employed to provide electrostatic repulsions between particles however, aggregation was still dominant for these reactions.

Nanoparticles functionalised with carboxylic ligands 4-MCA and 11-MUDA demonstrated enhanced stability within a narrow pH range, notably centred around pH 5 to 7. However, subsequent repetitions of these reactions revealed discrepancies, resulting in significant deviations (represented by error bars, (Figure 4-28 & Figure 4-29) in the summarised graph for both 11-MUDA and 4-MCA. This lack of reproducibility, coupled with the limited range of reduced flocculation, raised concerns regarding their suitability for molecular imprinting applications. An ideal nanoparticle for molecular imprinting should exhibit stability across a broader spectrum of pH values, ensuring consistently stable colloidal suspensions.

Furthermore, the plan to study the behaviour of nanoparticles in different pH mediums using ITC may need to be reconsidered

due to the high degree of variability observed in the stability of the particles. Gold nanoparticles tend to precipitate out of solution and adhere to surfaces, making it difficult to remove them via analytical equipment such as ITC. This is because corrosive aqua regia procedures are needed to remove the adhered particles, which are incompatible with expensive analytical equipment.

Therefore, it was explored if more organic nanomaterials could be used to overcome these issues. This is due to the high variability of these particles in different buffers and the required acid-washing procedures.

XI. POLYMERIC NANOPARTICLES

Polymeric nanoparticles have many applications, including drug delivery, cell therapy, cancer treatment, and imaging. [317] These particles are highly esteemed in drug delivery and therapy because they are easily modifiable. Their surface can be altered to enhance water solubility, allowing for the transport of pharmacologically active compounds that are typically insoluble. [318] Polymeric nanoparticles provide a more comprehensive range of monomers and cross-linkers, making them a more versatile option than gold nanoparticles that rely on thiol-ene and EDC-NHS chemistry. This increased variety in composition allows for greater flexibility in designing nanoparticles tailored to specific applications. Polymeric nanoparticles have been studied for their quick association with proteins to create a "protein corona" utilising ITC. [303,319,320] However, less attention has been given to their interaction with biomolecules, such as saccharides, which are naturally abundant on cell surfaces. [321]

This section first briefly outlines emulsion polymerisation theory before studying the polymeric nanoparticles synthesised in this section.

XII. INTRODUCTION TO EMULSION POLYMERISATION.

Polymeric nanoparticles have gained significant attention in MI due to their non-covalent ability to bind to valuable biomolecules, such as polysaccharides.[321] Combining covalent and non-covalent interactions can significantly enhance binding affinities during imprinting. The use of polymeric systems was next considered.

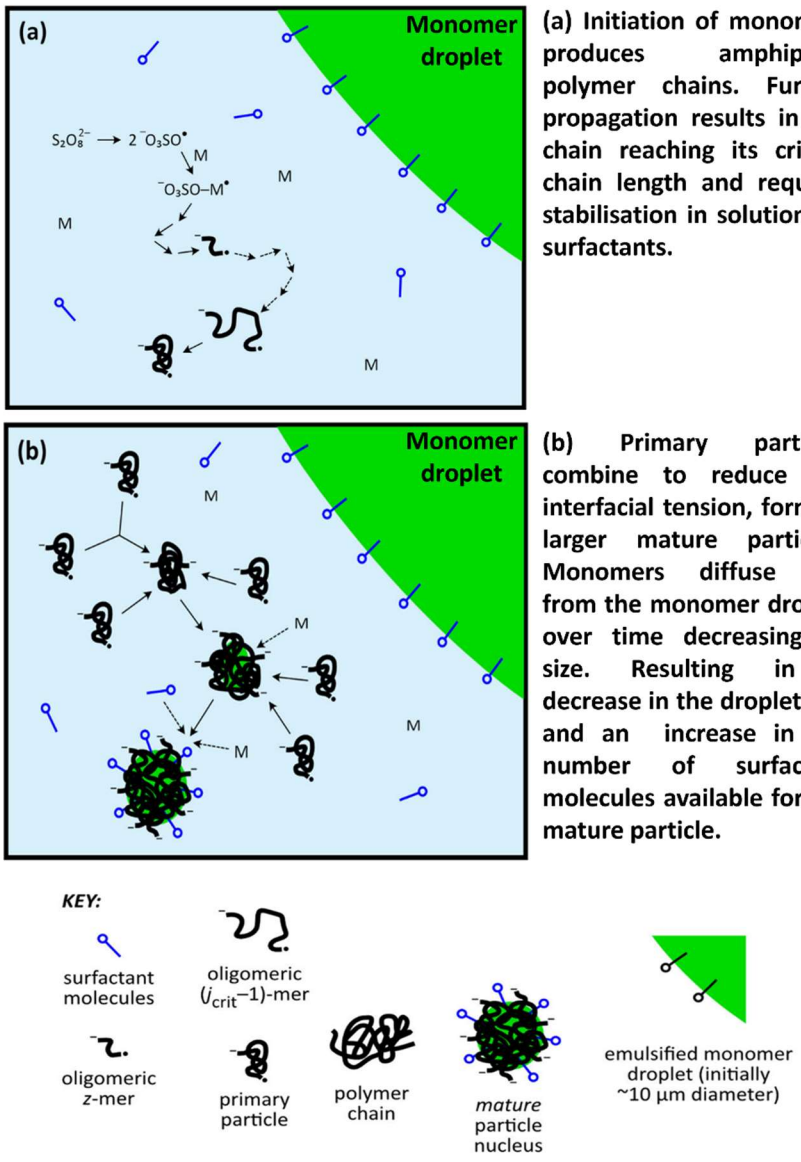
Polymeric nanoparticles can be synthesised via many different methods; emulsion polymerisation reactions are the most widely used in industry.[322] The most common synthesis route for these systems is free-radical polymerisation, which can be broken down into the following stages: Initiation, nucleation, propagation, and termination.[323]

First, an emulsion must be formed by mixing two immiscible liquids. In these systems, monomers gather to form large droplets, denoted as monomer-swollen droplets. These droplets supply the reagents for the polymerisation process and are pictorially depicted via the green droplets in

Figure 4-30. The reaction is initiated by reactive radicals, which instigate the polymerisation of monomers. The polymerisation leads to the creation of a polymeric monomer chain, as

Figure 4-30 illustrates. These chains are small and mobile, capable of interacting with other charged radical entities - a phenomenon known as propagation. The result is the chain's continued propagation, leading to the formation of longer chains.

Nucleation occurs when small clusters form from the polymerisation of smaller polymeric chains to form primary particles. As the clusters grow, they need extra stabilisation to stay in solution. Amphiphilic surfactant molecules may absorb onto the mature particle surface to provide this extra stabilisation. A lay pictorial summary of these processes is summarised below. [323]



(a) Initiation of monomers produces amphiphilic polymer chains. Further propagation results in the chain reaching its critical chain length and requires stabilisation in solution via surfactants.

(b) Primary particles combine to reduce the interfacial tension, forming larger mature particles. Monomers diffuse out from the monomer droplet over time decreasing its size. Resulting in a decrease in the droplet size and an increase in the number of surfactant molecules available for the mature particle.

Figure 4-30: Imaged adapted from literature[323] outlining initiation, nucleation and propagation to form polymeric nanoparticles in solution stabilised by surfactant molecules.

In a radical polymerisation process, the final stage is called "termination." During this stage, two radical entities merge to form a non-radical substance, which stops the reaction's propagation. Termination can also be achieved with the help of radical scavengers or by introducing oxygen.[324] Another way to induce termination is by adding solvents, which can break the emulsion. [325] The termination step plays a crucial role in determining the molecular weight and polydispersity of the polymer. [326]

Overall, polymeric nanoparticles may offer a greater variety of functional monomers for functionalisation than gold nanoparticles. [327] Poly – acrylamide (PAM) NPs (nanoparticles) were next explored for their potential use in MI experiments.

XIII. SYNTHESIS OF POLYACRYLAMIDE NANOPARTICLES (PAM)

Polymeric nanoparticles based on acrylamide (Aa) are commonly synthesised in industry through emulsion polymerisation methods. [322,327] Polyacrylamide (PAM) core-shell particles can be synthesised through free radical polymerisation reactions.[328] A typical water-in-oil (W/O) emulsions synthetic reaction is summarised in Figure 4-31.[321] This reaction was carried out to form PAM nanoparticles, with its synthesis and characterisation described within this section.

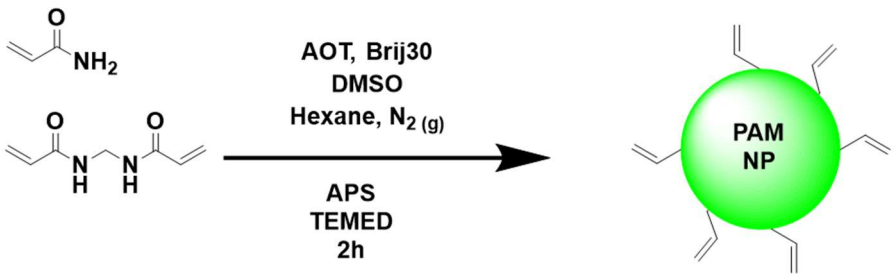


Figure 4-31: Synthetic scheme for synthesising PAM NPs via emulsion free radical polymerisation reactions adapted from previously reported literature.[321].

The polymerisation reaction requires the formation of an emulsion resulting in the mixing of immiscible solvents, such as hexane (2.15 mL) and dimethyl sulfoxide (100 µL). The emulsion's stabilisation is obtained via surfactants like dioctyl sulfosuccinate sodium salt (AOT, 80 mg, 0.18 mmol) and polyoxymethylene(23)lauryl ether (Brij-30, 162 µL, 0.425 mmol). The addition of monomers (Synthesis of polyacrylamide (PAM) nanoparticles) to this emulsion results in the formation of

monomer-swollen droplets due to their low solubility in the continuous phase (hexane). The polymerisation mixture was first degassed to ensure complete removal of oxygen, which could otherwise inhibit the free radical polymerisation.[324]

To initiate free radical polymerisation of Aa monomers. ammonium persulfate (APS, 3 µL, 10% w/v) and tetramethyl ethylenediamine (TEMED, 1.5 µL, 0.13 nmol) are added into the emulsion system under inert conditions. The initiation and interaction of radicals with monomers are illustrated in the accompanying figure.

The newly formed amphiphilic primary monomer radicals in solution (Figure 4-32) are free to move via Brownian motion, resulting in further polymerisation reactions that form a polymeric chain. This progression is recognised as propagation. The amphiphilic growing polymer chain aids the emulsion stability by separating the two phases, reducing surface tension. [323] As propagation continues, the growing nanoparticle becomes less soluble as it approaches the "critical chain length". At this point, additional stabilisation is necessary to prevent coalescence and precipitation from the solution; this is commonly achieved by adding surfactants into the polymerisation mix (AOT and Brij30). [323,326,327]

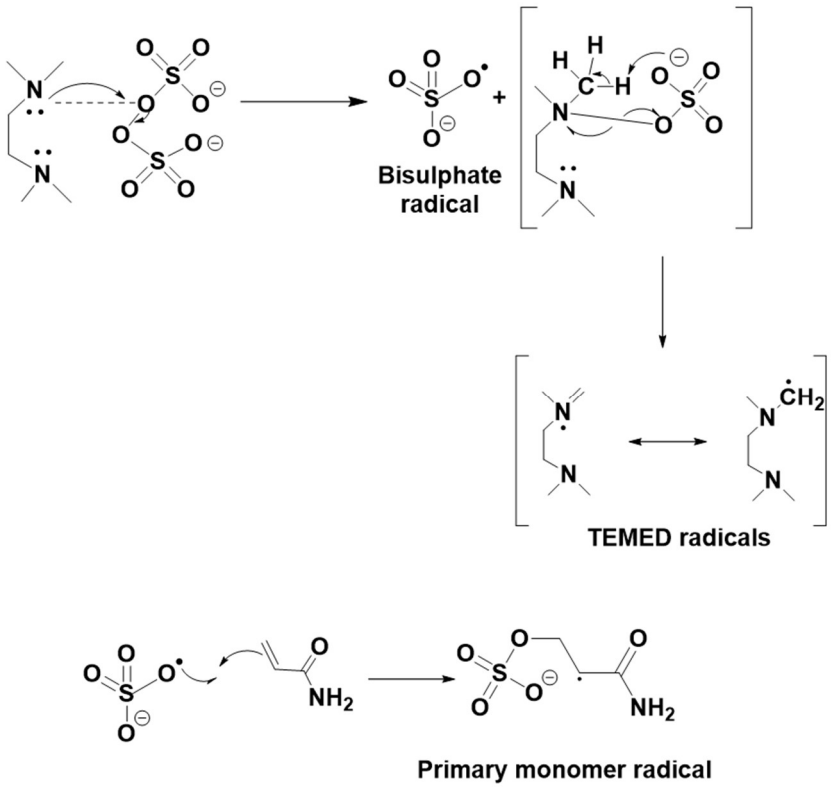


Figure 4-32: The formation of the sulphate-based radicals commonly facilitated by the addition of electron donors (TEMED, co-initiator). This process is fundamental for the initiation of polymerisation to form the nanoparticles from the primary monomer radical in a series of propagation reactions.

When multiple polymeric chains collide, they form a primary nanoparticle through nucleation. As the polymerisation process continues, monomers move from the swollen droplets into the continuous phase, reducing the surface area of these droplets and increasing free surfactant molecules available in the continuous phase. These molecules then migrate to the surface of the growing primary particle over time, providing stability to the newly formed particles. [326]

The resulting nanoparticles (Synthesis of polyacrylamide (PAM) nanoparticles) are coated in charged surfactants, which impart a negative charge (AOT) and long alkyl chains, imparting steric stabilisation in solution. The nanoparticles produced via this method are opaque and white in appearance. (Figure 4-33)



Figure 4-33: Emulsion created during polyacrylamide (PAM) nanoparticle synthesis.

The nanoparticle size was analysed via DLS and TEM (C.f. ***Dynamic light scattering (DLS) and zeta potential (ZP)*** and ***Transmission electron microscopy (TEM)***). A summary of these analyses is displayed below (Figure 4-34 and Figure 4-35). For a summary of synthetic repeats, refer to the appendix - Appendix 9-7.

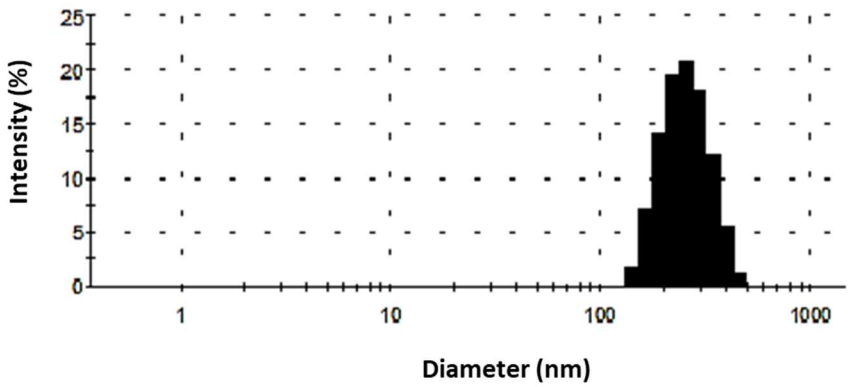


Figure 4-34: PAM DLS histogram displaying an average diameter of 448 ± 15 nm (n=3).

The DLS measurements confirmed the presence of multiple nanoparticle populations via the broad histogram (Figure 4-34). Quantitatively, the polydispersity was measured via the PDI value of 0.42. This is large for a nanoparticle suspension, which typically produces values under 0.1, corresponding to low polydispersity. The synthesised particles were significantly larger than those previously observed for gold nanoparticles (hydrodynamic diameter 34 nm). The average diameter of PAM particles was 448 ± 15 nm (n = 3).

The TEM images displayed in Figure 4-35 correlated with the DLS measurements. Microscopy images displayed inconsistent shapes and sizes with uncertain start and endpoints. Thus, the determination of a single particle size could not be accurately measured across multiple different TEM grid sections. The images show aggregation and may indicate that the sample may be coalescing in solution, which would rationalise the large average diameter observed via DLS.

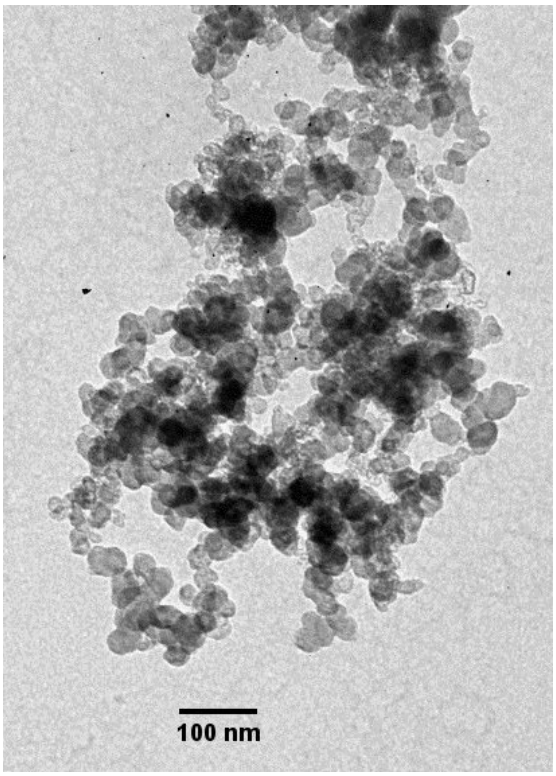


Figure 4-35: TEM image of PAM nanoparticles displaying inconsistent shapes and agglomerates.

Despite the undesirable size and coagulation, the PAM nanoparticles were next functionalised. If the functionalisation is successful, the size could be reduced by enhancing the stability of the particles in the future. The surfactant concentration, the cross-linker (bis-acrylamide) concentration, and the W/O ratio are known to influence colloidal stability and size. [325,329,330]

XIV. FUNCTIONALISATION OF POLYACRYLAMIDE (PAM) NANOPARTICLES WITH GLYCAN RECEPTORS.

Boronic acid functionality needs to be incorporated into the synthesis for PAM nanoparticles to be applicable for glycan sensing. A trial reaction was performed to evaluate the viability of PAM nanoparticles, baring glycan receptors (boronic acids). The free radical polymerisation of the Aa-based monomers was carried out in the presence of boronic acid groups, as depicted in figure 4-36, and the resultant white emulsion was analysed via DLS.

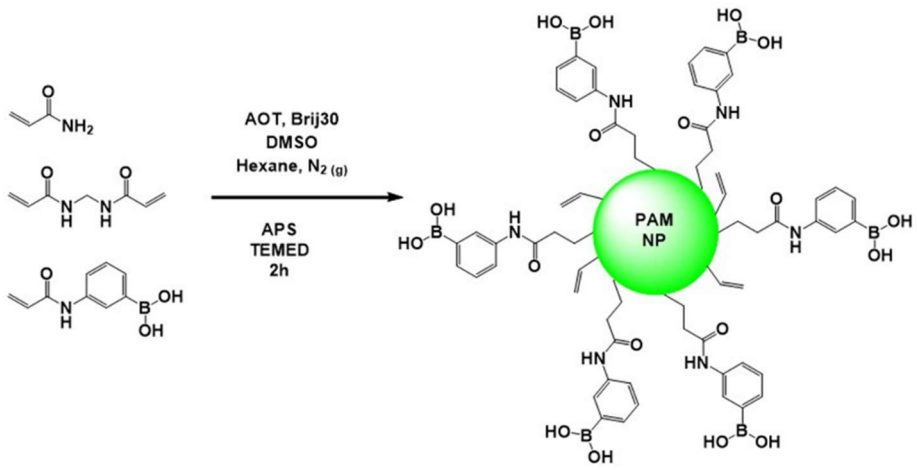


Figure 4-36: Synthesis of 3-Acrylamidophenylboronic acid-based polyacrylamide nanoparticles (APBA-PAM NPs).

The APBA-PAM nanoparticles were purified through centrifugation washes, as described in the section on the synthesis of polyacrylamide (pam) nanoparticles to produce white pellets (figure 4-37).



Figure 4-37: Pellets produced during the centrifugal washes for PAM-based nanoparticles.

As previously conducted for the PAM nanoparticles, the size was investigated via DLS measurements; for a tabulated summary of repeats, refer to Appendix 9-8. The hydrodynamic diameter of the PAM nanoparticles was calculated by averaging five individual measurements to obtain 306 ± 76 nm (n=5). A pictorial summary in a histogram is displayed below in Figure 4-38 – A. An outlier was discovered in the sample data; removal of the outlier resulted in a lower hydrodynamic diameter and standard deviation of 270± 22 nm (average of four individual measurements, n=4) (Figure 4-38 – A).The particles were also filtered via a 0.5 µm syringe filter and sonicated to break up any large remaining flocculates. The hydrodynamic diameter was 296 ± 7 nm (n=5) (Figure 4-38 – B).

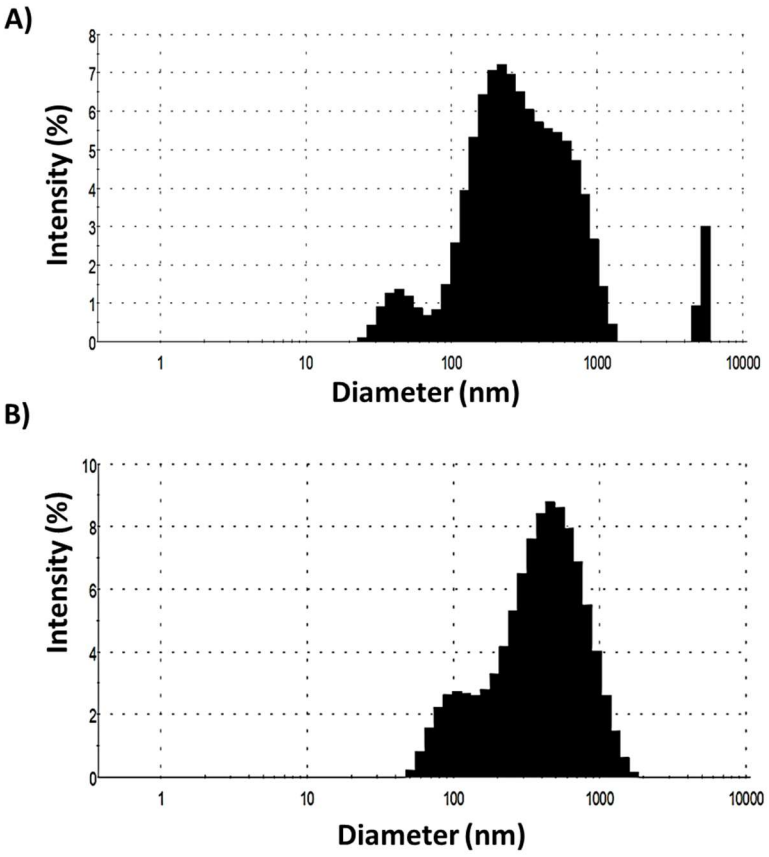


Figure 4-38: DLS histograms of APBA-PAM NPs displaying the broad array of sizes within the solution. The top histogram represents the nanoparticles following synthesis, and the bottom histogram represents the particles after filtration (0.5 µm) and sonicating for 10 minutes to break up any aggregates formed before measuring.

The observation that the filtered sample has a larger hydrodynamic diameter is perplexing, given that the primary objective of filtration is to eliminate large aggregates and produce a narrower distribution. However, it is conceivable that the aggregation may have occurred while undergoing filtration

and on standing (<60 minutes between measurements). As nanoparticles pass through a size exclusion membrane, some may adhere to the filter ("caking"), which can lead to blockages and even damage to the membrane. This, in turn, could result in small clusters of particles passing into the filtrate. The existence of these minute clusters in the filtrate has the potential to instigate the creation of larger particle agglomerates[323], resulting in a noteworthy shift in the observed hydrodynamic radius using DLS. [303,331] Furthermore, the DLS diameter calculated is heavily weighted towards larger particles and is most accurate when the PDI of the sample is low. [323] For more information on how DLS diameters are produced, refer to Dynamic light scattering (DLS) and zeta potential (ZP).

Given that the prior synthetic attempts produced a broad array of sizes, it suggests that the sample is aggregating over time to create a polydisperse colloidal solution, as previously observed for the unfunctionalised PAM nanoparticles. An Ostwald ripening mechanism is not suspected since the PDI values are too large; Ostwald ripening is usually accompanied by all particles growing larger to produce monodisperse larger particles with low PDI values. Ostwald ripening results in a reduction in the interfacial tension and is the driving force for Ostwald ripening and often leads to phase separation in polymeric emulsions.[323]

A further study could have been conducted to establish if flocculation or coalescence occurred. Flocculation of the filtered PAM particles on standing before being analysed may be verified by adding surfactant or sonication before a repeated measurement. If the sample showed a decrease in the observed

hydrodynamic diameter, it suggests that the PAM particles are of intermittent stability and are reversible flocculating. Particles which are not stable undergo coalescence and cannot have their hydrodynamic diameters reduced. Next, the stability of these particles was considered.

XV. INVESTIGATING THE STABILITY OF 3-ACRYLAMIDOPHENYL BORONIC ACID POLYACRYLAMIDE NANOPARTICLES (APBA-PAM).

This study examines the stability of APBA-PAM particles in solutions with varying pH levels. Future molecular imprints will rely on boronic acids (Figure 1-34) that perform most effectively within the pH range of 5 to 8. [130,148–150] Therefore, this study focuses on this pH range.

The preparation of buffers was next conducted. The buffers possessed different pH values ranging from 5 to 11 at a concentration of 10 mM using sodium acetate for pH 5, potassium phosphate for pH 7 and 8, and sodium carbonate for pH 9, 10, and 11. After removing the supernatant, the pellets were mixed with a buffer (10 mM, 3 mL) of varying pH. The nanoparticle solutions next underwent sonication and filtration to eliminate any large particulates, which ensured accurate observation of the DLS average diameters. The resulting solutions were measured the following day to ensure the particles had equilibrated to the new medium; the data can be found in Table 4-3.

Table 4-3: Tabulated DLS data for PAM NP redispersed into 3mL of 10 mM buffer and left overnight before measurements. Each diameter represents an average of 5 measurements (n = 5).

pH of buffer	Diameter (nm)	PDI
5	819 (± 118)	0.65
7	419 (± 90)	0.62
8	128 (± 21)	0.40

Based on the DLS data provided, it can be concluded that there is a correlation between the average diameter of PAM nanoparticles and the pH of the buffer. As the pH increases, the diameter of the particles decreases.

Since the pKa of the boronic acid is around 8, during the decrease in pH, the boronic acid undergoes a conformational change, resulting in the efflux of counterions and water molecules. This process is depicted in Figure 4-39.

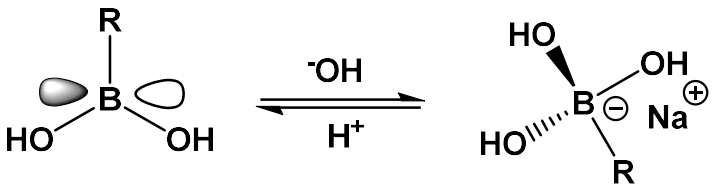


Figure 4-39: Change in boron hybridisation during pH study for APBA-PAM nanoparticles and the corresponding efflux of counter-ions and water molecules during this process.

The reduction in particle size may have been attributed to the APBA monomers possessing a negatively charged sp^3 hybridised boron centre at more significant proportions at increasing pH values, thereby improving the electrostatic repulsions. In contrast, the increasing particle size at lower pH values may be rationalised by considering the reduction in charged boronic groups and a conformational change in the polymer to a sp^2 boron centre. The net effect is a change in solubility, and particles begin to agglomerate and precipitate out of the solution. For clarity, the anionic AOT surfactant does not contribute to this observed trend owing to its highly acidic nature and, thus, no change in the observed charge throughout (pKa ~ -1.9).[332,333]

PAM-based polymers are well known in the literature for their swelling properties concerning drug delivery applications. A swelling mechanism should be considered. Since the PAM nanoparticles have been functionalised with an ionisable group (i.e. boronic acid), their swelling properties are now pH dependent. [334] If a swelling/collapsing mechanism were responsible for the observed trend, one would expect swelling of the particles to occur when the boronic acids possess a negative charge (i.e. $pH > pK_a$), as this attracts counter-ions and solvent molecules. In contrast, the neutral (i.e. pH < pKa) form is expected to be more hydrophobic. It is accepted to be formed with an efflux of counter-ions and solvent molecules, as shown above in Figure 4-39. However, as this was not the case, this mechanism was not thought to occur here.

To conclude, the observed trend appears to be in response to the nanoparticles flocculating at lower pH due to a reduction in surface charge.

XVI. SUMMARY OF POLYACRYLAMIDE (PAM) NANOPARTICLES.

There were significant inconsistencies in the sizes of PAM and APBA-PAM nanoparticles. Individual DLS measurements showed that their sizes ranged from 283 nm to 5 μm (C.f. ***Appendix 9-7***). The particles' polydispersity and size were not affected by sonication and filtration. Usually, particles that begin to flocculate in solution can be broken up by sonication and filtration. However, it was not believed to be the reason in this case. A follow-up study on adding AOT surfactants to the work-up procedure could further validate the findings if AOT does not improve particle stability; this confirms that the broad histograms and discrepancies between batches are due to factors other than flocculation. This method will help us understand nanoparticles' behaviour and their potential for MI.

Certain modifications are necessary to improve the reproducibility and polydispersity of the systems. The current protocol involves slowly adding co-monomers dropwise into the emulsion of the main acrylate monomer, which led to high polydispersity. To effectively address this issue, it is recommended to gradually add the co-monomer along with the dominant monomer to synthesise small seed particles.[329] After an hour of seed formation, the remaining portion of the co-monomer can be added to the mixture. This technique has been proven to significantly reduce the polydispersity of the polymeric nanoparticles, resulting in higher cross-linking densities and increased resilience to morphological changes.

[329,335] This approach was employed in the following section to synthesise polystyrene nanoparticles.

Future work on these systems should investigate different proportions of the bis-acrylamide cross-linker and its effect on the particle's resilience to environmental changes. Decreasing the cross-linker concentration reduces the system's cross-linking density and hence viscosity. The concentration of the cross-linker not only impacts its viscosity but also the polymer's permeability to solvent interactions, which may lead to swelling. [329] Previous studies have reported that low cross-linked materials cannot maintain their imprinted properties, resulting in a quick loss of imprinted properties and reduced resilience to environmental changes. [329,335] It is imperative that this is considered when using these monomers to form polymer nanoparticles as a base for MI.

In summary, there were noticeable variances in particle size among various batches of PAM and APBA-PAM nanoparticles. These variances may be attributed to potential swelling or aggregation mechanisms in response to their environmental changes and applied stimuli. Consequently, the employment of acrylate-based polymeric nanoparticles for imprinting purposes is restricted regarding appropriate monomers and their properties, prompting further investigation into alternative materials. [335]

XVII. Introduction to oil-in-water (O/W) emulsion polymerisation reactions.

An alternative option was considered due to the inconsistent results observed with the PAM NPs, which may interact extensively with water due to their hydrophilicity or aggregate easily in response to changes in the external environment.

Polystyrene (PS) nanoparticles were next explored, as they are biocompatible, robust, and resilient to swelling in the desired aqueous conditions. [151,336,337] Numerous reports in the literature describe them as a suitable choice for various applications, including MI, biosensors, cell imaging, *in-vivo* drug delivery, and capillary electrophoresis. [194,199,204,337–344]

Furthermore, they can tightly pack together, forming a rigid core through π-π stacking/interactions. This feature provides a stable foundation for MI, as the monomers are hydrophobic and, thus, are not susceptible to swelling, which can occur for PAM nanoparticles. Like PAM nanoparticles, PS nanoparticles are synthesised using emulsion polymerisation techniques, which will be briefly explained.

Oil-in-water (O/W) emulsions are the inverse of that previously described in Introduction to emulsion polymerisation. First, water-soluble initiators such as potassium or ammonium persulphate thermally decompose in the aqueous phase to form persulphate radicals. This event is summarised in figure 4-40.

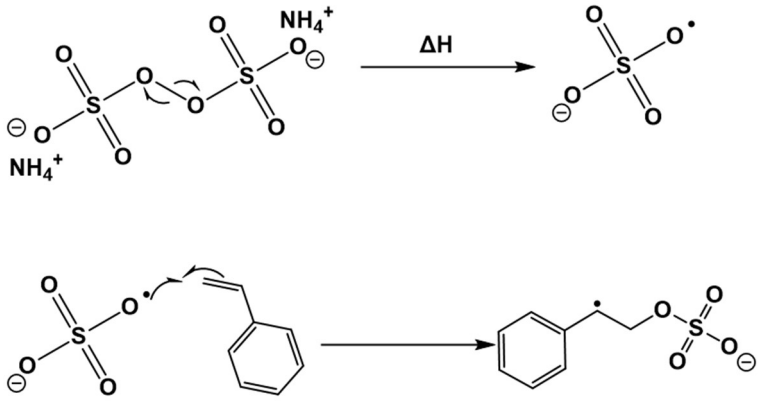


Figure 4-40: Formation of the primary monomer radical via thermal decomposition of the sulphate-based initiators. The primary radical monomer formed is used in the free radical polymerisation of styrene-based monomers to propagate further to form nanoparticles.

The persulphate radicals interact with monomers to form an amphiphilic primary monomer radical. As the radical monomer (figure 4-40) reacts with another, the growing ligand chain will continue propagating. As previously described elsewhere the propagating chains are stabilised via surfactant adsorption. The availability of surfactant molecules, therefore, limits the growth and stability. In the absence of surfactants or inadequate quantities, phase separation and polymer precipitation become an issue, and polymerisation ceases. The reaction is terminated when all the radicals are depleted, which terminates the chain reaction. This can be exacerbated by exposure to oxygen, which terminates the polymerisation reaction.[324]

XVIII. SYNTHESIS OF POLYSTYRENE (PS) NANOPARTICLES

The core-shell polystyrene (PS) nanoparticles were synthesised by previously reported methods to produce a white emulsion (figure 4-41). [345]

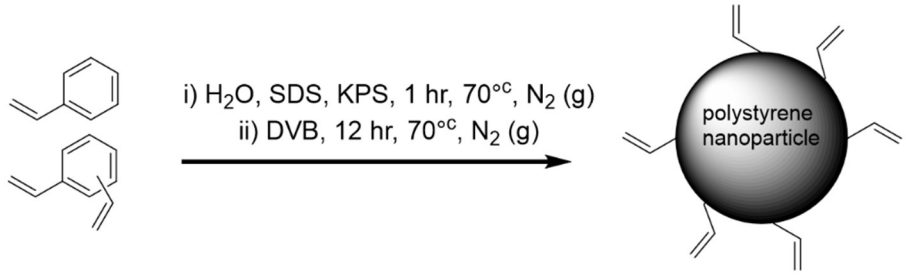


Figure 4-41: Synthesis of core-shell polystyrene (PS) nanoparticles via oil-in-water emulsion polymerisation.

Briefly, the divinyl benzene (DVB) and styrene were passed through a basic alumina column to remove any inhibitors preventing polymerisation between monomers. Next, the monomers and surfactant were placed in water under nitrogen whilst stirring. Removal of oxygen is crucial as it can lead to premature termination of the polymerisation reaction.[324]

Following degassing for 15 minutes at 70 degrees, the initiator was added, and the emulsion was allowed to react for one hour. To ensure the particles have a point of further modification, additional DVB is added after one hour and left to react overnight at 70 degrees under an inert atmosphere whilst stirring overnight; for the whole experimental protocol, refer to section: synthesis of polystyrene (ps) nanoparticles.

Analysis of the PS nanoparticles was conducted via DLS, ZP and TEM. The particles synthesised were first diluted for DLS and TEM by x1000 and x100, respectively. A summary of the data obtained is displayed below (figure 4-42).

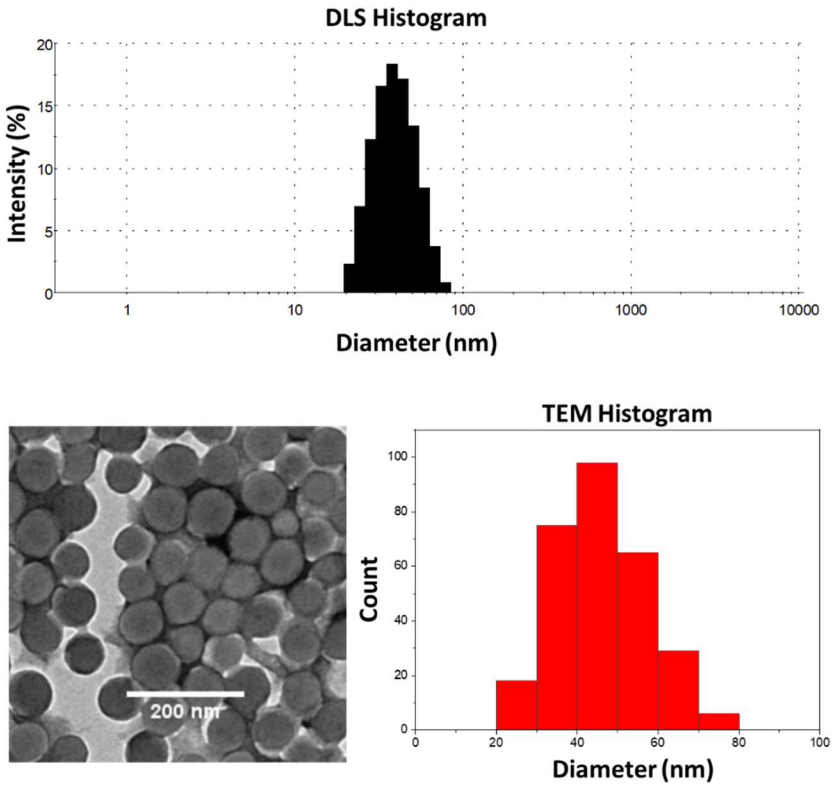


Figure 4-42: Size distribution histograms for PS nanoparticles. From top to bottom, left and right are the DLS histogram, the TEM image of particles, and the TEM data summarised in a histogram. The average size of the particles was found to be 48±2 nm via microscopic methods and 82 ±3 nm via DLS.

The synthesised latex particles represent a significant improvement over the previously discussed PAM nanoparticles (C.f. ***synthesis of polyacrylamide nanoparticles (pam)***). The latex particles boast a much narrower size distribution histogram. The calculated PDI obtained from DLS of 0.02 ± 0.015 supports this observation. Specifically, the particles measured 48 nm (n=2) by TEM and 82 nm in DLS (n=6); for a full tabulated summary of the repeats conducted and their corresponding analysis, refer to appendix 9-9.

These sizes contrast the broader size range observed in the PAM particles shown in figure 4-34 and figure 4-35. The nature of the styrene-based polymer backbone sterically limits reorientation processes, unlike the polymer backbone of acrylamide-based particles with greater degrees of freedom. [151] This could explain the greater consistency, reduced polydispersity, and reduction in particle size. Furthermore, the methodology employed for their synthesis was different from that of PAM particles. Here, the monomers are not all added initially for PS nanoparticles. First, the styrene core is formed, followed by adding a secondary amount of cross-linking co-monomer (DVB). Thus, the slow addition over time was thought to have been primarily responsible for the low PDI values measured.

FT-IR spectroscopy was also carried out to complement the TEM and DLS data above. The FT-IR spectra allow comparison between the chemical structure of the monomer alone and that of the PS particles. The styrene monomer used in the synthesis provides strong peaks in the fingerprint region of IR (below 1200 cm^{-1}) and is highlighted in Region 3 of figure 4-43. The observed

peaks in region 3 correspond to the out-of-plane bending of C-H groups.

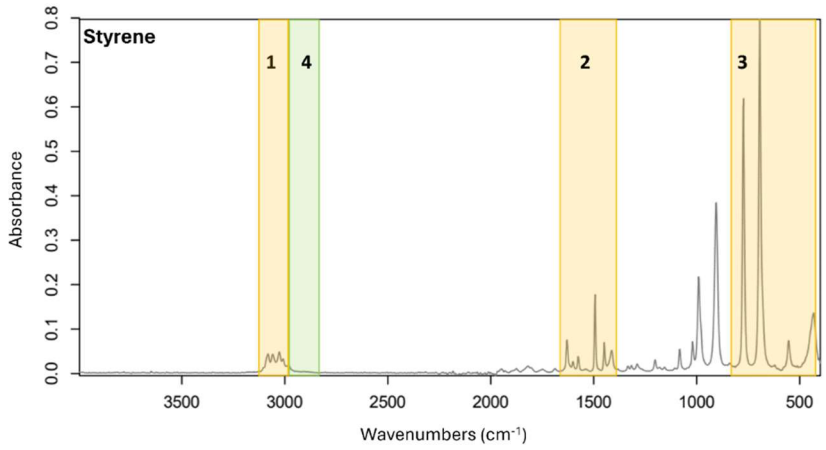


Figure 4-43: FT-IR spectra of the starting styrene reagent (monomer) displaying peaks in the expected regions for C-H and C=C vibrational and stretching IR active modes.

The peaks in region 2 are located around 1500 cm^{-1} and are thought to be produced from the C=C vibrations of the benzene ring. Finally, the broad region around 3000 cm^{-1} is commonly reported in the literature as the sp^2 C-H stretching mode. [346]

To compare the latex particles synthesised (figure 4-41) to the above FT-IR, the particles were dried under vacuum to yield a white powder of 0.282g (66%). The corresponding FT-IR spectrum of the white powder is shown below in figure 4-44.

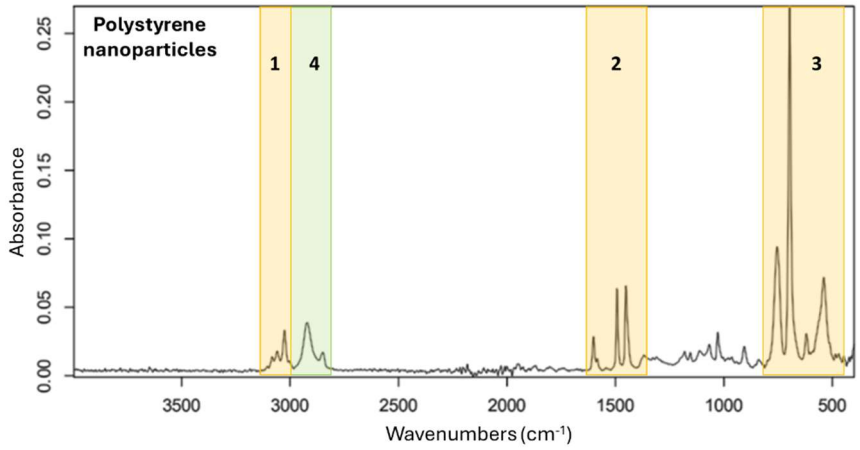


Figure 4-44: FT-IR spectra for PS nanoparticles displaying peaks in the expected regions for C-H and C=C vibrational and stretching IR active modes.

The PS nanoparticle spectrum showed similar out-of-plane C-H bending peaks in Region 3 to that observed for the styrene monomer (figure 4-43). Conversely, Region 2 displayed changes compared to the monomer spectra; here, the wavenumber for the C=C aromatic stretches shifts to lower wavenumbers. The shift suggests a change in the environment, suggesting polymerisation has occurred. Furthermore, the new set of peaks in region 4 in figure 4-44 is the most significant.

The new peaks for the white powder (figure 4-44) are situated at lower wavenumbers, indicating they are from weaker bonds per Hooks' law.[347] These new peaks represent the newly formed sp^3 carbons of the polymer backbone formed during polymerisation. These carbons will have greater mobility, hence the observed lower vibrational frequency.

The change in FT-IR spectra and the emergence of new peaks at lower vibrational frequencies suggest that the polymerisation of

the monomer has taken place and, hence, the formation of PS nanoparticles. Subsequent repeats of the experimental protocol yielded particles of comparable diameters and polydispersity. A summary is provided in the appendix (Appendix 9-9).

In summary, the observed findings agree with previously reported literature.[348] The emergence of the new peaks, the microscopy images, and the experimental PS FT-IR spectra congruent with prior literature reports concur that the formation of polystyrene nanoparticles had occurred. [348,349]

XIX. PURIFICATION OF POLYSTYRENE (PS) NANOPARTICLES

The synthesised nanoparticles required purification; the chosen method was centrifugation washes. The emulsion was first broken by removing the aqueous phase under vacuum, utilising tetrahydrofuran (THF) to form an azeotrope. [350] The white aqueous emulsion was mixed with THF to produce a 1:1 mixture by volume. Using THF causes the PS cores to swell, releasing any trapped reagents. To reduce the required centrifugation speeds and time and prevent degradation from excessive speeds. The nanoparticles were precipitated from the solution by adding an excess protic solvent such as ethanol.[325,329]

Following centrifugation, the white pellet was isolated and resuspended into THF and was again centrifuged to form a white pellet. The final washing step deviates to ensure the particles are returned to aqueous media via the resuspension in water. This is vital for future ITC binding studies to prevent “buffer mismatch.”

During the work-up procedure, difficulties arose during the re-suspension of the pellet into water. Manipulation of solvent ratios during work-up did not resolve the issue. Subsequent work focused on obtaining more water-soluble PS nanoparticles to ease purification.

XX. INCREASING THE SOLUBILITY OF POLYSTYRENE (PS) NANOPARTICLES

Further functionalisation of the particles was considered to enhance the water solubility of the PS nanoparticles. The aim was to conduct a 'one-pot' procedure to synthesise and functionalise the nanoparticles before conducting the work-up, like that of PAM nanoparticles.

A short cross-linker capable of reacting with the surface groups of the PS particles. Additionally, these molecules should be terminated with a useful functional group for the imprinting process. Therefore, the chosen cross-linker must be capable of interacting with vinyl groups. To satisfy this a bis-acrylamide type molecule was considered to participate in free radical polymerisation reactions with the PS particles. Thereby, permitting swift reaction times, typically within minutes when initiated with persulphate-type initiators as previously described.[328].

Furthermore, FT-IR can also view acrylamide groups, which provides a point of checking reaction completion. Therefore, the cross-linker N, N'-(1,2-Dihydroxyethylene)-bis-acrylamide (DHEBA) was selected due to its short length and FT-IR trackable groups.

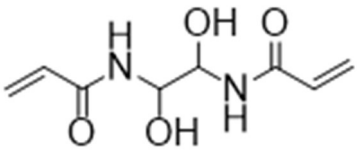


Figure 4-45: N, N'-(1,2-Dihydroxyethylene)-bis-acrylamide (DHEBA) used to functionalise the core-shell PS nanoparticles to improve their water solubility and provide a point of further functionalisation.

The DHEBA molecule will be frequently denoted as the cross-linker within this text. As shown below, the cross-linker was incorporated into the synthetic route via room temperature free radical reactions with potassium persulphate**,** forming DHEBA functionalised PS NPs (DHEBA-PS NPs).

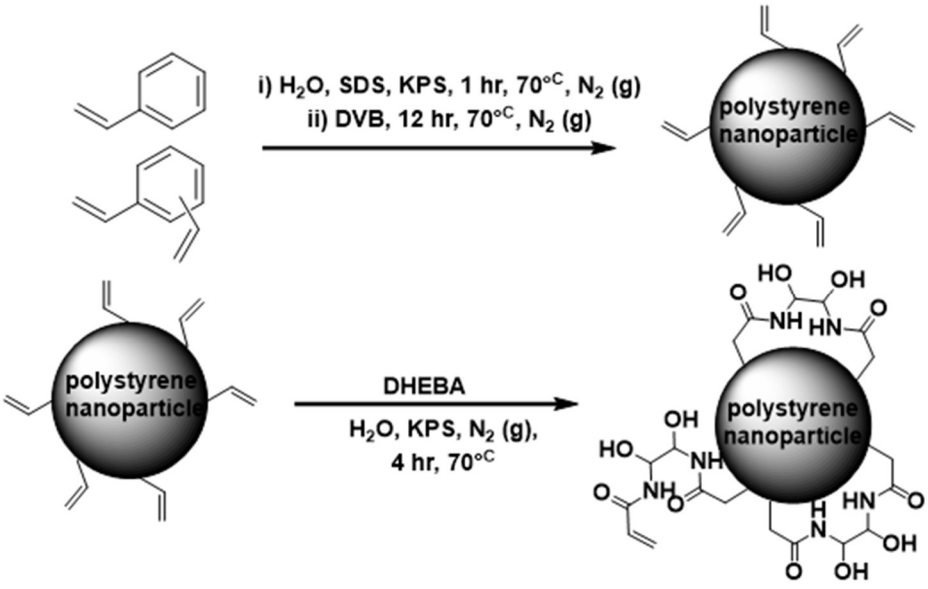


Figure 4-46: Synthesis of water-soluble polystyrene nanoparticles (DHEBA-PS NPs).

The first step was conducted as described in section: nanoparticles. After 12 hours, the DHEBA cross-linker was added with an additional KPS amount for the free radical polymerisation. The DHEBA was added after the robust styrene core-shell particles were formed. This ensured that the size and PDI stayed the same from what was previously observed.

An opaque white emulsion was produced, again subjected to centrifugation washes to remove the excess reagents as previously described. Prior washing steps yielded inconsistencies. Possible reasons for prior issues observed may have been the impact of centrifugation may have caused caking, which may have caused the difficulties of redispersing the particles.[331] In addition, it was thought the surfactant would have been significantly removed from the nanoparticles over several centrifugal rounds.[308] From our previous works with gold nanoparticles, the importance of surfactant concentration to prevent irreversible aggregation has been shown.

A surfactant stock of sodium dodecyl sulphate (SDS) was made to produce the same concentration in the reaction. The surfactant stock was used during washing instead of resuspending in THF. After using the SDS stock during the centrifugation steps, the results were more consistent and dependable, with almost all nanoparticles going back into the solution each time with little sonication required. Any precipitate left at the end was discarded from the eppendorf and assumed to be unfunctionalised nanoparticles (i.e. no DHEBA cross-linker on particles) or particulates which had undergone coagulation.

DLS measurements were conducted (dynamic light scattering (dls) and zeta potential measurements (zp)) to ensure that the nanoparticle had not undergone aggregation following centrifugation. The aim was to observe if a change in PDI and hydrodynamic diameter had occurred following centrifugation. An increase in these values indicates the presence of flocculation in the emulsion, which can lead to irreversible coagulation and precipitation of the polymer, which may have occurred previously for the PAM particles.

Before functionalisation, the core-shell nanoparticles had a very narrow distribution of sizes, as shown in figure 4-42. Following the purification of the DHEBA functionalised particles, the PDI values and average diameters increased, as summarised in Table 4-4.

Table 4-4: Summary of DLS measurements (n=5) of pure PS nanoparticles before and after the addition of DHEBA displaying the effect of washing with surfactants on the recorded size observed.

Sample description	DLS diameter (nm)	PDI
DHEBA functionalised particles washed with water and filtered (0.2 µm)	105 ± 1.5	0.15 ± 0.01
DHEBA functionalised particles washed with SDS and filtered (0.2 µm)	90 ± 2.0	0.08 ± 0.02
Plain core shell PS nanoparticles	82 ± 0.60	0.02 ± 0.02

The diameters of particles washed without surfactants were adversely affected, as depicted by the increased diameter. The changes were rationalised by centrifugation, forcing nanoparticles to come together to form a pellet. The nanoparticles that had been washed in SDS had greater stability and lower PDI value due to the presence of the charged surfactant. Following the centrifugation washes, the particles were subjected to sonication for 15 minutes to break up any flocculates that had formed during purification. This data follows the trend observed with gold nanoparticles, showing the importance of surfactants throughout nanoparticle functionalisation and purification.

After purification, the morphology of the functionalised particles was next investigated via TEM utilising Image-J software. [289] Due to the COVID-19 pandemic, I had to rely on other technicians to assist with the microscopy work. This additional effort and my work provided the necessary repeats and statistical analysis. It is important to note that the average diameter reported includes the imaging work performed by these technicians, namely Theresa Morris (UoB). Microscopy images revealed spherical nanoparticles with an average diameter of 54 ± 3 nm. The distribution of sizes recorded utilising is summarised in the histogram below (figure 4-47).

The DLS (table 4-4) and TEM (figure 4-47) diameters recorded were observed to increase following the incorporation of DHEBA into the synthetic protocol (figure 4-46), suggesting functionalisation had occurred.

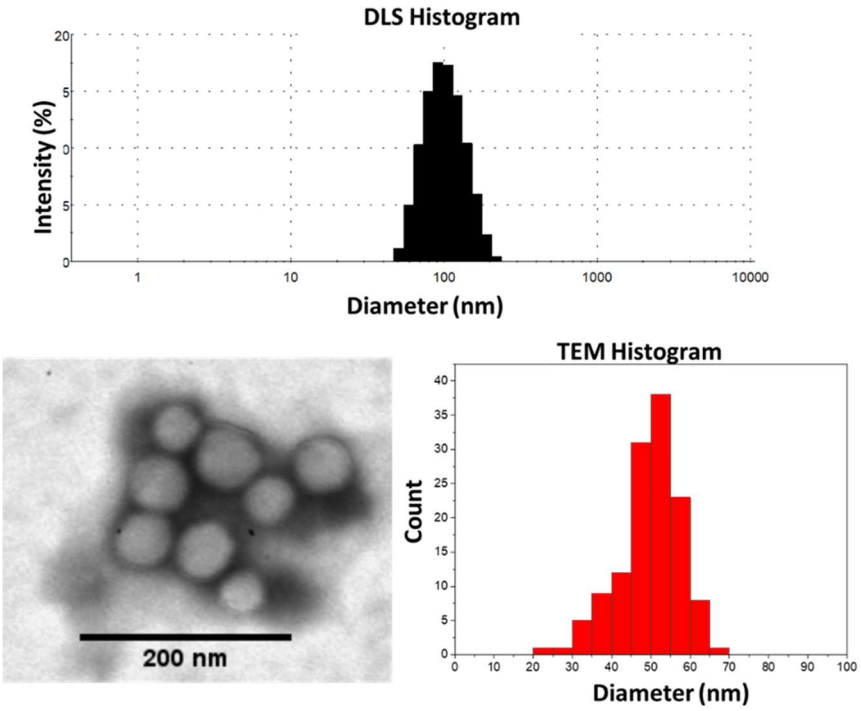


Figure 4-47: Characterisation of PS nanoparticles functionalised with DHEBA to obtain their size distributions and average diameter. From top to bottom, left and right, is the DLS histogram, the TEM image, and the TEM histogram.

The functionalised nanoparticles were next analysed using FT-IR after drying under a vacuum. This was done following purification through centrifugation, which resulted in a pure white powder with a mass of 18 mg/mL. Assuming no loss of DVB, styrene, or DHEBA, the synthesised DHEBA functionalised nanoparticles yield was 27%. It is typical to observe reduced yields when centrifugation methods isolate nanoparticles below 0.5 µm.[331,351]

In the event of a successful reaction, it is anticipated that the FT-IR spectra will exhibit additional peaks that correspond to new acrylamide functional groups. These groups are expected

to produce spectral changes in the following regions: ~ 1540 cm^{-1} and ~3300 – 3500 cm^{-1} (in-plane bend and stretching of N-H), ~1630 – 1680 cm^{-1} (vibrational modes of C=O), and ~3000 cm^{-1} (broad peak for O-H). [337,352–355] These new peaks and spectral changes are emphasised and depicted in figure 4-48 for the FT-IR spectra of DHEBA functionalised PS nanoparticles.

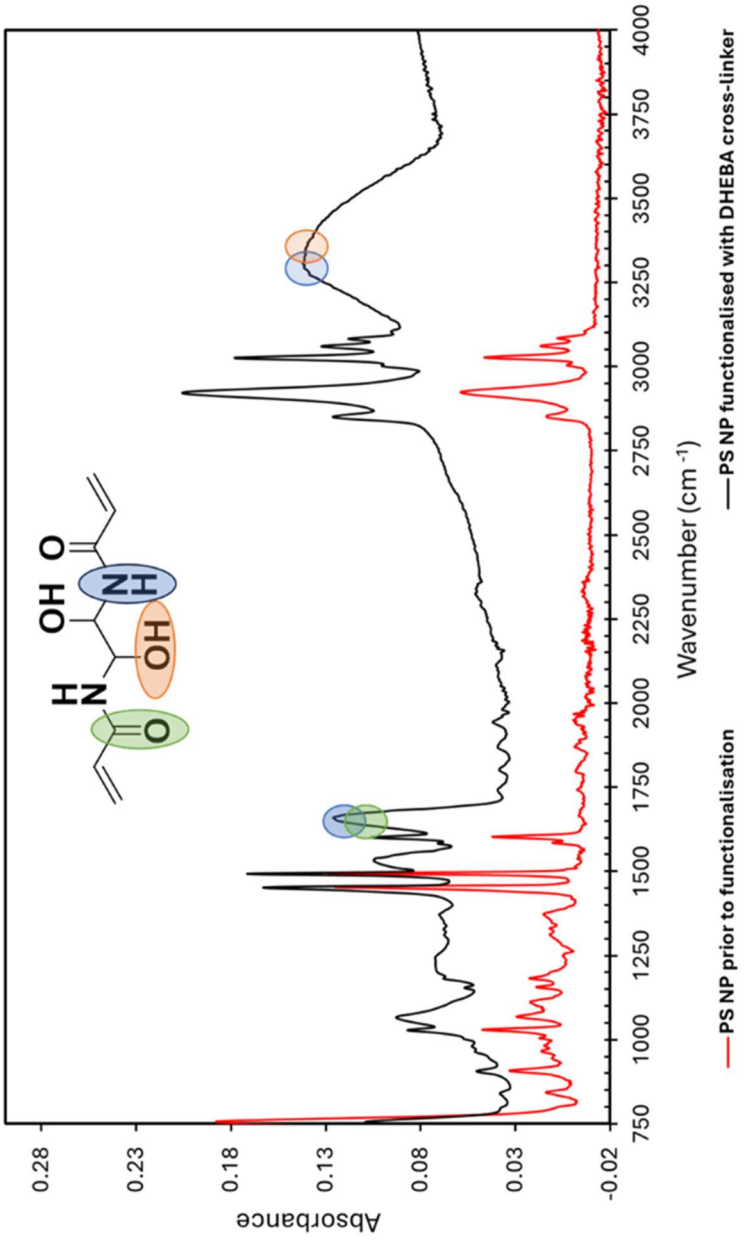


Figure 4-48: Stacked FT-IR spectra for comparison of before (Red) and after DHEBA was added to the PS nanoparticles (Black). New peaks and peak shifts are highlighted and colour-coded to their respective functional groups corresponding to those peaks/shifts.

The FT-IR spectrum of core-shell PS nanoparticles has been previously analysed (figure 4-44) and is being utilised for comparative purposes, illustrated via the red spectrum. The black spectrum for the DHEBA functionalised nanoparticles (DHEBA-PS) provides additional peaks corresponding to the new functionality on the particle's surface. Notably, the most important peaks are around 3000 cm^{-1}, which correspond to OH and NH vibrational modes, attributed to the presence of DHEBA in these nanoparticles.

To conclude, the emergence of new FT-IR vibrational modes and increased size provided compelling evidence that the latex particles have undergone functionalisation with DHEBA. A tabulated summary of the conducted size analysis for DHEBA-PS particles is provided in appendix 9-10.

XXI. INVESTIGATING THE STABILITY OF POLYSTYRENE (PS) NANOPARTICLES.

Next, as previously conducted for PAM nanoparticles, we wished to investigate the stability of the PS nanoparticles concerning changes in pH.

The particles were subjected to centrifugation before mixing the corresponding buffers with particles. The centrifugal washing steps were conducted as previously described (c.f. Purification of polystyrene (PS) nanoparticles). The white pellets were separated from the supernatants. Approximately 1 mL of white pellet was added to 1 mL of buffer and vigorously sonicated and vortexed in eppendorfs to resuspend the particles back into solution. The nanoparticles were left overnight in the eppendorfs to ensure they had enough time to respond to the new media before analysis via DLS.

Size measurements were obtained of the nanoparticles before and after the addition of buffered solutions for comparison. Each sample's averaged diameter was calculated along with its corresponding PDI. A summary of the DLS data obtained is displayed below in figure 4-49.

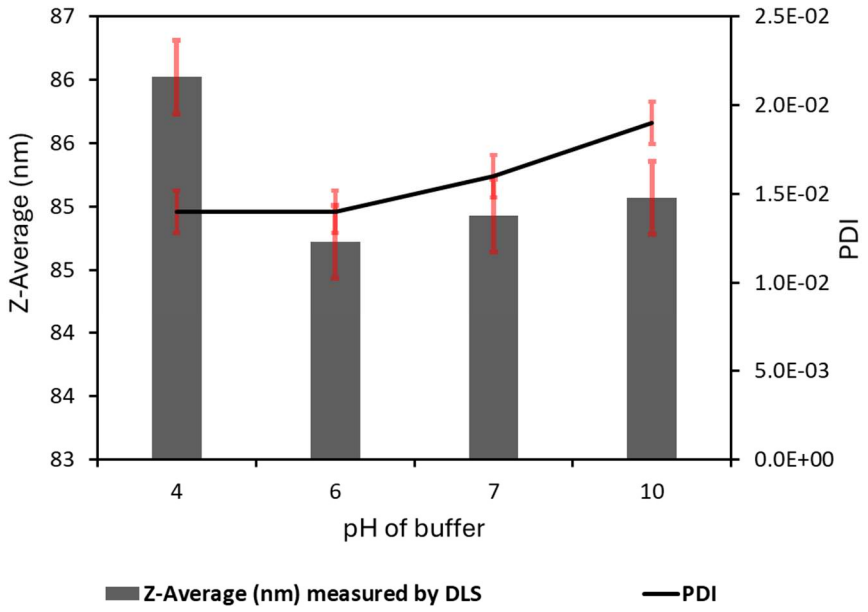


Figure 4-49: Graphical summary of the change in particle size and polydispersity when placed into different pH buffers (0.1M).

The diameter of the DHEBA-PS particles before incubation with buffer was measured and an average hydrodynamic diameter of 81 nm was provided via DLS. The DLS data (figure 4-49) for the particles suspended in buffers display minuscule variation in particle diameter across the different pH mediums. The difference between pH 4 and 6 samples is less than 2 nm. Therefore, there was a ±6% change in the hydrodynamic diameter, which was not deemed significant. More considerable diameter changes were previously observed for samples upon changing the dilution factor for DLS measurements (Appendix 9-9).

The resilience to diameter change was thought to be due to the hydrophobic monomers used in the core formation. These particles appear superior to PAM nanoparticles, due to their

smaller size and synthetic consistency. Furthermore, the pH study for these particulates displayed smaller discrepancies (smaller error bars) between repeats in comparison to that observed for the gold nanoparticles. Thus, an improvement over the gold nanoparticles.

In addition, regular DLS measurements were conducted to determine the long-term stability of the particles in solution when stored in the fridge after the work-up. A table summarising the changes observed during the study is provided below table 4-5.

Table 4-5: A tabulated summary of the difference (±3%) in hydrodynamic diameter measured over a year for a batch of neat concentrated DHEBA-PS nanoparticles.

Time period	DLS Diameter (nm)	PDI
Day 0	65 ± 0.9	$0.1 \pm 1.2 \times 10^{-2}$
1 Year	67 ± 1	$0.05 \pm 6 \times 10^{-4}$

The tabulated data showed that a batch of nanoparticles did not vary significantly (<±3%) in diameter over a year. The measured polydispersity of the sample remained well below 1, which is known to be consistent with increased monodispersity in polymeric nanoparticle samples. The tabulated DLS diameters recorded deviate from prior recordings due to a different batch of nanoparticles measured at a different concentration. As per previously tabulated DLS diameter, DLS values vary significantly depending on concentration. Variations in measurements due to concentration are displayed in appendix

9-9 and appendix 9-10. The trend, however, remains the same – the nanoparticle's size does not deviate over time.

XXII. FUNCTIONALISATION OF POLYSTYRENE NANOPARTICLES WITH GLYCAN RECEPTORS

The next challenge was to functionalise the water-soluble polystyrene nanoparticles with boronic acid (BA) or benzoboroxole (BOB) glycan receptors to see if they were stable after functionalisation. The functionalisation of PS particles whilst maintaining control over the particles size and their subsequent purification is a persistent challenge reported in literature.[329]

The incorporation of such glycan receptors (BA or BOB moieties) onto PS particles is essential for the MI. The functionalisation test will entail the addition of both DHEBA and BA moieties. The DHEBA molecules provide the necessary hydrophilic properties as previously discussed, whilst the incorporation of boronic acid groups, such as 3-acrylamidophenylboronic acid (APBA) or 3-acrylamidobenzoboroxle (AABOB), onto the surface provide the necessary glycan sensing units (

figure 4-50). For many reactions, the commercially available APBA will be used over AABOB as it does not require synthesis, has similar solubilities, and binds to cis-diols (Figure 1-33).

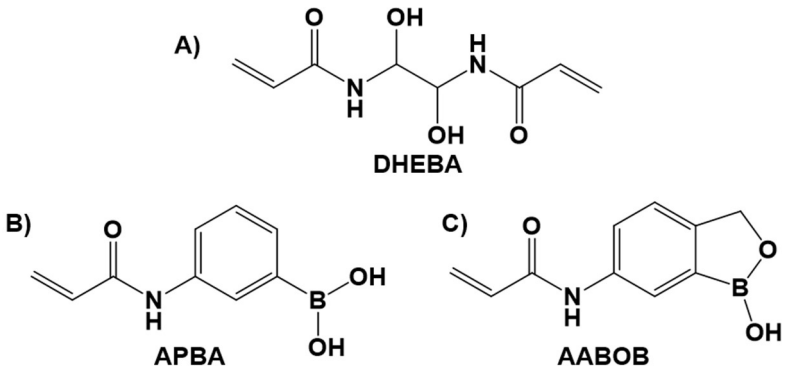


Figure 4-50: Aa-based molecules used to functionalise PS particles.

PS nanoparticles were synthesised according to the previously reported experimental protocol (Synthesis of polystyrene (PS) nanoparticles) to assess the stability of latex particles bearing glycan receptors. The PS particles were functionalised using Aa-based molecules (

Figure 4-50) through free radical polymerisation reactions. The reaction combined the DVB molecules' alkene groups with the glycan sensors' (AABOS or APBA) acrylamide (Aa) moiety to form a new carbon-carbon bond, as depicted in figure 4-51.

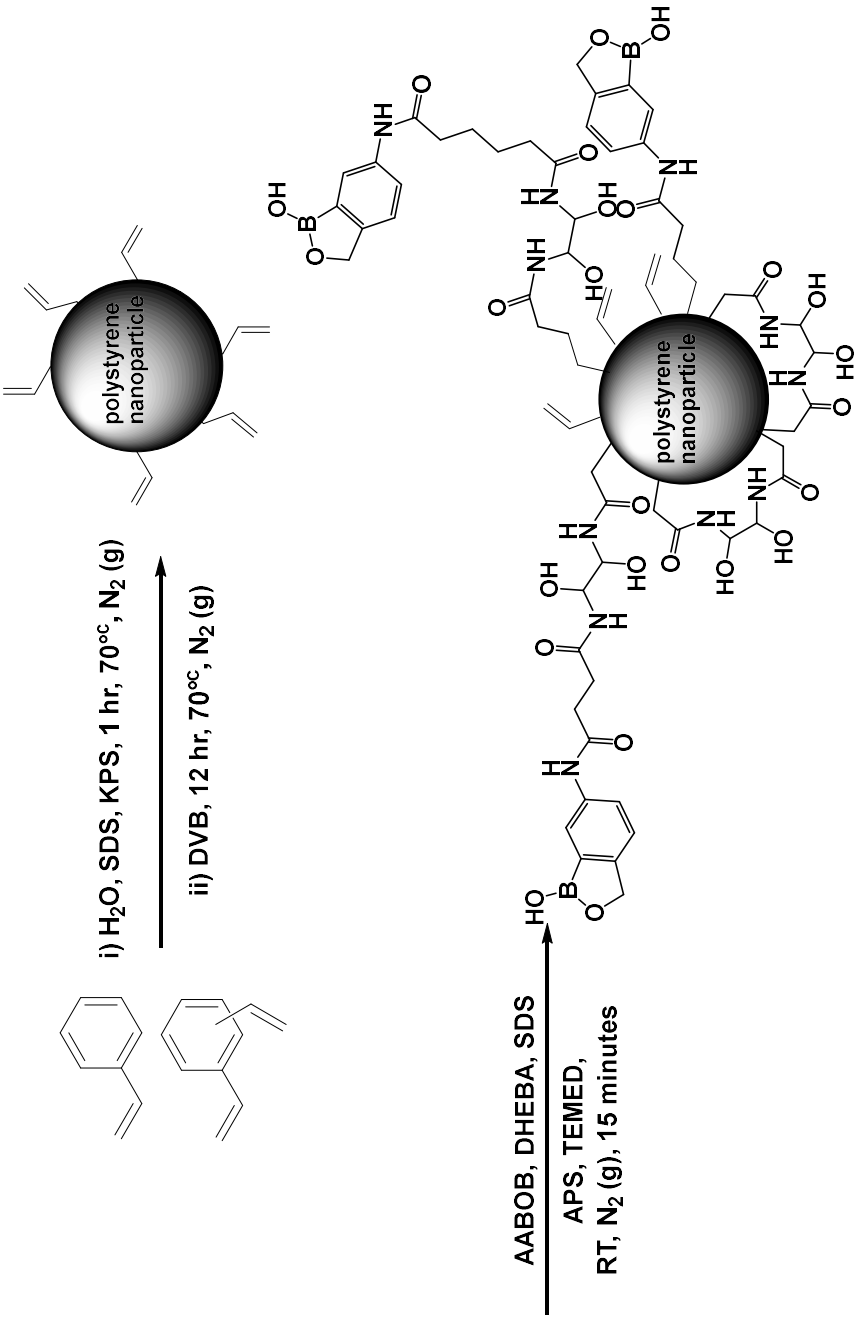


Figure 4-51: One-pot procedure evaluated for synthesising PS nanoparticles baring glycan sensors (AABOB or APBA).

It was known that the boronic acid-based moieties (

Figure 4-50) had limited solubilities in water. Therefore, it was necessary to evaluate whether a hydrophobic styrene-based

particle can bear sparingly soluble motifs on its surface and maintain its stability in solution for subsequent analysis.

To commence this trial, the core-shell latex nanoparticles (100 µL) previously synthesised (figure 4-41) were added to DHEBA (100 µL, 50 mM, dimethyl sulfoxide (DMSO)) and APBA (700 µL, 7.14 mM, DMSO). The polymerisation reaction began after adding APS (100 µL, 40 mg/mL) and TEMED (1 µL) under an inert atmosphere and was allowed to react for 15 minutes. Prior Mendes group MI provided the concentrations based on previous MI publications.[203] The time was selected to ensure the reaction had gone to completion. It is well-known that persulphate initiators are fast and reach their complete conversion over several minutes.[328] Thus, 15 minutes was ample time. These will formulate the basis of future free radical polymerisation reactions for functionalising the PS nanoparticles.

DLS measurements were conducted to assess the extent of reaction completion by viewing any change in the recorded hydrodynamic diameter. Before measuring the particle's size, they were diluted (1 in 100) with water owing to the sample volume required for the instrumentation. Thus, for comparison, the diameter for the core-shell latex particles which had been diluted by the same factor should be used for a close comparison (Appendix 9-10).The resultant histogram showing the distribution of sizes is provided below (figure 4-52).

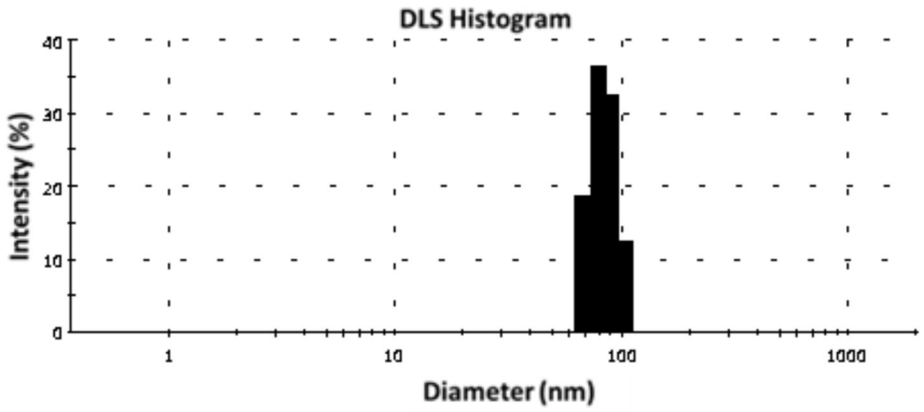


Figure 4-52: DLS histogram (n=3) for APBA/DHEBA functionalised nanoparticles following dilution (1 in 100). The particles possessed an averaged diameter of 89 ± 0.2 nm with a dispersity value (PDI) of 0.013 ± 0.01.

The size of the core-shell latex particles previously synthesised (figure 4-42, 86 nm, 1 in 1000, Appendix 9-9) was compared to the new batch. The nanoparticles were first synthesised, as shown in figure 4-51, and then incubated with APBA and DHEBA. This resulted in an average diameter of 89 nm, a 3% increase in size. Indicating a change on the particles surface may have occurred.

However, since DLS measurements are known to vary significantly based on concentration, pH, temperature, and ionic strength as previously discussed in Dynamic light scattering (DLS) and zeta potential (ZP), the results should be interpreted with caution. TEM measurements could have provided a better understanding of particle size independent of concentration and batch-to-batch variations. However, due to COVID-19 restrictions access at this present time was limited. To confirm the surface modification further analysis is required.

The stability of the particles was assessed via zeta potential measurements; the sample produced a value of -37.4 mV (n=5). Per previous reports' definitions, the nanoparticles had excellent stability in the solution. [239,241]

The functionalisation reaction was repeated to produce a milky white solution, with no visual signs of precipitation or layers forming on standing. The purification of the emulsion was necessary to remove any unreacted reagents and was conducted next.

To ease centrifugation attempts it was desirable first to precipitate out the particles. This is commonly conducted in for polymeric particles, which are highly challenging to purify owing to their light nature.[204,229,325,329,351] As previously used, ethanol was added in a 1:1 manner to the PS nanoparticles to precipitate out the nanoparticles, which were then subjected to centrifugation to collect a pellet.[325] Following centrifugation, the supernatant remained cloudy, indicating the nanoparticles were in the bulk of the solution. Indicating the particulates had not precipitated out of solution during the addition of ethanol. This may suggest the presence of more polar groups at the

surface, such as the boronic acid moieties incorporated into the synthesis.

The unsuccessful centrifugation prompted the use of alternative solvents to facilitate the formation of a clear supernatant. THF, acetonitrile (ACN), and water were incorporated into the washes to produce a 1:1 water-to-organic solvent ratio. The centrifugation with THF/H_2O and ACN/H_2O solvents provided a clear supernatant. ACN was selected for further centrifugation washing of these particles due to its greater compatibility with the plastic Nalgene centrifuge tubes.

The next challenge was resuspending these nanoparticles back into the water following centrifugal washes for subsequent analysis. The white pellets obtained were added back into the water after their collection. The sample was vortexed and sonicated to resuspend them back into the water to form a familiar opaque white emulsion. However, upon standing, the emulsion appeared to degrade over time to create two separate layers as shown in Figure 4-53.

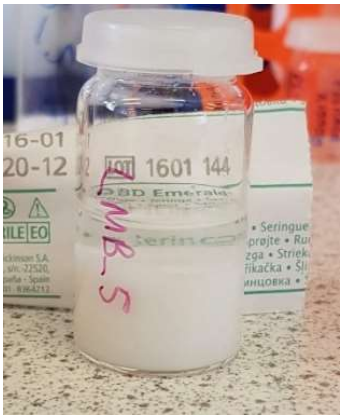


Figure 4-53: nanoparticles underwent phase separation upon standing overnight at room temperature after being purified.

The above solution was vigorously shaken by hand, followed by filtration through a 0.2 μM syringe filter to remove large aggregates. The filtrate was collected and sonicated and vortexed. The final solution obtained was transparent in colour, indicating the lack of nanoparticles in the solution. The particles were no longer "nano" and had begun to coalesce in solution upon standing, hence not a stable nano-emulsion.

The reaction was repeated and centrifuged in THF/H_2O and ACN/H_2O to ensure the same results were observed. Again, following centrifugation, the nanoparticles on standing formed two layers, indicating that they do not resuspend well into the water after adding APBA and DHEBA onto the surface.

Finally, a surfactant was trialled to resuspend the previously collected pellets; in the presence of surfactants, the particles did not resuspend efficiently. This highlights the challenges of nanoparticle functionalisation. Therefore, a series of optimisation tests were conducted as part of trial and error.

XXIII. OPTIMISATION OF ADDITION OF BENZOBOROXOLE RECEPTORS ONTO POLYSTYRENE (PS) NANOPARTICLES

Owing to the limited water solubility of the desired boronic acid-based moieties (glycan receptors), it was decided to trial a reaction with reduced concentrations of boronic acid (BA). In addition, the nanoparticles used for this series were first functionalised with DHEBA (figure 4-46) on the surface to enhance their water solubility; for experimental details, refer to Synthesis of polystyrene nanoparticles functionalised with DHEBA and 3-acrylamidobenzoboroxole/ 3-acrylamidophenylboronic acid. Following their synthesis, a small aliquot was reserved for a future DLS diameter comparison (C.f.

Appendix: 9-11). These nanoparticles were then used for functionalisation with DHEBA and APBA molecules to assess their stability. The concentrations trialled are provided below (Table 4-6).

Table 4-6: Tabulated concentration ranges trialled for adding APBA and DHEBA to core-shell polystyrene nanoparticles.

ID	Concentration
1	[APBA, DMSO] = 2.5 mM [DHEBA, DMSO] = 5 mM
2	[APBA, H_2O] = 35 µM [DHEBA, H_2O] = 5 mM
3	[APBA, H_2O] = 35 nM [DHEBA, H_2O] = 5 mM

The reactions always produced unstable emulsions when DMSO was used or when the concentration of the BA was above 35 nM. When DMSO was used, the emulsion underwent phase separation on standing, whilst, for reactions exceeding 35 nM, the emulsion displayed visible signs of precipitation. When the glycan sensing moiety (BA) concentration was reduced to the nanomolar range, following centrifugation attempts, the nanoparticle emulsion did not undergo phase separation nor possess white precipitates. DMSO was used in these reactions to aid the solubility of the boronic moieties and was previously used in the Mendes group publications for aiding the solubility of such molecules in aqueous media when functionalising 2D surfaces.[203]

It was thought that the presence of DMSO interacting with the sparingly soluble boronic moieties and hydrophobic styrene monomers may have resulted in increased hydrophobicity of DMSO. The net result of these solvent interactions may have made it immiscible with the water, thus destabilising the emulsion. Similar solvent-solute interactions have elsewhere been reported for comparable systems in literature – e.g. DMSO was previously reported to become immiscible upon interacting with a glycerol-based emulsion, resulting in phase separation according to prior reports. The phase separation is believed to be due to a change in the intermolecular forces, otherwise stabilising the system.[356–358].

In addition, the reduction in boronic acid concentration was likewise accompanied by a visual increase in emulsion stability. Thus, future functionalisation reactions with these moieties should be carefully planned to minimise the concentration where possible while ensuring accessible glycan receptor molecules on the surface for potential binding interactions.

The particles were analysed using TEM and DLS. Below is a pictorial summary of the size distribution obtained via microscopy and number and size-based measurements *(*Figure 4-54).

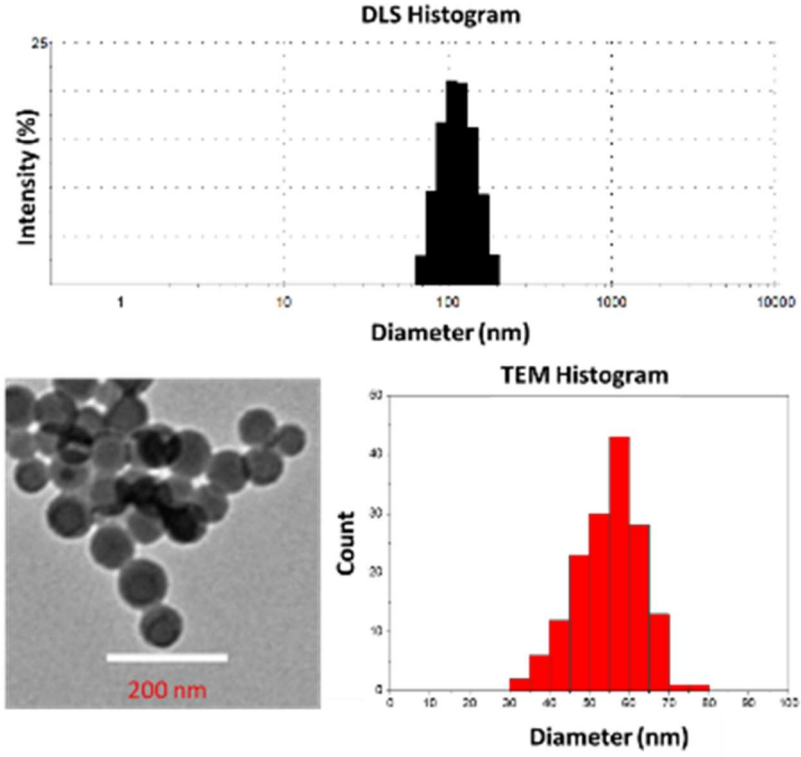


Figure 4-54: Characterisation of DHEBA/APBA PS nanoparticles to obtain their size distributions and average diameter. From top to bottom, left and right: DLS histogram (average diameter 83 nm, n = 2, C.f.

Appendix: 9-11), microscopy TEM image and the corresponding size distribution from TEM (67 nm, n = 2, C.f. Appendix 9-12).

Size increments were observed for both DLS and TEM. Specifically, the DLS provided a 22% increase (c.f. whilst TEM provided a 17% increase in diameter (Appendix 9-12***).*** The increase in size suggests a change in the nanoparticle's surface. A qualitative fluorescence binding study will be conducted next to verify the presence of the boronic receptors added.

XXIV. FLUORESCENCE SPECTROSCOPY STUDIES WITH POLYSTYRENE NANOPARTICLES

The PS nanoparticles bearing boronic receptors now have the capacities of interacting with cis diols to form boronate esters. One method of verifying the presence of cis diols is via the use of a common dye called Alizarin Red S (ARS). ARS on its own is weakly fluorescent however, in the presence of cis-diols it can form an adduct to form a boronate-ester which is more fluorescent than the original ARS as depicted via Figure 4-55. Therefore, we seek to observe an enhancement in the fluorescent signal with the nanoparticles synthesised.

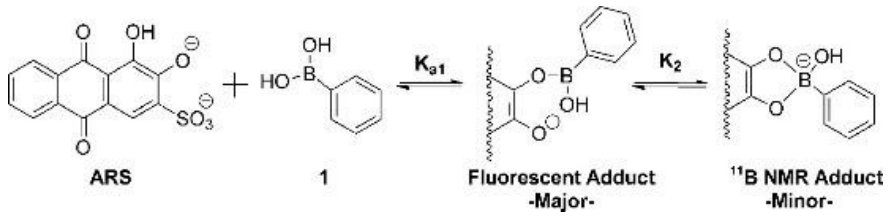


Figure 4-55: Fluorescent adduct formed between ARS and boronic acids.

A range of concentrations of ARS were made up and 200 µL of each solution was placed into separate wells in a 96 well plate (Greiner 96 F-bottom type), ensuring the liquid level was the same in each well for the focal height and gain adjustment of the instrument. For the fluorescent spectroscopy experiment the excitation and emission bandwidth were set to 520 (± 10) – 564 (± 10) nm and 545 (±10) – 625 (± 10) nm accordingly. For each set of fluorescent experiments, the focal height and gain was

automatically adjusted by CLARIO star Mars software. The corresponding raw data was exported and plotted to provide the below emission profile - Figure 4-56.

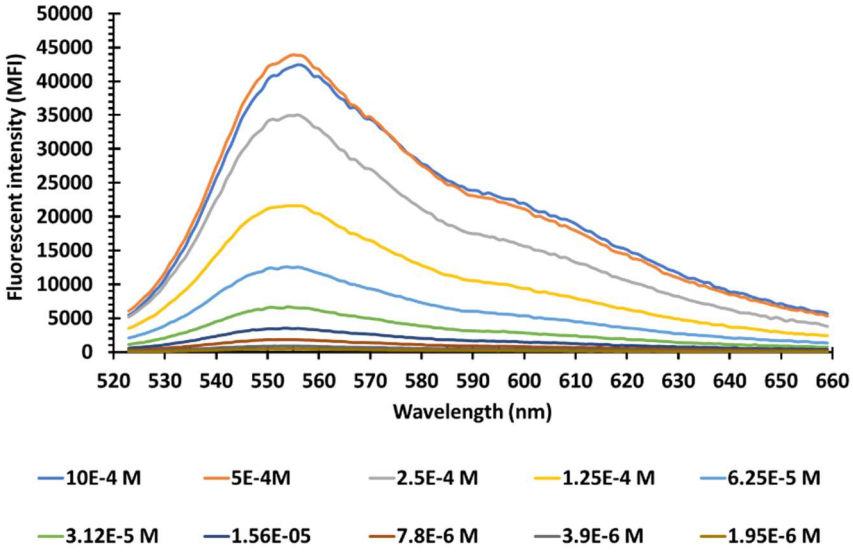


Figure 4-56: Fluorescence emission profile for ARS at pH 8 displaying a maximum emission profile at 555 nm.

The ARS dye was seen to emit ~ 540 – 580 nm which agrees with prior literature.[359,360] The fluorescent spectral scan of ARS provided a maximum around 555 nm. The relationship between the fluorescent signal and change in concentration for ARS was deemed to be a linear correlation as observed by the below bar chart (

Figure 4-57).

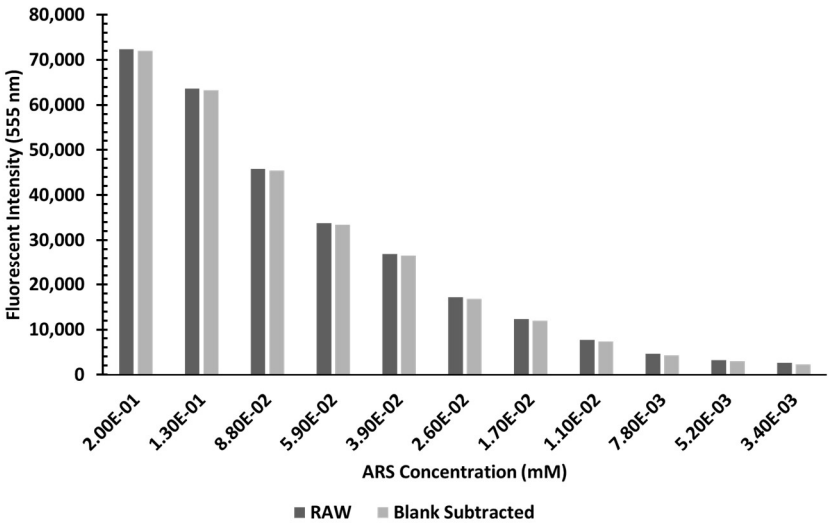


Figure 4-57: Graphical depiction showing the linear relationship between the concentration of ARS dye and the observed fluorescence signal at 555 nm.

Next the validation of the formation of the fluorescent adducts were necessary (Figure 4-55). Since benzoboroxoles more readily form boronate esters than their boronic acid derivatives as previously described they were used. In the microplates 100 µL (2 mM – 0.078 mM) of acrylamido benzoboroxole (AABOB) was added into each well. Followed by the addition of the 100 µL of ARS (0.02 mM / 2 µM). For the adduct formation studies it was important to allow the adducts to be formed therefore, prior to placing inside the CLARIO-Star instrument the plates were first shaken on an orbital shaker for one hour to ensure the samples had mixed. Furthermore, between well measurements the samples were also shaken (60 seconds, 100 rpm) inside the CLARIO-Star plate reader again to reduce the presence of any bubbles present which would result in erroneous values. The

increase in fluorescent intensity for each concentration of AABOB are provided below.

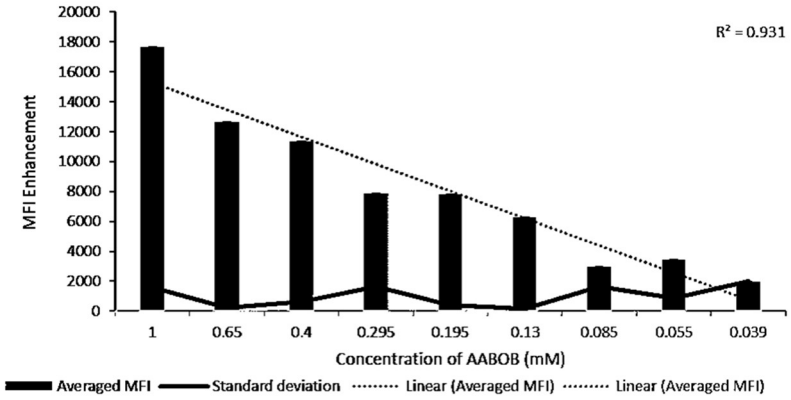


Figure 4-58: MFI (Median fluorescence intensity) enhancement observed for the reaction of ARS (2 µM) with various concentrations of AABOB to form fluorescent adducts at pH 8.

For control purposes, the fluorescent signal at 555 nm emitted by AABOB was measured across a range of concentrations used in the experiment, spanning from 1 mM to 39 µM. Additionally, the fluorescent intensity of ARS at a concentration of 0.01 mM was recorded. These measurements serve as reference points for normalising the data, allowing us to specifically assess the enhancement effect following adduct formation.

A clear enhancement was observed in Figure 4-58, with wells containing higher concentrations of AABOB produced higher signals compared to those with lower concentrations due to a higher proportion of ARS-AABOB adducts forming. The experiment was next to be repeated with the particles functionalised with AABOB receptors to view if an enhancement

could be observed indicating the presence of glycan receptors on the surface.

Into the 96 well plate, 100 µL of functionalised polystyrene nanoparticles were added with 100 µL of ARS. The resulting wells were allowed to react on an orbital shaker overnight. For the controls, ARS and polystyrene nanoparticles were diluted with buffer to produce the same concentration as observed in the reaction. The samples were again measured at 555 nm to produce Table 4-7.

Table 4-7: Tabulated summary for the fluorescent signals of the controls (ARS, AABOB~PS NPs and buffer) along with the normalised enhancement observed for the incubation of ARS with the AABOB functionalised nanoparticles (AABOB~PS NPs) at pH 8. The values reported are an average of three repeats conducted on the same day with the same stocks.

	ARS Dye	AABOB~PS NPs	Buffer	[ARS-AABOB~PS]
Fluorescent intensity (MFI)	67, 731 ± 531	518 ±65	99 ±10	14, 807 ±53

Following the subtraction of controls an enhancement of 14, 807 (MFI) was observed, indicating an adduct between ARS and the nanoparticles had formed. To confirm this, subsequent repeats (n=4) were conducted (

Appendix 9-13) which all provided enhancements >10,000 MFI.

To conclude, an increase in fluorescent intensity was observed for the wells which possessed both the ARS dye and the

polystyrene nanoparticles which had been previously functionalised with AABOB glycan receptors. Thus, indicating the possibility of the AABOB reacting with the cis-diols of the ARS dye (Figure 4-55). Future, experiments should be conducted in the future varying the concentration of the functionalised nanoparticles (AABOB~PS NPs) to view the change in fluorescence. If a clear trend were to be observed for increasing the concentration of nanoparticles in relation to ARS (fixed concentration), it would conclude that the values observed were related to an interaction specifically between the ARS dye and the functionalised particles.

XXV. POLYSTYRENE NANOPARTICLE

SUMMARY

So far, our investigations have revealed that polystyrene nanoparticles can be consistently produced with a narrow polydispersity, as indicated by their PDI value measured by DLS. These nanoparticles are amenable to functionalisation with relevant acrylamide molecules and can actively engage in free radical room temperature reactions, facilitating the incorporation of glycan receptors onto their surface. However, we encountered challenges in effectively introducing new functional groups (such as APBA or AABOB) onto the surface, as it necessitated maintaining the concentration of glycan receptors (APBA or AABOB) in the nM range to ensure long-term stability of the particles. Finding a balance between the density of surface pockets and particle stability may be necessary in future imprinting endeavours.

Moreover, we evaluated the stability of these particles in various buffers and observed minimal changes in their hydrodynamic diameters, indicating their resilience against morphological alterations. The success of incorporating glycan receptors onto the particle surface was assessed by monitoring changes in particle diameter and enhancements observed through fluorescent studies.

Further investigation is needed to confirm the anchoring of the AABOB receptors onto these particles. As previously discussed, additional microscopy images were planned to observe any potential size increase of the particles. Unfortunately, limited access to instrumentation during the COVID-19 pandemic

hindered these efforts. However, the forthcoming chapter aims to evaluate the binding capacity of the nanoparticles bearing the glycan receptors using Isothermal Titration Calorimetry (ITC), which will complement the Dynamic Light Scattering (DLS) and fluorescent data presented in this section.

Subsequent chapters will delve into the synthesis of Benzoboroxole receptors, the development of glycan boronate-esters, and their comprehensive characterisation.

XXVI. CHAPTER SUMMARY

Gold nanoparticles were first considered in this chapter, the nanoparticles were functionalised with thiol ligands which could permit the future use of thiol-ene or EDC-NHS chemistry for imprinting. The particles were studied for their reproducibility and their stability under different pH. It was found that the gold nanoparticles were only stable in a narrow range of pH 5-7. The nanoparticles we need should be stable across a wider range; the particles will be washed in slightly acidic buffers for template removal. This may cause gold nanoparticles to agglomerate, slowly reducing the number of available pockets. Furthermore, the imprinting work to be conducted may have to be done above this pH range (i.e. >>5), typically around 8, to promote the binding for boronate-ester formation, as this pH mimics the conditions found in living organisms and is optimal for the formation of boronate-esters.

Organic nanoparticles, with their broader selection of ligands and promising record in previous ITC studies and saccharide binding analyses, seemed like a viable alternative. We initially considered acrylamide (Aa) nanoparticles. However, their synthesis proved to be a challenge, often resulting in gel formation and non-uniform nanoparticles. These particles were significantly larger than our target PSA glycan, and their tendency to change sizes in different buffers raised concerns about potential distortions in the imprints sought after. These challenges underscored the complexity of our research and the need for a more stable platform.

Given these challenges, it was reasoned that a densely packed polymer would serve as a more stable platform less prone to swelling during the imprinting process, thus ensuring greater consistency.

Polystyrene (PS) nanoparticles emerged as a promising avenue for exploration due to their composition from hydrophobic aromatic monomers. These monomers pack together tightly, forming a hydrophobic core that exhibits minimal swelling compared to other polymer nanoparticles. Synthesised PS particles represented a significant advancement over their polyacrylamide counterparts. Upon surface modification with DHEBA molecules, purification became notably more straightforward, streamlining the process. Moreover, these nanoparticles proved amenable to further functionalisation via free-radical polymerisation reactions, facilitating the introduction of glycan sensing receptors (APBA or AABOB) onto their surface. The successful incorporation of the glycan receptor (AABOB) was confirmed through fluorescence spectroscopy, affirming the suitability of these nanoparticles as a stable core for molecular imprinting.

With the establishment and optimisation of a stable nanoparticle core for molecular imprinting, the subsequent focus shifted towards synthesising the desired glycan boronate-esters intended for imprinting onto the particle surfaces.

CHAPTER FIVE

I. SYNTHESIS OF THE GLYCAN BORONATE ESTER TEMPLATES FOR MOLECULAR IMPRINTING (MI).

This chapter aims to form glycan boronate-esters between sugars and boronic acid type receptors. Such species can form in water naturally as previously described in Covalent synthetic receptors. To enhance the formation of glycan boronate-esters anhydrous organic conditions are to be implemented to encourage the formation of a high order complex (Figure 2-1).

The process of adhering boronic acids to the glycan first prior to MI has its benefits such as restricting conformational changes leading to a reduction in the discrepancies between different MI cavities as previously discussed within Molecular imprinting (MI) on a 2D surface and Molecularly imprinting on a 3D surface.

The glycan receptors for MI were previously established as APBA and AABOB. These were selected for their acrylamide functionality, permitting enhanced control over the addition of the receptors onto the surface via room temperature free radical reactions. Thus, ensuring the produced cavity is accessible for a future binding interaction.[206] These are common issues for MIPs which leads to poor selectivity an affinity. In previously reported MINPs as discussed in the literature review, these possessed fewer boronic acid receptors to form the pockets.

It is hoped if multiple boronic acids are spatially orientated in the pocket a higher selectivity will be obtained than previously observed in literature owing to the reduction in movement of the target structure.

Thus, this chapter contains details on the synthesis of both the AABOB glycan receptor and its corresponding boronate-ester with the desired glycan target. Their characterisation is discussed within.

II. SYNTHESIS OF THE SYNTHETIC BORONATE RECEPTOR

To begin, it was first necessary to synthesise the glycan receptor. Two different acrylamide derivatives were used – 5-acrylamide-2(hydroxmethyl)phenylboronic acid (AABOB) and 3-acrylamide-phenylboronic acid (APBA). Both receptors can participate in free radical polymerisation and interact with sugars.

For this research AABOB was chosen over APBA, due to its increased binding capacity at physiological conditions.[130,151,361] The capacity of the receptor to bind to sugars at physiological conditions is important for the assay to work for the future application – use with clinical samples.

Furthermore, AABOB receptors are commonly used over their boronic acid derivatives (i.e. APBA) owing to their ability to favour pyranose sugars over their furanose tautomer. [62,152,154,284] Pyranose forms are abundant in nature and thus APBA glycan receptors have limited applications.

Whilst the pre-liminary data may entail the use of APBA, the desired MINPs and hence assay will entail the use of these non-commercial benzoboroxole based receptors which are superior.

The AABOB receptor can be synthesised under Schotten-Baumann conditions with an expected yield of 24%. [362,363] The reaction entails the nucleophilic attack of acroyl chloride (Figure 5-1) by amino - benzoboroxole (red), resulting in the formation of a new amide bond. The amide functionality was

chosen for these receptors to reduce the pKa of the boronic moiety.[148] In addition to providing a robust linker to attach onto the nanoparticles surface via radical polymerisation reactions, which are advantageous due to their fast reaction times (typically less than 10 minutes).[328].

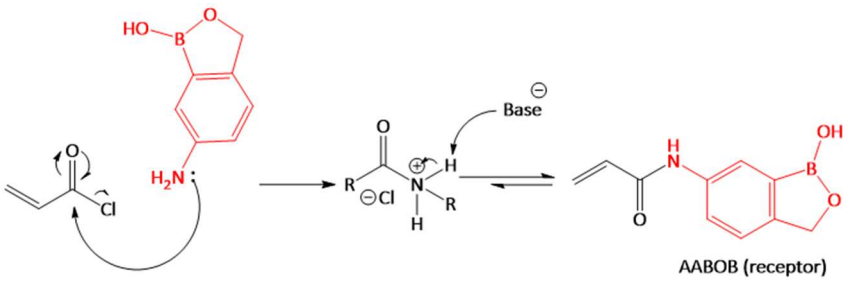


Figure 5-1: Mechanistic overview for the acylation of 5-amino-2(hydroxmethyl)phenylboronic acid (amino benzoboroxole) to form the desired acrylamido-benzoboroxole receptor (AABOB).

Briefly, 5-amino-2(hydroxmethyl)phenylboronic acid was placed into H_2O and THF and sonicated until completely dissolved. Upon dissolution, the reaction mixture was placed in an ice bath for preparation of the exothermic acylation reaction. Finally, acroyl chloride and sodium carbonate were added slowly and left to react stirring at room temperature for 4 hours. For full experimental protocol refer to: ***Synthesis of 5-acrylamide-2(hydroxmethyl)phenylboronic acid (AABOB).***

To assess the extent of reaction completion a TLC (Thin layer chromatography) was developed (DCM/MeOH) and viewed under UV light for spot identification (Figure 5-2).

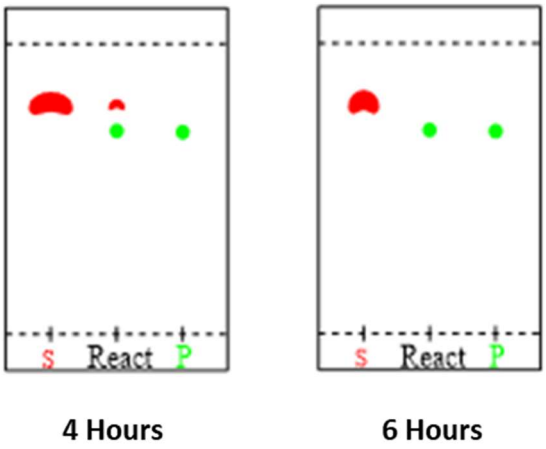


Figure 5-2: Illustration of the developed TLC plates (DCM/MeOH) developed (UV & $KMnO_4$) during the synthesis of AABOB for 4 and 6 hours respectively. To facilitate comparison 5-amino-2(hydroxmethyl)phenylboronic acid (S), the reaction mixture (React, at hour 4 or 6) and the desired product AABOB (P) were spotted and labelled accordingly above.

At hour 4, the reaction mixture (React, Figure 5-2 showed the presence of some starting material (S) still. As a result, the reaction was left to react until all traces of the starting material had reacted by TLC.

The crude mixture was reduced under vacuum to remove H_2O/THF to form a white crude solid. A hot dual solvent recrystallisation (H_2O/MeOH) was attempted to precipitate out the expected AABOB receptor slowly overnight. Upon the solution cooling down, and MeOH traces evaporating, it was expected that the AABOB receptor would precipitate out. However, very few precipitates (18%) were observed, due to the

ineffectiveness of this method, it was decided to change the work up process to maximise the yield further.

The final TLC showed the absence of 5-amino-2(hydroxymethyl)phenylboronic acid (React, Figure 5-2***)*** at hour 6 therefore the solution was reduced under vacuum, to isolate the product. The removal of methanol yielded the product in water. The work up on the crude product entailed the extraction from ethyl acetate. The extraction of the organic phase was repeated until the aqueous phase no longer had an orange hue. The resulting organic layers were collected and further washed several times in brine. The brine washes had two roles – to remove excess water molecules from the organic phase and to reduce the water solubility of the product. Therefore, the use of brine should maximise the yield.

The collected organic phases were dried over magnesium sulphate, before removing solvent under vacuum. The resulting yield was 64%, a significant improvement over the original 18% yield and previous literature (24%).[363] The isolated white solid was analysed via NMR (Figure 5-3) and MS (Figure 5-4). For information on these methods refer to ***Chapter Three*****.**

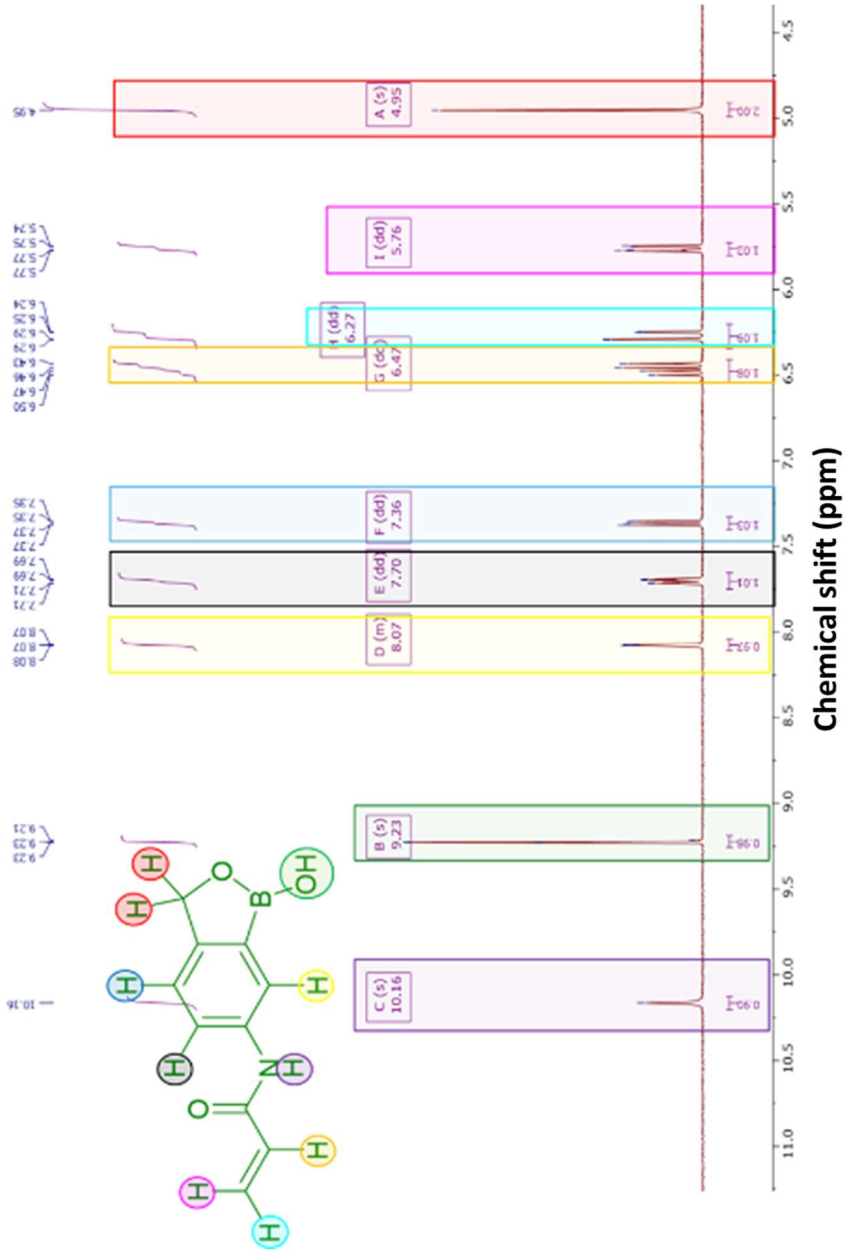


Figure 5-3: 1H NMR (400 MHz, DMSO) with the peak assignments for the synthesised 5-acrylamido-2-(hydroxymethyl)phenylboronic acid cyclic monoester (AABOB) receptor.

The observed NMR peaks are congruent with previously reported spectra.[363] For a comprehensive list of the assigned NMR signals, refer to Synthesis of 5-acrylamide-

2(hydroxmethyl)phenylboronic acid (AABOB). For ease, the corresponding peaks, and the functional groups responsible for these signals are clearly labelled. The 2D COSY 1H NMR used to aid assignments of the 1D 1H NMR is provided in Appendix 9-14.

MS was also conducted on a pure white solid to complement the structural analysis conducted via NMR. MS provides information on the masses of ions produced during ionisation. The corresponding TOF-MS spectra are displayed below - Figure 5-4. Christopher Williams, the mass spectroscopy officer at the School of Chemistry, performed the time-of-flight mass spectrometry (TOF MS) instrumentation running. I conducted the corresponding peak analysis and identification.

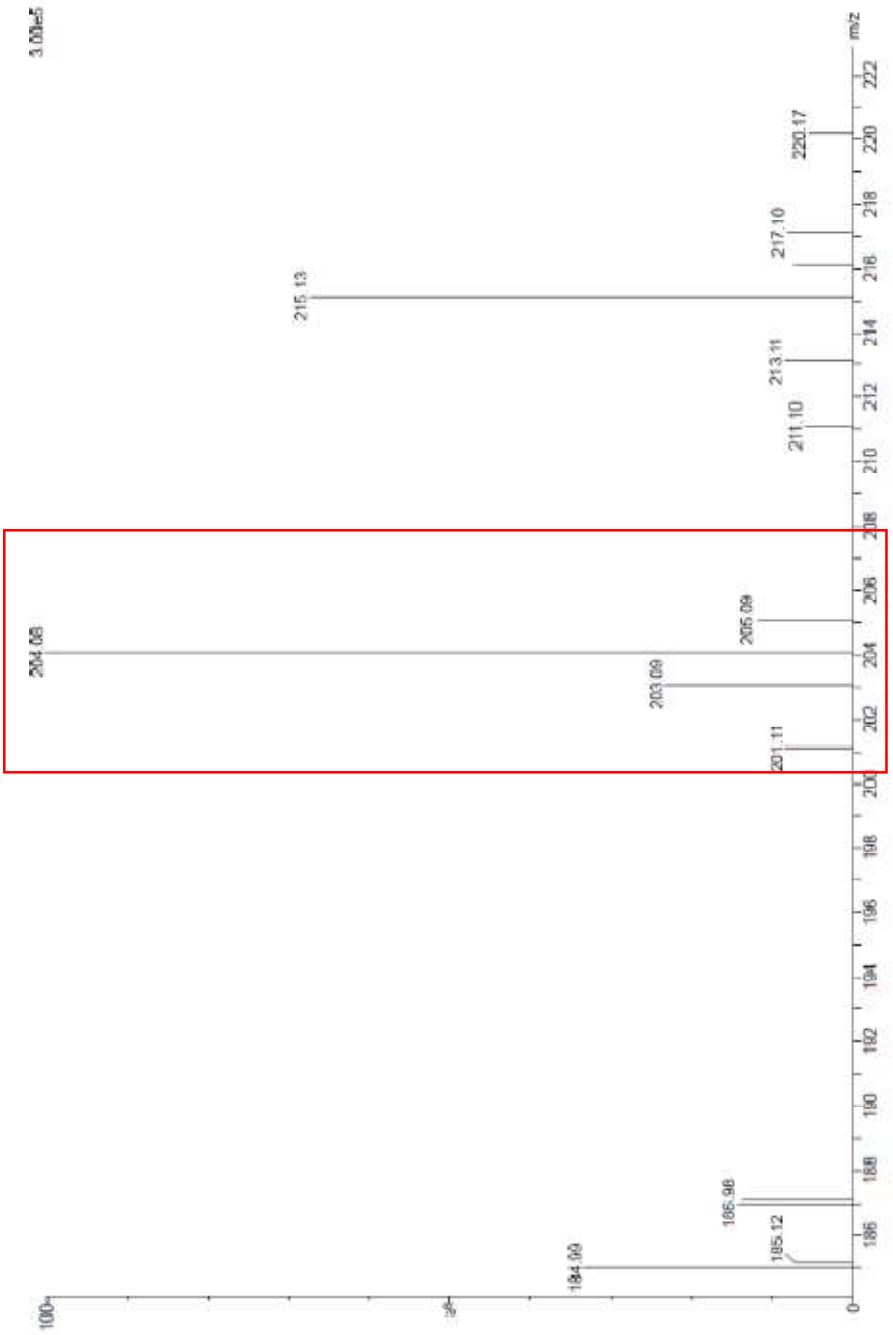


Figure 5-4: TOF MS spectra produced from the pure white solid (64%) from the Schotten-Baumann reaction. The cluster of peaks highlighted in red centred around 204 m/z is believed to be due to the AABOB receptor.

Subsequently, Chris provided all TOF MS spectra obtained in this section (Table 0-1).The MS spectra revealed peaks of the following m/z values: 204.08 and 203.08. The peak at 204.08 corresponds to the [AABOB + H] adduct and the adjacent peak at 203.08 corresponds to the exact mass of the AABOB receptor.

In the full TOF (Appendix 9-15) spectra ranging from 200 – 1900 m/z other peaks were also identified. Other clusters at higher m/z values may have arisen from the dimer formation of two AABOB units. The ion located at 610.19 m/z unit was believed to be due to the formation of these trimer species – thus confirming the likely hood of the presence of the AABOB. The structures corresponding to the ions 204.08, 203.08 and 610.19 m/z are presented below in Figure 5-5. The formation of dehydrated products, solvent adducts, and dimer and trimer molecules are commonly observed for boronic acid type molecules which can often complicate the characterisation of these molecules. [364–366]

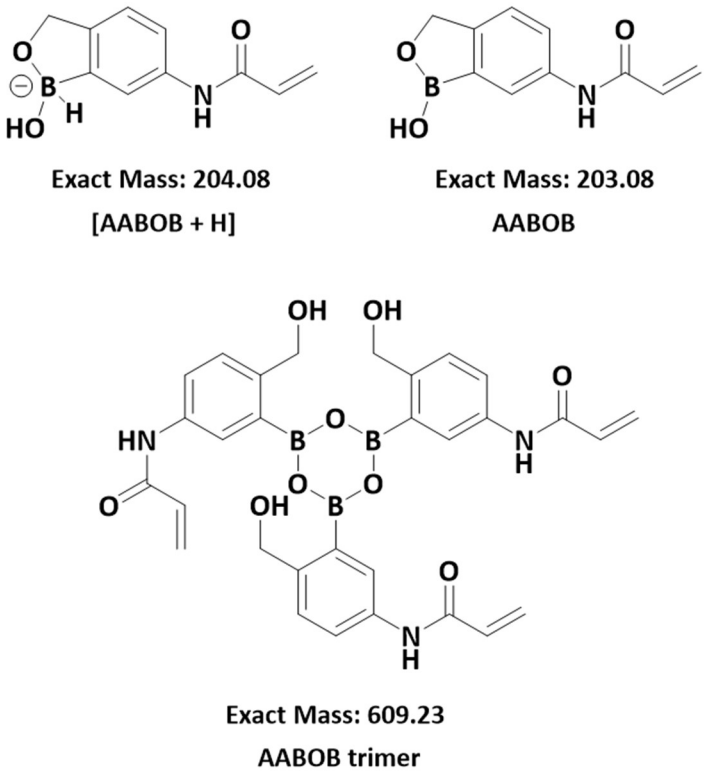


Figure 5-5: Structures of molecules detected by MS and their corresponding exact masses.

Therefore, the NMR and the MS spectra combined confirm that the receptor was produced. Thus, the required template for MI will next be discussed.

III. NMR STUDY OF BORONATE-ESTER FORMATION

After successfully synthesising (Synthesis of 5-acrylamide-2(hydroxmethyl)phenylboronic acid (AABOB)) and characterizing the benzoboroxole (AABOB, Figure 5-5) receptor, the next step was to form glycan boronate esters (Figure 2-1). To begin this process, a simple sugar was carefully selected, and its changes were studied through NMR to observe if binding had occurred. APBA and AABOB can bind sugars similarly, so commercially available APBA was used for a quick proof-of-concept NMR study. For this study, solutions containing APBA (5 mM), fructose (10 mM), and a mixture of both (APBA 5 mM + Fructose 10 mM) were prepared in a buffer under aqueous conditions. This study was conducted in a buffer with the sugar in excess in comparison to the glycan receptor since future nanoparticle interactions via ITC will also be studied in buffers with the sugar in excess. The corresponding ^{1}H NMR spectra produced for each of the three experiments were stacked for comparison of the aromatic region occurring between 5.6 – 8 ppm (Figure 5-6).

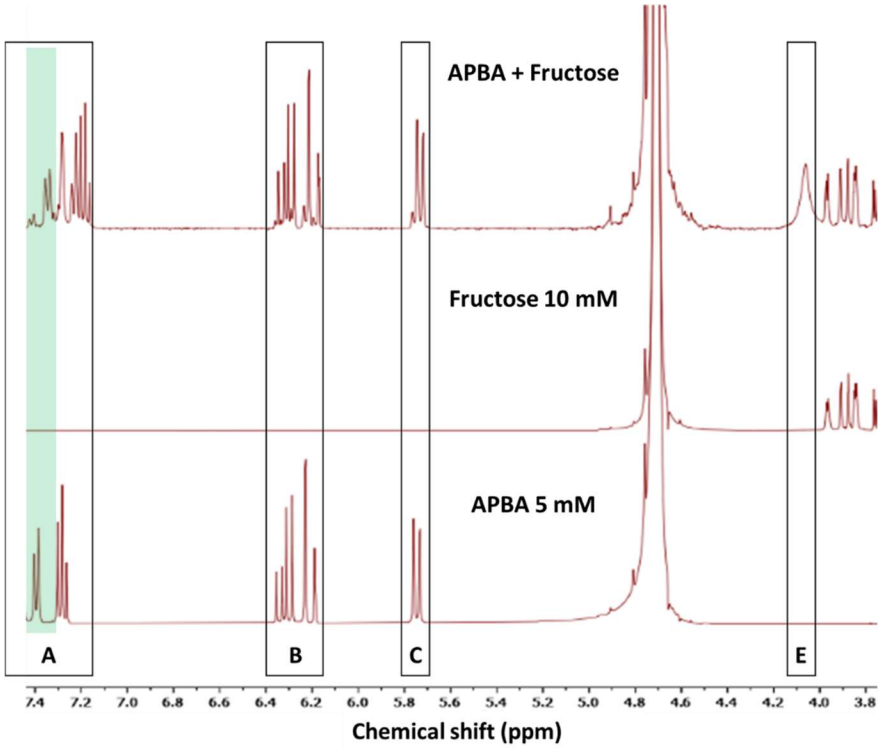


Figure 5-6: ^{1}H NMR for the reaction of phenylboronic acid (APBA, 5 mM)) and fructose (10 mM) stacked against the spectra of phenylboronic acid (APBA) alone and fructose alone. Regions displaying changes in peak splitting, peak shifts or the emergence of new peaks are clearly outlined via A-E.

The reaction mixture (APBA + Fructose) was analysed by ^{1}H NMR and the corresponding spectra is displayed above. The NMR showed four regions of change which are highlighted by A – E in Figure 5-6.

Region A which is situated between 7 – 7.4 ppm corresponds to the protons on the benzene ring of APBA. In region A there was a clear change in the peak multiplicity corresponding to the protons chemical environment changing. It was observed that some of the APBA peaks were lower in intensity in the NMR

spectra of the reaction mixture in comparison to the NMR of the glycan receptor alone. This corresponds to the substance being used up and diminishing in concentration due to the formation of a new product. This phenomenon is occurring in region A as highlighted in green.

If a reaction were occurring between the glycan receptor and the sugar, one would also expect changes to occur within the sugar protons chemical environment and hence the observed NMR peaks. This was observed in the spectra also, region E (3 – 4 ppm) highlights the emergence of new additional peaks which are broad and poorly resolved at higher chemical shifts. The peak broadening of the sugar peaks is commonly reported in literature upon binding with boronic acids to form the boronate-ester. [344,361]

When conducting future NMR binding studies between glycan receptors (i.e. APBA and AABOB) and molecules containing cis diols the described above changes provide a basis for comparison.

Next, attention was turned to the polymeric nanoparticle system and its intended glycan target. The nanoparticles previously synthesised (Synthesis of water-soluble polystyrene nanoparticles) are known to possess a molecule with hydroxyl groups – DHEBA. The structure of the DHEBA cross-linker used for the polystyrene particles is provided below - Figure 5-7.

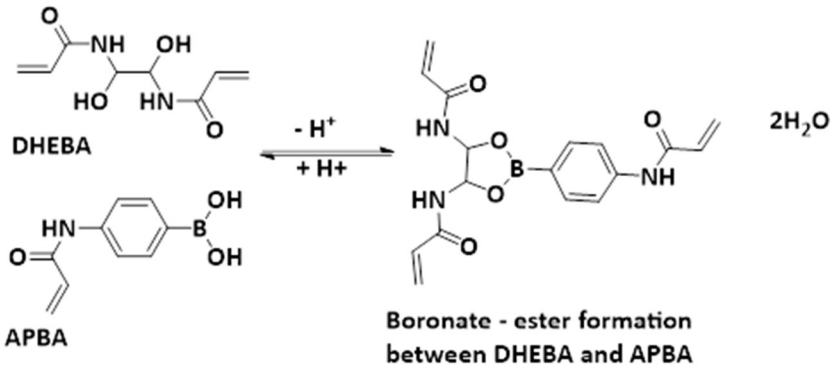


Figure 5-7: Schematic for the non-specific interaction that may occur on the nanoparticles surface if the orientation permits between the crosslinker (DHEBA) and a boronic acid receptor such as APBA.

The hydroxyl groups of DHEBA are depicted in a trans conformation however, in solution these are free to rotate about the carbon to form a cis-diol motif. Therefore, during these imprinting reactions there may be diols present on the nanoparticles surface which are not the template of interest. It is therefore necessary to view if there are any potential interactions between the DHEBA and APBA (or AABOB) receptors (Figure 5-7). If a binding interaction were to take place (Figure 5-7), it may inhibit the reaction between the sugar template and the boronic receptors on the nanoparticles surface. To study if such an interaction is possible an NMR was conducted under aqueous conditions. If no binding was present here, it is with confidence that no binding will take place on a nanoparticles surface where steric constraints occur.

The preliminary NMR study between fructose and the APBA receptor previously discussed (Figure 5-6) may serve as a basis for comparison. If DHEBA was to interact, the resulting proton signals in the ^{1}H NMR would be expected to broaden, shift, or

change in multiplicity as previously observed. As previously conducted for fructose, DHEBA was also deliberately used in excess. This is to represent a real scenario on the nanoparticles surface whereby the DHEBA cross-linker will be present all over the surface. In comparison, the glycan receptors (APBA or AABOB) are expected to be significantly lower in concentration on the surface of the nanoparticles owing to the formation of one or two pockets per particles. Therefore, for these NMR studies the concentration of the glycan receptor was >> the DHEBA concentration. The following solutions were made for the ^{1}H NMRs: APBA (5 mM), DHEBA (10 mM), and reaction mixture of APBA (5 mM) + DHEBA (10 mM) The corresponding stacked ^{1}H NMR spectra is illustrated in: Figure 5-8.

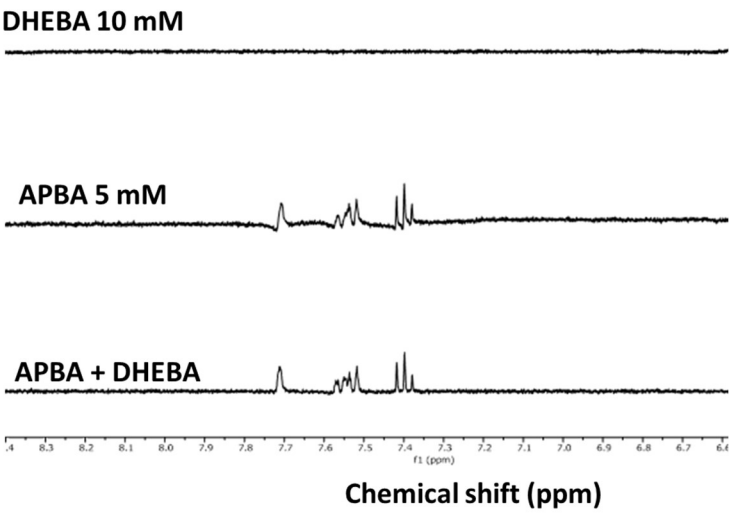


Figure 5-8: Stacked ^{1}H NMR (400 MHz, D_2O) spectrums to observe any interactions between the DHEBA cross-linker (10 mM) and the APBA glycan receptor (5 mM). The aromatic peaks of APBA display no clear changes in the presence of DHEBA.

Previously, for the interaction between fructose and APBA displayed significant differences in the aromatic protons' peaks (Figure 5-6). Therefore, this region was inspected first as highlighted in Figure 5-8 for DHEBA and APBA.

The aromatic proton peaks (Figure 5-8) displayed no new peaks, nor any peak shifts following the addition of DHEBA. Furthermore, there was no diminishing of intensity of the aromatic peaks of APBA in the presence of DHEBA for this reaction.

The lack of change in the ^{1}H NMR suggested that there was no appreciable binding nor non-specific interactions between the APBA receptor and the DHEBA molecule under physiological conditions. Thus, when DHEBA is present on a 3D nanoparticles

surface, it is believed to be unlikely for any significant interference to occur. Considering steric constraints will also be present on the surface also which further may hinder these processes.

To conclude, when aromatic boronic receptors form boronate-esters with available cis-diols the ^{1}H NMR shows visible changes for the aromatic protons of the boron receptor and the sugar protons. The aromatic protons of the boron receptor diminish in intensity as the new aromatic peaks form with greater intensity. This was observed in the case of incubation of fructose with APBA but not for DHEBA and APBA. Therefore, the next step was to synthesise the desired boronate ester complex ready for MI onto the DHEBA functionalised nanoparticles.

IV. SYNTHESIS OF BORONATE-ESTERS WITH NEUTRAL SUGARS

The next task was to prove the same interactions occur with larger saccharides. In this case, the synthesis (Figure 5-9) of the complex took inspiration from previously reported literature.[203,344,367,368] The formation of boronate-esters exists in equilibrium with their corresponding diols and boronic acid derivative as illustrated below. Therefore, to maximise the formation of the boronate-ester and manipulate the position of equilibrium to tend towards the product removal of the produced water from the reaction is required. To facilitate this, anhydrous solvents were used along with activated molecular sieves.

Briefly, the anhydrous solvents were first placed into a glass vial containing activated molecular sieves under inert conditions to remove any traces of moisture. Whilst the solvents were drying in the sieves the sugar (1 Eq) was weighed into a small glass vial along with the boronic acid receptor of choice (32 Eq). to which fresh molecular sieves were added and the glass vial was sealed and flushed with nitrogen. The dried dioxane and acetonitrile are then added to the vial under inert conditions and heated to 90 degrees whilst stirring. The reaction was left for 24 hours to form the boronate-ester complex.

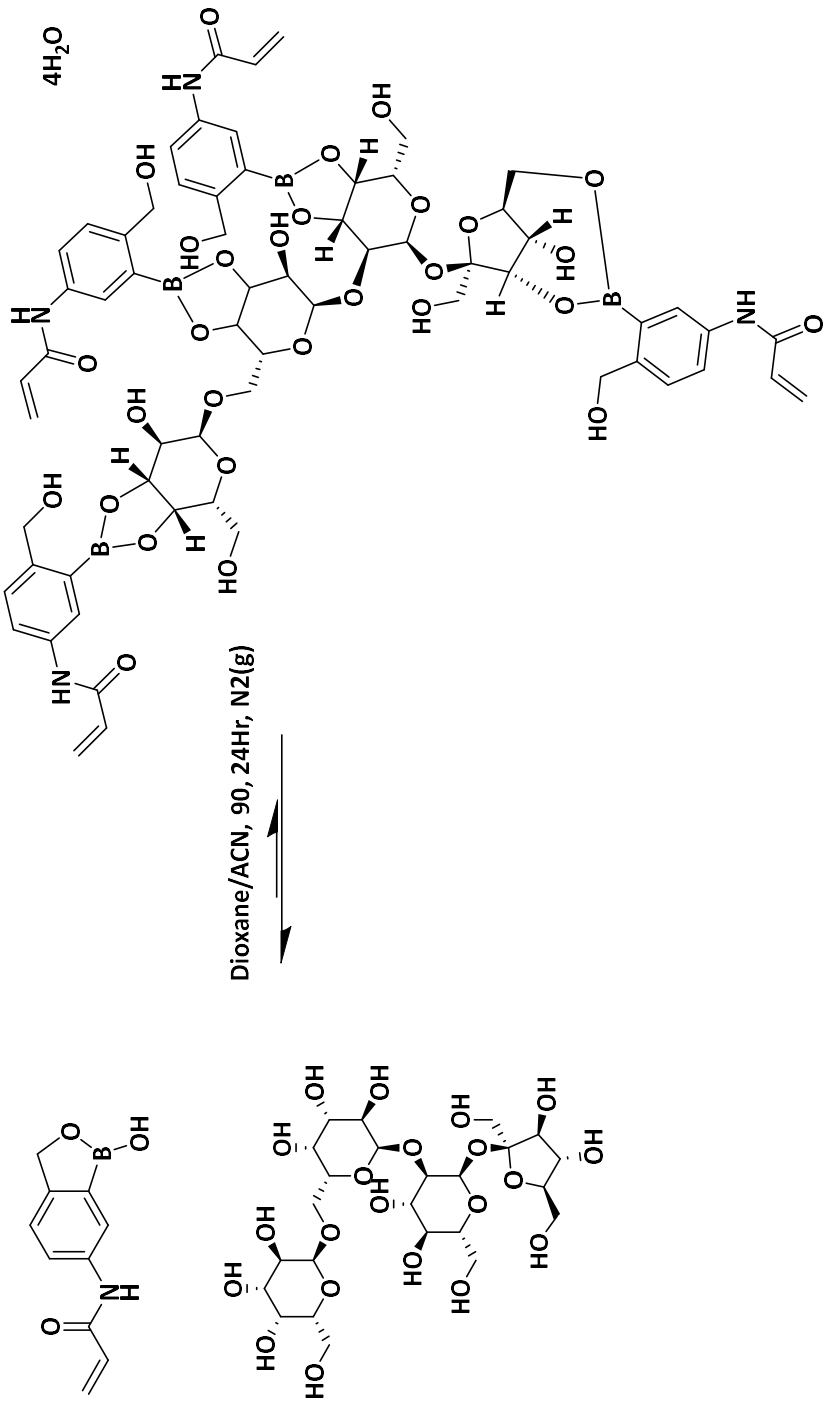


Figure 5-9: Synthesis of the boronate-ester complex for molecular imprinting under anhydrous conditions in the presence of activated molecular sieves to remove the 4 equivalents of water produced.

Boronate-esters formed with sugars have increased stability in anhydrous aprotic solvents and thus these were chosen over aqueous conditions.[369] Following 24 hours, the reaction was allowed to cool, and the solvent was removed under vacuum to yield a crude solid pale white solid as shown below.

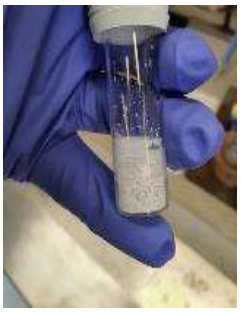


Figure 5-10: White precipitate collected from the formation of the boronate ester complex (5.7 mg, 81%) between Stachyose (1 Eq) and AABOB (32 Eq).

The resulting crude solid was dissolved in the minimum amount of acetonitrile to afford the product as a white precipitate. The white precipitate was collected, and the supernatant was subjected to another two rounds of centrifugation. The resulting solids were combined and dried under vacuum until further use. The full experimental protocol is provided in: Preparation of the glycan-boronate complex. TLC and flash chromatography of the boronate-ester formed was not conducted for this reaction. This is due to the unstable nature of boronate-esters. [369]

The supernatants from the centrifugation were also combined and reduced under vacuum for ^{1}H NMR analysis (Figure 5-11) to check for signs of the boronate-ester ensuring no product was

lost during the work-up procedure. The corresponding NMR is provided below.

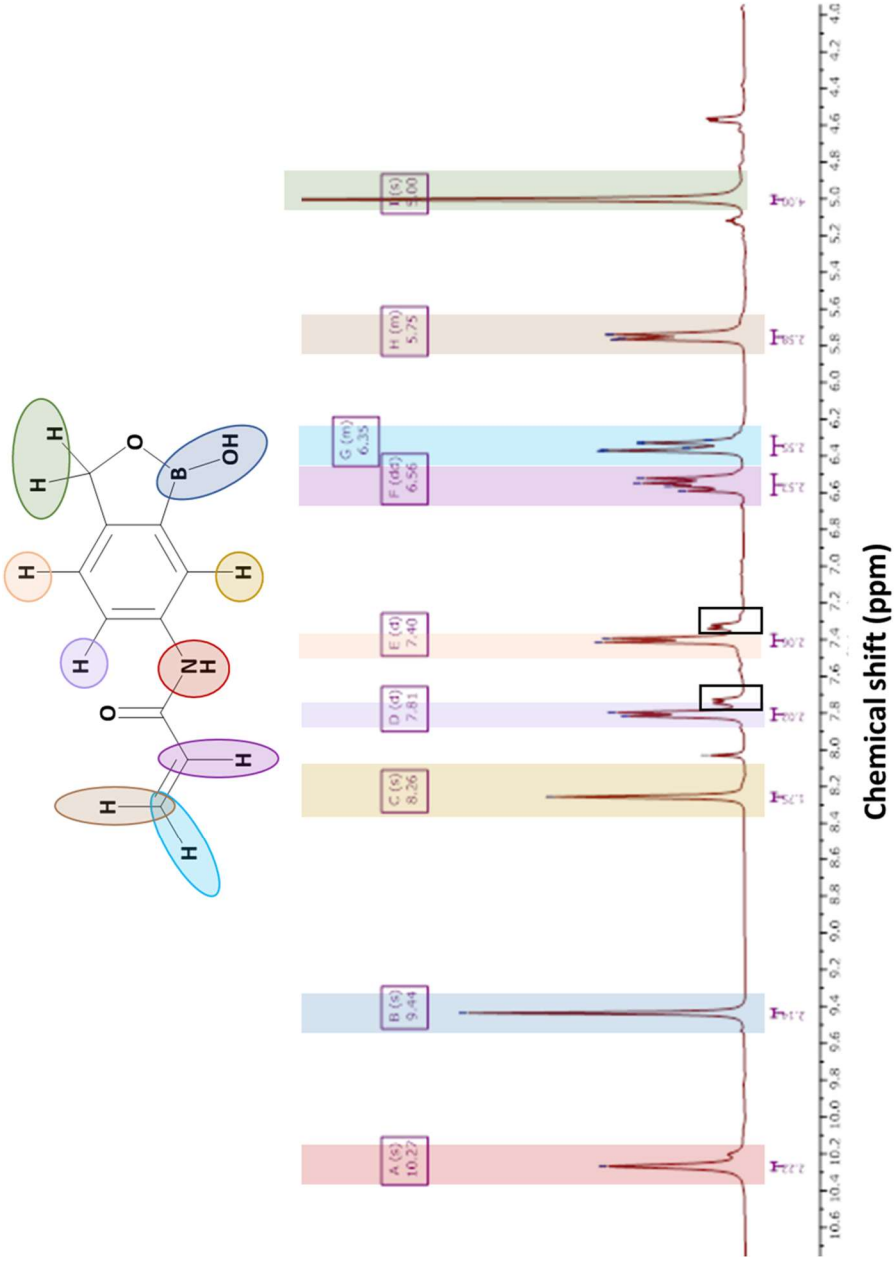


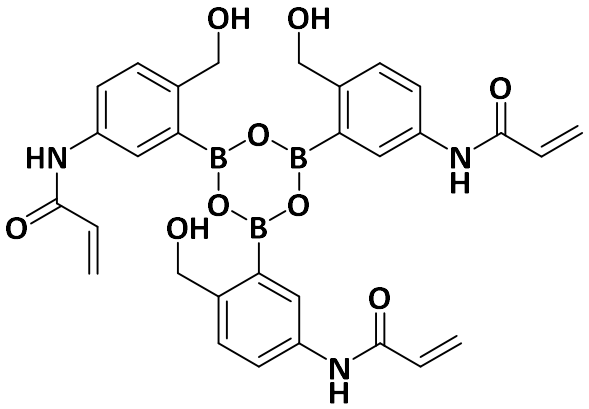
Figure 5-11: ^{1}H NMR (400 MHz, DMF) spectra of the supernatant collected from the work up procedure of the boronate-ester. The peaks obtained possessed the correct integration and peak multiplicity for the AABOB receptor.

The NMR displayed peaks analogous to that previously observed for the AABOB receptor previously synthesised (Figure 5-3). Subtle difference in the spectra previously discussed and the supernatant (Figure 5-11) were observed. Of most significance are the B-OH (peak A) and N-H (peak B) singlet peaks observed in the spectra for the collected supernatant from the reaction at 10.27 and 9.44 ppm respectively.[366] These peaks were not previously present in the NMR of AABOB (Figure 5-11) owing to the nature of DMSO solvent used which causes proton exchange to occur.

Furthermore, for the above supernatant NMR additional peaks were observed as highlighted in black boxes. These smaller peaks are situated downfield from the doublets at 7.81 (peak D) and 7.40 (peak E) ppm and correspond to the formation of a trimer in solution due to high receptor (Figure 5-12) concentration. This is due to the nature of phenylboronic acid derivatives to go undergo reversible condensation reactions in the presence of diols or other nucleophilic functional groups (i.e. the presence of another AABOB receptor).[365,366] Since the reaction entailed the use of 32 Eq of the AABOB receptor the likelihood of another receptor encountering another in solution and undergoing self-condensation are highly probable. The propensity of these receptors to form trimers and dimers will need to be controlled in the future MI works. The formation of these anhydride structures was previously observed in the TOF MS spectra of the pure AABOB receptor following its synthesis.

The ^{1}H NMR of the supernatant did not contain any other additional new peaks. Therefore, it was concluded based on NMR that there was no complexation present. Thus, most of the

boronate-ester complex was assumed to have been collected as a pellet during the centrifugation washing.



Exact Mass: 609.23
AABOB trimer

Figure 5-12: Trimer of AABOB which forms at high concentrations of the AABOB in solution, previously observed in the MS spectra.

To conclude, from the NMR spectra of the supernatant there was an indication that the work-up was successful in removing most of the excess of the 32 Eq of the AABOB receptor used in the synthesis. To confirm the presence of the boronate-ester further analysis was performed on the isolated white solid. The NMR of the white solid was not conducted due to the low concentrations of stachyose present in the reaction making it not feasible (< mmol) in addition to the expected many overlapping peaks making peak multiplicity and integration not feasible.

Structural analysis was next conducted to view how many receptors had bound to the tetra-saccharide stachyose. It was expected that there would be more than one boronate-ester complex had formed. In total there are more than 4 structures

which may have formed from the reaction. However, for the purpose of this thesis we will only discuss the major forms which are provided below (Figure 5-13) [203]

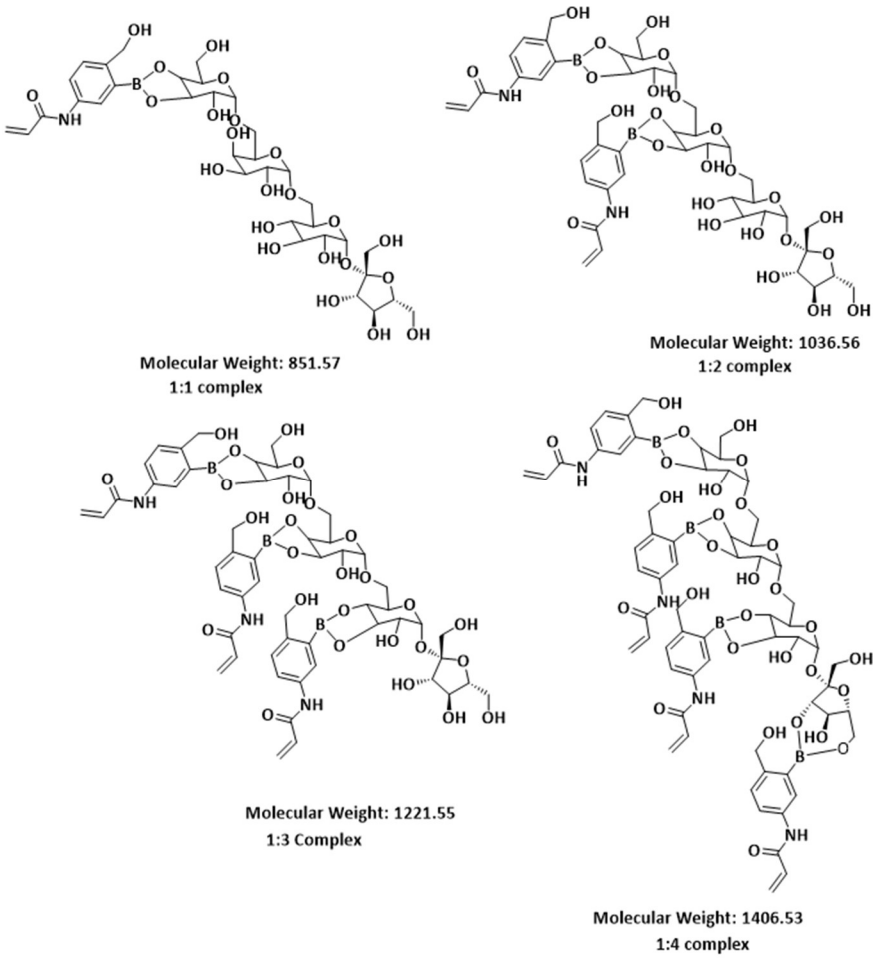


Figure 5-13: Boronate-esters of interest formed from the interaction of stachyose with the AABOB receptor under anhydrous conditions.

Thus, due to the multiple species present direct injection into MS was not ideal for structure determination. Preferably a method that first separates the components before MS was desired. LC-MS was chosen to analyse the boronate-esters formed (Figure 5-13). The use of a hydrophobic c-18 column was selected, to try to reduce the loss of product due to strong interactions with the stationary phase. Polar columns should be avoided for the boronate-esters owing to the strong interactions which result the loss and degradation of the desired product 7 8. Furthermore, LC-MS only needs small quantities present in solution to separate and identify individual components by MS which makes it advantageous for these reactions which are of the mg scale.

Previous literature reported the use of LC-MS with a C18 column and acetonitrile and a buffer to isolate a mixture of 7 closely related boronic acid functionalised molecules.[364] Therefore, this served as a starting point for the instrument method. However, the use of aqueous buffers resulted in poorly resolved broad peaks in the chromatograms. This was thought to be due to the boronate-esters degrading in solution due to the large presence of water. Alternative gradients were also trialled such as a methanol and acetonitrile gradient (MeOH/ACN:H_2O gradient). However, no ions corresponding to one of the four major complexes (Figure 5-13) were observed for this method (Appendix 9-16).

Alternative, columns such as the Restek biphenyl column and alternative solvent systems without water were carried out also. The biphenyl columns are known to be better for aromatic groups such as the AABOB receptors used during the synthesis.

When the biphenyl column is used with organic solvents such as acetonitrile it is known to behave alike a C18 column providing similar separation. However, all attempts to produce a well resolved LC chromatogram accompanied with a clear MS spectra failed highlighting the challenges of isolation and detection of boronate-esters. It was concluded, isolation of single species via flash chromatography or high-performance chromatography was not feasible.

Identification of the product was necessary to advance, so TOF-MS with different ionisation techniques were trialled. ASAP was considered due to the LC-MS highlighting the obtained white solid had some solubility issues. ASAP overcomes this as this method can be used on a solid.

Alongside ASAP ionisation, ES was also conducted for direct injection MS. Both positive and negative mode (Appendix 9-17, Appendix 9-18 & Appendix 9-19). The positive ionisation mode was observed to produce better peaks corresponding to the expected masses for both ES and ASAP. Furthermore, it was discovered that ES + worked the best for these compounds when they could be solubilised (ACN/MeOH or isopropyl alcohol (IPA)/NH_3). The TOF MS ES displayed a high proportion of the starting material AABOB (Figure 5-14) suggesting no boronate-ester complex was found.

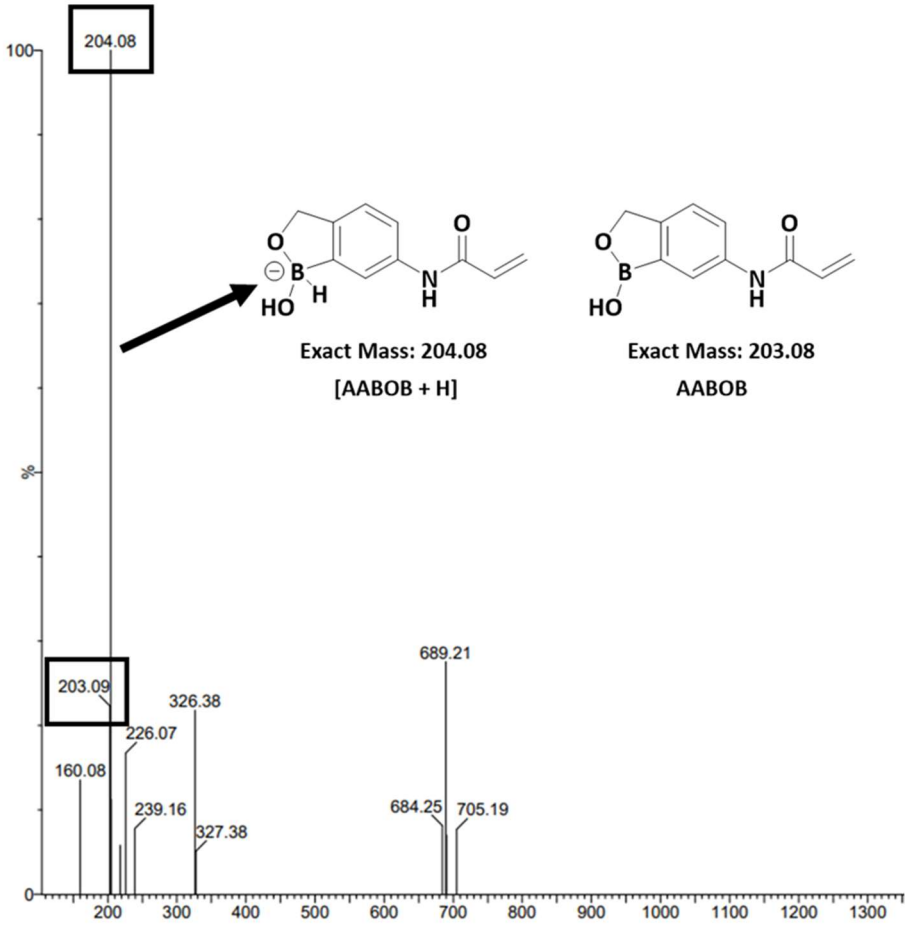


Figure 5-14: TOF MS ES + spectra produced for the white solid from the boronate-ester complex formation. No borate-ester ion could be found with significant intensity. The highest intensity cluster of peaks belonged to the receptor.

However, upon further inspection at around 1000-2000 m/z units' masses can be observed which correspond to boronate-ester complexation. However, the intensity of these peaks is not significant. This observation makes it hard to conclude if the ester formed appreciably. There are numerous possibilities: the ester did form to an appreciable extent but decomposed, the ester did not form to an appreciable extent or the glycan-boronate ester did not ionise well under these conditions

applied. It is believed that the boronate-ester did form but, the presence of smaller ions dominated the spectra due to their short flight times, the use of ES ionisation also inherently biases the formation of hydrophobic ions, thus the glycan-based structures are harder to ionise. Finally, the scan range used was extremely broad, resulting in reduced sensitivity.[370] A combination of these reasons was thought to have contributed to the lack of ions observed by MS corresponding to the boronate ester.

To conclude, it was discovered isolation of these species via chromatography methods such as TLC, LC-MS and flash chromatography are not feasible due to the dynamic nature of the ester. The isolation of specific single boronate-esters thus was not further trialled. Instead TOF MS was conducted with different solvents and ionisation modes to view if any boronate-esters had formed to a significant extent. However, the results were inconclusive with the AABOB dominating the spectra. Closer inspection to the 1000-2000 region by filtering for ions of the desired mass displayed low intensity peaks corresponding to the presence of boronate-esters Therefore, greater evidence is required to advance.

V. INDIRECT ANALYSIS OF BORONATE-ESTER FORMATION VIA MS METHODS.

It was decided to move onto an alternative methodology to analyse the formed products, which is outlined in Figure 5-15.The method entails the formation benzoylated sugars to yield information indirectly on where AABOB receptors were previously bound. The functionalisation of glycan structures is commonly conducted to "tag" glycans with additional groups, commonly hydrophobic moieties to ease the analysis via MS which is a challenge for these hydrophilic molecules. [203,370]

The newly synthesised benzoyl esters should be more stable than the reversible boronate esters formed with the sugars. The benzoyl esters should not degrade in water, which eradicates the previous concerns. Therefore, LC-MS and MS may be easier to conduct on the protected sugars to infer where the AABOB receptors were originally bound.

Briefly, stachyose and the AABOB receptor were placed in a vial with 1,4-dioxane and acetonitrile as previously described and left to react under anhydrous inert conditions at 90 degrees for 24 hours. Prior to the benzoylation the complexation solvents were first removed under vacuum to yield a white solid and some precipitation present from the molecular sieves. To the crude solid pyridine (0.5 mL) was added and the resulting mixture was placed in an ice bath to cool to zero degrees. Upon cooling, an excess of benzoyl chloride was added. The reaction was removed from the ice bath and left to react at room temperature for a further five hours (Preparation of the glycan-boronate complex).

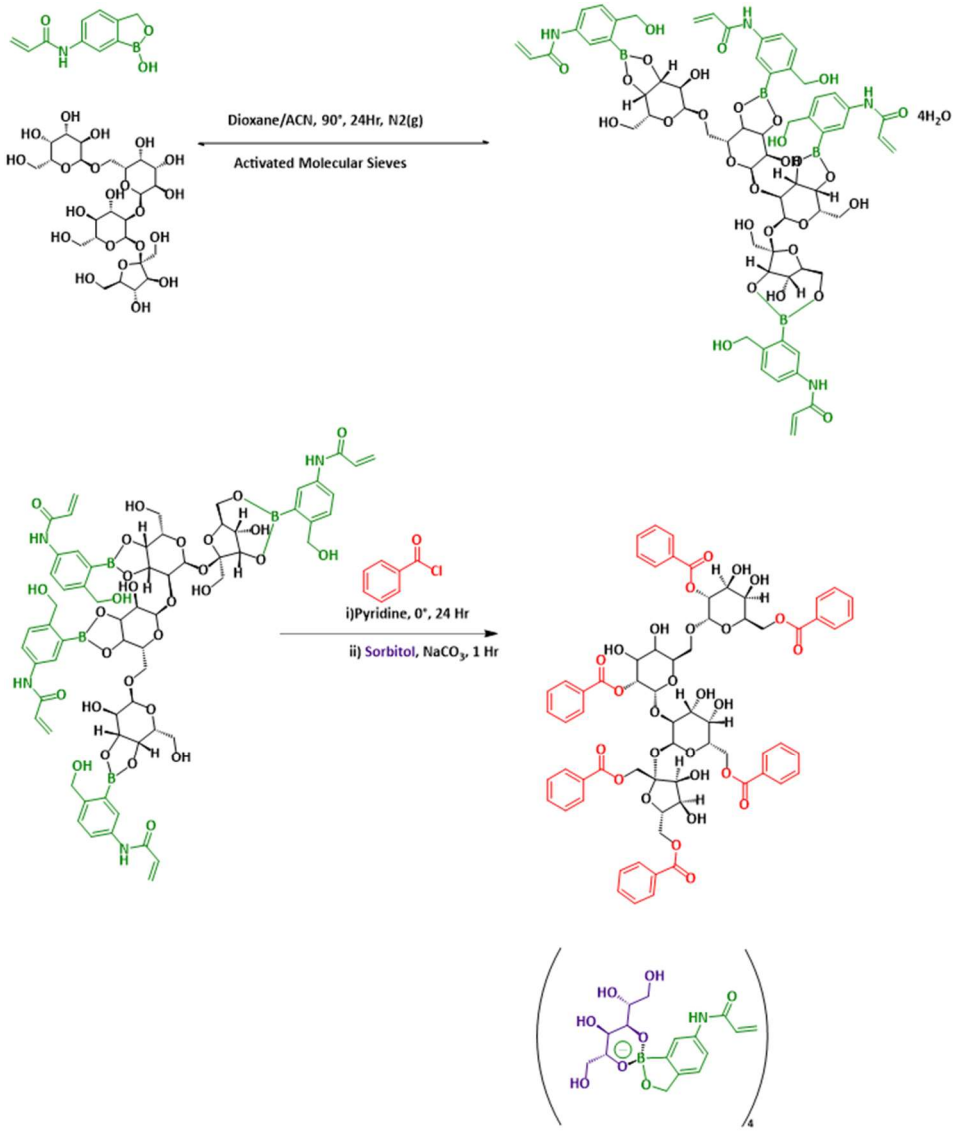


Figure 5-15: Synthesis of the boronate-ester followed by the protection of unreacted hydroxyl sugar groups by benzoyl chloride. Analysis of the benzoylated sugar provides information on the original formed boronate-ester indirectly.

Following the benzoylation, filtration of the compound was necessary to remove the molecular sieves precipitate formed earlier and any other solid impurities present. Celite and toluene were used to conduct the filtration and removal of excess pyridine. Toluene was then removed under vacuum to yield a crude yellow oil. To remove the excess AABOB receptors the yellow oil was dissolved in a saturated sorbitol mixture and left to stir at room temperature for 1 hour. The resulting solution of unbound receptor and the benzoylated stachyose required separating next via extraction. The organic product was collected in ethyl acetate and the undesired side products were isolated in the aqueous layer. For a full experimental protocol refer to Benzoylation of the complex sugar. The resulting benzoylated sugar was obtained as a yellow oil as displayed below.

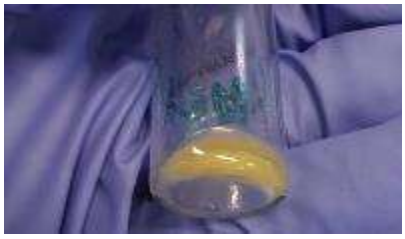


Figure 5-16: Yellow oil obtained for benzoylated stachyose species.

The crude yellow oil (Figure 5-16) was first inspected via ^{1}H NMR (Figure 5-17), as previously conducted for the formation of boronate-esters with fructose and DHEBA (Figure 5-6).

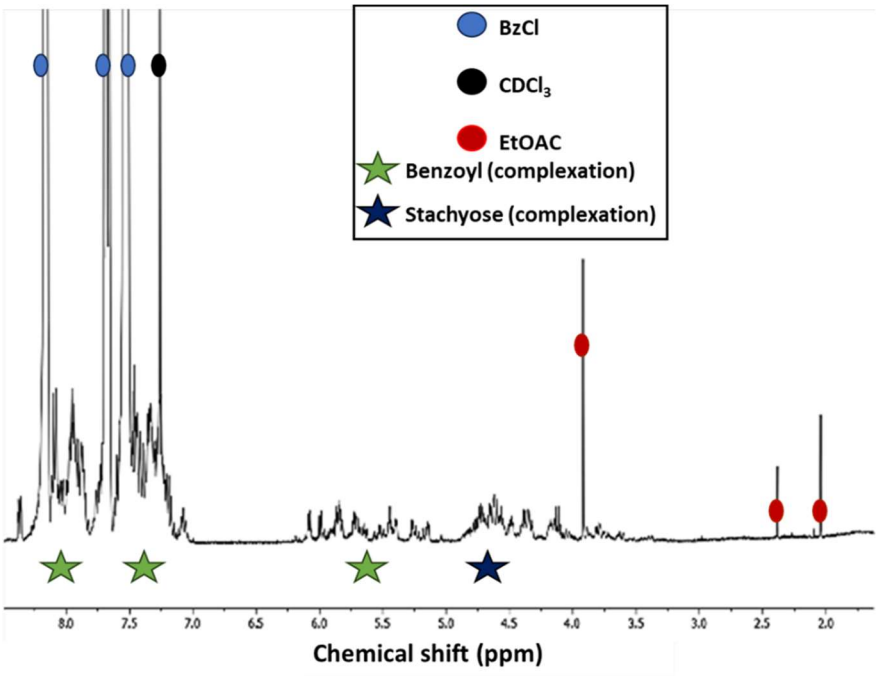


Figure 5-17: ^{1}H NMR (400 MHz, $CDCl_3$) of the crude yellow oil extracted from the organic phase.

The NMR (Figure 5-17) showed a large presence of benzoyl chloride around 7- 8 ppm. In addition, overlaying were peaks of smaller intensity in the same region which are believed to be due to the complexation of the benzoyl groups to the hydroxyl groups of stachyose. As previously discussed earlier, the esterification with saccharides leads to peak broadening in the aromatic region either due to slow exchange times which cannot be resolved by standard ^{1}H NMR or due to the formation of many different complexes formed. [361]. Therefore, no integration, multiplicity and hence J values could be determined due to the vast array of compounds present in solution.

In addition, there was evidence that stachyose was present in solution due to the many overlapping peaks (4 – 5 ppm). which were shifted downfield from the expected sugar peak region.[151] All other solvent peaks were labelled and identified. [371]

The NMR suggested the benzoylation of stachyose has gone to completion. Next, suitable conditions for column chromatography were needed to purify the different esters that had formed in solution. It is expected that there will be traces of unreacted stachyose and possible some AABOB receptor which was not removed during the extraction. Therefore, flash chromatography is necessary. The presence of smaller hydrophobic molecules such as benzoyl chloride (BzCl) and AABOB may hinder the MS analysis due to being preferentially ionised. [370] Previous MS data (Figure 5-14) showed the presence of large peaks of starting materials which may have hindered the viewing of the complex.

TLC was conducted to deduce suitable chromatography conditions. The TLC conducted in pure Hexane (Hex) showed the presence of BzCl, which moved with the solvent front whilst all other species remained in the baseline (

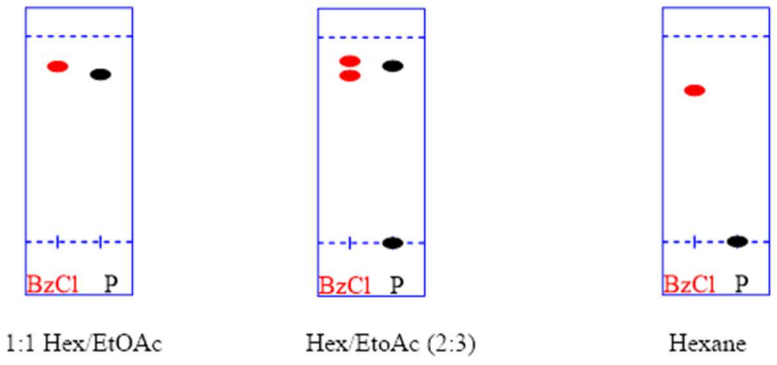


Figure 5-18).

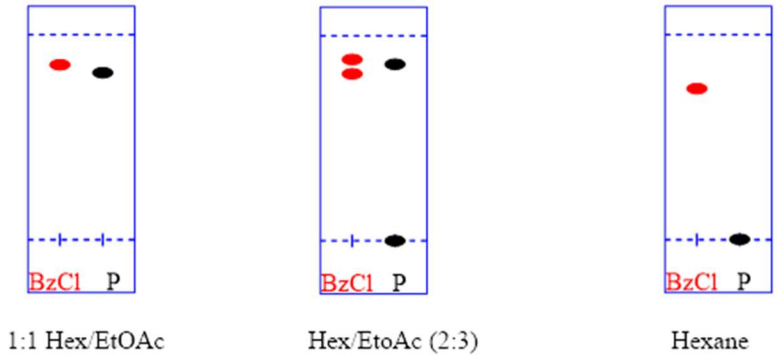


Figure 5-18: Finding the correct column conditions to separate benzoyl chloride (BzCl) from the desired benzoylated stachyose molecules (P).

It was decided to conduct a gradient column starting at pure hexane to first elute all the BzCl. Once the fractions from the column no longer showed BzCl presence via TLC, the polarity of the mobile phase was increased slowly, to begin to move the other spots in the baseline. Since stachyose is very polar, even with 100% ethyl acetate, it should not move appreciably from the baseline of the TLC/Column. Therefore, the only components left are the products themselves, providing the extraction of AABOB via the basic sorbitol wash was successful. At the end of the gradient column anything still bound to the column will be cleaved with methanol and collected separately for analysis. The fractions collected from flash chromatography were viewed via ^{1}H NMR and LC-MS.

The ^{1}H NMR of some of the fractions believed to be the benzoylated stachyose molecules are displayed below in Figure 5-19.

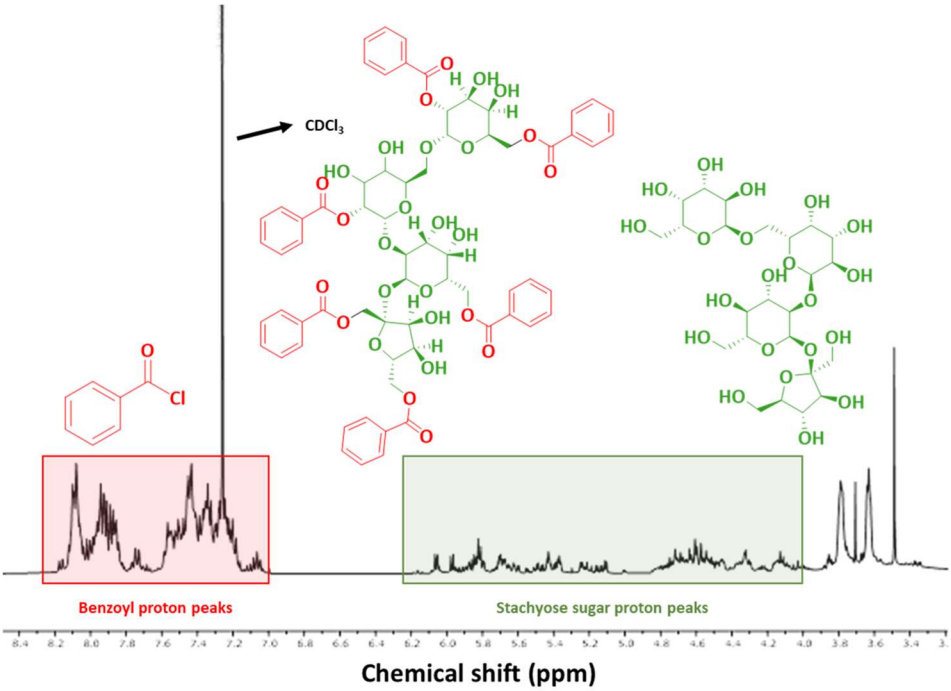


Figure 5-19: ^{1}H NMR (400 MHz, $CDCl_3$) of the yellow oil (73%) from column chromatography to remove excess BzCl (red) and unreacted stachyose (green). The NMR Indicates the presence of many benzoyl units in different chemical environments along with the presence stachyose.

The NMR (Figure 5-19) of the yellow oil (73%) after column chromatography was conducted in deuterated chloroform, as it is known stachyose alone is insoluble in this solvent. Therefore, any sugar peaks in the region < 5 ppm must correspond to any alkyl moieties such as a functionalised stachyose.

The NMR revealed the presence of some stachyose peaks as highlighted in green indicating the stachyose had reacted with benzoyl chloride (red). Furthermore, the large peaks that previously dominated the spectra (Figure 5-17) were absent confirming the success of flash chromatography. The remaining benzoyl peaks were significantly broader in nature indicating a

change had occurred for these protons' environment.[361] Therefore, the NMR indicated the benzoylation of the stachyose molecule had been achieved. To understand the extent of boronate ester formation further analysis is required.

Next, liquid chromatography in tandem with MS (LC-MS) was attempted to reduce the number of different compounds hitting the detector at once, to simplify analysis. Previous MS conducted on the boronate-esters, revealed that ES ionisation in positive mode suited the molecules better than ASAP. Since these compounds are derived from the former boronate esters the previous MS methods may still be applicable. Thus, LC-MS was conducted using electrospray as the ionisation mode. Although chromatography had previously been done to remove the excess of BzCl, unreacted AABOB and stachyose, the different benzoylated products had not been separated during this procedure. The different benzoylated products are due to the possibility of more than one boronate ester being formed during the initial reaction with stachyose and AABOB. For clarity, the new benzoylated stachyose structures of interest and their corresponding masses are provided below (Figure 5-20).

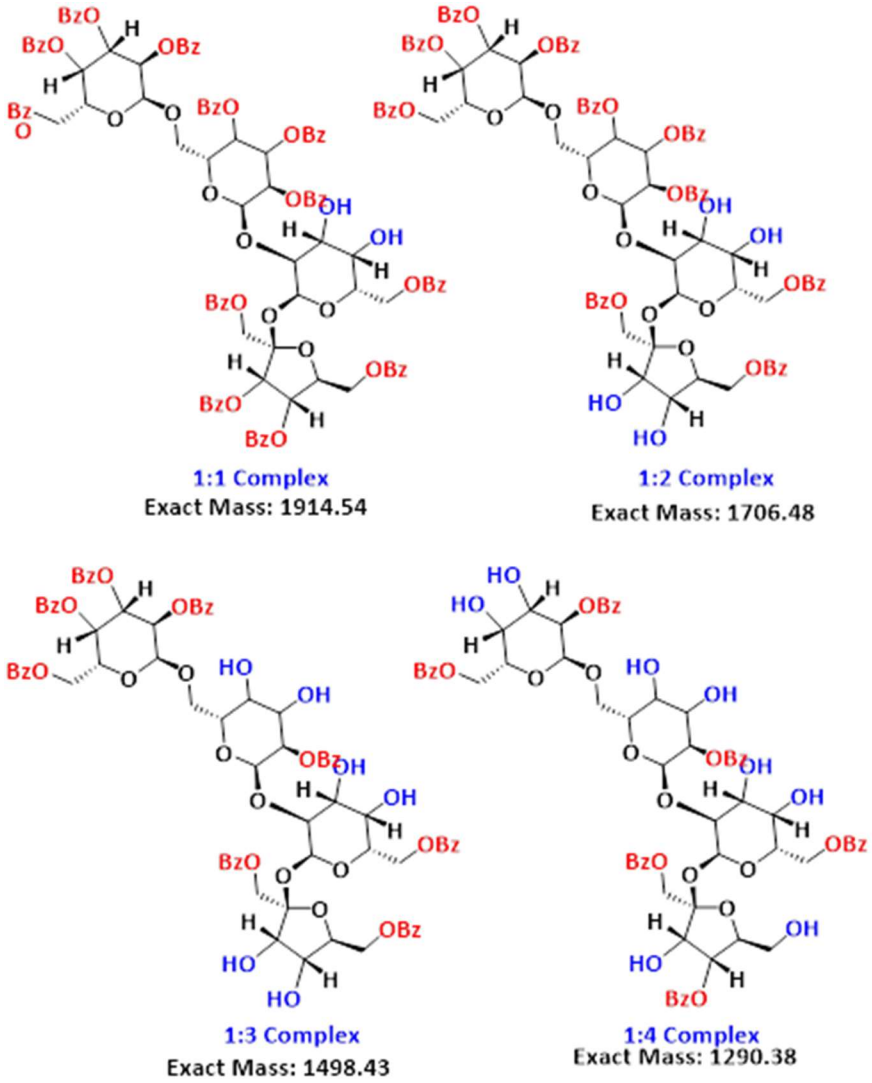


Figure 5-20: Benzoylated stachyose products of interest and their corresponding exact masses. The blue hydroxyl groups depict where the AABOB receptor was bound to prior to being cleaved off the product with sorbitol.

Owing to the challenges faced previously with obtaining suitable chromatography and MS conditions, it was decided to start with a known pure compound that is structurally like the compound of interest. Therefore, before the above yellow oil could be analysed, a control molecule was first required.

For this study it was thought a fully benzoylated stachyose (Figure 5-21) could be a good model, its similar in size and contains the same functional groups.

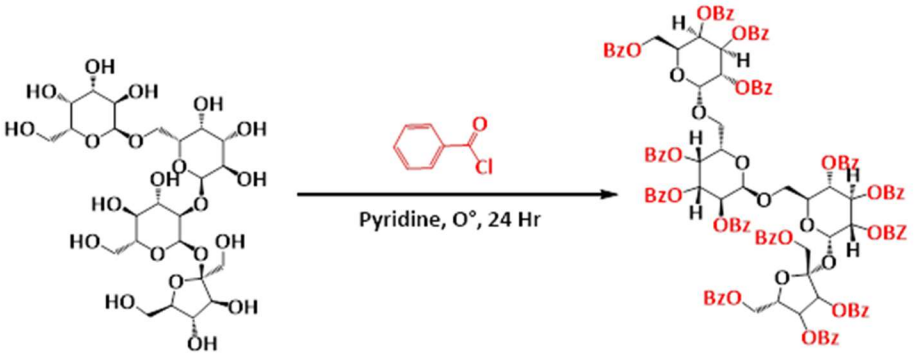


Figure 5-21: Synthesis of the control molecule (fully benzoylated stachyose) for LC-MS studies.

Firstly, the control of the LC-MS compound was synthesised (Figure 5-21) as per previously discussed methods (Preparation of the glycan-boronate complex using a large excess of BzCl (Eq 50). Following five hours a TLC was conducted to check for any unreacted stachyose present. If stachyose was present the reaction was left to further react for a longer period. Following reaction completion, the solvent was removed under vacuum to reveal a crude yellow oil. The resulting oil was purified via flash chromatography (DCM/MeOH) prior to analysis. The final oil obtained was subjected to LC-MS to determine suitable solvents, gradients, ionisation, and cone voltages for these series of molecules.

Common solvents used in LCMS are water, methanol (MeOH), acetonitrile (ACN), and water containing tiny amounts of acids such as trifluoroacetic acid (TFA)/formic acid (FA). Our sample had limited solubility in water, so water cannot be used as the only solvent in the mobile phase. Equally, the C-18 columns

cannot carry 100% organic solvents such as acetonitrile, due to pressure build up. A compromise was made, and a mixture of organic and aqueous based mobile phases were selected. Different stationary and mobile phases were trialled as highlighted in Table 5-1.

Table 5-1: LC-MS conditions trialled.

Method	Solvent	Gradient	Ionisation mode	MS scan Range (m/z)	Cone voltage
A	ACN / H_2O (1:1)	5% - 95% organic in 40 min	ES + and ES -	600-2200	-/+ 10 -/+ 40 -/+ 80 -/+ 100
B	ACN (0.1% FA) / H_2O (1:1)	5% - 95% organic in 40 min	ES + and ES -	600-2200	-/+ 10 -/+ 40 -/+ 80 -/+ 100
C	Ammonium acetate (pH 7) / ACN (1:1)	5% - 95% organic in 40 min	ES + and ES -	1000-2200	-/+ 10 -/+ 40 -/+ 80 -/+ 100
D	ACN + MeOH / Water (1:1)	5% - 95% organic in 40 min	ES + and ES -	600-2200	-/+ 10 -/+ 40 -/+ 80 -/+ 100
E	ACN + MeOH / Water (1:1) [LC] [MS] – NH_4 acetate (pH 7, 10 mM)) + IPA (1:1)	5% - 95% organic in 40 min	ES + and ES -	1000-2200	-/+ 10 -/+ 40 -/+ 80 -/+ 100

From the LC-MS attempts it was found method E (Table 5-1) was the most efficient as a solvent system for the separation of the species in solution with a C18 column. Previously LC-MS yielded a blank MS spectrum for the boronate-esters (Appendix 9-16), however for the protected version of these species some ions were formed to produce the below MS ion chromatogram.

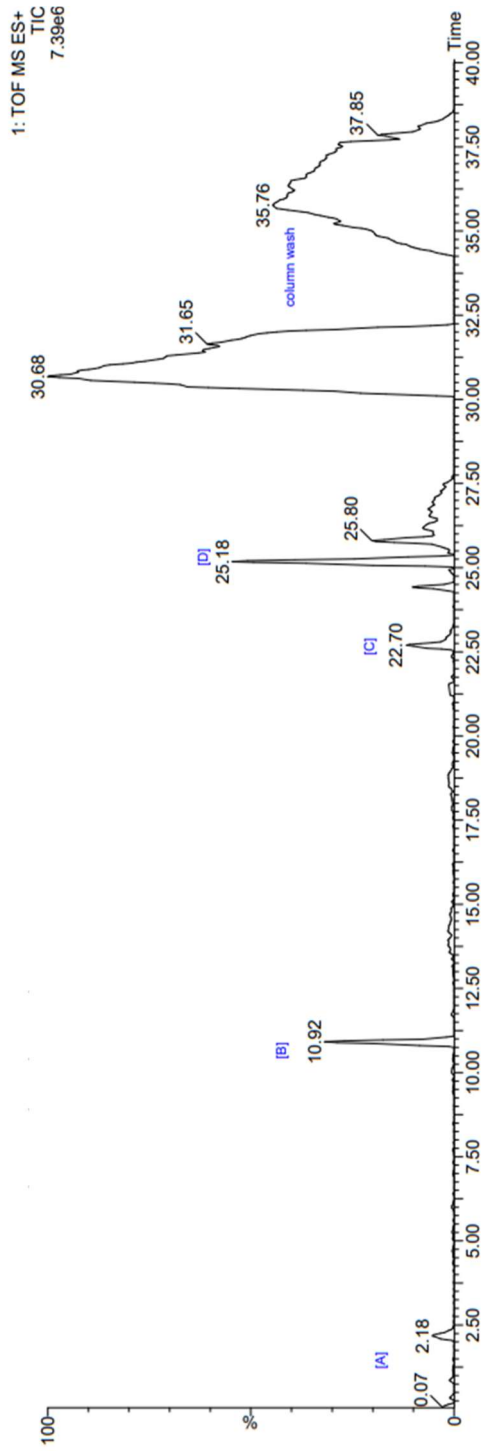


Figure 5-22: MS ion chromatogram from the LC-MS analysis of the fully benzoylated stachyose molecule.

To view if the species of interest was present, a search was conducted utilising Waters MassLynx analysis software.[372] The fully benzoylated stachyose species (c.f. Figure 5-21) has a mass of 2124.09 g mol^{-1}. From the ion chromatogram produced a cluster of peaks situated around 2141 m/z was identified within peak D (c.f. ***Figure 5-22***). For clarity, this ion cluster is displayed below.

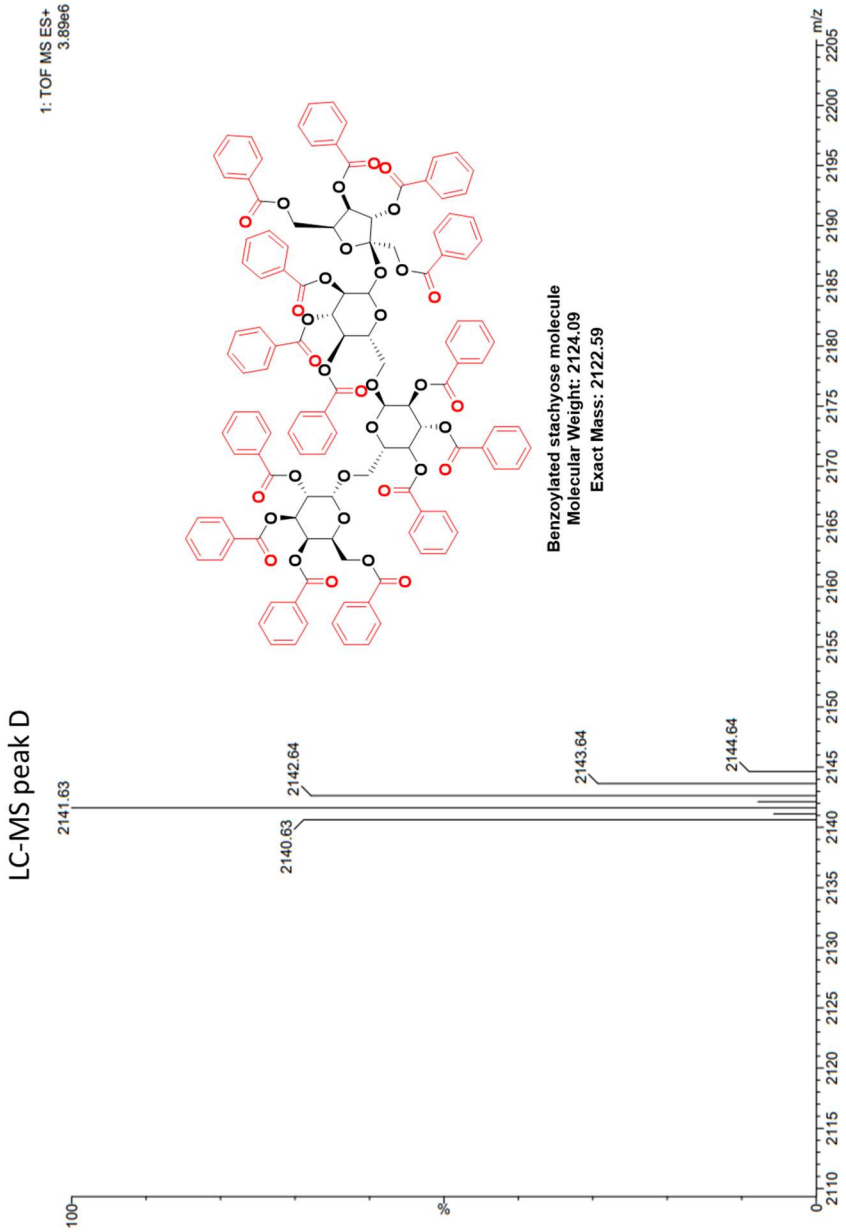


Figure 5-23: Cluster of ions within peak D of the ion chromatogram from the LC-MS run of benzoylated stachyose (MW = 2124 g mol^{-1}). Benzoylated species flies with an ammonium ion to form [M + NH4]+ion (NH_4, MW = 18 g mol^{-1}).

The benzoylated species was identified to fly with an ammonium ion. The ammonium ion originates from the use of ammonium acetate buffers (Table 5-1). From these works it was observed the compounds did not consistently ionise (method A-D, Table 5-1) following their elution from the chromatography column. To aid ionisation post elution from the column an additional step was incorporated. This additional step entails the addition of 100 mM ammonium acetate buffer (50% IPA, pH 7) to the eluted species. The addition of buffer aids the ionisation of large molecules by donating protons.[373] The flow rate was controlled to enable a final ammonium acetate buffer concentration of 10 mM, once mixed with the column outputs. This was mixed prior to reaching the MS component of the LCMS instrument (Method E, Table 5-1). Therefore, using an ACN/MeOH and water solvent system slowly increasing over 40 minutes to a 95% organic solvent system, separation of any unreacted stachyose and benzoyl chloride that had not been removed previously was achieved, with the desired compound eluting at around 25 minutes to provide an ammonium solvent adduct.

With suitable conditions located for the control molecule (fully benzoylated stachyose) the attention was returned to the original benzoylated stachyose esters formed from the boronate-ester complexes (Figure 5-20). The LC-MS was thus conducted with the same conditions (method E, Table 5-1) for the previously synthesised protected boronate ester species. The resulting ion chromatogram was produced (Figure 5-24), which closely resembles that previously observed for the control benzoylated stachyose species (Figure 5-22).

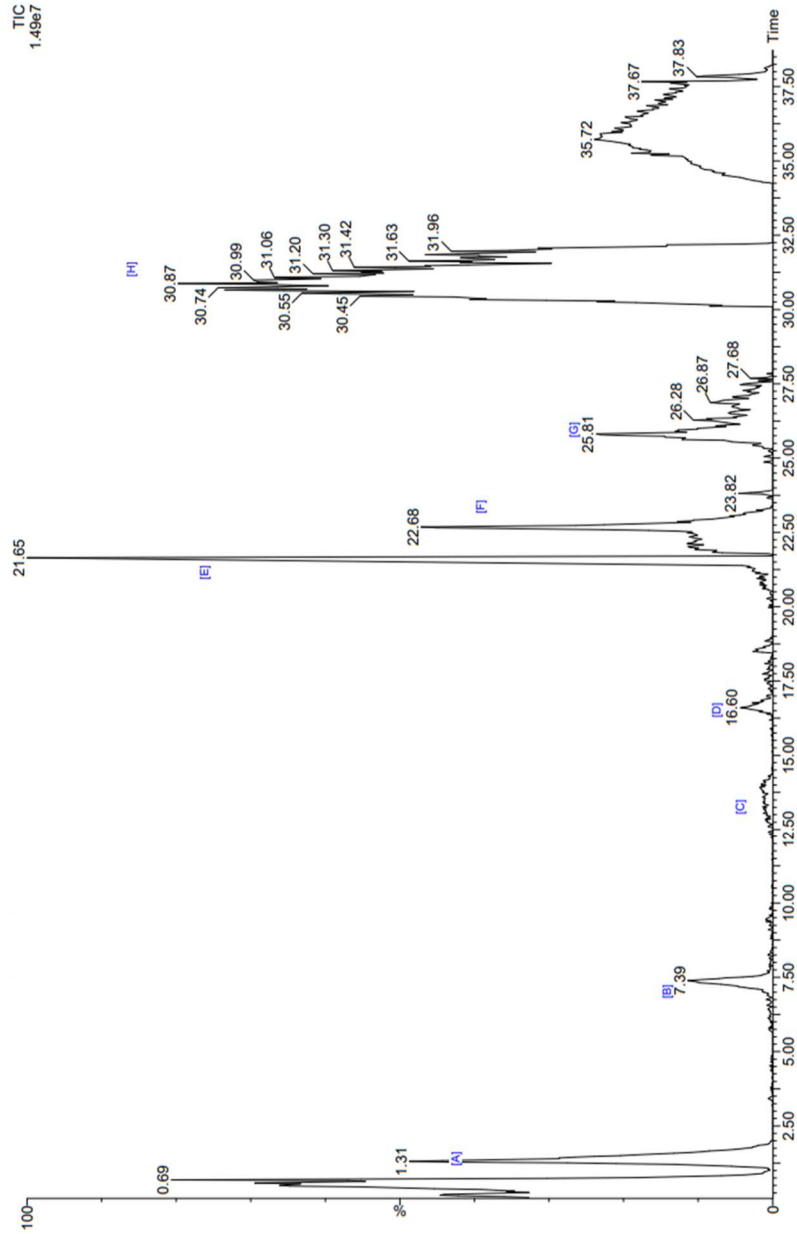


Figure 5-24: Ion chromatogram produced from the LC-MS run of the benzoylated stachyose molecules formed to indirectly assess the boronate ester formation of AABOB and stachyose.

As previously, conducted the resulting chromatogram was searched for ions corresponding to the species of interest (Figure 5-20). No single fraction produced exact masses on interest. However, the eluted fraction G showed promise with a significant array of ions forming. Fraction G which eluted around 30 minutes displayed a cluster of peaks situated around 1398.99 m/z units as displayed below.

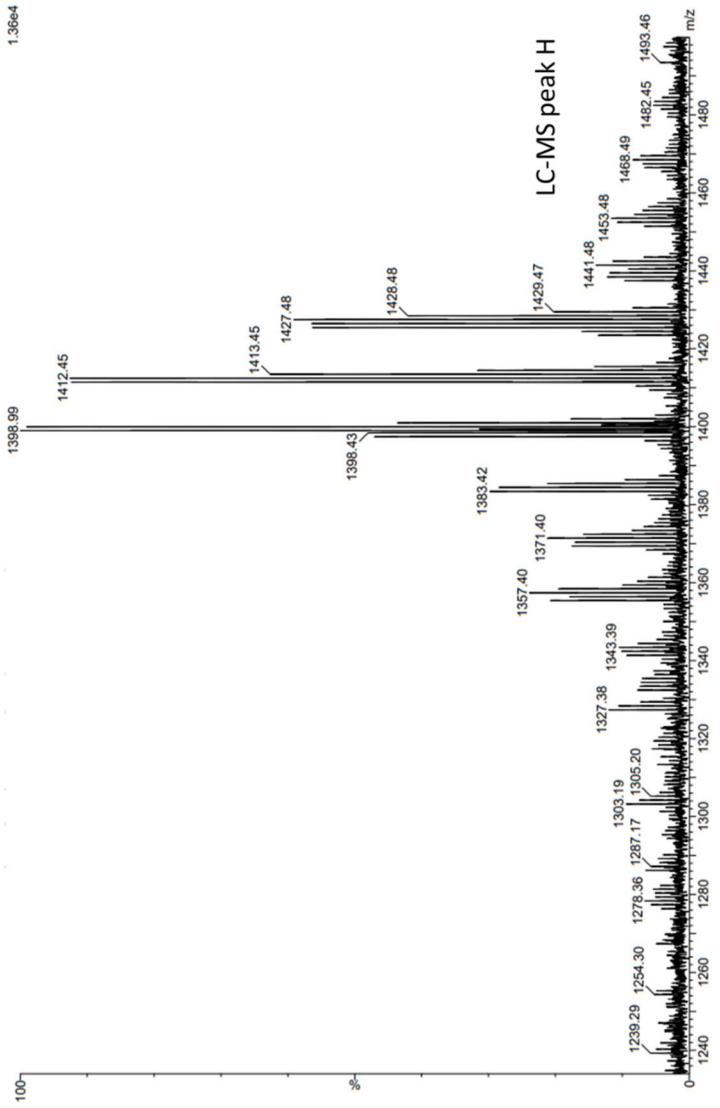


Figure 5-25: TOF MS ES + spectrum produced for fraction H (peak H) from the LC-MS diode array.

The main ion at 1398.99 m/z was thought to be due to the presence of the 1:4 benzoylated stachyose species which possess a mass of 1291. If this species were to form a solvent adduct with either ammonium, methanol or acetonitrile the expected ion masses are: 1309.26, 1324.26 and 1333.26, respectively. However, no exact masses were found but ions of 1305 and 1327 where identified (Figure 5-25). These ions, however, are less than 5% out of the expected mass. Given that the scan range (number of m/z channels) was extremely broad, one can expect the signal to noise ratio and hence the resolution and sensitivity to be reduced. [370]

To conclude, despite identifying suitable ionisation conditions for the fully control benzoylated sugar, when applied to other benzoylated species of interest, no exact mass could be identified. Although ions within ±5 % of the desired masses were identified. It was postulated if an alternative ionisation could provide exact masses for these species. Therefore, MALDI was next trialled (Matrix assisted laser desorption ionisation (MALDI)

MALDI involved the use of a matrix to aid ionisation of molecules, it is sometimes used for the analysis of proteins and other large biomolecules. A common matrix used for such biomolecules is 2,5-dihydroxybenzoic acid (DHB). [83,374] Different solvent conditions for the matrix were evaluated (Table 5-2), taking inspiration from the previously trialled LC-MS conditions. It was thought the formic acid or ammonia could aid ionisation, which is an issue for this series of compounds. For information on MALDI preparations refer to Preparation of MALDI matrixes

Table 5-2: Conditions trialled for MALDI MS .

Matrix	Matrix solvent	Sample solvent
2,5-dihydroxybenzoic acid (DHB) – 1 mg mL^{-1}	MeOH in 2 M NH_3	ACN
	ACN / H_2O (1:1)	EtOAc
	ACN (0.1% FA)/ H_2O (1:1)	DCM

The best conditions for these compounds were found to be methanol with 2 M of ammonia, the correspond MALDI spectrum is provided below (Figure 5-26). The subsequent repeats are provided in the appendix (Appendix 9-20 & Appendix 9-21).

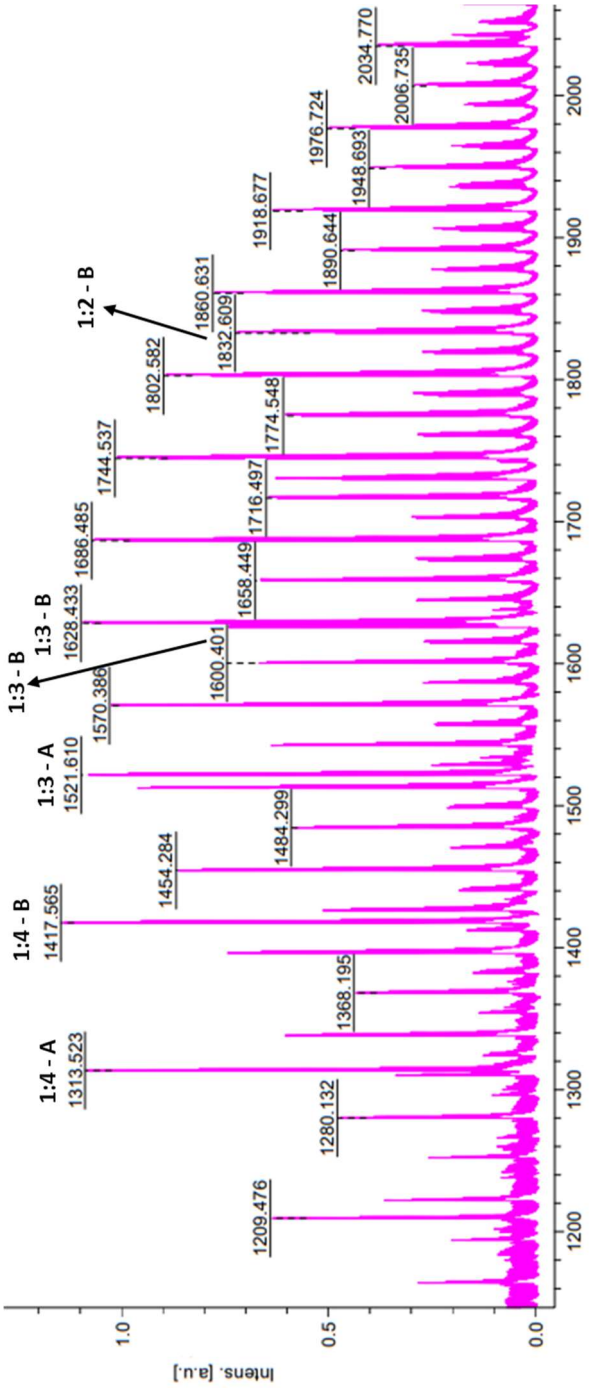


Figure 5-26: MALDI spectra obtained from the benzoylated stachyose species.

The MS spectra obtained from MALDI was more consistent and reproducible in comparison to prior ES attempts. The spectra always produced an array of ions corresponding to the complexes flying with sodium ions. Listed below are the structures identified by MALDI.

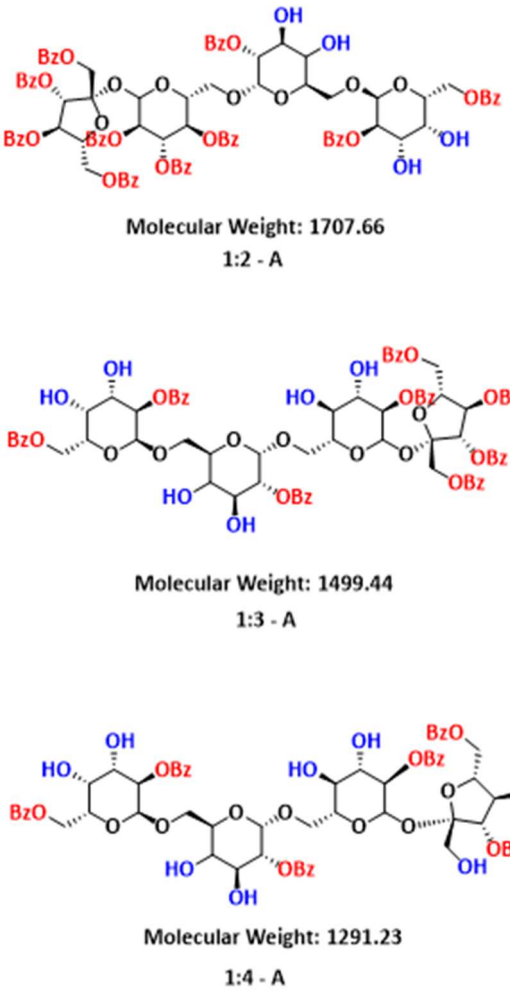
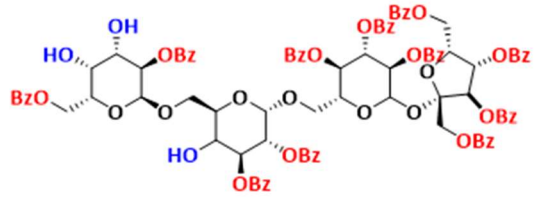
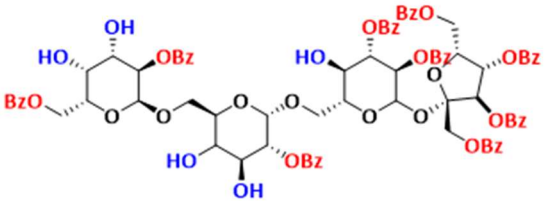


Figure 5-27: Benzoylated structures arising from the cyclic boronate ester formation observed via MALDI.



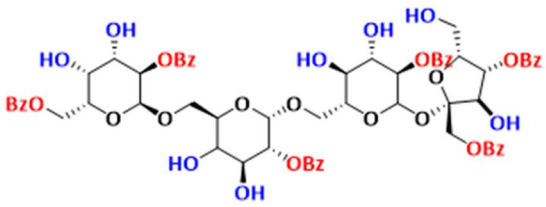
Molecular Weight: 1811.77

1:2-B



Molecular Weight: 1603.55

1:3 - B



Molecular Weight: 1291.23

1:4 - B

Figure 5-28: Benzoylated structures arising from the cyclic boronate ester formation observed via MALDI.

To evaluate the extent of formation the intensities of the ions were normalised in relation to each other. It was thought the benzoylated species which are remarkably similar should ionise with equal probability size their structures only vary by one Benzoyl unit. Thus, the proportion of each boronate-ester (indirect determined through the benzoylated species) are displayed below (Table 5-3*)*.

Table 5-3: Tabulated summary of proportions of boronate esters present (indirectly identified via benzoylated stachyose species). Intensities of MS peaks were normalised in relation to each other with the assumption all benzoylated species ionise with equal probability.

M/Z peak	Ion identified	Molecule ID	Proportion present
1313.52	[M+Na]+	1:4 - A	39%
1521.61	[M+Na]+	1:3 - A	42%
1729.65	[M+Na]+	1:2 - A	18%
N/A	N/A	1:1 - A	0%

From the MALDI analysis it was confirmed that the stachyose boronate esters were forming to an appreciable extent. Of significance it was observed the 1:3 – A species was more abundant than the 1:4 – A species (Figure 5-27). The 1:4 – A species was thought to be present in slightly lower abundance due to the C2 hydroxyl group of β-D-fructofuranose not being available for binding. The C2 hydroxyl group is part of the α-1,β-2 glycosidic linkage. Thus, the AABOB receptor would have had to bind to the hydroxyl groups of the C3 and C6. The five membered cyclic boronate esters are preferred over the six membered rings. The formation of the boronate esters with a higher amount of AABOB receptors (i.e. 1:4 and 1:3 species) are more beneficial for MI over the 1:2 and 1:1 boronate ester complexes.

To conclude, the boronate-esters were synthesised and characterised indirectly via the use of MALDI MS to infer on the locations of the AABOB receptors. The higher order complexes

were found to form to a greater extent over the 1:1 and 1:2 complexes which is favourable for MI to provide a greater number of interactions with the target glycan and hence a multivalent approach. The multivalent approach is thought to enhance the binding constants of an interaction. The attention was next directed to more clinically relevant sugars such as sialic acid.

VI. STUDY TO EVALUATE THE EXTENT OF BORONATE-ESTER FORMATION WITH CHARGED SUGARS

Prior established literature has found that sialic acid is often present in the glycoproteins of patients with aggressive prostate cancer.[3,17,55,66] The study has established a connection between the presence of α-2,3-sialic-terminated glycans in the serum of patients with aggressive prostate cancer. [55] Therefore, identifying sialic acid and monitoring changes in the glycosidic bonds that connect the termini glycans could lead to the development of innovative diagnostic tools. The previous section only looked at neutral oligosaccharides, so sialic acid presents a unique challenge. It is a charged monosaccharide with a glycerol side chain and carboxylic acid group, as Figure 5-29 illustrates.

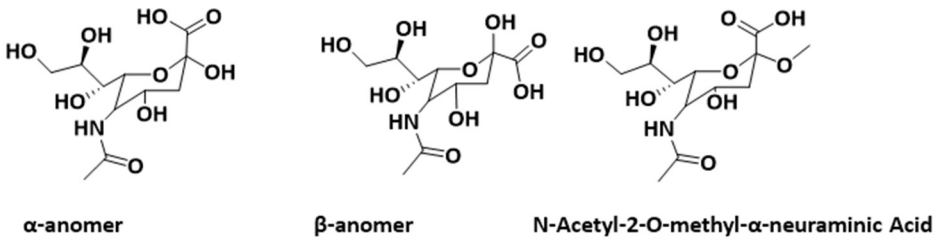


Figure 5-29: Sialic acid in its pyranose chair conformations. The alpha anomer is commonly observed in glycoproteins[130,375] whilst the beta anomer dominates in aqueous mediums. The methylated alpha sialic acid derivative will be used within this section as it closely resembled the glycoform present in PSA.

Recent studies have shown that benzoboroxole-based receptors, including AABOB receptors, can be used to detect sialic acid.[130] Interestingly, these receptors work best in acidic pH levels, which is different from their typical binding behaviour that usually works best in alkaline pH environments (pH >> pKa). [130] This is because the negatively charged boron centre of the receptor forms a more stable species in alkaline pH levels, but it is not favourable for boronate esters due to the electrostatic repulsion between the negatively charged sp3 boron centre and the negatively charged carboxylic acid group (Covalent synthetic receptors). As a result, most boron-based receptors that target sialic acid are designed to interact with the negatively charged carboxylic acid groups in a complementary manner.

Several studies have been conducted on targeting sialic acid, and they often use charged species such as lanthanides, urea, and boronic acid derivatives. [54,94,376–384] These charged species can interact with the COOH group of the sialic acid through non-covalent interactions, which enhances the binding affinity. [378,383,385] One common approach is the use of thiourea-type receptors, which are sometimes combined with boronic receptors to create a cooperative receptor. This use of charged species in receptor design is a significant aspect of our research, as it provides a basis for our exploration of AABOB receptors.

There is a lack of consensus in the literature regarding the preferred binding site of boron-based receptors.[130] Some argue that the binding primarily takes place in the acid group[386], while others claim it occurs on the glycerol side chain.[387] This lack of

consensus is significant because it directly impacts our study on AABOB receptors. If the preferred binding mode is at the acid side group, this would negatively impact our AABOB receptors because the acid side group is not naturally available for AABOB to bind to. This means there is no group for the receptor to bind to, potentially undermining the efficacy of AABOB receptors in targeting the glycerol chain of sialic acid.

This research aims to investigate the capability of AABOB receptors in targeting the glycerol chain of the alpha methylated sialic acid derivate. Due to the 1,2-cis diol of these sugars being *exo*-cyclic it is known these sites react much more slowly than the strained hydroxyl groups on sugar rings.[388] The methylated alpha derivative closely resembles the sialic acid glycan form in nature. [130,375] Our approach involves boronate-ester formation in a dry environment, followed by protection of the unreacted hydroxyl groups using the same technique used for stachyose. The proposed sialic acid boronate esters of interest are depicted below.

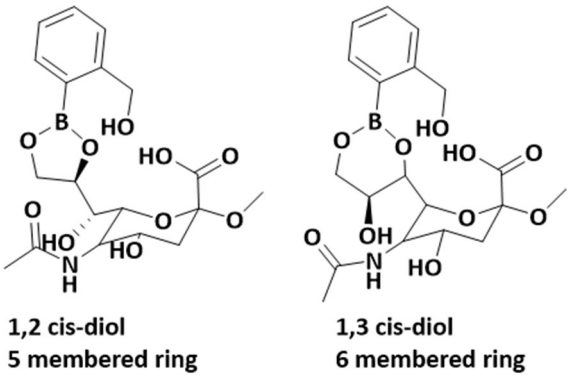


Figure 5-30: Five and Six membered boronate esters formed between AABOB and N – acetyl – 2 – O – methyl – α - neuraminic acid (α-methyl – sialic acid) in organic media.

We will use functionalised sialic molecules obstructing the acid-binding site, ensuring that any binding observed is solely attributable to the sialic acid glycerol side chain. The extent of boronate-ester formation will be thus determined indirectly via analysis of the protected sialic acid by NMR and MS.

VII. THE SYNTHESIS OF BORONATE ESTERS WITH NEURAMINIC ACID DERIVATIVES.

The boronate-ester formation reaction was conducted as displayed in Figure 5-31. Briefly, the sialic acid derivative (20 mg, 0.062 mmol, 1 Eq) and 2-(hydroxymethy)phenylboronic cyclic monoester (BOB) (25 mg, 0.18 mmol, 3 Eq) was suspended in a 6:1 mixture of anhydrous acetonitrile (420 µL) and 1,4-dioxane (2.4 mL). The reaction mixture was left for 24 hours at 90 degrees under inert atmosphere. The formed boronate-ester was then protected via the benzoylation of any unreacted hydroxyl groups. Thus, the solvent was removed under vacuum prior to adding pyridine (25 mL) and benzoyl chloride (50 µL, 0.41 mmol). The work up procedure was conducted as previously described. For full experimental protocol refer to ***Benzoylation of the complex sugar***.

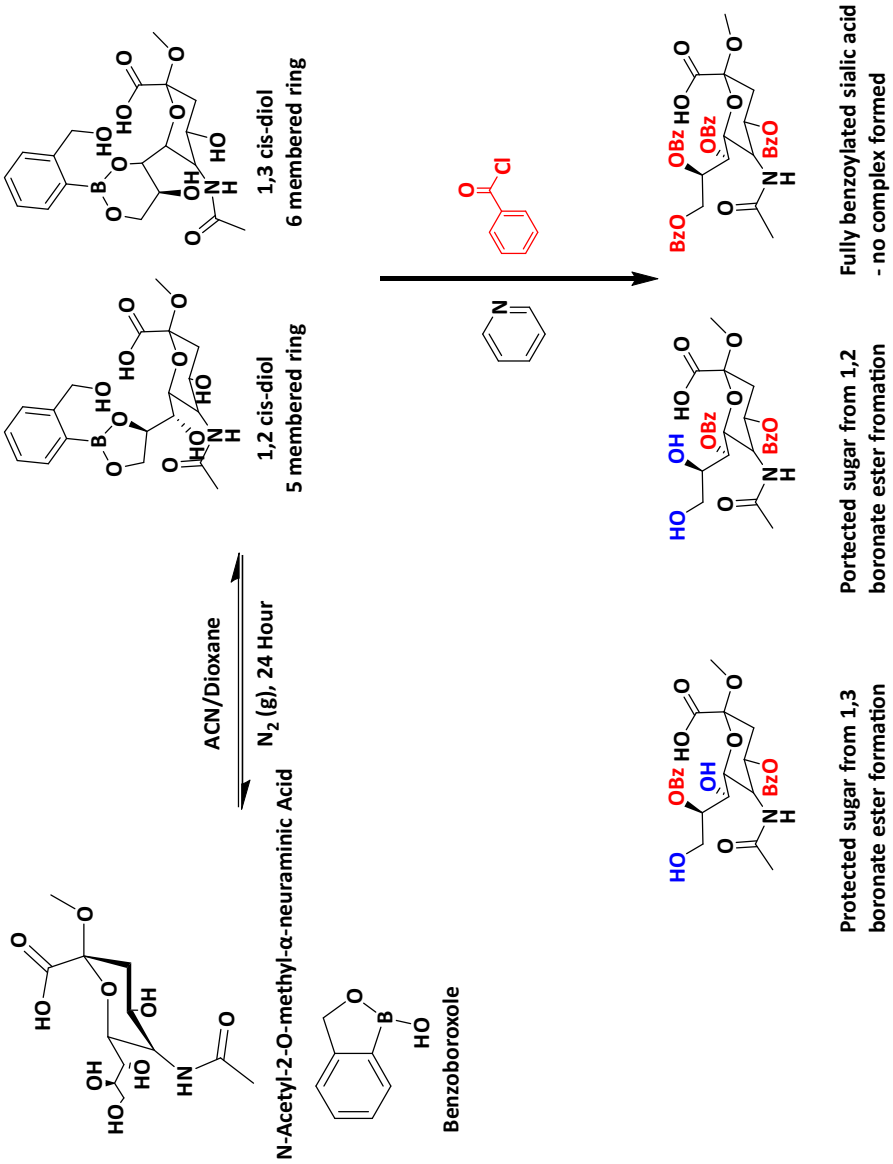


Figure 5-31Indirect method of determining boronate-ester formation between Benzoboroxole based synthetic receptors and N-Acetyl-2-O-methyl-α-neuraminic acid. Two products are possible depending on the binding mode of the receptor.

The extent of boronate ester formation was examined via TLC. The TLC plate (

Figure 5-32) showed the presence of several spots for the reaction mixture, some of which hinted the formation of new species. Following UV analysis, the TLC plate was finally viewed via potassium permanganate dye to view anything which is not UV active. The use of $KMnO_4$ dye showed the presence of sialic acid in the baseline for the reaction mixture. Indicating, that the reaction had not fully going to completion after 24 hours.

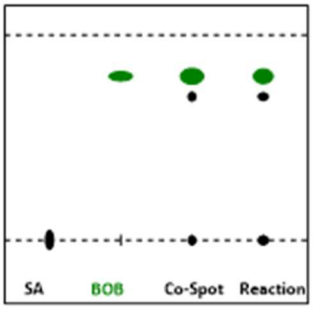


Figure 5-32: TLC plate (1:1 Hex/EtOAc) developed via UV and $KMnO_4$ dye. Reaction mixture after 24 hours in the presence of AABOB under anhydrous aprotic conditions was studied via TLC to look for evidence of any new species formed.

The benzoylation reaction was continued since the product was only required for characterisation. Following the benzoylation reaction a TLC was conducted(Figure 5-33). The TLC revealed the presence of three species in the reaction lane, one of which was the sialic acid starting material, the other two had different Rf values to that of BOB and benzoyl chloride. TLC indicated the presence of two products which needed to be isolated and analysed to see if any glycan boronate-esters had formed.



Figure 5-33: TLC (5% EtOAc/Hex 95%) plate developed after UV and $KMnO_4$ after the Benzoylation protection reaction of sialic acid. Reaction (R) in lane 1, showed the presence of two spots close together, owing to the small scale of the reaction and the spots being close to one another preparative TLC was next explored for analysis of the spots observed.

The work up procedure began by the precipitation of BzCl, the reaction was diluted in the minimum amount of toluene to induce precipitation. The removal of the fine precipitate was achieved via filtration with Celite. Toluene was removed under reduced pressure to produce the crude product.

After adding the 1 M solution of sodium carbonate / sorbitol, and ethyl acetate, a white precipitate formed. The resulting solution was left to stir for one hour to remove boronic moieties from the sugar. The white precipitate was collected before the extraction of the organic phase for future analysis.

The organic layers were collected and dried over $MgSO_4$ prior to solvent removal under vacuum to yield a yellow oil (45 mg). Both the white precipitate, and the yellow oil (45 mg), were left drying

under vacuum overnight. The yellow oil (27 mg) and the precipitate from work up were subjected to NMR analysis.

It was thought the white precipitate produced during the work up procedure may have been a salt so D_2O was attempted to dissolve it. However, the solid did not dissolve well in aqueous conditions, the solid dissolved well in CDCl3, as did the yellow oil obtained from the organic phase. The NMR of the white solid confirmed it was not any derivative of the Benzoic acid, the AABOB, nor sialic acid, so it was discarded.

The ^1H NMR of the yellow oil collected after the work up displayed a vast array of proton environments in the aromatic region. The peaks corresponding to the benzoyl chloride are highlighted in red (7.5 ppm (ddt), 7.67 (m) and 8.09 (m) Appendix 9-22). In addition, there was a notable broadening of peaks in this region highlighted in green suggesting the presence of a complex formed.

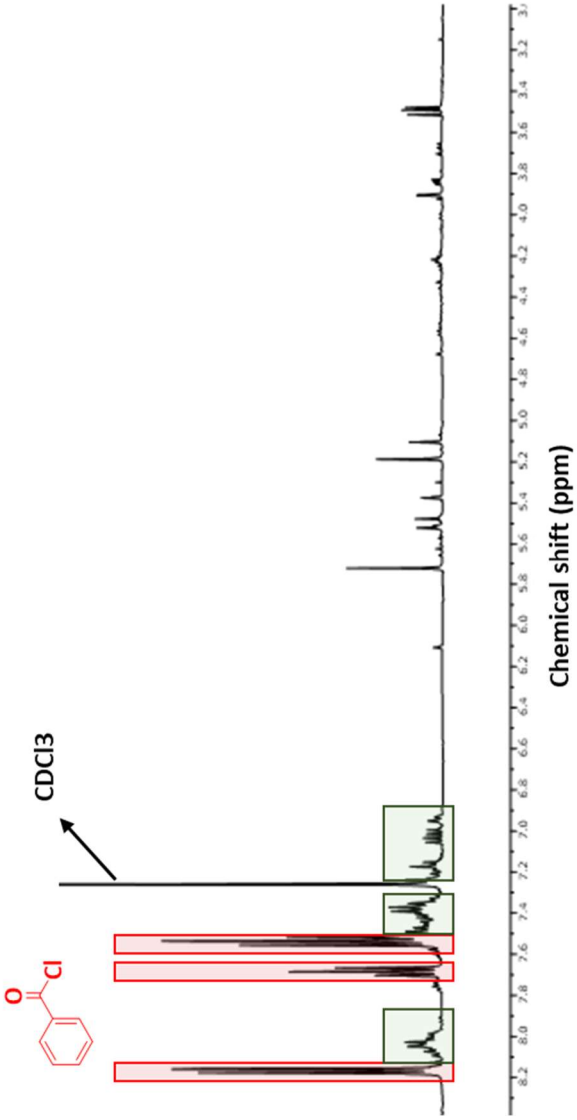


Figure 5-34: ^{1}H NMR (400 MHz, $CDCl_3$) of the yellow oil. The aromatic region displayed an excess of benzoyl chloride (red) present in addition to the presence of new peaks (green).

Upon magnification of the aliphatic region (~3 – 4 ppm) the NMR (Appendix 9-23) displayed some peaks; this region is known to usually correspond to the following protons: C5 and C6. [389] Peaks occurring > 5ppm correspond to C8, C4 and C7, respectively. [389] Thus, indicating the presence of sialic acid. However, due to the limited sample quantity the NMR was poorly resolved limiting the ability to provide integration and

multiplicity due to the sensitivity limits of NMR. However, the presence of sugar peaks in the spectra prompted further investigation. Due to the small quantity (~ mg) of the sample standard flash chromatography was not applicable for purification. Thus, preparative TLC was next conducted to isolate the protected benzoylated species that had formed.

To confirm the correct conditions for the preparative TLC, further TLC were conducted. It was found that a mixture of Hexane/EtOAc (98:2) provided the best separation (Figure 5-35).

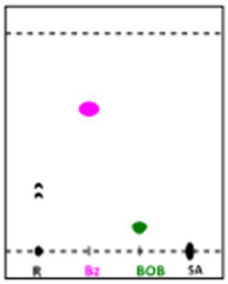


Figure 5-35: TLC prior to Preparative TLC to confirm the correct solvent conditions and Rf values. The Rf values of BOB and the products (R for Reaction) are 0.25 and 0.35, respectively.

When running preparative TLC, you should always run the plate multiple times. Therefore, with these Rf values, there was a risk of the spots in lane 1 (reaction) being widely dispersed on the TLC plate. It was decided to run the plate three times in 100% hexane (Lane 1 Reaction Rf value = 0.163) and the bands would be viewed under UV after each run. After the first preparative plate ran, it was viewed under a UV lamp to check on the progress, which showed several overlapping bands in the

bottom. Following another two runs in the chamber the plate showed 3 distinct bands via UV viewing (Figure 5-36). These bands were carefully etched off the glass plate into separate beakers for washing. Since we were not interested in collecting any unfunctionalised sialic acid, and the crude product had shown good solubility in chloroform.

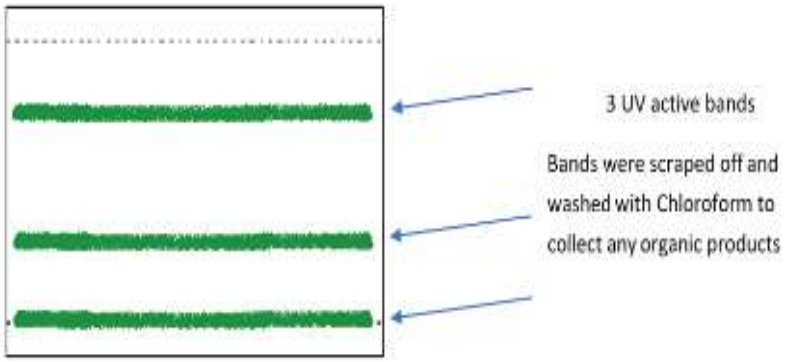


Figure 5-36: Schematic diagram representing the final distribution of bands across the preparative TLC plate after running it in hexane three times.

Chloroform was once again used to wash the solid silica containing the UV active samples. The silica was then filtered away and the organic solvent was removed under vacuum to produce three samples for analysis.

For reference, the three samples collected from chromatography will now be denoted bottom, middle and top bands. The ^{1}H NMR of the bands were conducted. It was anticipated that the bottom would only contain the starting sialic acid molecule. In the avoidance of doubt in case product was present Chloroform was used to view the bottom band and is displayed below.

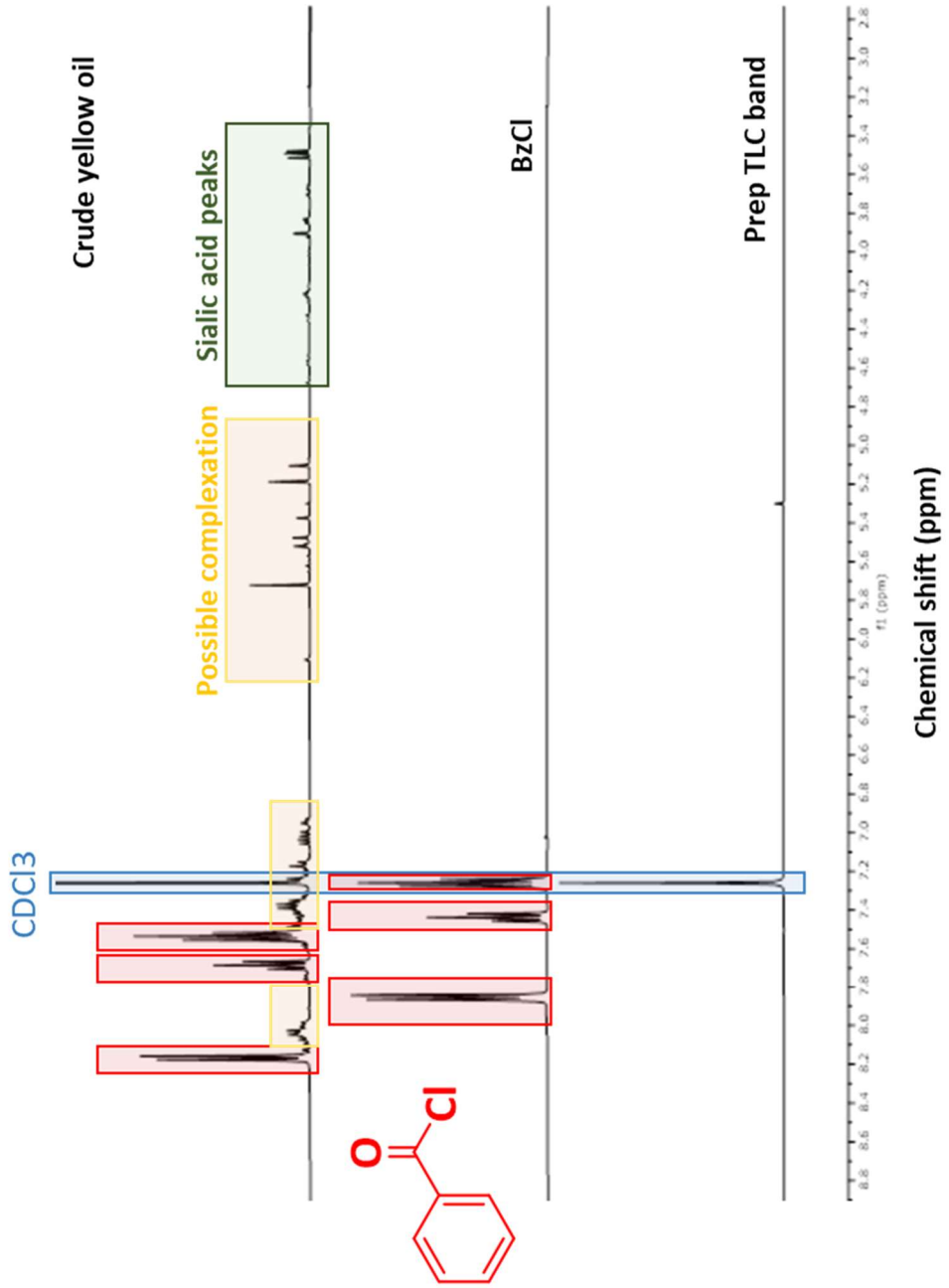


Figure 5-37: Stacked ^{1}H NMR (400 MHz, $CDCl_3$) for viewing the bottom band collected from the prep TLC plate. Bottom TLC band is stacked against the BzCl protecting molecule and the crude yellow oil isolated from the reaction.

The Baseline NMR is shown in Figure 5-37, it shows no appreciable sialic acid peaks. The aromatic region does not reflect one that has been complexed with some sugar as previously seen with stachyose. It was therefore deduced, that the bottom band of preparative only contained sialic acid which was not extracted off the silica with chloroform washes owing to its insolubility. The middle band was next looked at (Figure 5-38).

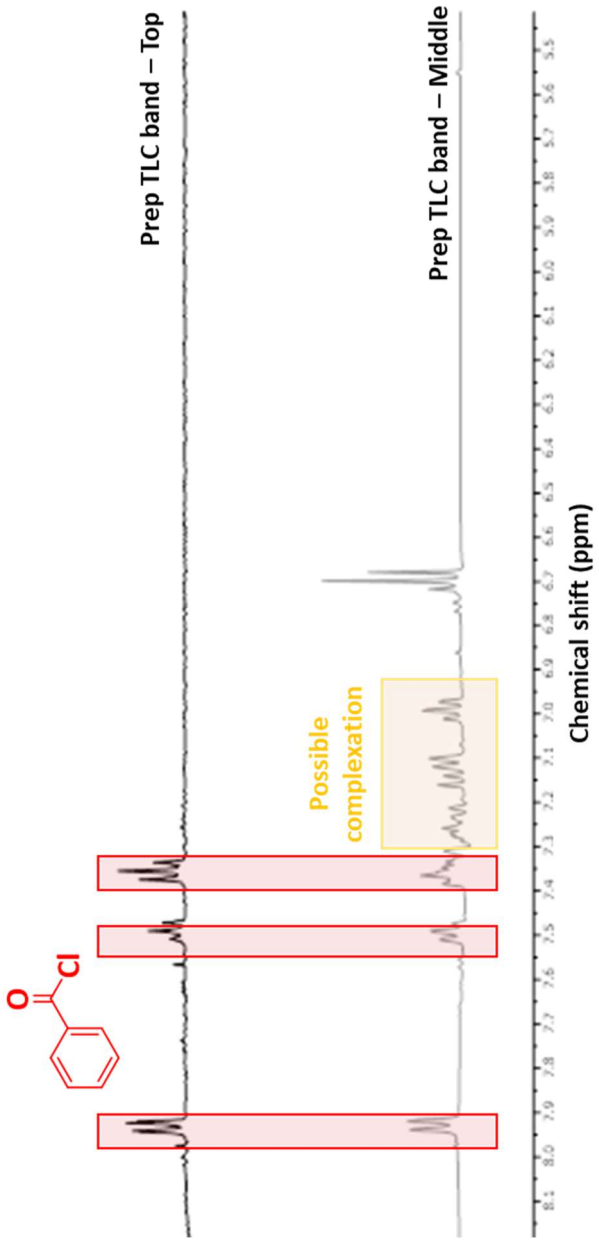


Figure 5-38: 1H NMR (400 MHz, CDCl3) for top and middle bands isolated from the prep TLC plate. The aromatic region has become broadened in nature and requires further investigation for boronate ester confirmation.

The middle bands ^{1}H NMR (Figure 5-38), showed the presence of new aromatic peaks (yellow) in addition to the benzoyl chloride peaks (red). The presence of new unidentified peaks prompter further investigation via MS. The corresponding ions of interest are depicted below (Figure 5-39).

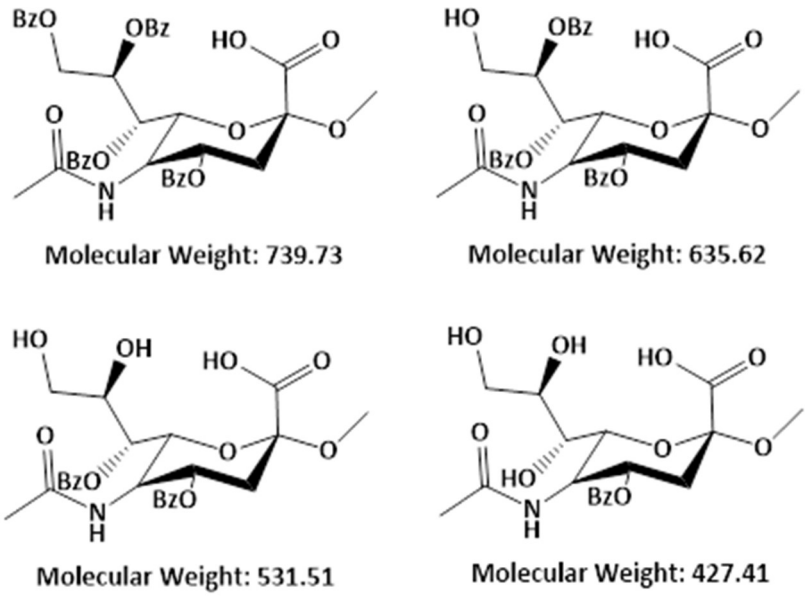


Figure 5-39: Structures that may arise in the MS data for the preparative TLC bands.

The three collected bands from NMR were analysed via TOF-MS spectroscopy. First the top band of the prep TLC plate which via NMR displayed a strong presence of BzCl. The corresponding MS is illustrated below.

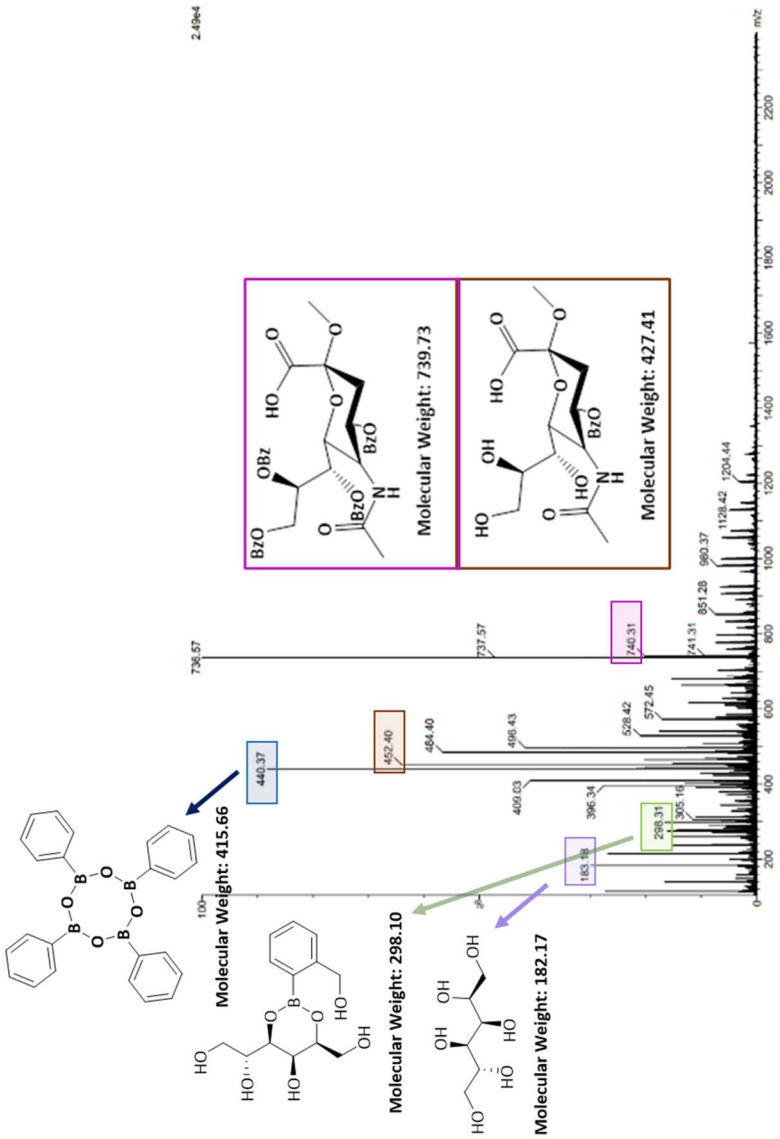


Figure 5-40: TOF MS data for the top band indicating the possibility of a fully benzoylated N-Acetyl-2-O-methyl-α-neuraminic acid via the cluster of ions situated around 736.

The MS of the top band revealed the possibility of a fully benzoylated sialic acid, due to the cluster of ions situated around 736 m/z units. This would make sense to find this species moving with 100% hexane solvent, as the vast majority of the polar hydroxyl groups would have been protected with a hydrophobic benzoyl group. The lower intensity of the sialic acid ions in comparison to the formation of the dehydrated cyclic boron molecules may have arisen due to the inherent bias of electrospray ionisation for hydrophobic analytes. In ES ionisation hydrophobic molecules tend to be concentrated near the surface of the droplet, in contrast the more hydrophilic molecules such as sugars are solvated near the middle of the droplet. Therefore, the protons generated from the oxidation of water in the ESI capillary build up on the surface of the droplet and reach the surface analytes first. [370]

The MS of the middle band did not reveal any ions of significance, the dominant ion for this spectrum had a mass like sialic acid (Appendix 9-24). Finally, the last prep TLC band was analysed via MS. The annotated spectrum is provided below.

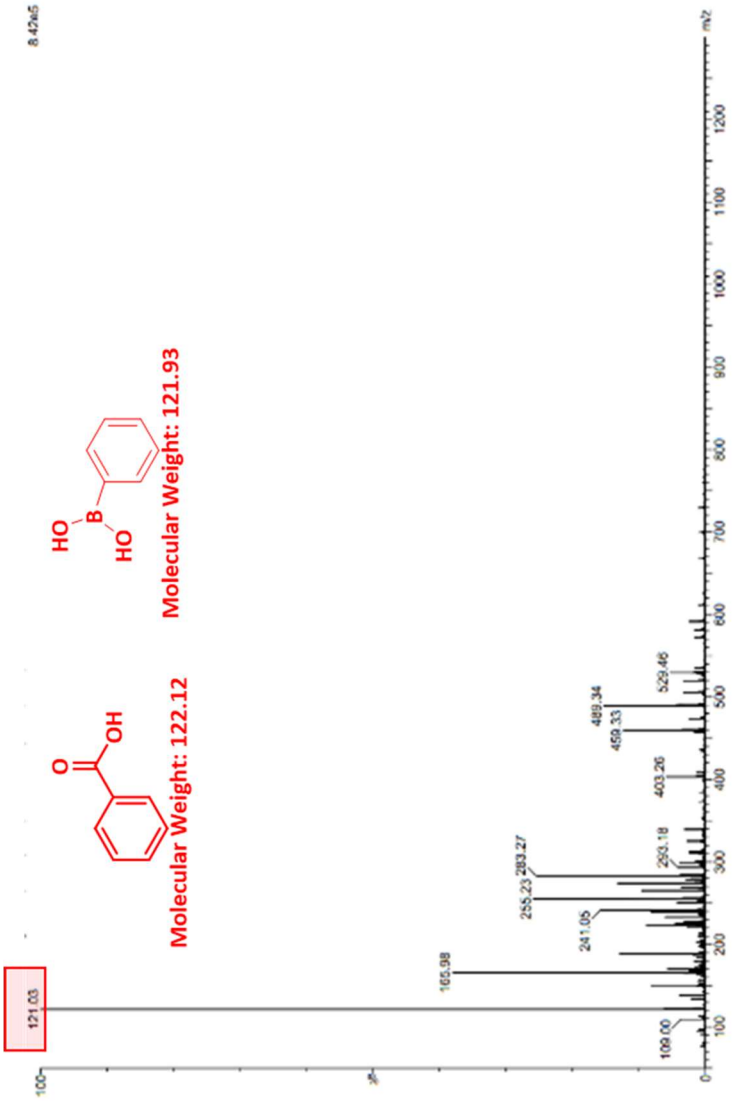
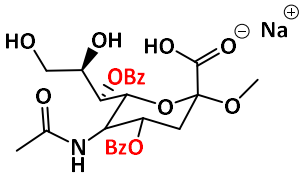


Figure 5-41: TOF MS ES for the bottom band.

Thus, the MS for both the top (Figure 5-40) and bottom band (Figure 5-41), seemed to hint towards no complexation between sialic acid and the BOB receptor. From this information, the reaction protocol, and its conditions were reconsidered. A plausible reason for not observing any signs of formation during the MS may have been because of salt formation during the benzoylation step. If the product was a salt (Figure 5-42), the product may have been lost to the aqueous phase during the work up procedure.



Molecular weight 555

Figure 5-42: Product lost during the work up phase in the aqueous layer.

Therefore, an alternative means of studying these species was next conducted.

VIII. NMR STUDY OF BORONATE-ESTER FORMATION WITH N-ACETYL-2-O-METHYL-A-NEURAMINIC ACID

The previous reaction workup produced a white precipitate which when analysed via NMR could not be identified by NMR. Furthermore, the NMR and the MS showed no conclusive evidence of complex formation. It was most likely the work-up procedure was not appropriate for these compounds. A benzoylated sialic acid would be more water soluble than the benzoylated stachyose, owing to the carboxylic acid and the acetyl groups of sialic acid. Thus, it was possible the product may have had solubility in the aqueous phase.

Before making a definitive conclusion on this binding interaction it was decided to study the reaction in-situ, therefore deuterated anhydrous NMR solvents were purchased to study this reaction directly without the need of work-up. This was not previously done for the stachyose boronate ester because the complex was significantly larger. The reaction between the protected Sialic acid and Benzoboroxole should only produce a small number of products. The possible products for this reaction are highlighted below Figure 5-43.

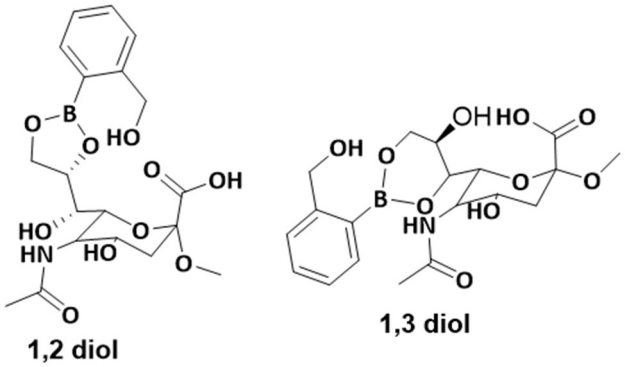


Figure 5-43: Products that can form in the reaction between the BOB and N-Acetyl-2-O-methyl-α-neuraminic acid.

The reaction was repeated on a small scale in the presence of deuterated acetonitrile and dioxane with the same proportions as previously used. After 24 hours the reaction mixture was submitted for ^{1}H NMR analysis as shown in Figure 5-44.

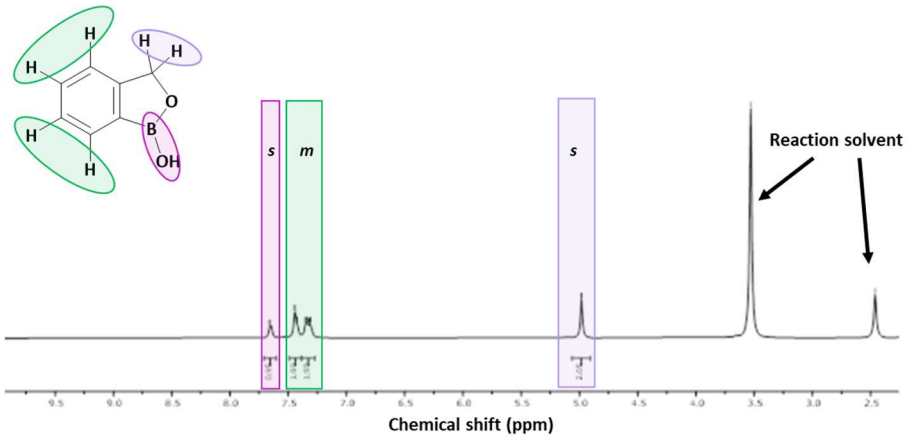


Figure 5-44: ^{1}H NMR (500 MHz, 6:1 dioxane/acetonitrile) of the reaction mixture displaying the correct integration and chemical shifts for the BOB receptor molecule along with the presence of dioxane solvent.

Following sample removal from the instrument a white precipitate had formed in the NMR tube. The NMR revealed a lack of sialic acid peaks in acetonitrile/dioxane mixture. It was

suggesting the resulting sialic acid starting material, and any product formed had precipitated out in the NMR tube overnight. It was apparent these solvent conditions were not appropriate for this sugar.

The deuterated solvent and precipitate were emptied out of the NMR tube and into a vial for solvent removal via spin vacuum. The resulting solid was dissolved in dimethyl formamide (DMF), to account for any product precipitation. The resulting proton NMR in DMF for the reaction is shown.

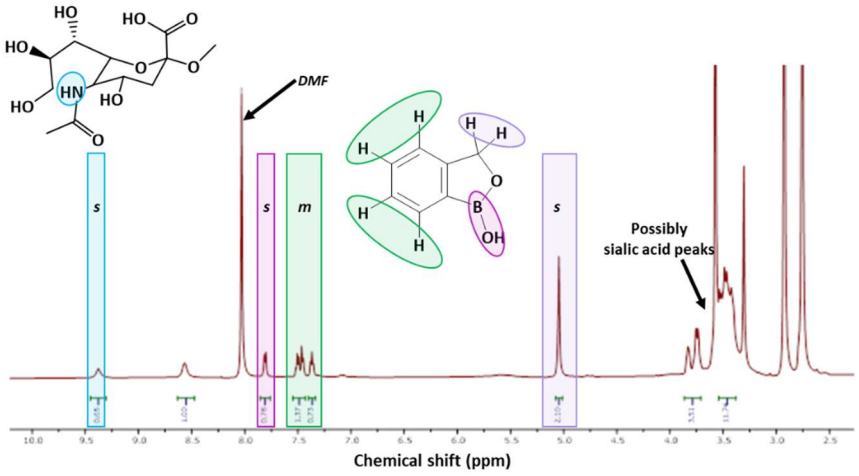


Figure 5-45: ^{1}H NMR (500 MHz, DMF, ACN, Dioxane)after spin-vacuum was used to remove the bulk of dioxane and acetonitrile.

The resulting NMR was an improvement over the previous NMR, since both the aromatic BOB peaks and the sialic acid peaks were now present.[389] Therefore, DMF was a better solvent for these species, so the reaction was repeated in the presence of deuterated DMF and after 24 hours an aliquot was taken and analysed via NMR. For comparison, the NMR of the reaction aliquot was stacked against the BOB and sialic acid proton spectra.

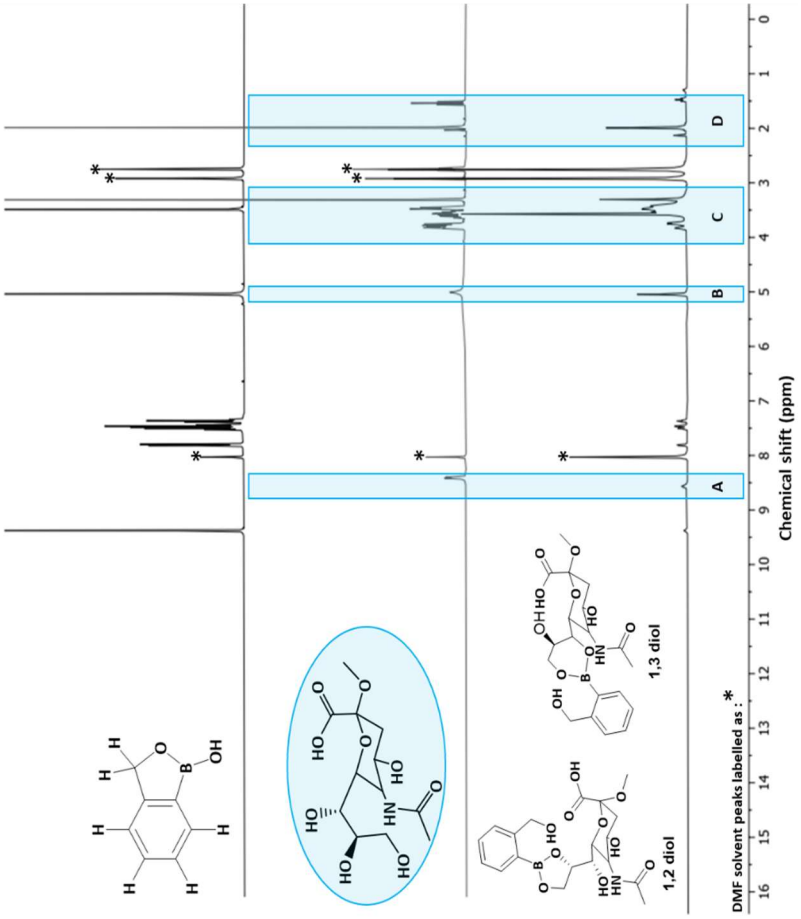


Figure 5-46: Stacked ^{1}H NMR (400 MHz, DMF) of BOB, N-Acetyl-2-O-methyl-α-neuraminic acid and the reaction mixture.

The NMR of the reaction mixture displayed some changes for the sialic acid proton peaks. For example, region C showed broadening of the sugar region which is indicative of boronate ester complexation from previously reported literature. [151,389,390] In addition, peak A which is believed to be due to (-NH) was observed to shift slightly indicative of a change in chemical environment. The BOB singlet at ~ 5 ppm was observed to shift. To complement the NMR, MS was also conducted which is more sensitive than NMR. It is expected there will be a mixture of species present (i.e. BOB, methylated sialic acid and any

complex formed). The TOF ES – revealed the presence of the desired boronate ester with sialic acid along with the presence of the starting sialic acid. The structures and their ions located are provided in the below section of MS. For the full MS showing all ions and peaks refer to the appendix (Appendix 9-26).

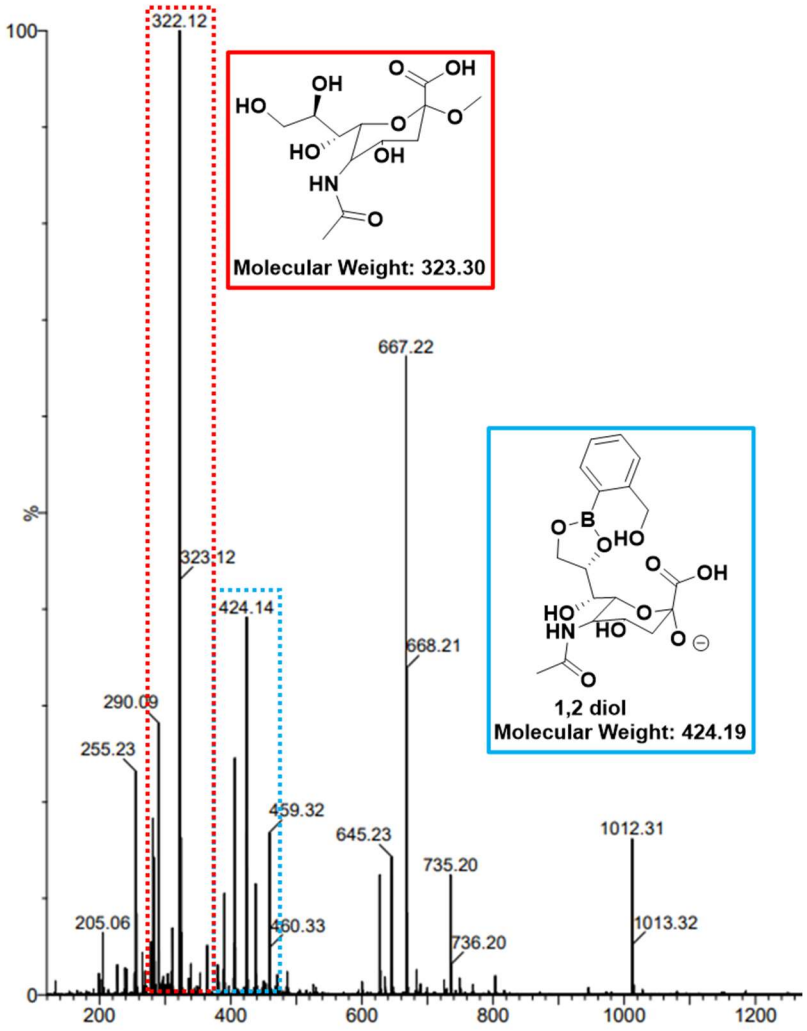


Figure 5-47: N-Acetyl-2-O-methyl-α-neuraminic acid.

The MS revealed the exact mass for the boronate ester (Appendix 9-25) confirming, that AABOB receptors can be used to bind to the glycerol moiety of N-Acetyl-2-O-methyl-α-neuraminic acid. However, as observed from the TLC following 24 hours (Figure 5-33) the reaction mixture still contained

significant presence of starting material. Hence, optimal conditions are yet still to be obtained to improve the yield of these boronate ester species.

Future experiments are required to confirm anything further. It is thought both the equivalences of BzCl and BOB could have been increased further. Increasing the BOB may have led to a greater amount of complexation via pushing the equilibrium position to the right. Additionally, to make the binding more favourable to the glycerol side chain, future experiments may entail the use of BOB molecules which possess a positively charged group on the benzene ring. Finally, MALDI MS may have provided better MS spectra, owing to the difficulties surrounding ionisation via ES methods.

IX. SUMMARY

To conclude, the boronate ester with stachyose was synthesised and its characterisation was successfully conducted indirectly via benzoylation and MALDI. The use of LC-MS was explored to try and separate out the boronate esters formed. However, the isolation of the species using a C18, or biphenyl column was not successful leading to complicated and unclear MS ions.

The synthetic protocol was applied to other charged sugars to see if we can target a wider range of sugars outside of fructose and stachyose which have little clinical relevance. Neuraminic acid is of key interest as it is commonly over-expressed in cancerous cells and present in abundance as a termini glycan of glycoproteins. Our studies revealed the formation of boronate-esters are possible with charged sugars and BOB type receptors. However, it was shown the reaction does not go to completion after 24 hours. Therefore, optimal conditions and hence further experiments are needed to optimise the equivalents of BOB, the solvent system , temperature, and reaction time. Alternatively, to ease the boronate ester formation it was postulated if modification of the BOB benzene ring may aid the boronate ester formation through complementary non-covalent interactions. These groups would be positively charged to better aid the ester formation. Thus, future work should focus on how to better target sialic acids glycerol side chain which is present on-going work within the Mendes group.

The rational for the next chapter, is to place the boronate-esters of stachyose onto the nanoparticles surface. The boronate-esters will be formed with the acrylamide-based receptors which will be able to participate in polymerisation reactions with the nanoparticles surface groups.

CHAPTER SIX

I. METHOD DEVELOPLEMT FOR THE FORMATION OF MOLECULAR IMPRINTS (MI)

In this chapter, we delve into the development of specific cavities on the surface of PS nanoparticles that can selectively bind to glycan motifs (Figure 2-2), including the clinically significant sialic acid. The stachyose boronate ester formation has proven effective and will be utilised in the creation of MINPs. This research has the potential to significantly advance the field of nanotechnology by providing a new method to synthesise MINPs with high selectivity and affinity for oligosaccharides.

Our objective is to create reliable water-soluble PS nanoparticles that contain sugar-binding receptors arranged in the optimal spatial orientation for efficient binding. Previous studies have successfully developed molecularly imprinted nanoparticles (MINPs) for caffeine, cholesterol, and phenylalanine via emulsion polymerisation. [204,391,392] However, more research is needed on producing MINPs with high selectivity and affinity for oligosaccharides in biologically relevant media. [204] This gap in the field necessitates further exploration and investigation.

Emulsion techniques offer a multitude of advantages when it comes to imprinting core-shell particles. They enable the utilisation of a diverse range of materials, such as styrene,

divinyl benzene, and methacrylate derivatives, to yield consistently uniform monodisperse particles. [392] This method involves forming cavities that ensure the precise placement of templates on the surface, allowing for efficient template diffusion in and out of pockets while preventing any entrapment within the polymeric scaffolds. [392] The resulting suspensions will undergo a comprehensive assessment using various techniques like DLS, ZP, TEM, and ITC to determine the level of MI attained.

II. DEVELOPMENT OF GLYCAN IMPRINTS ON NANOPARTICLES.

The prior works has established PS nanoparticles as stable supports that can withstand fluctuations in pH levels. These supports can be altered through free-radical polymerisation reactions to increase solubility in water. The current project aims to use these nanoparticles to create imprints on their surfaces, as previously outlined in Figure 2-2. To achieve this, stachyose boronate-esters from Chapter Five will be employed. The tetra saccharide for imprinting is depicted below comprises galactose, glucose, and fructose monomers, as Figure 6-1 illustrates.

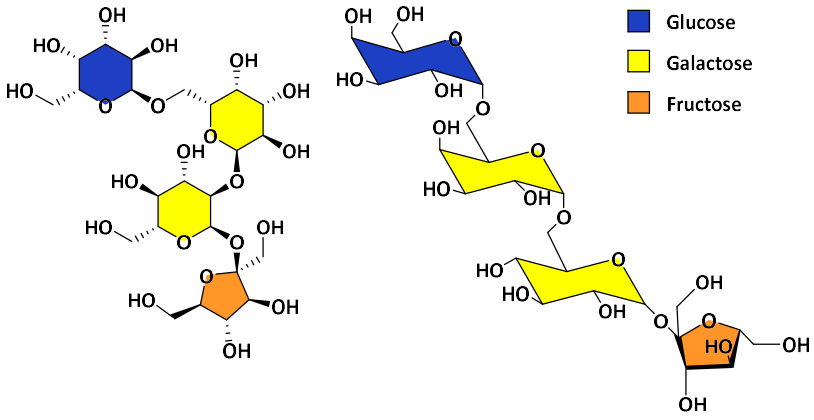


Figure 6-1: Stachyose in its ring conformation on the left- vs its natural formation in aqueous conditions. Stachyose is composed of α-D-galactose, α-D-glucose, and β-D-fructose units. The fructose monomer in its natural conformation exists as a furanose 5 membered ring in contrast to the other monomers which naturally exist as a pyranose form

Using the process outlined in Synthesis of water-soluble polystyrene nanoparticles, new nanoparticles were created and treated with DHEBA, resulting in a surface area of 7853 nm^2 (see Polystyrene nanoparticles calculations for details). Previous studies have shown that stachyose boronate esters have a much smaller surface area of approximately nine nm^2.[203,209] To estimate the number of theoretical molecules and mass, a protocol was established based on the assumption that the particles were uniform in size and spherical and that no side reactions occurred under optimal conditions. These calculations provide a starting point and may cover up to approximately half of the particles' surface.

To create molecular imprints (MI) on PS NPs, we followed a protocol adapted from a previous publication within the research group. [203] In a 5 mL round bottom flask, 750 µL of polystyrene nanoparticles and 100 µL of SDS 0.1% w/v, along with 2.95 mg of a complex in 2 mL phosphate buffer pH 8 was added. After stirring and degassing the solution, the polymerisation was initiated by adding APS and TEMED. The DHEBA cross-linker was added five minutes later to form a polymeric scaffold around the boronate ester. The solution was left to react for an additional 15 minutes. The full protocol is provided, refer to: Development of polystyrene nanoparticles baring pocket imprints.

Table 6-1 presents the results of the analysis of the nanoparticles using DLS, ZP, and TEM to identify any alterations in their size. Considering their already diluted nature, the crude particles underwent an initial DLS assessment without any dilution. The DLS analysis revealed an increase in the particles'

hydrodynamic diameter and a notable rise in polydispersity, as depicted in Figure 6-2.

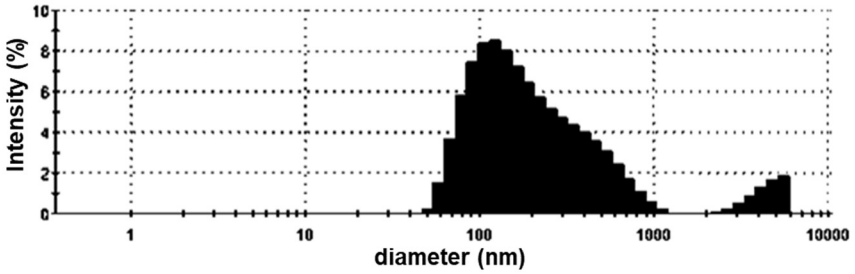


Figure 6-2: DLS histogram produced for the trial of developing MINPs. Several populations were present to give an averaged (n=3) hydrodynamic diameter of 162 ± 7 nm and a PDI value of 0.37 (±0.01).

There was a suspicion that precipitation within the solution led to the formation of particles larger than 1000 nm in size. The presence of these particulates, as depicted in Figure 6-3

Figure 6-3: Precipitate present at the end of the reaction for DHEBA functionalised polystyrene nanoparticles with the boronate ester complex.

, would impact the instrument's count rate, altering the correlation function and indicating an added population of particles in the DLS intensity histogram (C.f. ***Dynamic light scattering (DLS) and zeta potential (ZP)***). [244,351] However, the correlation function (raw data) did not depict multiple exponential decays which are typically observed for extensive precipitation. This validates the accuracy of the measurements and rules out any discrepancies. [244] Nonetheless, the solution exhibited signs of precipitation, which impeded the possibility of conducting ITC analysis.

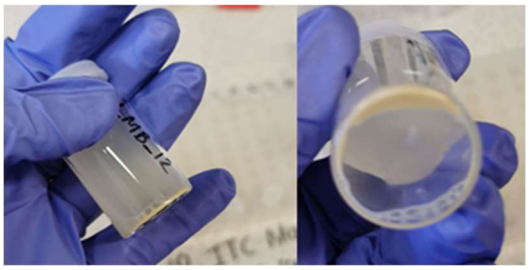


Figure 6-3: Precipitate present at the end of the reaction for DHEBA functionalised polystyrene nanoparticles with the boronate ester complex.

Microscopy was also conducted to supplement DLS. However, it was difficult to view the particulates under the microscope. This is usually observed when one of the following occurs: agglomeration during drying on the grid, excessive staining, insufficient particle concentration, or unstable particles. This could be because of the small amount of nanoparticles (~ µL) used in these reactions. A tabulated summary is below.

Table 6-1: Tabulated summary of data collected from the first trial of producing MINPs.

Technique	Data
DLS	162 ± 7 nm
ZP	-22 ± 1.7 mV
PDI	0.37 ± 0.011
TEM	62 ± 12 nm

The variance observed in DLS measurements can be attributed to the presence of molecular sieves. Molecular sieves play a crucial role in synthesising boronate esters by eliminating any trace of water in the reaction mixture (Figure 5-9). Following this step, the product is centrifuged to obtain a precipitate. Nonetheless, the final pellet obtained from centrifugation may also contain degraded molecular sieves (C.f. ***Preparation of the glycan-boronate complex***). As a result, large solid particles stemming from the sieves may have overestimated the DLS diameter. To verify this, an additional measurement conducted after filtering the isolated solution would have been helpful. Furthermore, the quality of the TEM images could have been improved. The number of nanoparticles counted needed to be increased (less than 200 particles), meaning that the particles measured may not represent the entire sample.[290]

Three fresh batches of the stachyose boronate-ester complex were synthesised to replicate the previous experiment and explore two new conditions (Preparation of the glycan-boronate complex). This study aimed to analyse the impact of varying the boronate-ester complex. The reactions were categorised as A-C, as Table 6-2 illustrates.

Table 6-2: Tabulated quantities of complex trialled, to assess the stability and size of particles in relation to different amount of complex used.

ID	Complex quantity placed into 2mL buffer
A	4 mg
B	3 mg
C	1 mg

The experiment was repeated with the previous protocol but with a notable deviation. Unfortunately, due to COVID-19-related needle shortages, degassing and purging the glassware with nitrogen was not feasible. It is worth mentioning that the existence of oxygen can hinder the efficacy of free radical polymerisation reactions.[324] While creating the complex solution (Table 6.2), there were difficulties in dissolving solutions A and B. As a result, it would be advisable to experiment with various solvents for molecular imprinting in future reactions. After adding the polymerisation agents, the reaction was left to stir at room temperature for 15 minutes (C.f. ***Development of polystyrene nanoparticles baring pocket imprints***).

After completing the polymerisation process, both reactions A and B showed the presence of solid particles in the solution. To ensure accurate size analysis through DLS, it was necessary to filter the solution using a 0.22 µm syringe filter. The previous histograms may have been distorted due to the existence of large aggregates. The filtered solution was then analysed using

TEM to determine the size. Interestingly, no increase in size was observed via TEM. To eliminate any bias, around 400 nanoparticles were measured, and the average diameter was found to be 51 ± 10 nm (with a population size of 391 particles).

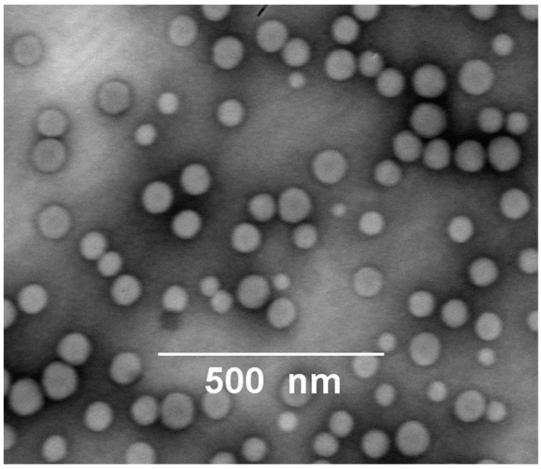


Figure 6-4 TEM image displaying dispersion of polystyrene nanoparticles following their reaction with boronate esters (reaction A). The particles had an average diameter of 51 ± 10 nm (population size = 391 particles).

The microscopy images showed that the particulate sizes were heterogeneous, which was different from the previous batches of nanoparticles (Figure 4-47). The presence of precipitation led to the hypothesis that there was an insufficient boronate ester complex to functionalise the particles to the desired extent (~1/2 surface coverage). This resulted in some of the particulates remaining unfunctionalised, thereby producing a wider range of sizes observed by TEM (i.e. SD = ± 10 nm). The previously synthesised DHEBA functionalised particles, known to provide a diameter of around 50 nm by microscopy (Figure 4-47 & Appendix 9-10), concluded that the particles'

functionalisation was incomplete. Ultimately, all three nanoparticle samples displayed white solid particulates that flocculated following storage for some time, further validating the findings of an unstable suspension that was yet to be optimised.

III. INCORPORATION OF ORGANIC SOLVENTS FOR MOLECULAR IMPRINTING

To improve the solubility of the stachyose boronate ester complex in water-based reactions, DMF was added to the molecular imprinting process—this modification aimed to circumvent the precipitation and enhance the reaction. The boronate ester complex was dissolved in DMF before being added to the nanoparticles for polymerisation. The DLS analysis of the resulting nanoparticles is presented below.

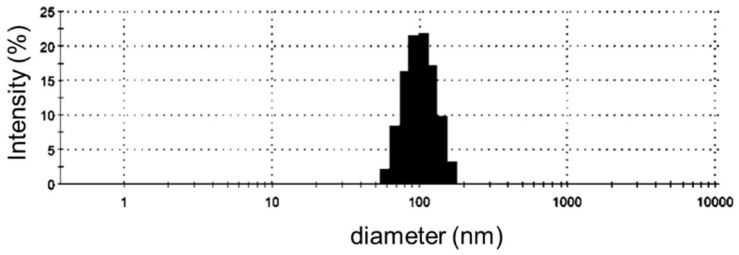


Figure 6-5: DLS histogram for PS nanoparticles after MI of the complex (DMF. A hydrodynamic diameter of 100 ± 3 nm (PDI: 0.053 ±0.02) was obtained.

The data presented demonstrate a significant improvement in the particles' polydispersity (Table 6-1), with an average size of around 100 nm and a PDI of 0.05. DLS therefore indicates the possibility of surface modification (25% increase, Appendix 9-10) , while the zeta potential of -23.5 mV suggests intermittent stability in the solution.[241] Purification of the particles was

necessary to perform ITC to determine if they contained any imprints. This will next be discussed.

IV. PURIFICATION OF NANOPARTICLES AFTER MOLECULAR IMPRINTING

Following the reaction with the stachyose boronate ester, the nanoparticles required purification before conducting ITC binding studies. This process involves removing the stachyose template from the particle surface to reveal MI cavities. In previous literature, centrifugal washes were used for the purification and template removal of MINPs synthesised via emulsion polymerisation methods. [204,351] Therefore, this method was also assessed in this study. To remove the template, the pH of the nanoparticle solution was lowered below the pKa of the benzoboroxole to break the boronate ester bond. The nanoparticles were diluted into ammonium acetate buffer (pH 5.6, 0.5% surfactant) and left to stir at room temperature for an hour before centrifugation. The centrifugal washing steps aimed to collect the nanoparticles as a white pellet and leave the unbound template molecules and other reagents in the supernatant. The centrifugal conditions evaluated for these particles are tabulated in Table 6-3.

Table 6-3: Tabulated summary of centrifugation conditions (Beckman XPN 80, Type 70 Ti Rotor) trialled for the template removal from the MINPs.

Rota Speed (RPM)	Duration (minutes)	Observations
32,000	60 minutes	White pellet with yellow hue
	30 minutes	
	15 minutes	
15,000	15 minutes	White pellet

Challenges arose in the nanoparticle purification process following the addition of the boronate ester complex to their surface. The primary issue was that the particles remained suspended in solution despite centrifugation, due to their low density. To address this, an ultra-centrifuge (Beckmann XPN 80) was trialled. Precipitation had been previously used to isolate nanoparticles as a pellet, but using a co-solvent for precipitation may complicate subsequent ITC binding studies.

For an accurate assessment of the heat produced from a potential binding interaction between imprinted particles and the target molecule (stachyose), it was crucial that the sample and reference cell used in ITC had identical solvent compositions. The presence of any additional solvent in the sample that could not be matched in the reference cell would lead to a 'buffer mismatch,' thereby compromising the accuracy of our results.[393–395]

Tests with various speeds and times of centrifugation were conducted to obtain a clear supernatant and white pellet

particles without the use of a co-solvent. We found that 15,000 RPM (revolutions per minutes) for 15 minutes was the most appropriate condition to achieve the desired outcome. Although higher speeds resulted in a more transparent supernatant, they caused the particles to turn yellow, which was undesirable. Additionally, speeds exceeding 30,000 RPM produced a yellow gel, indicating polymer degradation.[329,396]

To validate the applicability of these conditions, we subjected DHEBA functionalised polystyrene nanoparticles to the same centrifugation conditions. They all formed a white pellet with no gel formation, indicating that these conditions were suitable for light polymeric particles. After centrifuging polystyrene nanoparticles, we needed to determine whether any binding occurred.

V. ITC BINDING STUDIES OF POLYSTYRENE NANOPARTICLES

Before conducting the ITC binding studies, it was necessary to establish controls and a suitable reference. The nanoparticles underwent boronate ester treatment, which was dissolved in approximately mL of DMF. Although the particles were washed through centrifugation and isolated as a white pellet, it was uncertain that all traces of the solvent were removed. To ensure no lingering traces of DMF, the imprinted particles were freeze-dried, resulting in a fine white powder weighing 23.3 mg.

To conduct the binding study, stock solutions of 2 mg/mL of imprinted PS nanoparticles and 80 mM stachyose were prepared. A phosphate buffer (20 mM, pH 8, 0.5% SDS) was used as a solvent for both stock solutions to promote the formation of boronate esters between the AABOB receptors present on the surface of the imprinted PS nanoparticles and stachyose. The ligand concentration was set to be intentionally higher, to add excessive equivalences of ligand per ITC injection. This allows significant stepwise increases which can aid signal – to – noise when studying very weak binding systems or systems at low concentrations.[252] Finally, the solutions were filtered and degassed before being inserted into the ITC instrument.

The instrument was set up to inject 2 µL of stachyose (80 mM, pH 8) into the ITC cell 40 times while measuring the heat throughout the titration. The stirring rate was set at 125 rpm, the temperature was maintained at 25 degrees Celsius, and the

peak height-to-width ratio was set to medium. The instrument waited between injections for 180 to 300 seconds.

The heat produced for the dilution of stachyose (ΔH dil) was first recorded to assess the instrument status and provide a control isotherm.

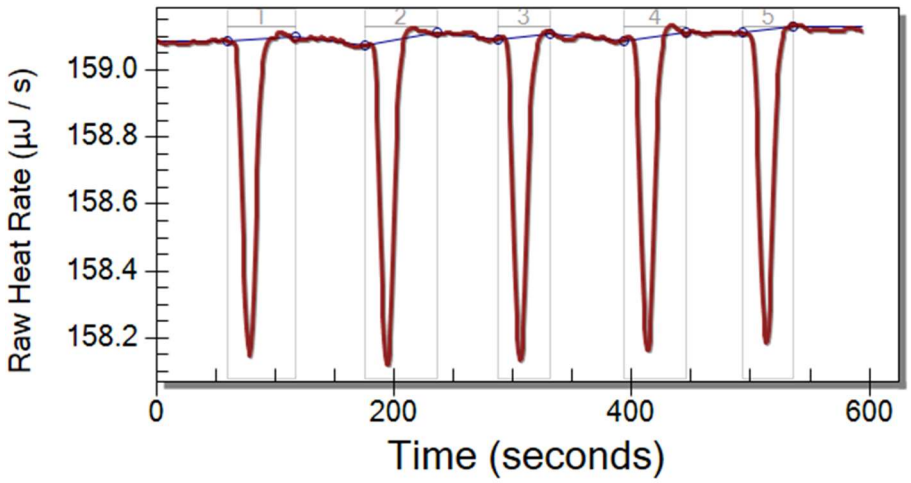


Figure 6-6: Raw data produced for the heats (exothermic) produced from the dilution of 80 mM stachyose into phosphate buffer (20 mM, pH 8, 0.5% SDS).

A control experiment was performed using stachyose (Figure 6-6) to confirm the cleanliness of the ITC cell and its readiness for binding experiments. The injection baseline remained consistent during the experiment, indicating that the cell was suitable for subsequent binding experiments. The interval of 150-300 seconds was appropriate for the instrument to return to baseline before the next aliquot of ligand was injected.

To ensure that only interactions between particles and sugar were measured, the heats of dilution for stachyose (ΔH dil

stachyose) were averaged and subtracted from subsequent binding measurements.

Next, nanoparticles' binding capacity towards stachyose was assessed. The imprinted nanoparticles (2 mg/mL) were placed into the ITC cell, while stachyose (80 mM) was placed into the instrument's syringe. No bubbles were introduced into either the reaction cell or syringe since bubbles can cause erroneous baselines and heat.

The ITC instrument parameters were kept the same for the experiment. For more information on the experimental parameters, refer to: ***Isothermal titration calorimetry (ITC)***. However, the corresponding experiment did not show any significant binding between nanoparticles and stachyose (Figure 6-7). The heats from these injections were all under 1 µJ/s following the subtraction of controls (ΔH dil stachyose & ΔH dil nanoparticles (Appendix 9-27).

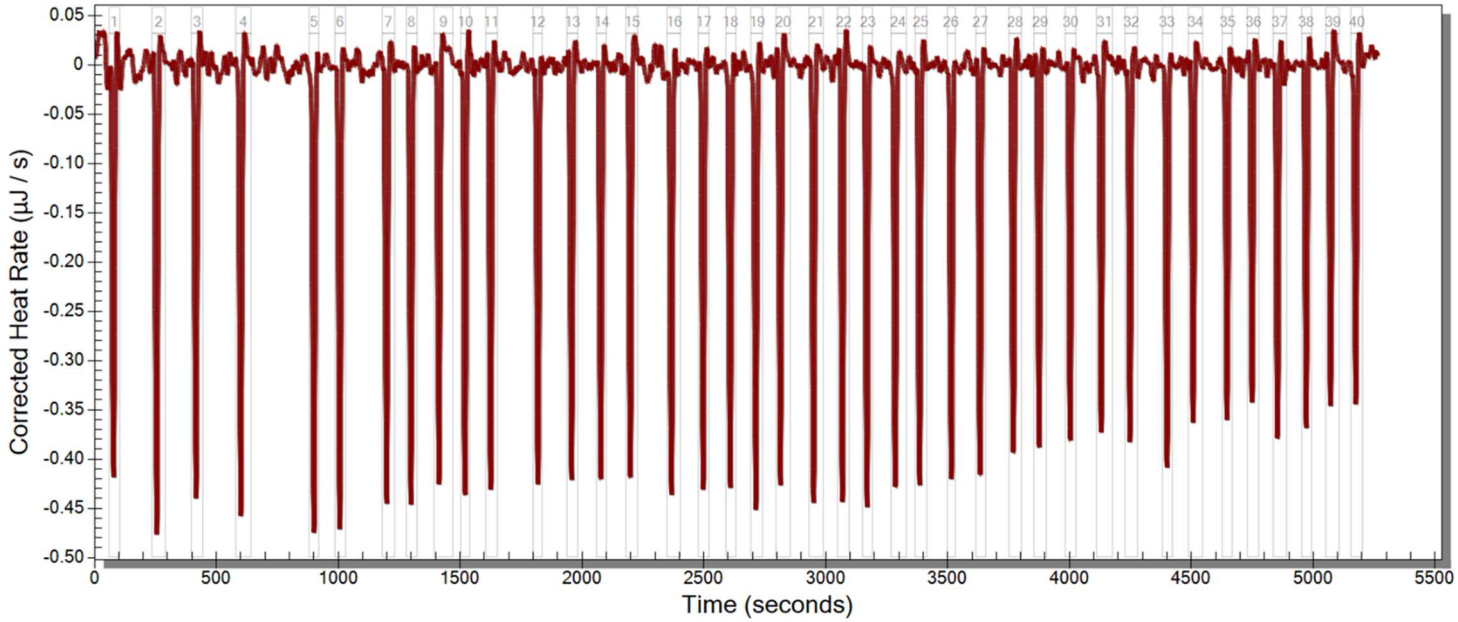


Figure 6-7: ITC raw heats produced for the interaction of imprinted nanoparticles (2 mg/mL) with stachyose (80 mM) at pH 8 (20 mM phosphate buffer).

Based on the absence of a sigmoidal curve in the isotherm, there was no binding between the nanoparticles and stachyose. This suggests that the surface of the nanoparticles does not contain any boronic groups, and therefore, no MI occurred. To determine if the nanoparticles became unstable as a result of freeze drying, a sample of 2 mg of the dried-out nanoparticles was reconstituted in buffer and analysed using DLS. Prior to analysis, the solution was filtered with a 0.5 µm syringe filter to eliminate any precipitation or large aggregates. DLS analysis revealed an average diameter of 3539 nm (PDI = 0.82).

During the preparation of nanoparticles for ITC (Figure 6-5), it was noted that their size was approximately 100 nm. Unfortunately, the nanoparticles irreversibly aggregated during the drying process, forming large agglomerates (> 3000 nm) that reduced the available binding pockets. This led to minimal or no heat production during ITC, as shown in Figure 6-7. Despite employing ultrasonication to resuspend the particles, stable suspension could not be achieved as per DLS diameter measurements. Consequently, a new batch of DHEBA nanoparticles and boronate ester complex were synthesised, and the imprinting reaction was reattempted, as explained in the "***Development of polystyrene nanoparticles bearing pocket imprints***" section.

After polymerising the nanoparticles and complex, the residual DMF solvent was not removed by drying. This approach was taken to assess whether adjustments need to be made to the existing nanoparticle protocol to investigate stable nanoparticles using ITC. Drying the nanoparticles could have

compromised their morphology and any developed surface features.

The experimental protocol referenced in the passage, "***Development of polystyrene nanoparticles baring pocket imprints***," was conducted both with and without DHEBA. The inclusion of DHEBA enhances the particles' selectivity and restricts the conformation of AABOB receptors on their surface, thereby increasing their selectivity towards the target. It is essential to consider the cross-linking density to achieve optimal results. The suspensions that resulted from the study were analysed using DLS, ZP, and TEM techniques before moving on to ITC. A table summarising the size analysis of the imprinted particles in the presence and absence of DHEBA is provided below.

Table 6-4: Tabulated summary of the size analysis conducted for crude nanoparticles imprinted in the presence and absence of DHEBA.

	Imprinted in presence of DHEBA	Imprinted in the absence of DHEBA
Hydrodynamic diameter (nm)	100 ± 3	113 ± 3
Zeta potential (mV)	- 24 mV	- 23 mV
Polydispersity	0.05 ± 0.023	0.10 ± 0.005
Microscopy diameter (nm)	56 ± 9 (Population size = 358 particles)	55 ± 9 (Population size = 265 particles)

The hydrodynamic diameter and zeta potential observed via DLS was consistent with the previously reported data (Figure 6-5). Of interest the particles lacking the DHEBA polymeric scaffolding displayed a greater degree of polydispersity. However, it is known that the values reported via DLS are heavily dependent on external factors as previously discussed**.** Thus, the difference in concentration owing to the lack of DHEBA added into the reaction mixture may have attributed to the discrepancies observed (Table 6-4).

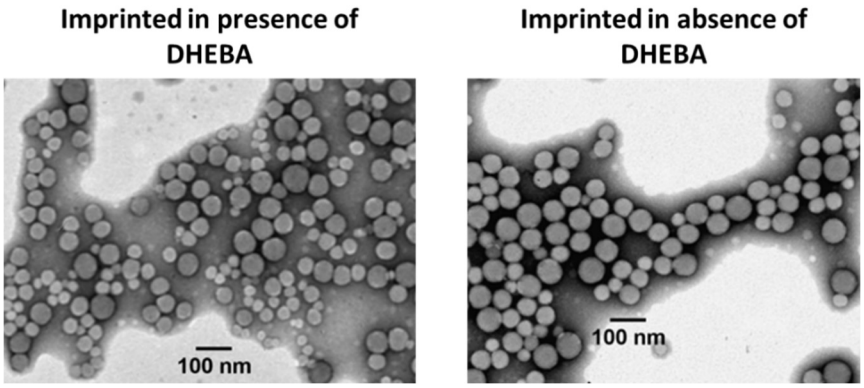


Figure 6-8: Microscopy images for the nanoparticles after imprinting with and without DHEBA cross-linker. Both particle batches were observed to possess a similar distribution of sizes present.

The microscopy images (Figure 6-8) confirmed that there was slight difference in the size and polydispersity within the two batches of nanoparticles. Following the MI protocol the nanoparticles were observed to increase in size by 11 % in comparison to their DHEBA functionalised nanoparticle predecessor (Table 4-4). The increase in diameter indicated a change on the nanoparticles surface may had occurred. To

confirm this ITC was next conducted following template removal via centrifugation.

The ITC experiments were conducted as previously described (Isothermal titration calorimetry (ITC)) to provide the following isotherms – Figure 6-9 & Figure 6-10.

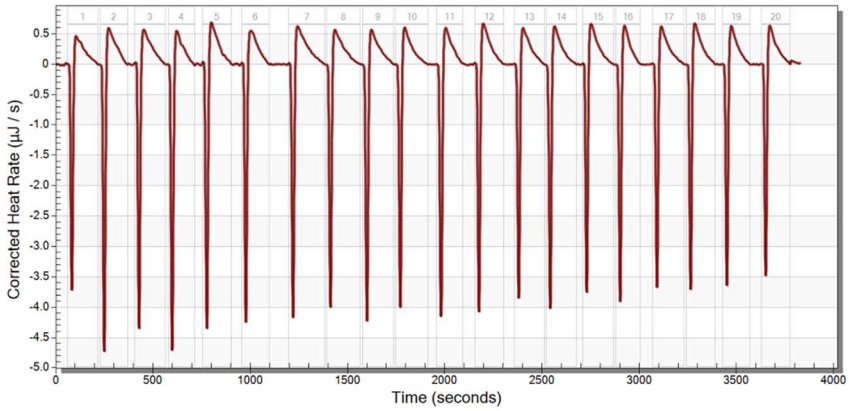


Figure 6-9: Corrected heats produced for the reaction of imprinted polystyrene nanoparticles (DHEBA) with stachyose at pH 8.

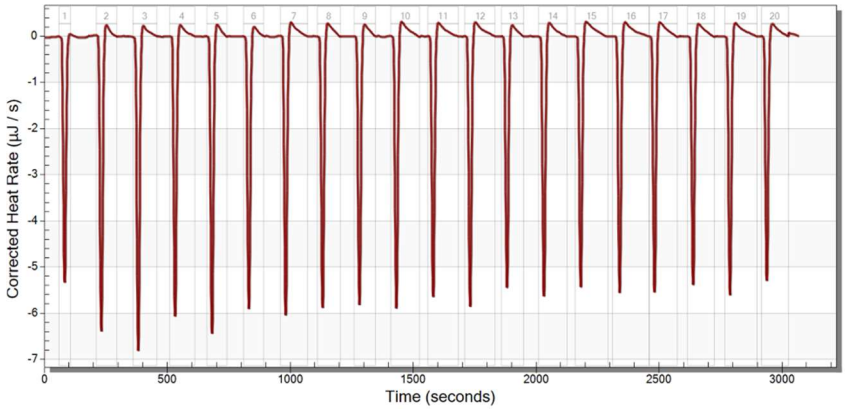


Figure 6-10: Corrected heats produced for the reaction of imprinted polystyrene nanoparticles (without DHEBA) with stachyose at pH 8.

Both batches of nanoparticles displayed exothermic isotherms however, neither isotherm displayed a clear binding isotherm. Any heats produced from these reactions were thought to be due to the inherent “buffer mismatch.” When the sample cell and syringe do not contain 100% the same solvent system erroneous heats can be produced. [395]

For example, a previous study found that the presence of just 2% organic solvent (red isotherm of Figure 6-11) was found to cause incorrect heats of reaction to be observed, which in the case of this study resulted in a reduction in the observed binding. When the solvents were matched a clear binding sigmoidal isotherm was produced (blue isotherm of Figure 6-11). [394]

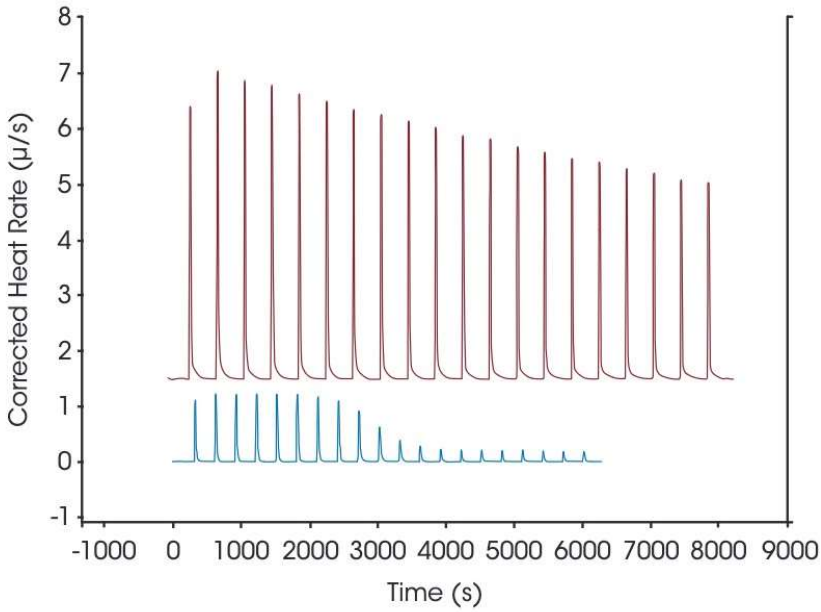


Figure 6-11: ITC isotherms taken from literature [394] to illustrate the discrepancies in the heats produced when buffer mismatch is present. The blue isotherm depicts a steeper change in heats produced and hence a clearer inflection points for when the solvents are matched well in both the syringe and cell. In contrast, the red isotherm depicts inaccurate heats with a shallower binding profile due to buffer mismatch in the cell and syringes.

Furthermore, the isotherms produced displayed clear over shooting of the signal upon returning to baseline and a negative compensation power (µJ / s). The heats occurring below zero compensation power are an instrumentation error, indicating the reactions exothermicity drives compensation to below zero, thus invalidating the collected data for collection of thermodynamic parameters (i.e. Ka). [395] To resolve this, adjusting the reference power of the instrument may have aided

this. Regarding the signal overshoot, this may have been resolved in subsequent ITC runs via modulation of the feedback to a lower setting. [247]

If the overshooting is not related to the feedback setting, the observed phenomena may have arisen due to numerous other reasons. Such as, several ligand binding processes at different sites with different binding affinities, or single binding event composed of two sequential steps occurring at separate times. [247] Thus, additional experiments with different temperature, ionic strength, buffer composition should be trialled to assess whether a real binding event appears under different conditions.

A possible reason for the lack of binding profile observed for the nanoparticles following MI (Figure 6-9 & Figure 6-10) may be due to the purification procedures. During the centrifugation washes and template removal, the nanoparticles would often form a yellow solid as previously discussed. [329,396] The reduction of the centrifugation speed although solved the formation of the yellow gel like substance. It resulted in not all nanoparticles being precipitated out of solution and thus a significant loss in yield of particles. Furthermore, the resuspension of the particles into water was not always successful with large precipitates often having to be filtered from the suspension. Thus, resulting in an overall reduction in concentration of nanoparticles and hence a reduction in the number of potential binding sites. To verify if the centrifugation process resulted in an unstable suspension the nanoparticles size and polydispersity were measured (C.f. Table 6-5). The particles

polydispersity and diameters were both observed to increase in size following the purification.

Table 6-5: Summary of the polydispersity (PDI) and hydrodynamic diameters from DLS for the MINPs with and without DHEBA cross-linker.

	MI with DHEBA	MI without DHEBA
DLS	150 ± 4 nm	214 ± 6 nm
PDI	0.24 ± 0.01	0.25 ± 0.01

The nanoparticles used in the ITC experiments showed significant increases (50% for MI with DHEBA and 89% for MI without DHEBA) in their polydispersity following their purification (Table 6-5). Thus, the data suggests there was an issue with the purification process. The extensive use of ultra-centrifugation may have led to a change in the particles morphology which other authors have elsewhere raised the same concerns on the impact of centrifugation forces. [331,351] TEM revealed the presence of agglomeration, with many of the grids displaying overlapping particles, as illustrated via Figure 6-12.

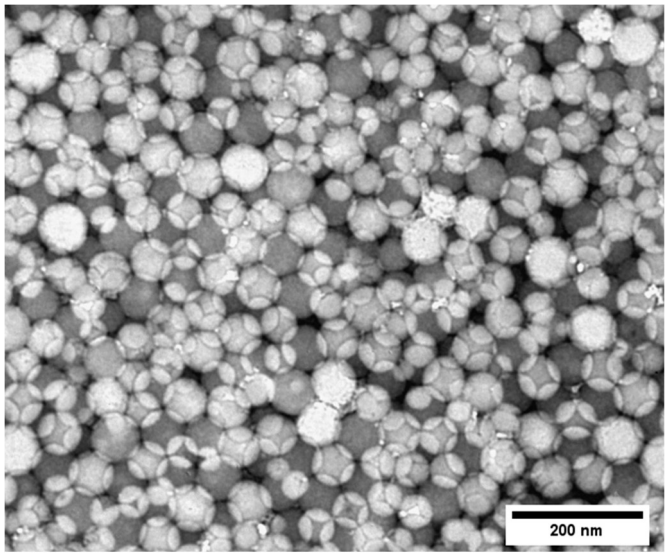


Figure 6-12: TEM image of polystyrene nanoparticles following centrifugation for the purification of PS nanoparticles following MI.

To conclude, it was thought the significant presence of agglomerates due to the high centrifugal force required for purification may have hindered the ITC binding studies. The centrifugation was necessary to remove the template and DMF used during the imprinting process to conduct ITC. Thus, an alternative purification method for these particles is required to remove the DMF and the stachyose from the particles which does not result in particle deformation due to excessive ultracentrifugation speeds. Alternative filtration-based methods and dialysis may be used. However, filtration-based methods such as use the of filtration centrifuge tubes result in significant caking and arduous long processing times due to the relatively small volume of sample that can be processed for each run.[331] The use of dialysis permits the use of larger samples for processing, however, reports have claimed it "inadequately removes large molecule impurities." [331] Thus, both methods do

not offer significant improvements over the use of ultracentrifugation. Therefore, a new suitable method is required for purification.

VI. APPLICATION OF SOLID-PHASE SYNTHESIS TO POLYSTYRENE NANOPARTICLES

The previous experiments entailed the use of washing the template away with acidic buffer and several centrifuges runs to separate the MINPs away from the template ready for ITC binding studies. However, the process was arduous, not consistent and led to a significant increase in the polydispersity of the particulates which was thought to be due to particles coalescing. Thus, an alternative method is required to purify the nanoparticles. The aim of this section is to explore alternative methods.

An alternative strategy for the template removal from the nanoparticles trialled involved the use of a solid support. The idea was to attach the nanoparticles to a solid support, to mitigate the need of using a centrifuge. An illustration of this idea is outlined in Figure 6-13. Briefly, this idea entails the use of a glass bead which has the template attached to the surface. The addition of the AABOB receptor to the glass beads thus results in the formation of boronate esters, providing a solid support with the template of interest for MI attached to. Any unbound AABOB receptor can be easily washed away to leave the glass beads with the boronate esters of interest. Next the polystyrene particles previously synthesised are added to the glass beads. Since the polystyrene nanoparticles possess terminal alkene groups these can be polymerised to the AABOB receptors covalently bound to the sugar and hence the glass bead. The net result is polystyrene nanoparticles with the

template attached to the surface via the use of a solid support. Finally, DHEBA may be added to add an extra layer on the nanoparticles around the template to form a polymeric scaffold which should increase the selectivity of the particles towards the template.

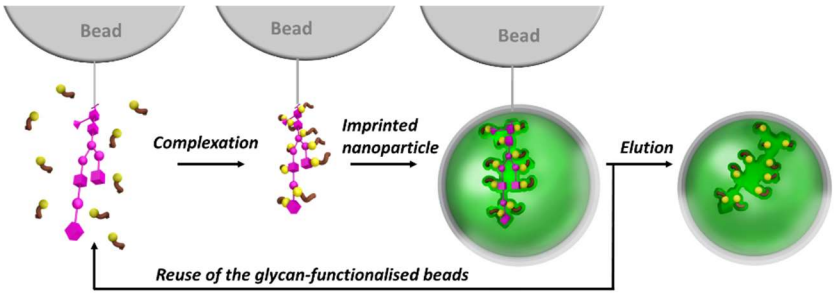


Figure 6-13: Use of glass beads to facilitate washing steps of polystyrene nanoparticles.

The resulting MINPs may be purified by breaking the boronate ester bond which cleaves the particles from the functionalised glass beads. Thus, this process removes the need for arduous centrifugation steps. This idea takes inspiration from literature in which MI is conducted on a solid surface to permit the use of heat or pH modulation to remove the template from the polymeric particles. [232,233,397] Some examples were previously discussed in the literature review (molecularly imprinting on a 3d surface). The synthesis of the glass beads required will next be discussed.

VII. PREPARATION OF GLASS BEADS FOR MOLECULAR IMPRINTING

To trial this method, the glass beads were first prepared utilising a previously reported method from literature. First the glass beads (75 µm diameter, 1g) were activated by boiling in 4 M NaOH (0.8 mL) at 100 °C for 15 minutes after which they were washed with ultra – pure water until the pH of the solution was around 7. Finally, the activated glass beads are washed in acetone prior to drying in an oven at 80 °C for 3 hours. For the full experimental protocol for the activation of glass beads refer to Preparation of the glass beads. Next, the glass beads were salinised via the addition of (3-aminopropyl)trimethoxysilane (APTMS) to the dried beads to provide a terminated amine group for the attachment of the sugar template to be imprinted onto the polystyrene nanoparticles (C.f. **Silanisation of glass beads ready for MI**.). An illustration of the preparation of the glass beads is shown in Figure 6-14, this procedure was conducted by Dr Norman within the Mendes research group owing to the limited laboratory access due to COVID-19.

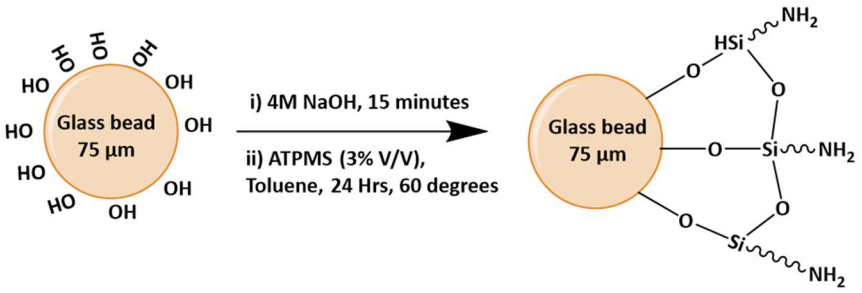


Figure 6-14: Reaction scheme for the salinisation of glass beads used in the solid phase synthesis of MINPs.

Following the preparation of glass beads, next a sugar template was selected for MI, the template required a compatible functional group to covalently bind to the amino functionalised glass beads (Figure 6-14) Therefore, the commercially available 3-aminopropyl-β-d-lactose (Figure 6-15) was used for these imprinting trials owing to the amino functional group.

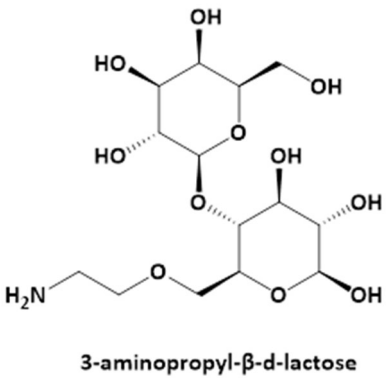


Figure 6-15: Sugar (3apLac) used in the MI of polystyrene nanoparticles using glass beads as a solid support.

Following the addition, of the sugar to the glass bead surface (Functionalisation of glass beads with 3-aminopropyl-β-d-lactose for molecular imprinting.) the beads were used for the

formation of boronate esters for MI conducted by Dr Norman (Preparation of the glycan-boronate complex). Briefly, to a 6:1 anhydrous dioxane: acetonitrile mixture (700 µL), 250 mg of 3apLac functional beads, 5-acrylamido-2-(hydroxymethyl)phenyl boronic acid cyclic monoester (AABOB, 1.55 mg, 7.01 µmol) and molecular sieves (100 mg) was added. The reaction was sealed and purged with argon for 10 minutes. Following degassing, the solution was heated to 90 °C and left to react overnight. The resulting glass beads were purified via washing with more acetonitrile and dioxane (anhydrous 6:1 mixture, x5, 10 mL) before transferring to a clean 10 mL round bottomed flask and dried in a vacuum oven at 80 °C for 3 hours.

The functionalised glass beads are now ready for their reaction with polystyrene nanoparticles to begin MI. The glass beads have been used by Dr Norman within the group to previously show that MI when conducted around the sugar on beads provided acrylamide based polymeric nanoparticles which are selective for their target. A binding isotherm was observed via ITC for the reaction of the MINPs and lactose, however no binding was observed when in the presence of stachyose. Thus, displaying a high degree of selectivity. However, due to the weak heats produced no binding constant (Ka) could be calculated for these series of reactions (Figure 6-16).

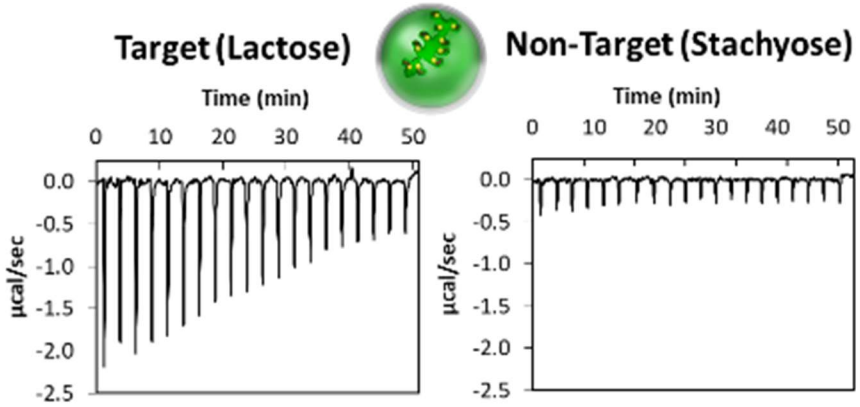


Figure 6-16: ITC isotherms conducted by Dr Norman within the Mendes research group for the molecularly imprinted polymeric nanoparticles for the selective detection of Lactose. The beads displayed a weak binding isotherm towards Lactose but not binding was observed when the beads were exposed to stachyose (non-template).

The experiments conducted by Dr Norman were used as a starting point for the synthesis of MI polystyrene nanoparticles baring a pocket selective for lactose. Thus, the aim is to study the polystyrene nanoparticles synthesised within this section via ITC which has so far proven challenging.

VIII. INCORPORATION OF FUNCTIONALISED GLASS BEADS TO AID THE DEVELOPMENT OF MINPS

This section aims to use the glass beads synthesised by Dr Norman to form MINPs using the previously synthesised polystyrene nanoparticles (C.f. ***Synthesis of water-soluble polystyrene nanoparticles***). The two experiments were proposed for this trial, denoted imprinted and non-imprinted. The non-imprinted particles were used as a control, the synthesis previously described within this chapter does not include the addition of AABOB to the glass beads. Thus, the addition of DHEBA polystyrene nanoparticles will not result in boronate ester formation and thus no isotherm should be detected via ITC for these series. In contrast, the imprinted glass beads possess the acrylamide group of the AABOB receptor and can therefore participate in free radical polymerisation reaction with the nanoparticles DHEBA groups.

The previously synthesised nanoparticles (1 mL, phosphate buffer pH 9) was added to 500 mg of functionalised glass beads. The reaction was sealed before adding APS (22.9 µL, 87 mM) and TEMED (1µL) and was left to react for 15 minutes. The beads were first washed with pH 9 phosphate buffer to remove any loosely non-specifically bound polystyrene nanoparticles. Followed by pH 7 buffer and finally pH 5. For the final buffer wash, the beads were left to soak for 10 minutes, followed by sonication to ensure the polystyrene nanoparticles were all collected from the beads. The pH 5 elution was collected for further analysis. The use of a buffer with a pH << pKa of AABOB

results in the nanoparticles becoming removed from the glass beads. Thus, the elution should contain MI polystyrene nanoparticles with AABOB receptors in the correct spatial orientation for future binding with lactose. The lactose remains covalent bound to the glass beads since the aqueous buffer has no effect on the covalent bond between the sugar and glass bead. In tandem, non-imprinted particles were also synthesised via the above method, for this reaction the beads only baring lactose were used and not beads with the boronate ester present. The pH elution's for both reactions were next analysed via ITC to assess the extent of pocket formation.

IX. ANALYSIS OF NANOPARTICLES PRODUCED FROM SOLID-PHASE SYNTHESIS.

To avoid buffer mismatch in the ITC experiments the buffer (pH 9 phosphate buffer) used in the polymerisation reactions was also used for the ITC controls. Since the final buffer wash of the beads was conducted at pH 5, it was therefore necessary to adjust the pH back to 9 via the addition of NaOH. As before, the sugar template (1 mM Lactose, pH 9) was placed in the syringe, and the nanoparticles (pH 5 buffer elution off beads basified to pH 9) were placed in the ITC cell. All other conditions were kept the same as previously.

Four ITC experiments were planned – the binding study for the imprinted NPs and sugar, the binding study for non-imprint species and sugar, the binding study for AABOB and lactose, and finally the heat of dilution for lactose. The raw isotherms for both the imprinted and non-imprinted particles are shown in Figure 6-17 and Figure 6-18.

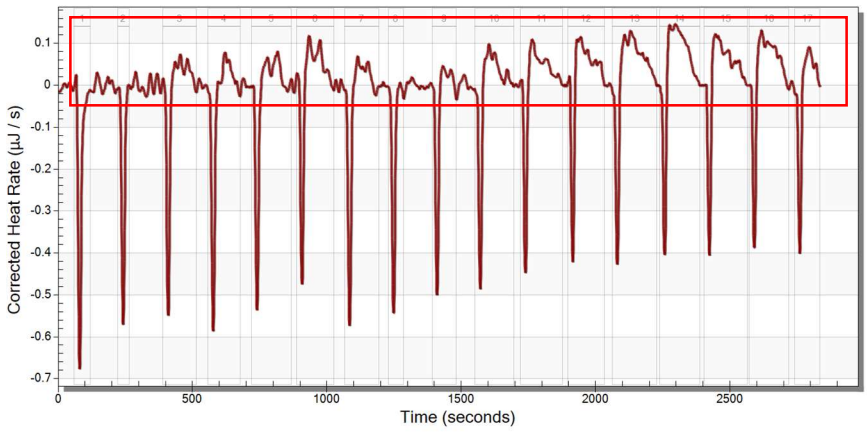


Figure 6-17: Heats produced for the MINPs collected from the bead washing in the presence of 1 mM lactose at pH 9. The reaction was terminated after 17 injections due to the unstable baseline as highlighted in red.

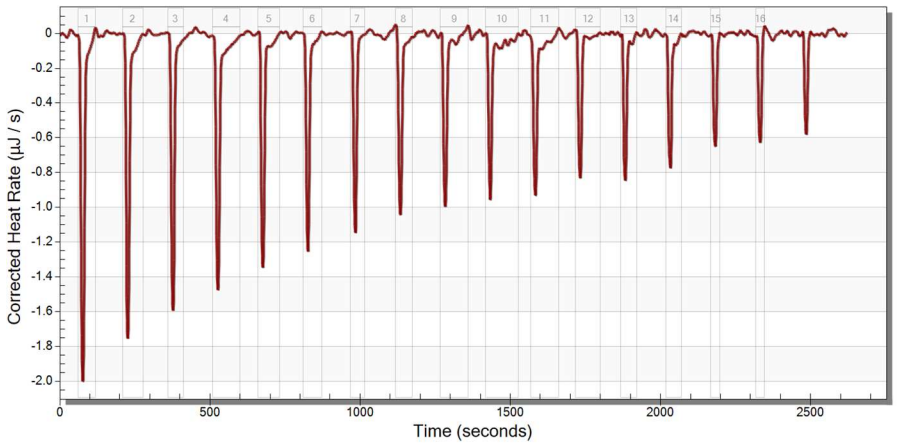


Figure 6-18: Heats produced for the interaction of lactose (1 mM) and the solution collected from glass beads washing (final elution pH 5) at pH 9.

The isotherm for the imprinted glass bead reaction (Figure 6-17) was terminated early at injection 17 due to the unstable baseline as highlighted in red. Unstable baselines may arise due to bubble formations in the cell or syringe, precipitation within the cell or due to an unclean ITC cell prior to experiment

starting. The syringe was checked, and no bubbles could be located, the ITC cell was deep cleaned before use and is unlikely to be the cause. Thus, it is plausible the nanoparticles when diluted into the buffer after removing from the glass beads were unstable due to the lack of surfactants present. The raw data was processed utilising NanoAnalyse TA instrumentation software. [398] Owing to the weak nature of the interaction between AABOB and lactose, the C value was expected be << 5, therefore the n value was set to 1.[251,252,393] An independent binding model was assumed, meaning the binding of a lactose sugar to one pocket does not influence the binding of another sugar to another pocket nearby. The processed data for the elution collected for the imprinted glass bead reaction is provided below.

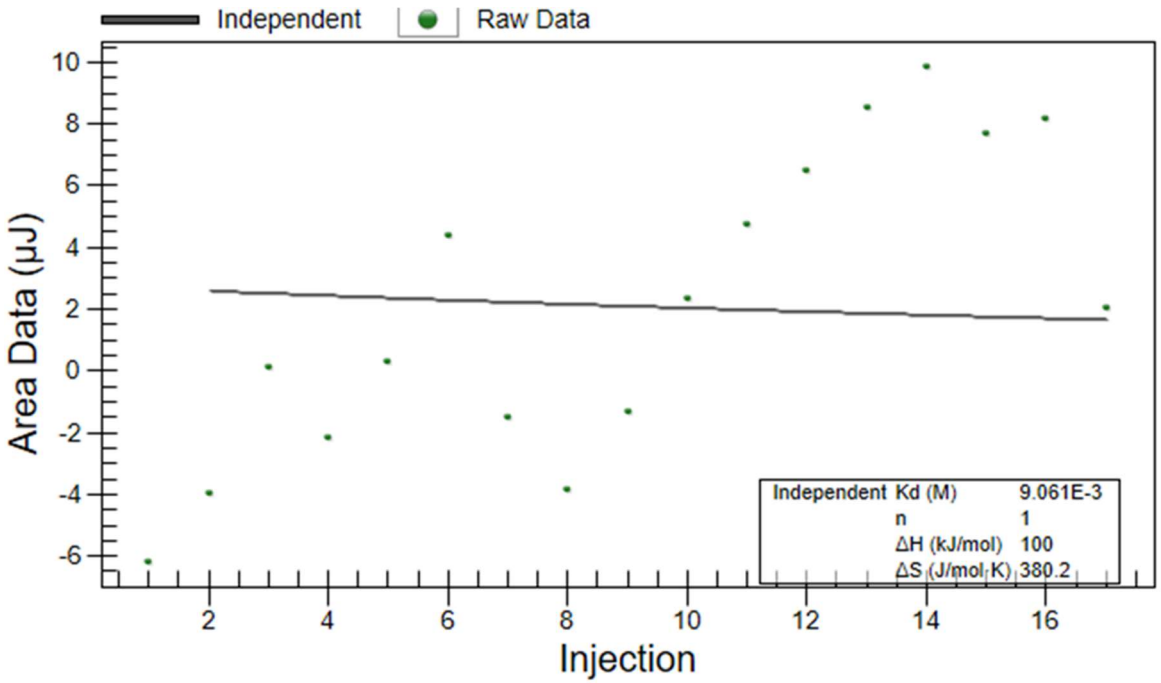


Figure 6-19: NanoAnalyse software fitting for an independent binding model applied to the data from the imprinted glass bead experiment.

No binding model could be fitted for the imprinted glass bead reaction, the corrected heats produced for the raw isotherm were observed to be under << 2 μJ s^{-1} and thus are insignificant. The independent binding model was also applied to the isotherm produced for the non – imprinted glass bead reaction and the corresponding processed data is displayed below.

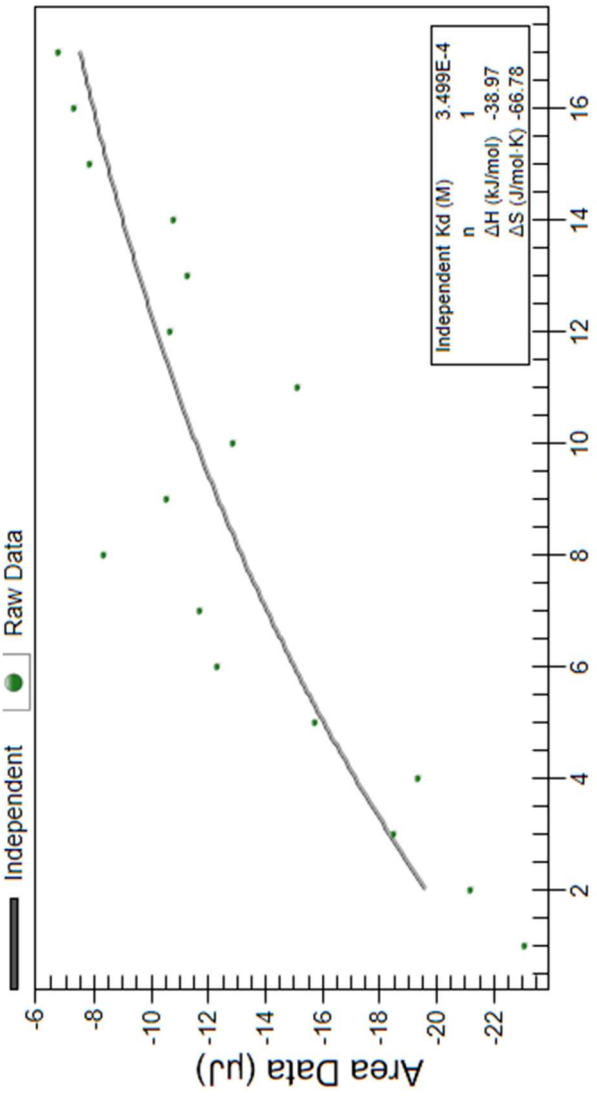


Figure 6-20: NanoAnalyse software fitting for an independent binding model applied to the data from the non - imprinted glass bead experiment.

The isotherm shape resembled a previous binding experiment conducted by another group member previously discussed (Figure 6-16). However, for this reaction there should be no particles present in the solution since they would have been washed away during the purification buffer washes. If particles were still present in this sample, the particles would only be able to interact through non – covalent interactions owing to the lack of AABOB receptors present for this reaction. The lactose may be able to interact with the DHEBA molecules present on the surface of the polystyrene nanoparticles. The non – specific binding between DHEBA and lactose was investigated via an ITC experiment between DHEBA functionalised nanoparticles and lactose. The corresponding experiment revealed no binding and is displayed below (Figure 6-21).

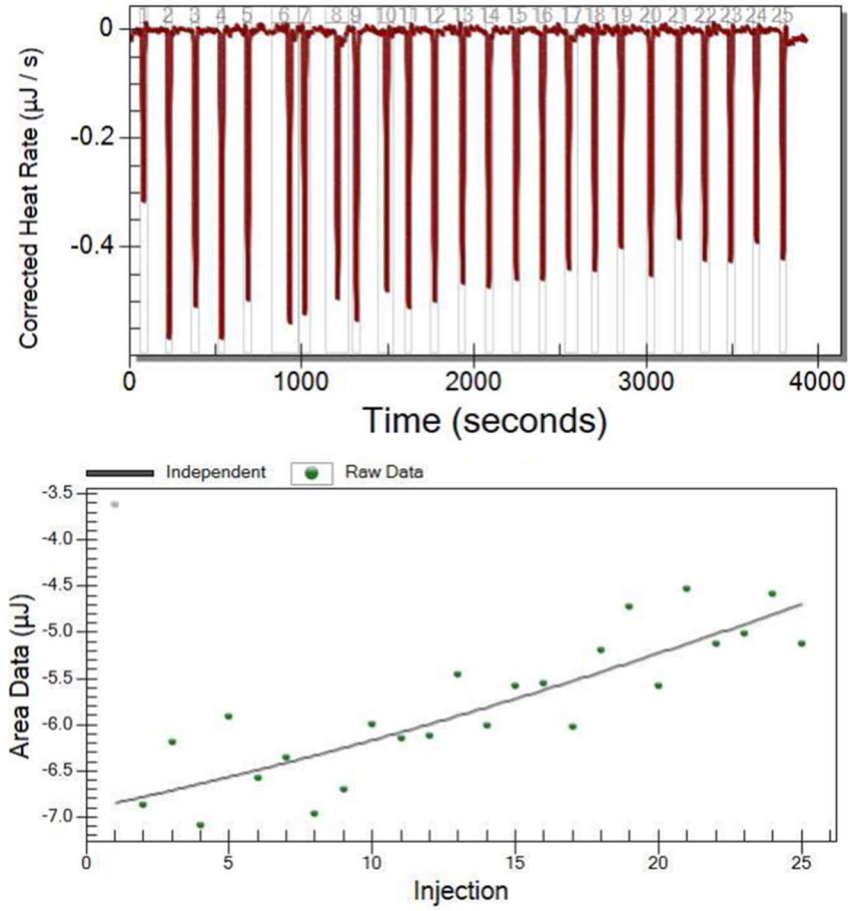


Figure 6-21: Control isotherm for the interaction of DHEBA functionalised nanoparticles with 80 mM Stachyose.

The resulting isotherm is like that of the non – imprinted isotherm (Figure 6-20), thus the heats were produced were not due to a specific binding interaction. It was believed the erroneous heats were most likely due to "buffer mismatch" (Figure 6-11) between the ITC cell and the syringe which are known to produce isotherms analogous to those depicted in Figure 6-18). Any subsequent repeats with these particles did not yield stable baselines within the ITC instrument (Appendix 9-28). owing to the instability of the particles isolated from the glass beads. The baselines observed are common for samples which are precipitating inside the ITC Cell. [247]

Thus, if any imprinted nanoparticles had been produced, they were unable to be viewed by ITC due to their instability.

A future study should consider the inclusion of surfactants to improve the stability of the particles. For example, the previous ITC study for the particles entailed the use of 0.5% surfactant to stabilise the particles within the ITC cell. The method adopted for the glass beads excluded the use of surfactants and any surfactants present on the particles surface prior to the imprinting may have been washed away during the heavy buffer washing steps of the glass beads. Thus, the lack of surfactants may have attributed towards the instability of the particles.

X. SUMMARY

It was investigated if stachyose could be selectively imprinted on polystyrene nanoparticles. From the DLS, TEM and ZP data there was an additional layer added onto the nanoparticles surface. However, no binding isotherms were obtained. The template removal step always caused instability of the emulsion.

An alternative template removal approach was trialled. Lactose functionalised glass beads were used during the molecular imprinting process of polystyrene nanoparticles. The purification of the particles avoided the use of excessive centrifugation speeds. The gentle washing steps are analogous to previously reported literature for the template removal process.[203,233] However, no binding isotherms could be produced for these particles owing to their instability. The use of surfactant was avoided during the imprinting to avoid any potential interference with the pocket formation. This may have been a contributory factor towards the particle instability.

Future experiments should look to incorporate the addition of surfactants into the protocols discussed within this section to assess if the stability of particles is increased. The particle stability is vital to assess the formation of pockets on the particles via ITC.

Additionally, a study could be conducted in the future via fluorescence, like the study conducted for the AABOB functionalised nanoparticles. If the fluorescence intensity was seen to increase in the presence of ARS, then it provides information into the accessibility of the pockets for the target

template molecule. The pocket access was previously questioned due to the centrifugation process.

Thus, the works provided within are inconclusive regarding the extent of molecular imprinting and hence pocket formation. They do, however, provide a starting point for the development of such particles in the future which is known to be highly challenging.

CHAPTER SEVEN

I. CONCLUSIONS

The objective of this project was to enhance the specificity of MI materials. Excellent specificity was demonstrated in a previous method, which was applied to a 2D surface.[203] However, MINPs have the potential to exhibit even greater binding constants compared to 2D systems. Therefore, the goal was to modify a previously reported 2D protocol to a 3D nanoparticle, which is a novel approach in this field because there are few MINPs currently available that are selective for oligosaccharides prepared via emulsion polymerisation and free radical polymerisation. This study aimed to address this issue. Emulsion polymerisation was used to create latex seeds due to its ability to create uniform and repeatable monodisperse samples.

The study identified polystyrene nanoparticles as ideal candidates for molecular imprinting work due to their inherent ability to resist rearrangement because of the aromatic nature of their backbone. They form rigid and robust cores that can maintain the precise spatial arrangement of any functional groups on their surface.[392] However, functionalising these nanoparticles with aromatic benzoboroxole-based receptors was a significant challenge. The study found that only a limited number of receptors could be placed on the surface in the nanomolar range. Trying to increase the number of receptors beyond this limit resulted in nanoparticle instabilities.

Boronate esters with stachyose were found to form adequately, with a high degree of 1:3 and 1:4 complexes observed to form by MALDI. However, when more clinically relevant sialic acid was considered, challenges arose due to the different binding nature. [130] The preferred binding mode of a 1,2-cis-diol present on the pyranose ring was unavailable for naturally occurring sialic acid derivatives in glycoproteins.[388] Therefore, the binding had to be enhanced at the undesirable glycerol alkyl chain. In the presence of anhydrous DMF, the complex was observed to form via NMR and MS, although this was not favourable. Further optimisation is required to try different reaction conditions to enhance this formation, as most of the starting material was still present after 24 hours, indicating the complexity of the process.

The formation of high-order boronate esters with stachyose and AABOB was successfully confirmed. Next, attempts were made to functionalise DHEBA-coated particles with these complexes. Three different complex concentrations were assessed, aiming to cover at least 1/10th of the particle's surface area while reducing the concentration due to its limited solubility in water. Although minor challenges were encountered regarding solubility, they were overcome by incorporating DMF into the imprinting protocol. Despite facing some issues with particle stability after centrifugation, an increase in particle size was observed via TEM and DLS. It was believed that excessive centrifugation speeds caused this aggregation, which was necessary to isolate the template stachyose from the particles. However, this experience provided valuable insight, and it was suspected that excessive centrifugation speeds adversely affected the pockets' morphology and the colloidal stability,

resulting in particle coalescence, as confirmed via TEM. Overall, the study gained valuable experience, and it was believed that these challenges could be overcome via the use of solid support.

A potential solution, which holds promise for addressing the issue at hand, was proposed. The proposed method involved utilising lactose-functionalised glass beads for molecular imprinting around the sugar attached to the beads. By adjusting the pH, the particles could be easily removed without centrifugation. The sugar could be recycled on the glass beads, and the resulting particles could be swiftly collected in a buffer for ITC analysis. However, it should be noted that this protocol was not specifically designed for the integration of functionalised polystyrene nanoparticles. Despite this, it has been successfully implemented by the Mendes group to produce acrylamide-based nanoparticles around the sugar molecule, exhibiting selectivity towards lactose via ITC analysis, demonstrating its potential.

II. FUTURE DEVELOPMENTS

While the studies did not result in molecularly imprinted polymeric nanoparticles (MINPs), they have significantly deepened our understanding of the complex challenges in creating stable nanoparticles with boronate-ester complexes on their surface. These insights serve as a foundation for future research and development.

The development of these works should explore the use of multiple receptors for the oligosaccharides. For example, in the case of stachyose, it may be more advantageous to use phenylboronic acid and benzoboroxole due to both pyranose and furanose rings. It has been observed that the binding of benzoboroxoles at the glycerol side chain is not favourable in the presence of DMF and other organic solvents when it comes to sialic acid. However, using charged functional groups can provide additional non-covalent interactions that complement covalent binding modes to enhance binding affinity. [54,378,383,385] This approach was previously utilised in literature and is yet to be translated to a polymeric molecularly imprinted nanoparticle such as those synthesised within.

As a future experiment, adding charged urea or guanidine derivatives at the meta position of the phenyl ring of the boronic receptors could be considered to compare the extent of binding. Furthermore, binding studies in the future may benefit from the use of ITC over NMR, as reported in this thesis.

The research conducted on gold nanoparticles has shown that surfactants play a significant role in stabilising nanoparticles. However, in the MI studies, surfactants were not used to avoid

any potential interference or non-specific interactions that could have complicated the ITC binding studies. This careful approach, while it may have affected the stability of the particles, was necessary to ensure the integrity of our findings. More than the use of surfactants alone is required to ensure particle stability. The concentration of the boronate ester applied to the surface must be optimised to strike a balance between particle stability and the enhancement of observed heat signals via ITC. The heat signals from ITC required significant amplification as they were minimal (<< 2 μJ s^{-1} due to the low concentration range used (pM – nM range of pockets). Concentrating the particles, whilst it may be feasible, may not necessarily result in a perfect ITC isotherm that possesses a clear inflection point owing to the weak nature of the binding. Therefore, the proposed binding study may not be ideally suited for analysis via ITC but may be more suitable for surface plasmon resonance (SPR).

To gauge the degree of pocket formation, polymeric nanoparticles can be linked to a gold SPR (Surface Plasmon Resonance) chip using thiol-ene chemistry. This approach effectively addresses the problem of nanoparticle agglomeration or precipitation during ITC (Isothermal Titration Calorimetry) binding and obviates the need for surfactants in the binding investigation. Furthermore, it does away with the worry of inaccurate solvent matching, which had previously been a concern.

In conclusion, despite the challenges encountered in creating molecularly imprinted polymeric nanoparticles (MINPs) with boronate-ester complexes on their surface, this research has

provided valuable insights that lay the groundwork for future investigations. The exploration of multiple receptors for oligosaccharides and the consideration of charged functional groups offers promising avenues for enhancing binding affinity. Additionally, the careful approach taken in the experimental design, balancing particle stability with the sensitivity of binding studies, underscores the meticulous nature of the research. Looking ahead, integrating innovative techniques such as Surface Plasmon Resonance (SPR) holds exciting potential for overcoming existing limitations and advancing our understanding of nanoparticle behaviour. With continued innovation, the pursuit of molecular imprinting technologies promises exciting application opportunities in various fields.

CHAPTER EIGHT

I. GENERAL METHODS AND MATERIALS

II. CHEMICALS AND MATERIALS

All chemicals and solvents were from Sigma-Aldrich unless otherwise stated. 5-Amino-2-(hydroxymethyl)phenylboronic acid cyclic monoester was purchased from TCI chemicals. Stachyose was purchased from Acros organics. Sialic acid was purchased from Carbosynth. NMR solvents were purchased from GOSS scientific. TEM grids were purchased from EM resolutions.

III. DATA ANALYSIS

All graphs were plotted with Origin or Excel software, with chemical structures created in ChemDraw.

IV. DYNAMIC LIGHT SCATTERING (DLS) AND ZETA POTENTIAL MEASUREMENTS (ZP)

DLS and zeta potential measurements were taken on Malverns "Zetasizer Nano" instrument. Measurements were recorded at a backscattering angle of 173°, and a temperature of 25°C. To improve measurements, samples were filtered with a syringe filter (0.22 μM pore size). This removed dust and other fibres which would otherwise shift the distribution curve. Multiple measurements were conducted, and an average is provided denoted Z-average or the hydrodynamic diameter for the size measurements. For a comprehensive summary of the workings of DLS measurements refer to section Dynamic light scattering (DLS) and zeta potential (ZP).

V. GLASSWARE CLEANING

For all reactions involving gold, glassware was first soaked in aqua regia (4:1 hydrochloride acid: nitric acid) for a minimum of 4 hours. The glassware was removed from the bubbling red solution, and the solution was neutralised with aqueous saturated sodium carbonate. Finally, glassware was rinsed with milli-Q water to remove acidic residues.

VI. TRANSMISSION ELECTRON MICROSCOPY (TEM)

Preparation of TEM samples entailed drying 4 µL of a diluted aqueous nanoparticle solution on a 300-mesh copper formvar grid. For non-metallic nanoparticles, 4 µL of 2% phosphotungstic acid stain was added on top. To prevent aggregate formation or excessive stain patches, excess liquid was removed after addition using lint free tissue. TEM samples were viewed using a JEOL 1400 BIO-TEM microscope. TEM data obtained from the microscope was processed using Image-J, origin pro and excel.

VII. ISOTHERMAL TITRATION CALORIMETRY (ITC)

ITC binding studies were conducted on a TA instruments nano-LV instrument running in aqueous mode. All samples were prepared in fresh buffer on the day of the ITC measurement to reduce buffer mismatch with the samples being filtered and degassed prior to insertion into the instrument. Into the ITC cell 300 µL of the receptor was inserted whilst the syringe contained the receptor of choice. The general experimental operating conditions are as follows: 20 x 2 µL injections with an equilibration interval of 150 – 300 seconds between injections. The stirring rate was set to stir continuously at 125 rpm whilst maintaining a cell temperature of 25 degrees throughout the binding experiment. The ITC instrument was cleaned before and after use to ensure no erroneous heats were produced from a dirty cell.

For this thesis, the expected heats were exceedingly small and hence weak in nature. Thus, to obtain suitable binding isotherms the binding stoichiometry was set to 1 (n = 1). [319] The fixing of the n value is a well-known method for when studying known binding interactions in which the C values are well below 5. For more information regarding the C value and ITC the reader is referred to the referenced publication. [254]

VIII. UV-VIS SPECTROSCOPY MEASUREMENTS

UV-Vis spectroscopy measurements were conducted on a Cary-50 instrument. UV/vis data was normalised to avoid the dilution effects. Identification of LSPR peak for gold nanoparticles conducted on cary-50 was done using neat nanoparticles and isolating the λmax for the data set. Changes in the λmax value can be used as an indication to changes on the surface of the gold particles due to the surface plasmon effect.

IX. PREPARATION OF LC-MS SAMPLES

All samples were dissolved in HPLC grade solvents and run on a Waters SDQ2 LC-MS instrument with Thames Restek columns (C18 or BP). The HPLC gradients applied were 95% water: 5% organic to 5% water:95% organic over 45 minutes unless otherwise specified.

For Analysis of indirect boronate ester formation the LC-MS samples were ran on a modified HPLC gradient on the c18 column. The high-performance liquid chromatography (HPLC) gradients applied were 95% water: 5% organic to 5% water:95% organic. Whereby the organic solution was a mixture of Methanol and Acetonitrile (1:1). Following elution from the column the outputs are mixed with 100 mM Ammonium acetate: IPA (1:1) to enhance ionisation owing to IPA being an excellent proton donator. The concentration upon mixing with respect to the LC flow rate should not be over 10 mM to avoid ion clusters and background noise in the MS spectra, thus the flow rate is adjusted to obtain 10 mM.

X. PREPARATION OF MALDI MATRIXES

All samples were ran on a Bruker Ultraflextreme MALDI-TOF mass spectrometer with a DHB matrix. The 1 mg/mL 2,5-Dihydroxybenzoic acid (DHB) matrix was prepared in Methanol (containing 2 M ammonia) and stored in the fridge until use. The sample (1 µL) and matrix (1 µL) were mixed on the plate (Bruker Daltonics, MTP 384 polished steel) at the day analysis. The solvent for sample dissolution varied depending on the analyte usually this was ACN, DCM or EtOAc. Before MALDI analysis the plates were dried in a fumehood to ensure crystal formation of the DHB matrix with the analyte. Calibration of the MALDI-TOF-MS instrument was performed with standard peptide mixtures from Bruker Daltonics. The samples were ran in reflection-positive (RP_PepMix_700-3500) ion mode and each sample were probed in multiple separate locations on the plate and the spectra were averaged using FlexAnalysis.

XI. THE SYNTHESIS OF GOLD NANOPARTICLES

A 1% stock solution of $AuCl_4.xH_2O$ (0.5mL, 25mM) was diluted in 50 mL mili-Q water and heated under reflux. Upon boiling, 34 mM Trisodium Citrate dehydrate (1.2 mL) was quickly added, forming a ruby red solution. Once this colour change had occurred, the heat was turned off and left for a further 15 minutes for the reaction to complete. After cooling to room temperature, the nanoparticles were isolated by centrifugation and re-suspended in either Ethanol or Water.

XII. FUNCTIONALISATION WITH 1,4-BENZENEDIMETHANETHIOL OR CYSTEAMINE HYDROCHLORIDE

In a clean small vial, 166-500 µL of citrate-capped nanoparticles was added to either an ethanolic solution of BDMT (1 mM after dilution), or an aqueous solution of cysteamine hydrochloride (1mM after dilution). The resulting pale pink solution was left to stir at room temperature. After 4 hours, the pale pink solution was centrifuged for 10 minutes at 16,000 rpm to isolate the nanoparticles. This was followed by their resuspension in ethanol.

XIII. FUNCTIONALISATION OF GOLD NANOPARTICLES WITH THIOLS IN THE PRESENCE OF TWEEN-20.

Gold nanoparticles previously synthesised with sodium citrate (1.6 nM, 2 mL) were added to a solution of tween-20 (3 mg mL-1 in reaction) and left for thirty minutes stirring at room temperature. Following surfactant physisorption, the thiol of interest was added in excess to provide a concentration of 1 mM in the reaction. The LSPR peaks of the gold nanoparticles were compared before and after confirming a change on the nanoparticles surface.

XIV. FUNCTIONALISATION WITH 11-MERCAPTOUNDECANOIC ACID OR 4-MERCAPTOBENZOIC ACID

The following 10 mM buffer solutions were prepared: citric acid buffer (pH 3), acetic acid buffer (pH 5), phosphate buffer (pH 7, pH 8, pH 9), and sodium carbonate (pH 11). Tween-20 was dissolved into the above buffers to produce the following concentrations: 11, 1.83, and 0.36 mg/mL. Equal volumes of buffered tween-20 solutions, and purified citrate capped gold nanoparticles (0.8 nM), were placed into small glass vials fitted with stirrer bars. A pale pink solution was produced after stirring at room temperature for 30 minutes. Then, 11-MUDA or 4-MCA (Equal volume to Tween-20, 0.5 mM) was added. Resulting mixture was left to stir for 4 hours at room temperature.

XV. SYNTHESIS OF POLYACRYLAMIDE (PAM) NANOPARTICLES

Polyacrylamide nanoparticles synthesis was adapted from a literature procedure. [321] Hexane (2.15 mL), AOT (80 mg, 0.18 mmol) and Brij-30 (162 µL, 0.425 mmol) was added to a 25 mL two neck round bottom flask, the resulting mixture was degassed and stirred. The monomers acrylamide (39.8 mg, 0.56 mmol) and methylene-bis-acrylamide (12.2 mg, 0.0791 mmol) were dissolved in 100 µL DMSO to make the monomer solution. The monomer solution was added dropwise over the degassed surfactant solution in hexane. The cloudy emulsion solution was left stirring and degassing for a further 10 minutes. Initiation of free radical polymerisation was facilitated by addition of APS (3 µL, 10% w/v) and TEMED (1.5 µL, 0.13 nmol), to ensure the reaction goes to completion it was left stirring at room temperature under argon for two hours. Typically, free-radical polymerisation reactions conducted with APS initiators are completed within several minutes.[328]Isolation and purification of plain acrylamide nanoparticles was achieved via precipitation with ethanol followed by centrifugal washing with water (x3), 5,000 RPM, 30 minutes.

XVI. SYNTHESIS OF FUNCTIONALISED POLYACRYLAMIDE NANOPARTICLES

Hexane (21.5 mL), AOT (0.8 g, 1.80 mmol) and Brij-30 (1.62 mL, 4.25 mmol) was added to a 50 mL two neck round bottom flask, resulting mixture was degassed and stirred. The following monomers were dissolved in 1 mL DMSO by sonication: acrylamide (0.477 g, 80% mmol), methylene-bis-acrylamide (0.122 g, 10% mmol) and 3-acrylamido-phenylboronic acid (0.159 g, 10% mmol). Monomer solution was added to the reaction via syringe, and the resulting solution was stirred and degassed at RT for 10 minutes. To initiate free radical polymerisation, ammonium persulfate (30 µL, 10% w/v) and TEMED (15 µL, 0.13 nmol) were added, and the resulting emulsion was left to stir under nitrogen. After 2 hours, the nanoparticles were precipitated by the addition of ethanol. Purification of nanoparticles was achieved by 3x water centrifugation washes, each round at 5,000 RPM for 30 minutes.

XVII. SYNTHESIS OF POLYSTYRENE (PS) NANOPARTICLES

Polystyrene nanoparticles synthesis was adapted from a previously reported literature procedure.[345] Styrene and di-vinylbenzene monomers were passed through a basic alumina column to remove stabilisers.

Sodium dodecyl sulphate (0.175 g, 0.61 mmol), purified styrene (9.5 g, 91.2 mmol), and purified divinylbenzene (0.48 g, 3.69 mmol) were dissolved in milli-Q water (125 mL) in a round bottom flask, fitted with a reflux condenser, and septum. The reaction was stirred at 180 rpm to produce a milky white solution. The flask was purged with nitrogen, and the reaction heated to 70°C for 20 minutes. Potassium persulphate (0.39 g, 1.43 mmol) was then added, and the resulting milky solution was left to react for a further hour. Di-vinylbenzene (0.105 g, 0.81 mmol) was then added into the reaction. The mixture was left at 70°C for an additional 24 hours. After cooling to room temperature, water was removed, and nanoparticles were re-dispersed in minimum volume in THF. The dissolved particulates were then placed in a clean dry centrifuge tube diluted with ethanol (approx. double volume of THF). The white pellets were collected by centrifugation (20,000 RPM, 15 minutes). Re-dispersion/centrifugation process was repeated twice to ensure removal of all impurities.

XVIII.SYNTHESIS OF WATER-SOLUBLE POLYSTYRENE NANOPARTICLES

Sodium dodecyl sulphate (43.7 mg, 0.15 mmol), purified styrene (2.89 g, 27.7 mmol) and purified divinylbenzene (2.2 mg, 2.19 mmol) were dissolved in 25 mL of milli-Q water in a 100 mL two neck round bottomed flask. The flask was purged with nitrogen and heated to 70°C. An aqueous solution of potassium persulphate (6.25 mL, 194 mg, 0.72 mmol) was then added. The milky emulsion was left to react for a further hour. Divinylbenzene (0.48 mg, 0.48 mmol) was then added by syringe into the reaction. The resulting mixture was left to react at 70°C for 24 hours. Following the formation of the polystyrene nanoparticles, SDS (24.6 mg, 1 mL H_2O, 0.085 mmol), N,N'-(1,2-dihydroxyethylene)-bis-acrylamide (3 mL, 0.40 mmol) and potassium persulphate (2mL, 0.37 mmol) were added, and was left to stir for 24 hours while heating at 70°C. The resulting nanoparticles were three times purified by centrifugation and washing with water (14,000 RPM, 90 minutes, 15°C). Solvent removal of the nanoparticles yielded a pure white solid (18 mg/mL, 27%).

XIX. SYNTHESIS OF POLYSTYRENE NANOPARTICLES FUNCTIONALISED WITH DHEBA AND 3-ACRYLAMIDOBENZOBOROXOLE/ 3-ACRYLAMIDOPHENYLBORONIC ACID

Polystyrene nanoparticles (1.5 mL, x10 dilution) were placed into a round bottom flask with DHEBA (1.5 mL, 50 mM), 3-acrylamidobenzoboroxole/3-acrylamidophenyl boronic acid (1 µL, 5mM) and phosphate buffer (9.5 mL, pH 7.4). The resulting solution was purged with nitrogen for 10 minutes. The reaction was initiated by the addition of APS (1.5 mL, 0.175M), and TEMED (1 mL, 67 mM). Termination of the reaction occurred at 2 hours by exposure to air. The nanoparticles were subjected to water washes for purification (Centrifugation conditions: 3 x 18,000 RPM, 45 minutes, 15°C).

XX. SYNTHESIS OF 5-ACRYLAMIDE-2(HYDROXMETHYL)PHENYLBORONIC ACID (AABOB)

5-Amino-2-(hydroxymethyl)phenylboronic acid cyclic monoester (0.50 g, 3.35 mmol) was dissolved in a 1:1 mixture of THF/H2O (11.6 ml). The solution was cooled with an ice-bath and sodium carbonate (1.12 g, 13.40 mmol) and acryloyl chloride (0.54 ml, 6.71 mmol) were then added. The reaction mixture was stirred at room temperature for 5 hours and its progress was monitored by TLC to confirm completion. The organic layer was extracted and washed with brine several times. The organic layers were combined and dried over $MgSO_4$ and the solvent was removed to produce a white solid (0.43g, 64%).^{1}H NMR (400 MHz, DMSO-d_6): δ 10.17 (s, 1H), 9.23 (s, 1H), 8.08 (d, J = 1.7 Hz, 1H), 7.70 (dd, J = 8.2, 2.0 Hz, 1H), 7.36 (dd, 2H), 6.47 (dd, J = 17.0, 10.1 Hz, 1H), 6.27 (dd, J = 17.0, 2.1 Hz, 1H), 5.76 (dd, J = 10.1, 2.1 Hz, 1H), 4.95 (s, 0H). TOF-MS (ESI+): 204.08 m/z for $C_{10}H_{10}BNO_3$; [M+H].

XXI. PREPARATION OF THE GLYCAN-BORONATE COMPLEX

3.33 mg (1 Eq, 4.5 μM) of sugar and boronic acid receptor (32 Eq Stachyose / 3 Eq Sialic acid) was added to a 5mL round bottom flask (containing molecular sieves 3Å). The flask was sealed and flushed with nitrogen, before adding 0.9 mL of 1,4-dioxane (anhydrous) and 0.15 mL of acetonitrile (anhydrous). The reaction was left at 90 degrees for 24 hours under inert atmosphere.

After 24 hours the solvent was removed to yield a crude solid, to which acetonitrile was added to produce a precipitate. The white precipitate (5.7 mg, 81% yield) was collected via centrifugation (2 minutes at 8,000 rpm). The solid was used immediately to prevent degradation. The supernatant was collected and dried for NMR analysis to ensure no product was lost during purification.

XXII. BENZOYLATION OF THE COMPLEX SUGAR

The complex was prepared as described above. Following the 24-hour reaction, the acetonitrile/dioxane solvents was removed. The crude was dissolved in pyridine (0.5 mL) and cooled in an ice bath. At 0 degrees Benzoyl chloride (50 µL, 0.41 mmol) was added and left to stir at room temperature for 5 hours. Following 5 hours the reaction mixture was diluted the minimum amount of toluene and the precipitate was filtered through celite.

The solvent was removed under reduced pressure and the crude was dissolved in a mixture of ethyl acetate (5 mL) and 1 M sorbitol / Sodium carbonate (5 mL) and stirred for 1 hour. Extraction of the organic layer was completed by washing the aqueous phase with ethyl acetate three times. The organic phases were collected and dried over magnesium sulphate, followed by concentrating under reduced pressure to yield a yellow oil (33.4 mg, 73%). The crude product was passed through a flash column starting at 100% Hexane to elute BzCl, followed by a gradient column Hex/EtOAc (95:5 → 100% EtOAc). Collected fractions were analysed via LC-MS and MALDI.

XXIII. DEVELOPMENT OF POLYSTYRENE NANOPARTICLES BARING POCKET IMPRINTS

DHEBA functionalised polystyrene nanoparticles (750 µL) and SDS 0.1% w/v (100 µL) were added to a round bottom flask. The stachyose boronate-ester complex (2.95 mg) was placed in 2 mL phosphate buffer pH 8. The resulting solution was left to stir and degas. The polymerisation reaction was initiated by the addition of APS (750µL, 87 mM) and TEMED (500µL, 3.33 mM). After 5 minutes the DHEBA (500 µL, 50 mM) cross-linker was added to the reaction to form an imprint. The solution was left to react for a further 15 minutes.

Following polymerisation, the nanoparticles were washed with 10 mM ammonium acetate buffer pH 5.6 to remove stachyose and unreacted reagents. The nanoparticles were isolated via centrifugation to form a white pellet. The resulting particles were use in ITC binding studies.

XXIV. PREPARATION OF THE GLASS BEADS

Glass beads (75 µm diameter, 1g) surfaces were activated for functionalisation by boiling in 4 M NaOH (0.8 mL) at 100 °C for 15 minutes. Following 15 minutes, the beads are thoroughly washed 8 times with 30 mL of ultra-pure water until the pH of the solution was around 7 before washing in acetone (2 x 30 mL) Finally, the beads are dried in an oven at 80 °C for 3 hours.

XXV. SILANISATION OF GLASS BEADS READY FOR MI.

Previously activated glass beads were placed in a beaker and added to 3-aminopropyl)trimethoxysilane (APTMS, 0.4 mL, 3% v/v) in anhydrous toluene and was left to react overnight at 60 °C. The resulting amine functionalised glass beads were washed with acetone (30 mL x8) followed by methanol (30 mL x2) before drying in an oven at 150 °C for 30 minutes. Amine functional beads will be stored under vacuum at room temperature prior to use.

XXVI. FUNCTIONALISATION OF GLASS BEADS WITH 3-AMINOPROPYL-B-D-LACTOSE FOR MOLECULAR IMPRINTING.

Amino-functionalised glass beads previously synthesised (1g) was added to 0.5 mL of NHS linker (ethylene glycol-bis succinic acid N-hydroxysuccinimide, aqueous suspension 7 % w/v) and left to react for 30 minutes. Following 30 minutes, the beads were rinsed ultra-pure water until the supernatant decanted from the beads appeared clear. A further 5 washings (8 mL) was conducted to ensure complete removal of the NHS linker not bound to the glass beads.

To a 7 mL vial, 250 mg previously prepared NHS functionalised glass beads were suspended in ultra-pure water (1 mL) and the MI template of interest (3-aminopropyl-β-d-lactose (3apLac) (63 µg, 0.15 µmol)). The resulting solution of glass beads was left to react for 30 minutes on an orbital shaker. The 3apLac functionalised beads was washed eight times (8 x 30 mL ultra-pure water) followed a further wash with HPLC grade methanol (x3, 30 mL) before drying in a vacuum oven at 80 °C for 4 hours.

XXVII. HYBRID APPROACH TO PRODUCING MINPS UTILISING GLASS BEADS.

500 mg of functionalised glass beads were donated (imprinted and non-imprinted), to which 1 mL of polystyrene nanoparticles previously synthesised (Phosphate buffer pH 9) were added. The reaction was sealed before adding APS (22.9 µL, 87 mM) and 1µL neat of TEMED. The reaction was left on an orbital shaker for 15 minutes. The glass beads were washed with pH 9 phosphate buffer, pH 7 and pH 5 buffer. The pH 5 elution was collected for further analysis via ITC.

I. REFERENCES

1 Cancer Statistics for the UK, https://www.cancerresearchuk.org/health-professional/cancer-statistics-for-the-uk#heading-Zero, (accessed 31 December 2022).

2 J. Munkley and D. J. Elliott, *Oncotarget*, 2016, **7**, 35478–89.

3 E. Scott and J. Munkley, *Int J Mol Sci*, , DOI:10.3390/IJMS20061389.

4 C. Ohyama, M. Hosono, K. Nitta, M. Oh-eda, K. Yoshikawa, T. Habuchi, Y. Arai and M. Fukuda, *Glycobiology*, 2004, **14**, 671–679.

5 S. F. Shariat, A. Semjonow, H. Lilja, C. Savage, A. J. Vickers and A. Bjartell, *Acta Oncol*, 2011, **50 Suppl 1**, 61–75.

6 C. G. Roehrborn and L. K. Black, *BJU Int*, 2011, **108**, 806–813.

7 L. M. Hurwitz, I. Agalliu, D. Albanes, K. H. Barry, S. I. Berndt, Q. Cai, C. Chen, I. Cheng, J. M. Genkinger, G. G. Giles, J. Huang, C. E. Joshu, T. J. Key, S. Knutsen, S. Koutros, H. Langseth, S. X. Li, R. J. MacInnis, S. C. Markt, K. L. Penney, A. Perez-Cornago, T. E. Rohan, S. A. Smith-Warner, M. J. Stampfer, K. H. Stopsack, C. M. Tangen, R. C. Travis, S. J. Weinstein, L. Wu, E. J. Jacobs, L. A. Mucci and M. B. Cook, *J Natl Cancer Inst*, 2021, **113**, 727–734.

8 Prostate cancer statistics | Cancer Research UK, https://www.cancerresearchuk.org/health-professional/cancer-statistics/statistics-by-cancer-type/prostate-cancer#heading-Zero, (accessed 13 August 2023).

9 H. G. Rittenhouse, J. A. Finlay, S. D. Mikolajczyk and A. W. Partin, *Crit Rev Clin Lab Sci*, 1998, **35**, 275–368.

10 A. Gratacós-Mulleras, A. Duran, A. Asadi Shehni, M. Ferrer-Batallé, M. Ramírez, J. Comet, R. de Llorens, R. Saldova, E. Llop and R. Peracaula, *Scientific Reports 2020 10:1*, 2020, **10**, 1–14.

11 About prostate cancer | Prostate Cancer UK, https://prostatecanceruk.org/prostate-information/about-prostate-cancer, (accessed 17 April 2019).

12 Cancer Research UK, Prostate cancer | Cancer Research UK, https://www.cancerresearchuk.org/about-cancer/prostate-cancer, (accessed 17 April 2019).

13 I. E. Tothill, *Semin Cell Dev Biol*, 2009, **20**, 55–62.

14 A. Yu, J. Zhao, W. Peng, A. Banazadeh, S. D. Williamson, M. Goli, Y. Huang and Y. Mechref, *Electrophoresis*, 2019, **39**, 3104–3122.

15 S. Hatakeyama, T. Yoneyama, Y. Tobisawa, H. Yamamoto and C. Ohyama, *Transl Androl Urol*, 2021, **10**, 1850.

16 S. Brooks, T. Carter, L. Royle, D. Harvey, S. Fry, C. Kinch, R. Dwek and P. Rudd, *Anticancer Agents Med Chem*, 2008, **8**, 2–21.

17 G. Tabarés, C. M. Radcliffe, S. Barrabés, M. Ramírez, R. N. Aleixandre, W. Hoesel, R. A. Dwek, P. M. Rudd, R. Peracaula, R. de Llorens, N. Aleixandre, W. Hoesel, R. A. Dwek, P. M. Rudd, R. Peracaula and R. de Llorens, *Glycobiology*, 2006, **16**, 132–145.

18 A. Varki, R. D. Cummings, M. Aebi, N. H. Packer, P. H. Seeberger, J. D. Esko, P. Stanley, G. Hart, A. Darvill, T. Kinoshita, J. J. Prestegard, R. L. Schnaar, H. H. Freeze, J. D. Marth, C. R. Bertozzi, M. E. Etzler, M. Frank, J. F. G. Vliegenthart, T. Lütteke, S. Perez, E. Bolton, P. Rudd, J. Paulson, M. Kanehisa, P. Toukach, K. F. Aoki-Kinoshita, A. Dell, H. Narimatsu, W. York, N. Taniguchi and S. Kornfeld, in *Essentials of Glycobiology [Internet]*, Oxford University Press, Fourth Ed., 2015, vol. 25, pp. 1323–1324.

19 T. G. Barclay, M. Ginic-markovic, P. D. Cooper and N. Petrovsky, *JOURNAL OF EXCIPIENTS AND FOOD CHEMICALS*, 2012, **3**, 67–68.

20 G. T. Williams, J. L. Kedge and J. S. Fossey, *ACS Sens*, 2021, **6**, 1508–1528.

21 A. P. Davis, *Org Biomol Chem*, 2009, **7**, 3629–3638.

22 E. Maverakis, K. Kim, M. Shimoda, M. E. Gershwin, F. Patel, R. Wilken, S. Raychaudhuri, L. R. Ruhaak and C. B. Lebrilla, *J Autoimmun*, 2015, **57**, 1–13.

23 A. Varki, *Glycobiology*, 2017, **27**, 3–49.

24 R. D. Cummings, *Mol Biosyst*, 2009, **5**, 1087–1104.

25 T. Keser, M. Tijardović, I. Gornik, E. Lukić, G. Lauc, O. Gornik and M. Novokmet, *Molecular and Cellular Proteomics*, 2021, **20**, 100044.

26 K. Bastian, E. Scott, D. J. Elliott and J. Munkley, *International Journal of Molecular Sciences 2021, Vol. 22, Page 455*, 2021, **22**, 455.

27 G. Tabarés, C. M. Radcliffe, S. Barrabés, M. Ramírez, N. Aleixandre, W. Hoesel, R. A. Dwek, P. M. Rudd, R. Peracaula and R. de Llorens, *Glycobiology*, 2006, **16**, 132–145.

28 R. Saldova, Y. Fan, J. M. Fitzpatrick, R. W. G. Watson and P. M. Rudd, *Glycobiology*, 2011, **21**, 195–205.

29 J. Munkley and D. J. Elliott, *Oncotarget*, 2016, **7**, 35478–35489.

30 Y.-C. Wang, S. E. Peterson and J. F. Loring, *Cell Res*, 2014, **24**, 143–160.

31 M. A. Akmal, N. Rasool and Y. D. Khan, *PLoS One*, , DOI:10.1371/JOURNAL.PONE.0181966.

32 X. Zhang and Y. Wang, *J Mol Biol*, 2016, **428**, 3183–3193.

33 M. Wang and R. J. Kaufman, *Nature*, 2016, **529**, 326–335.

34 E. Buxbaum, in *Fundamentals of Protein Structure and Function*, Springer US, Boston, MA, 2007 Ed., 2007, pp. 3–47.

35 K. Xiao and Z. Tian, *J Proteome Res*, 2019, **18**, 2885–2895.

36 H. Lodish, A. Berk, S. L. Zipursky, P. Matsudaira, D. Baltimore and J. Darnell, in *Molecular Cell biology*, W. H. Freeman, 4th Ed., 2000.

37 § J. L. Mellquist, ‡, § L. Kasturi, ‖ and S. L. Spitalnik and ‡ S. H. Shakin-Eshleman*, , DOI:10.1021/BI972217K.

38 V. S. Ananthanarayanan, S. K. Brahmachari and N. Pattabiraman, *Arch Biochem Biophys*, 1984, **232**, 482–495.

39 D. L. Nelson and M. M. Cox, in *PRINCIPLES OF BIOCHEMISTRY*, W.H. Freeman and Company, New York, fourth edi., p. 123.

40 J. J. Lyons, J. D. Milner and S. D. Rosenzweig, *Front Pediatr*, 2015, **3**, 147638.

41 M. Maurizio, *Nat Chem Biol*, 2007, **3(6)**, 313–20.

42 P. Stanley, N. Taniguchi and M. Aebi, in *Essentials of Glycobiology*, Cold Spring Harbor Laboratory Press, 3rd Ed., 2015.

43 L. R. Ruhaak, D. A. Barkauskas, J. Torres, C. L. Cooke, L. D. Wu, C. Stroble, S. Ozcan, C. C. Williams, M. Camorlinga, D. M. Rocke, C. B. Lebrilla and J. V. Solnick, *EuPA Open Proteom*, 2015, **6**, 1–9.

44 G. Chen, Y. Y. Wang, X. Qin, H. Li, Y. Guo, Y. Y. Wang, H. Liu, X. Wang, G. Song, F. F. Li, F. F. Li, S. Guo, L. Qiu and Z. Li, *Electrophoresis*, 2013, **34**, 2407–2416.

45 V. Poonthiyil, P. T. Nagesh, M. Husain, V. B. Golovko and A. J. Fairbanks, *ChemistryOpen*, 2015, **4**, 708–716.

46 S. F. Shariat, A. Semjonow, H. Lilja, C. Savage, A. J. Vickers and A. Bjartell, *Acta Oncol*, 2011, **50 Suppl 1**, 61–75.

47 E. Llop, M. Ferrer-Batallé, S. Barrabés, P. E. Guerrero, M. Ramírez, R. Saldova, P. M. Rudd, R. N. Aleixandre, J. Comet, R. de Llorens and R. Peracaula, *Theranostics*, 2016, **6**, 1190–204.

48 W.-L. Ho, W.-M. Hsu, M.-C. Huang, K. Kadomatsu and A. Nakagawara, *J Hematol Oncol*, , DOI:10.1186/S13045-016-0334-6.

49 L. Sisinni, M. Pietrafesa, S. Lepore, F. Maddalena, V. Condelli, F. Esposito and M. Landriscina, *Int J Mol Sci*, 2019, **20**, 857.

50 K. Kodar, J. Stadlmann, K. Klaamas, B. Sergeyev and O. Kurtenkov, *Glycoconj J*, 2012, **29**, 57–66.

51 L. Ellgaard and A. Helenius, *Nat Rev Mol Cell Biol*, 2003, **4**, 181–191.

52 J. Munkley and D. J. Elliott, *Oncotarget*, 2016, **7**, 35478.

53 W. L. Ho, W. M. Hsu, M. C. Huang, K. Kadomatsu and A. Nakagawara, *J Hematol Oncol*, 2016, **9**, 1–15.

54 M. Regueiro-Figueroa, K. Djanashvili, D. Esteban-Gómez, T. Chauvin, É. Tóth, A. De Blas, T. Rodríguez-Blas and C. Platas-Iglesias, *Inorg Chem*, 2010, **49**, 4212–4223.

55 A. Gratacós-Mulleras, A. Duran, A. Asadi Shehni, M. Ferrer-Batallé, M. Ramírez, J. Comet, R. de Llorens, R. Saldova, E. Llop and R. Peracaula, *Scientific Reports 2020 10:1*, 2020, **10**, 1–14.

56 B. N. Vajaria and P. S. Patel, *Glycoconj J*, 2017, **34**, 147–156.

57 Z. Gao, M. Xu, S. Yue, H. Shan, J. Xia, J. Jiang and S. Yang, *Current research in pharmacology and drug discovery*, 2022, **3**, 100079.

58 Z. Gao, Z. Wu, Y. Han, X. Zhang, P. Hao, M. Xu, S. Huang, S. Li, J. Xia, J. Jiang and S. Yang, *ACS Omega*, 2022, **7**, 17894–17906.

59 Y. Miura, M. Hato, Y. Shinohara, H. Kuramoto, J. I. Furukawa, M. Kurogochi, H. Shimaoka, M. Tada, K. Nakanishi, M. Ozaki, S. Todo and S. I. Nishimura, *Molecular & Cellular Proteomics*, 2008, **7**, 370–377.

60 K. Kodar, J. Stadlmann, K. Klaamas, B. Sergeyev and O. Kurtenkov, *Glycoconj J*, 2012, **29**, 57–66.

61 S. Tommasone, F. Allabush, Y. K. Tagger, J. Norman, M. Köpf, J. H. R. Tucker and P. M. Mendes, *Chem Soc Rev*, 2019, 48, 5488–5505.

62 S. Tommasone, F. Allabush, Y. K. Tagger, J. Norman, M. Köpf, J. H. R. Tucker and P. M. Mendes, *The challenges of glycan recognition with natural and artificial receptors*, Royal Society of Chemistry, 2019, vol. 48.

63 M. Mazik, *ChemBioChem*, 2008, **9**, 1015–1017.

64 N. Bloise, M. Okkeh, E. Restivo, C. Della Pina and L. Visai, *Nanomaterials*, 2021, **11**, 289.

65 M. V. Dwek, A. Jenks and A. J. C. Leathem, *Clinica Chimica Acta*, 2010, **411**, 1935–1939.

66 E. Llop, M. Ferrer-Batallé, S. Barrabés, P. E. Guerrero, M. Ramírez, R. Saldova, P. M. Rudd, R. N. Aleixandre, J. Comet, R. de Llorens and R. Peracaula, *Theranostics*, 2016, **6**, 1190–204.

67 R. Tian, X. Li, H. Zhang, L. Ma, H. Zhang and Z. Wang, *ACS Omega*, 2022, **7**, 30405–30411.

68 N. T. Chen, J. S. Souris, S. H. Cheng, C. H. Chu, Y. C. Wang, V. Konda, U. Dougherty, M. Bissonnette, C. Y. Mou, C. T. Chen and L. W. Lo, *Nanomedicine*, 2017, **13**, 1941–1952.

69 F. Compostella, O. Pitirollo, A. Silvestri and L. Polito, *Beilstein Journal of Organic Chemistry*, 2017, **13**, 1008–1021.

70 G. Sánchez-Pomales, T. A. Morris, J. B. Falabella, M. J. Tarlov and R. A. Zangmeister, *Biotechnol Bioeng*, 2012, **109**, 2240–2249.

71 R. Bhat, I. García, E. Aznar, B. Arnaiz, M. C. Martínez-Bisbal, L. M. Liz-Marzán, S. Penadés and R. Martínez-Máñez, *Nanoscale*, 2017, **10**, 239–249.

72 M. Martínez-Carmona, D. Lozano, M. Colilla and M. Vallet-Regí, *Acta Biomater*, 2018, **65**, 393–404.

73 F. Kveton, A. Blsakova, P. Kasak, J. Tkac, F. Kveton@savba, F. K. Sk, A. Blsakova@savba and A. B. Sk, *Nanomaterials 2020, Vol. 10, Page 1406*, 2020, **10**, 1406.

74 S. Yonezawa, T. Nakamura, S. Tanaka and E. Sato, *JNCI: Journal of the National Cancer Institute*, 1982, **69**, 777–785.

75 S. Edwardraja, A. Eichinger, I. Theobald, C. A. Sommer, A. J. Reichert and A. Skerra, *ACS Synth Biol*, 2017, **6**, 2241–2247.

76 K. L. Bicker, J. Sun, J. J. Lavigne and P. R. Thompson, *ACS Comb Sci*, 2012, **13**, 232–243.

77 Y. Qiu, T. H. Patwa, L. Xu, K. Shedden, D. E. Misek, M. Tuck, G. Jin, M. T. Ruffin, D. K. Turgeon, S. Synal, R. Bresalier, N. Marcon, D. E. Brenner and D. M. Lubman, *J Proteome Res*, 2008, **7**, 1693–1703.

78 J. Hofmann and K. Pagel, *Angewandte Chemie International Edition*, 2017, **56**, 8342–8349.

79 H. V. Giles, A. Wechalekar and G. Pratt, *Br J Haematol*, 2022, **198**, 641–653.

80 H. Shimaoka, H. Kuramoto, J. I. Furukawa, Y. Miura, M. Kurogochi, Y. Kita, H. Hinou, Y. Shinohara and S. I. Nishimura, *Chemistry – A European Journal*, 2007, **13**, 1664–1673.

81 R. A. Dwek, *Chem Rev*, 1996, **96**, 683–720.

82 H. Takahashi, T. Kamiyama, N. Hirane, N. Kobayashi, T. Aiyama, A. Nagatsu, S. Shimada, T. Orimo, T. Kakisaka, M. Fukai, H. Yokoo, H. Kamachi, S. I. Nishimura and A. Taketomi, *Oncol Rep*, 2020, **44**, 2757–2769.

83 S. I. Nishimura, K. Niikura, M. Kurogochi, T. Matsushita, M. Fumoto, H. Hinou, R. Kamitani, H. Nakagawa, K. Deguchi, N. Miura, K. Monde and H. Kondo, *Angewandte Chemie International Edition*, 2005, **44**, 91–96.

84 Y. Miura, K. Kato, Y. Takegawa, M. Kurogochi, J. I. Furukawa, Y. Shinohara, N. Nagahori, M. Amano, H. Hinou and S. I. Nishimura, *Anal Chem*, 2010, **82**, 10021–10029.

85 Y. Miura, M. Hato, Y. Shinohara, H. Kuramoto, J. I. Furukawa, M. Kurogochi, H. Shimaoka, M. Tada, K. Nakanishi, M. Ozaki, S. Todo and S. I. Nishimura, 2008, **7**, 370–377.

86 Y. Akimoto, K. Nouso, H. Kato, K. Miyahara, C. Dohi, Y. Morimoto, H. Kinugasa, T. Tomoda, N. Yamamoto, K. Tsutsumi, K. Kuwaki, H. Onishi, F. Ikeda, S. Nakamura, H. Shiraha, A. Takaki, H. Okada, M. Amano, S. I. Nishimura and K. Yamamoto, *Pancreatology*, 2015, **15**, 432–438.

87 D. Noro, T. Yoneyama, S. Hatakeyama, Y. Tobisawa, K. Mori, Y. Hashimoto, T. Koie, M. Tanaka, S. I. Nishimura, H. Sasaki, M. Saito, H. Harada, T. Chikaraishi, H. Ishida, K. Tanabe, S. Satoh and C. Ohyama, *International Journal of Molecular Sciences 2017, Vol. 18, Page 1731*, 2017, **18**, 1731.

88 M. Amano and S. I. Nishimura, in *Methods in Enzymology*, Academic Press, 2010, vol. 478, pp. 109–125.

89 A. G. Gebrehiwot, D. S. Melka, Y. M. Kassaye, I. F. Rehan, S. Rangappa, H. Hinou, T. Kamiyama and S. I. Nishimura, *PLoS One*, 2018, **13**, e0209515.

90 Y. Miura, M. Hato, Y. Shinohara, H. Kuramoto, J. I. Furukawa, M. Kurogochi, H. Shimaoka, M. Tada, K. Nakanishi, M. Ozaki, S. Todo and S. I. Nishimura, *Molecular and Cellular Proteomics*, 2008, **7**, 370–377.

91 Y. Miura and S. I. Nishimura, *Trends in Glycoscience and Glycotechnology*, 2008, 20, 17–27.

92 N. Fujitani, Y. Takegawa, Y. Ishibashi, K. Araki, J. I. Furukawa, S. Mitsutake, Y. Igarashi, M. Ito and Y. Shinohara, *J Biol Chem*, 2011, **286**, 41669.

93 Y. Ishibashi, Y. Tobisawa, S. Hatakeyama, T. Ohashi, M. Tanaka, S. Narita, T. Koie, T. Habuchi, S. I. Nishimura, C. Ohyama and T. Yoneyama, *Prostate*, 2014, **74**, 1521–1529.

94 R. Liu, Q. Cui, C. Wang, X. Wang, Y. Yang and L. Li, *ACS Appl Mater Interfaces*, 2017, **9**, 3006–3015.

95 S. Jin, Y. Cheng, S. Reid, M. Li and B. Wang, *Med Res Rev*, 2010, **30**, 171–257.

96 E. Klein, M. P. Crump and A. P. Davis, *Angewandte Chemie International Edition*, 2005, **44**, 298–302.

97 S. Edwardraja, A. Eichinger, I. Theobald, C. A. Sommer, A. J. Reichert and A. Skerra, *ACS Synth Biol*, 2017, **6**, 2241–2247.

98 L. Köhler, W. Seichter and M. Mazik, *European J Org Chem*, 2020, **2020**, 7023–7034.

99 A. K. Tewari and R. Dubey, *Bioorg Med Chem*, 2008, **16**, 126–143.

100 S. Kubik, *Angewandte Chemie - International Edition*, 2009, **48**, 1722–1725.

101 B. Leibiger, M. Stapf and M. Mazik, *Molecules*, 2022, **27**, 7630.

102 M. Mazik, *Chem Soc Rev*, 2009, **38**, 935–956.

103 M. Mazik and C. Sonnenberg, *Journal of Organic Chemistry*, 2010, **75**, 6416–6423.

104 M. Mazik and H. Cavga, *Journal of Organic Chemistry*, 2007, **72**, 831–838.

105 J. Lippe and M. Mazik, *Journal of Organic Chemistry*, 2013, **78**, 9013–9020.

106 M. Mazik and M. Kuschel, *Chemistry - A European Journal*, 2008, **14**, 2405–2419.

107 A. P. Davis, *Chem Soc Rev*, 2020, **49**, 2531–2545.

108 A. P. Davis, *Chem Soc Rev*, 2020, **49**, 2531–2545.

109 N. Koch, J.-R. Rosien and M. Mazik, *Tetrahedron*, 2014, **70**, 8758–8767.

110 K. Thakur, M. A. Shlain, M. Marianski and A. B. Braunschweig, *European J Org Chem*, 2021, **2021**, 5262–5274.

111 M. Mazik, W. Radunz and R. Boese, *Journal of Organic Chemistry*, 2004, **69**, 7448–7462.

112 G. Joshi and A. P. Davis, *Org Biomol Chem*, 2012, **10**, 5760–5763.

113 K. Thakur, M. A. Shlain, M. Marianski and A. B. Braunschweig, *European J Org Chem*, 2021, **2021**, 5262–5274.

114 Y. Kikuchi, Y. Tanaka, S. Sutarto, K. Kobayashi, H. Toi and Y. Aoyama, *J Am Chem Soc*, 1992, **114**, 10302–10306.

115 A. P. Davis, R. S. Wareham, W. Ellis, T. K. Hollis, W. Odenkirk, J. Whelan, R. Ostrander, A. L. Rheingold, B. Bosnich, M. E. Huttenloch, J. Diebold, U. Rief, H. H. Brintzinger, A. M. Gilbert, T. J. Katz, H. Wiesenfeldt, A. Reinmuth, E. Barsties, K. Evertz and H. H. Brint, *Angew. Chem. Int. Ed. Engl*, 1998, **37**, 4045.

116 C. Nativi, O. Francesconi, G. Gabrielli, A. Vacca and S. Roelens, *Chemistry - A European Journal*, 2011, **17**, 4814–4820.

117 O. Francesconi, C. Nativi, G. Gabrielli, M. Gentili, M. Palchetti, B. Bonora and S. Roelens, *Chemistry – A European Journal*, 2013, **19**, 11742–11752.

118 O. Francesconi, C. Nativi, G. Gabrielli, I. De Simone, S. Noppen, J. Balzarini, S. Liekens and S. Roelens, *Chemistry - A European Journal*, 2015, **21**, 10089–10093.

119 A. Ardá, F. J. Cañada, C. Nativi, O. Francesconi, G. Gabrielli, A. Ienco, J. Jiménez-Barbero and S. Roelens, *Chemistry – A European Journal*, 2011, **17**, 4821–4829.

120 M. F. Bravo, M. A. Lema, M. Marianski and A. B. Braunschweig, *Biochemistry*, 2021, **60**, 999–1018.

121 A. P. Davis and R. S. Wareham, *Angewandte Chemie - International Edition*, 1999, 38, 2978–2996.

122 A. P. Davis and T. D. James, in *Functional Synthetic Receptors*, John Wiley & Sons, Ltd, 2005, pp. 47–48.

123 E. Klein, M. P. Crump and A. P. Davis, *Angewandte Chemie International Edition*, 2005, **44**, 298–302.

124 C. Ke, H. Destecroix, M. P. Crump and A. P. Davis, *Nat Chem*, 2012, **4**, 718–723.

125 N. P. Barwell, M. P. Crump, A. P. Davis, N. P. Barwell, M. P. Crump and A. P. Davis, *Angewandte Chemie International Edition*, 2009, **48**, 7673–7676.

126 N. P. Barwell, M. P. Crump, A. P. Davis, N. P. Barwell, M. P. Crump and A. P. Davis, *Angewandte Chemie International Edition*, 2009, **48**, 7673–7676.

127 N. P. Barwell, M. P. Crump, A. P. Davis, N. P. Barwell, M. P. Crump and A. P. Davis, *Angewandte Chemie International Edition*, 2009, **48**, 7673–7676.

128 P. Rios, T. S. Carter, T. J. Mooibroek, M. P. Crump, M. Lisbjerg, M. Pittelkow, N. T. Supekar, G. J. Boons and A. P. Davis, *Angewandte Chemie - International Edition*, 2016, **55**, 3387–3392.

129 T. S. Carter, T. J. Mooibroek, P. F. N. Stewart, M. P. Crump, M. C. Galan and A. P. Davis, *Angewandte Chemie International Edition*, 2016, **55**, 9311–9315.

130 A. Di Pasquale, S. Tommasone, L. Xu, J. Ma and P. M. Mendes, *J Org Chem*, , DOI:10.1021/acs.joc.0c00173.

131 Y. Xiong, M. Li, Q. Lu, G. Qing and T. Sun, *Polymers (Basel)*, 2017, **9**, 249.

132 G. Das and A. D. Hamilton, *J Am Chem Soc*, 1994, **116**, 11139–11140.

133 O. Francesconi, C. Nativi, G. Gabrielli, M. Gentili, M. Palchetti, B. Bonora and S. Roelens, *Chemistry – A European Journal*, 2013, **19**, 11742–11752.

134 B. Tapia, G. Yagudayeva, M. F. Bravo, K. Thakur, A. B. Braunschweig and M. Marianski, *Carbohydr Res*, 2022, **518**, 108574.

135 B. Tapia, G. Yagudayeva, M. F. Bravo, K. Thakur, A. B. Braunschweig and M. Marianski, *Carbohydr Res*, 2022, **518**, 108574.

136 M. Mazik, H. Bandmann and W. Sicking, *Angew. Chem. Int. Ed*, , DOI:10.1002/(SICI)1521-3773(20000204)39:3.

137 J. Lippe and M. Mazik, *Journal of Organic Chemistry*, 2015, **80**, 1427–1439.

138 M. Mazik and C. Sonnenberg, *Journal of Organic Chemistry*, 2010, **75**, 6416–6423.

139 M. Mazik and H. Cavga, *Journal of Organic Chemistry*, 2006, **71**, 2957–2963.

140 M. Mazik, H. Bandmann and W. Sicking, *Angew. Chem. Int. Ed*, , DOI:10.1002/(SICI)1521-3773(20000204)39:3.

141 M. Mazik, A. Hartmann and P. G. Jones, *Chemistry - A European Journal*, 2009, **15**, 9147–9159.

142 M. Mazik, H. Cavga and P. G. Jones, *J Am Chem Soc*, 2005, **127**, 9045–9052.

143 M. Mazik and W. Sicking, *Tetrahedron Lett*, 2004, **45**, 3117–3121.

144 M. Mazik and C. Sonnenberg, *Journal of Organic Chemistry*, 2010, **75**, 6416–6423.

145 X. Yang, Y. Cheng, S. Jin and B. Wang, in *Artificial Receptors for Chemical Sensors*, 2010, p. 171.

146 S. Striegler, *Curr Org Chem*, 2005, **7**, 81–102.

147 S. Cho, S. Y. Hwang, D. X. Oh and J. Park, *J Mater Chem A Mater*, 2021, **9**, 14630–14655.

148 H. R. Mulla, N. J. Agard and A. Basu, *Bioorg Med Chem Lett*, 2004, **14**, 25–27.

149 Z. Liu and H. He, *Acc Chem Res*, 2017, **50**, 2185–2193.

150 L. Zhu, S. H. Shabbir, M. Gray, V. M. Lynch, S. Sorey and E. V. Anslyn, *J Am Chem Soc*, 2006, **128**, 1222–1232.

151 S. Schumacher, M. Katterle, C. Hettrich, B.-R. R. Paulke, D. G. Hall, F. W. Scheller and N. Gajovic-Eichelmann, *Journal of Molecular Recognition*, 2011, **24**, 953–959.

152 G. F. Whyte, R. Vilar and R. Woscholski, *J Chem Biol*, 2013, **6**, 161–174.

153 W. Kowalczyk, J. Sanchez, P. Kraaz, O. E. Hutt, D. N. Haylock and P. J. Duggan, *Peptide Science*, 2018, **110**, e23101.

154 W. Kowalczyk, J. Sanchez, P. Kraaz, O. E. Hutt, D. N. Haylock and P. J. Duggan, *Peptide Science*, 2018, **110**, e23101.

155 J. Ye, Y. Chen and Z. Liu, *Angewandte Chemie*, 2014, **126**, 10554–10557.

156 D. Li, T. Tu and X. Wu, *Analytical Methods*, 2018, **10**, 4419–4429.

157 Z. Bie, Y. Chen, J. Ye, S. Wang and Z. Liu, *Angewandte Chemie - International Edition*, 2015, **54**, 10211–10215.

158 W. Huang, X. Hou, Y. Tong and M. Tian, *RSC Adv*, 2019, **9**, 5394–5401.

159 H. Zhu, H. Yao, K. Xia, J. Liu, X. Yin, W. Zhang and J. Pan, *Chemical Engineering Journal*, 2018, **346**, 317–328.

160 L. Sun, D. Lin, G. Lin, L. Wang and Z. Lin, *Analytical Methods*, 2015, **7**, 10026–10031.

161 Z. Lin, L. Sun, W. Liu, Z. Xia, H. Yang and G. Chen, *J. Mater. Chem. B*, 2014, **2**, 637–643.

162 X. Xue, R. Lu, M. Liu, Y. Li, J. Li and L. Wang, *Analyst*, 2019, **144**, 641–648.

163 A. Matsumoto, A. J. Stephenson-Brown, T. Khan, T. Miyazawa, H. Cabral, K. Kataoka and Y. Miyahara, , DOI:10.1039/c7sc01905j.

164 X. tai Zhang, G. jian Liu, Z. wei Ning and G. wen Xing, *Carbohydr Res*, 2017, **452**, 129–148.

165 H. Fang, G. Kaur and B. Wang, *J Fluoresc*, 2004, **14**, 481–489.

166 S. Xu, A. C. Sedgwick, S. A. Elfeky, W. Chen, A. S. Jones, G. T. Williams, A. T. A. Jenkins, S. D. Bull, J. S. Fossey and T. D. James, *Front Chem Sci Eng*, 2020, **14**, 112–116.

167 J. K. Awino, R. W. Gunasekara and Y. Zhao, *J Am Chem Soc*, 2016, **138**, 9759–9762.

168 D. Li, H. Xia and L. Wang, *Talanta*, 2018, **184**, 235–243.

169 C. Cannizzo, S. Amigoni-Gerbier and C. Larpent, *Polymer (Guildf)*, 2005, **46**, 1269–1276.

170 X. Wu, Z. Li, X. X. Chen, J. S. Fossey, T. D. James and Y. B. Jiang, *Chem Soc Rev*, 2013, **42**, 8032–8048.

171 D. G. Hall, *Chem Soc Rev*, 2019, **48**, 3475–3496.

172 M. Y. Qi, H. K. Wu, M. Anpo, Z. R. Tang and Y. J. Xu, *Nano Research 2022 15:12*, 2022, **15**, 9967–9975.

173 P. C. Trippier and C. McGuigan, *Medchemcomm*, 2010, **1**, 183–198.

174 J. N. Cambre and B. S. Sumerlin, *Polymer (Guildf)*, 2011, **52**, 4631–4643.

175 J. Norman, S. Tommasone and P. M. Mendes, *Mater Today Chem*, 2022, **24**, 100939.

176 S. Shinkai, K. Tsukagoshi, Y. Ishikawa and T. Kunitake, *J Chem Soc Chem Commun*, 1991, 1039–1041.

177 A. Pal, M. Bérubé and D. G. Hall, *Angewandte Chemie - International Edition*, 2010, **49**, 1492–1495.

178 A. Pal, M. Bérubé and D. G. Hall, *Angewandte Chemie - International Edition*, 2010, **49**, 1492–1495.

179 M. S. Melicher, A. S. Walker, J. Shen, S. J. Miller and A. Schepartz, *Org Lett*, 2015, **17**, 4718–4721.

180 T. D. James, K. R. A. S. Sandanayake and S. Shinkai, *J Chem Soc Chem Commun*, 1994, 477–478.

181 Y. Egawa, R. Miki and T. Seki, *Materials*, 2014, **7**, 1201.

182 T. D. James, K. R. A. S. Sandanayake and S. Shinkai, *Angewandte Chemie International Edition in English*, 1994, **33**, 2207–2209.

183 B. M. Chapin, P. Metola, S. L. Vankayala, H. L. Woodcock, T. J. Mooibroek, V. M. Lynch, J. D. Larkin and E. V. Anslyn, *J Am Chem Soc*, 2017, **139**, 5568–5578.

184 J. D. Larkin, J. S. Fossey, T. D. James, B. R. Brooks and C. W. Bock, *Journal of Physical Chemistry A*, 2010, **114**, 12531–12539.

185 W. Ni, G. Kaur, G. Springsteen, B. Wang and S. Franzen, *Bioorg Chem*, 2004, **32**, 571–581.

186 S. Franzen, W. Ni and B. Wang, *Journal of Physical Chemistry B*, 2003, **107**, 12942–12948.

187 X. Sun, B. M. Chapin, P. Metola, B. Collins, B. Wang, T. D. James and E. V. Anslyn, *Nat Chem*, 2019, **11**, 768–778.

188 G. Fang, H. Wang, Z. Bian, J. Sun, A. Liu, H. Fang, B. Liu, Q. Yao and Z. Wu, *RSC Adv*, 2018, **8**, 29400–29427.

189 J. C. Pickup, F. Hussain, N. D. Evans, O. J. Rolinski and D. J. S. Birch, *Biosens Bioelectron*, 2005, **20**, 2555–2565.

190 M. S. Steiner, A. Duerkop and O. S. Wolfbeis, *Chem Soc Rev*, 2011, **40**, 4805–4839.

191 A. Jahanban-Esfahlan, L. Roufegarinejad, R. Jahanban-Esfahlan, M. Tabibiazar and R. Amarowicz, *Talanta*, 2020, **207**, 120317.

192 M. Dabrowski, P. Lach, M. Cieplak and W. Kutner, *Biosens Bioelectron*, 2018, 102, 17–26.

193 G. Wulff, *Microchimica Acta*, 2013, 180, 1359–1370.

194 G. Ertürk and B. Mattiasson, *Sensors (Basel)*, , DOI:10.3390/S17020288.

195 G. Wulff, *Angewandte Chemie International Edition in English*, 1995, **34**, 1812–1832.

196 G. Wulff and S. Schauhoff, *Journal of Organic Chemistry*, 1991, **56**, 395–400.

197 E. G. Vlakh, V. A. Korzhikov, A. V Hubina and T. B. Tennikova, *Russian Chemical Reviews*, 2015, **84**, 952–980.

198 D. Refaat, M. G. Aggour, A. A. Farghali, R. Mahajan, J. G. Wiklander, I. A. Nicholls and S. A. Piletsky, *Int J Mol Sci*, 2019, **20**, 6304.

199 A. Poma, A. P. F. Turner and S. A. Piletsky, *Trends Biotechnol*, 2010, 28, 629–637.

200 L. Li, Y. Lu, Z. Bie, H. Y. Chen and Z. Liu, *Angewandte Chemie - International Edition*, 2013, **52**, 7451–7454.

201 H. Brahmbhatt, A. Poma, H. M. Pendergraff, J. K. Watts and N. W. Turner, *Biomater Sci*, 2016, **4**, 281–287.

202 A. Stephenson-Brown, A. L. Acton, J. A. Preece, J. S. Fossey and P. M. Mendes, *Chem Sci*, 2015, **6**, 5114–5119.

203 S. Tommasone, Y. K. Tagger and P. M. Mendes, *Adv Funct Mater*, 2020, **30**, 2002298.

204 S. R. Carter and S. Rimmer, *Adv Funct Mater*, 2004, **14**, 553–561.

205 F. Canfarotta, S. A. Piletsky and N. W. Turner, *Methods in Molecular Biology*, 2020, **2073**, 183–194.

206 A. Poma, A. Guerreiro, M. J. Whitcombe, E. V. Piletska, A. P. F. F. Turner and S. A. Piletsky, *Adv Funct Mater*, 2013, **23**, 2821–2827.

207 T. Schrader, S. Kubik and M. Braun, *Angew Chem Int Ed Engl*, 2024, **63**, e202402244.

208 R. Kirchner, J. Seidel, G. Wolf and G. Wulff, *Journal of Inclusion Phenomena*, 2002, **43**, 279–283.

209 A. Stephenson-Brown, A. L. Acton, J. A. Preece, J. S. Fossey and P. M. Mendes, *Chem Sci*, 2015, **6**, 5114–5119.

210 S. J. Machera, J. Niedziółka-Jönsson, M. Jönsson-Niedziółka and K. Szot-Karpińska, *ACS Omega*, 2023, **8**, 26253–26262.

211 S. Wang, J. Ye, Z. Bie and Z. Liu, *Chem Sci*, 2014, **5**, 1135–1140.

212 Y. Zhao, *J Mater Chem B*, 2022, **10**, 6607–6617.

213 M. Gagliardi and B. Mazzolai, *http://dx.doi.org/10.4155/fmc.14.140*, 2015, **7**, 123–138.

214 A. Cecchini, V. Raffa, F. Canfarotta, G. Signore, S. Piletsky, M. P. Macdonald and A. Cuschieri, *Nano Lett*, 2017, **17**, 2307–2312.

215 K. Smolinska-Kempisty, A. Guerreiro, F. Canfarotta, C. Cáceres, M. J. Whitcombe and S. Piletsky, *Scientific Reports 2016 6:1*, 2016, **6**, 1–7.

216 Y. Garcia, K. Smolinska-Kempisty, E. Pereira, E. Piletska and S. Piletsky, *Analytical Methods*, 2017, **9**, 4592–4598.

217 M. M. Ali, S. Zhu, F. R. Amin, D. Hussain, Z. Du and L. Hu, *Theranostics*, 2022, **12**, 2406–2426.

218 I. Bose and Y. Zhao, *ACS Catal*, 2022, **12**, 3444–3451.

219 M. Arifuzzaman and Y. Zhao, *Journal of Organic Chemistry*, 2016, **81**, 7518–7526.

220 L. Duan and Y. Zhao, *Journal of Organic Chemistry*, , DOI:10.1021/acs.joc.9b01629.

221 M. Zangiabadi and Y. Zhao, *Nano Lett*, 2020, **20**, 5106–5110.

222 M. Zangiabadi and Y. Zhao, *Nano Lett*, 2020, **20**, 5106–5110.

223 X. Li, M. Zangiabadi and Y. Zhao, *J Am Chem Soc*, 2021, **143**, 5172–5181.

224 K. Chen, Y. Zhao, R. Li and / Chemcomm, *Chemical Communications*, 2022, **58**, 1732–1735.

225 Y. Zhao, *J Mater Chem B*, 2022, **10**, 6607–6617.

226 D. Myers, in *Surfactant Science and Technology*, Wiley, 4th edn., 2006, pp. 136–144.

227 S. Fa and Y. Zhao, *Chemistry of Materials*, 2019, **31**, 4889–4896.

228 R. W. Gunasekara and Y. Zhao, *J Am Chem Soc*, 2017, **139**, 829–835.

229 M. Zangiabadi and Y. Zhao, *Nano Lett*, 2020, **20**, 5106–5110.

230 Y. Zhao, *J Mater Chem B*, 2022, **10**, 6607–6617.

231 I. Chianella, A. Guerreiro, E. Moczko, J. S. Caygill, E. V. Piletska, I. M. P. De Vargas Sansalvador, M. J. Whitcombe and S. A. Piletsky, *Anal Chem*, 2013, **85**, 8462–8468.

232 S. P. Tang, F. Canfarotta, K. Smolinska-Kempisty, E. Piletska, A. Guerreiro and S. Piletsky, *Analytical Methods*, 2017, **9**, 2853–2858.

233 M. V. Sullivan, F. Allabush, D. Bunka, A. Tolley, P. M. Mendes, J. H. R. Tucker and N. W. Turner, *Polym Chem*, 2021, **12**, 4394–4405.

234 S. S. Piletsky, S. Rabinowicz, Z. Yang, C. Zagar, E. V. Piletska, A. Guerreiro and S. A. Piletsky, *Chemical Communications*, 2017, **53**, 1793–1796.

235 R. Mahajan, M. Rouhi, S. Shinde, T. Bedwell, A. Incel, L. Mavliutova, S. Piletsky, I. A. Nicholls and B. Sellergren, *Angew Chem Int Ed Engl*, 2019, **58**, 727.

236 Z. Bie, Y. Chen, J. Ye, S. Wang and Z. Liu, *Angewandte Chemie - International Edition*, 2015, **54**, 10211–10215.

237 D. Li, T. Tu and X. Wu, *Analytical Methods*, 2018, **10**, 4419–4429.

238 L. M. Harwood, T. D. W Claridge, lor X. F A O, L. M. Harwood Professor and T. Ow Claridge, in *Introduction to Organic Spectroscopy*, ed. Davies Stephen, Oxford University Press, 1997, pp. 13–17.

239 J. Stetefeld, S. A. McKenna and T. R. Patel, *Biophys Rev*, 2016, **8**, 409.

240 F. Giorgi, D. Coglitore, J. M. Curran, D. Gilliland, P. Macko, M. Whelan, A. Worth and E. A. Patterson, *Sci Rep*, , DOI:10.1038/S41598-019-48754-5.

241 A. Kumar and C. K. Dixit, in *Advances in Nanomedicine for the Delivery of Therapeutic Nucleic Acids*, ed. R. C. and N. G. Surendra Nimesh, Woodhead Publishing, 2017, pp. 44–58.

242 Zetasizer Nano | DLS, ELS & SLS Light Scattering Instruments | Malvern Panalytical, https://www.malvernpanalytical.com/en/products/product-range/zetasizer-range/zetasizer-nano-range, (accessed 8 May 2020).

243 T. G. F. Souza, V. S. T. Ciminelli and N. D. S. Mohallem, *J Phys Conf Ser*, 2016, **733**, 012039.

244 S. K. Filippov, R. Khusnutdinov, A. Murmiliuk, W. Inam, L. Y. Zakharova, H. Zhang and V. V Khutoryanskiy, *This journal is Cite this: Mater. Horiz*, 2023, **10**, 5354.

245 A. Kumar and C. K. Dixit, *Advances in Nanomedicine for the Delivery of Therapeutic Nucleic Acids*, 2017, 43–58.

246 B. J. Inkson, in *Materials Characterization Using Nondestructive Evaluation (NDE) Methods*, Elsevier Inc., 2016, pp. 17–43.

247 M. Bastos and A. Velazquez-Campoy, *European Biophysics Journal*, 2021, **50**, 363–371.

248 S. K. Filippov, A. Papagiannopoulos, A. Riabtseva and S. Pispas, *Colloid Polym Sci*, 2018, **296**, 1183–1191.

249 C. Song, S. Zhang and H. Huang, *Front Microbiol*, 2015, **6**, 1049.

250 Isothermal Titration Calorimetry | Biomolecular Interactions Analysis | Malvern Panalytical, https://www.malvernpanalytical.com/en/products/technology/microcalorimetry/isothermal-titration-calorimetry, (accessed 9 April 2020).

251 J. Broecker, C. Vargas and S. Keller, *Anal Biochem*, 2011, **418**, 307–309.

252 W. B. Turnbull and A. H. Daranas, *J Am Chem Soc*, 2003, **125**, 14859–66.

253 B. W. Sigurskjold, *Anal Biochem*, 2000, **277**, 260–266.

254 W. B. Turnbull and A. H. Daranas, *J Am Chem Soc*, 2003, **125**, 14859–14866.

255 R. W. Smith, in *Encyclopedia of Forensic Sciences: Second Edition*, Academic Press, 2013, pp. 603–608.

256 T. Harwood, Laurence M, Claridge, in *Introduction to Organic Spectroscopy*, ed. S. Davies, 1997, pp. 70–79.

257 M. H. J. Selman, M. Hoffmann, G. Zauner, L. A. McDonnell, C. I. A. Balog, E. Rapp, A. M. Deelder and M. Wuhrer, *Proteomics*, 2012, **12**, 1337–1348.

258 Atmospheric Solids Analysis Probe (ASAP) | Waters, https://www.waters.com/waters/library.htm?cid=511436&lid=10101278, (accessed 10 October 2022).

259 H. Friebolin, in *Basic One- and Two-Dimensional Spectroscopy*, Wiley-VCH, Fourth., 2005, pp. 1–41.

260 derrick kaseman, S. Ozcan and S. Du, NMR: Theory - Chemistry LibreTexts, https://chem.libretexts.org/Bookshelves/Physical_and_Theoretical_Chemistry_Textbook_Maps/Supplemental_Modules_(Physical_and_Theoretical_Chemistry)/Spectroscopy/Magnetic_Resonance_Spectroscopies/Nuclear_Magnetic_Resonance/NMR_-_Theory, (accessed 10 October 2022).

261 Splitting and Multiplicity (N+1 rule) in NMR Spectroscopy - Chemistry Steps, https://www.chemistrysteps.com/splitting-multiplicity-n1-rule-nmr/, (accessed 10 October 2022).

262 H. Horvath, *J Quant Spectrosc Radiat Transf*, 2009, **110**, 787–799.

263 E. G. Wrigglesworth and J. H. Johnston, *Nanoscale Adv*, 2021, **3**, 3530–3536.

264 E. G. Wrigglesworth and J. H. Johnston, *Nanoscale Adv*, 2021, **3**, 3530–3536.

265 T. Klar, M. Perner, S. Grosse, G. von Plessen, W. Spirkl and J. Feldmann, *Phys Rev Lett*, 1998, **80**, 4249.

266 T. R. Jensen, M. L. Duval, K. Lance Kelly, A. A. Lazarides, G. C. Schatz and R. P. Van Duyne, *Journal of Physical Chemistry B*, 1999, **103**, 9846–9853.

267 G. Mie, *Ann Phys*, 1908, **330**, 377–445.

268 M. Quinten, in *Optical Properties of Nanoparticle Systems*, Wiley, 2011, pp. 123–176.

269 A. Ismail, A. Rani, K. A. Mohamad, G. B. Kumar and C. Fuei, in *Current Advances in Microdevices and Nanotechnology*, Penerbit UTHM, Universiti Tun Hussein Onn, 2019, vol. 1, pp. 20–29.

270 B. van Grinsven, K. Betlem, T. J. Cleij, C. E. Banks and M. Peeters, *Journal of Molecular Recognition*, 2017, **30**, e2563.

271 S. Ramanavicius, A. Jagminas and A. Ramanavicius, *Polymers (Basel)*, , DOI:10.3390/POLYM13060974.

272 S. Tommasone, F. Allabush, Y. K. Tagger, J. Norman, M. Köpf, J. H. R. Tucker and P. M. Mendes, *Chem Soc Rev*, 2019, **48**, 5488–5505.

273 S. Tommasone, F. Allabush, Y. K. Tagger, J. Norman, M. Köpf, J. H. R. Tucker and P. M. Mendes, *Chem Soc Rev*, 2020, **49**, 642–642.

274 S. K. Wang and C. M. Cheng, Glycan-based diagnostic devices: current progress, challenges and perspectives, (accessed 13 May 2020).

275 S. S. Agasti, S. Rana, M. H. Park, C. K. Kim, C. C. You and V. M. Rotello, *Adv Drug Deliv Rev*, 2010, **62**, 316.

276 F. Compostella, O. Pitirollo, A. Silvestri and L. Polito, *Beilstein Journal of Organic Chemistry*, 2017, **13**, 1008–1021.

277 P. M. Tiwari, K. Vig, V. A. Dennis and S. R. Singh, *Nanomaterials (Basel)*, 2011, **1**, 31–63.

278 S. Zeng, K. T. Yong, I. Roy, X. Q. Dinh, X. Yu and F. Luan, *Plasmonics*, 2011, **6**, 491–506.

279 Y.-C. Yeh, B. Creran and V. M. Rotello, *Nanoscale*, 2012, **4**, 1871–1880.

280 R. Sardar, A. M. Funston, P. Mulvaney and R. W. Murray, *Langmuir*, 2009, **25**, 13840–13851.

281 H. Tyagi, A. Kushwaha, A. Kumar and M. Aslam, *Nanoscale Res Lett*, 2016, **11**, 362.

282 F. Vitale, I. Fratoddi, C. Battocchio, E. Piscopiello, L. Tapfer, M. V. Russo, G. Polzonetti and C. Giannini, *Nanoscale Res Lett*, 2011, **6**, 103.

283 F. Zhou, M. Wang, L. Yuan, Z. Cheng, Z. Wu and H. Chen, *Analyst*, 2012, **137**, 1779–1784.

284 P. Mitchell, S. Tommasone, S. Angioletti-Uberti, J. Bowen and P. M. Mendes, *ACS Appl Bio Mater*, 2019, **2**, 2617–2623.

285 Y. Gao and L. Torrente-Murciano, *Nanoscale*, 2020, **12**, 2740–2751.

286 Y. Gao and L. Torrente-Murciano, *Nanoscale*, 2020, **12**, 2740–2751.

287 D. Ghosh, D. Sarkar, A. Girigoswami and N. Chattopadhyay, *J Nanosci Nanotechnol*, 2011, **11**, 1141–1146.

288 D. Grasseschi, R. A. Ando, H. E. Toma and V. M. Zamarion, *RSC Adv*, 2014, **5**, 5716–5724.

289 C. A. Schneider, W. S. Rasband and K. W. Eliceiri, *Nature Methods 2012 9:7*, 2012, **9**, 671–675.

290 W. Haiss, N. T. K. Thanh, J. Aveyard and D. G. Fernig, *Anal Chem*, 2007, **79**, 4215–4221.

291 P. Cao, N. Wang, D. Chen, S. Sun, H. Ma and M. Lin, *Gold Bull*, 2021, **54**, 97–103.

292 B. G. Ershov, E. V. Abkhalimov, V. I. Roldughin, V. M. Rudoy, O. V. Dement'Eva and R. D. Solovov, *Physical Chemistry Chemical Physics*, 2015, **17**, 18431–18436.

293 A. Heuer-Jungemann, N. Feliu, I. Bakaimi, M. Hamaly, A. Alkilany, I. Chakraborty, A. Masood, M. F. Casula, A. Kostopoulou, E. Oh, K. Susumu, M. H. Stewart, I. L. Medintz, E. Stratakis, W. J. Parak and A. G. Kanaras, *Chem Rev*, 2019, **119**, 4819–4880.

294 A. B. Lowe, *Polym. Chem.*, 2010, **1**, 17–36.

295 M. Fernandez-Villamarin, L. Brooks and P. M. Mendes, *Adv Opt Mater*, 2019, **7**, 1–15.

296 Y. Liu, W. Hou, H. Sun, C. Cui, L. Zhang, Y. Jiang, Y. Wu, Y. Wang, J. Li, B. S. Sumerlin, Q. Liu and W. Tan, *Chem Sci*, 2017, **8**, 6182–6187.

297 S. Link and M. A. El-Sayed, *Journal of Physical Chemistry B*, 1999, **103**, 8410–8426.

298 X. Liu, M. Atwater, J. Wang and Q. Huo, *Colloids Surf B Biointerfaces*, 2007, **58**, 3–7.

299 J. L. Wai and S. Y. New, *RSC Adv*, 2020, **10**, 1088–1094.

300 R. E. Ionescu, *Biosensors (Basel)*, , DOI:10.3390/BIOS12080581.

301 K. A. And, V. H. Pérez-Luna*, K. Aslan and V. H. Pérez-Luna, *Langmuir*, 2002, **18**, 6059–6065.

302 Gerd H. Woehrle, † and Leif O. Brown, J. E. Hutchison*, G. H. Woehrle, L. O. Brown, J. E. Hutchison, Gerd H. Woehrle, † and Leif O. Brown and J. E. Hutchison*, *J Am Chem Soc*, 2005, **127**, 2172–2183.

303 L. Guyon, A.-C. Groo and A. Malzert-Fréon, *Mol Pharm*, 2021, **18**, 44–64.

304 X. Liang, H. Wei, Z. Cui, J. Deng, Z. Zhang, X. You and X. E. Zhang, *Analyst*, 2010, **136**, 179–183.

305 A. Kumar and C. K. Dixit, in *Advances in Nanomedicine for the Delivery of Therapeutic Nucleic Acids*, ed. R. C. and N. G. Surendra Nimesh, Elsevier Inc., 2017, pp. 44–58.

306 C. Atallah, C. Charcosset and H. Greige-Gerges, *J Pharm Anal*, 2020, **10**, 499–516.

307 A. M. Mohammad, A. I. Abdelrahman, M. S. El-Deab, T. Okajima and T. Ohsaka, *Colloids Surf A Physicochem Eng Asp*, 2008, **318**, 78–83.

308 K. Aslan and V. H. Pérez-Luna, *Langmuir*, 2002, **18**, 6059–6065.

309 K. S. Mayya, V. Patil and M. Sastry, *Langmuir*, 1997, **13**, 3944–3947.

310 C. S. Weisbecker, M. V. Merritt and G. M. Whitesides, *Langmuir*, 1996, **12**, 3763–3772.

311 H. T. Phan and A. J. Haes, *Journal of Physical Chemistry C*, 2018, **122**, 14846–14856.

312 A. R. Studart, E. Amstad and L. J. Gauckler, *Langmuir*, 2007, **23**, 1081–1090.

313 R. L. Pinals, L. Chio, F. Ledesma and M. P. Landry, *Analyst*, 2020, **145**, 5090–5112.

314 A. Michota and J. Bukowska, *Journal of Raman Spectroscopy*, 2003, **34**, 21–25.

315 S. M. Rosendahl and I. J. Burgess, *Electrochim Acta*, 2008, **53**, 6759–6767.

316 D. Wang, R. J. Nap, I. Lagzi, B. Kowalczyk, S. Han, B. A. Grzybowski and I. Szleifer, *J Am Chem Soc*, 2011, **133**, 2192–2197.

317 R. Haag, F. Kratz, R. Haag and F. Kratz, *Angewandte Chemie International Edition*, 2006, **45**, 1198–1215.

318 M. Szczęch and K. Szczepanowicz, *Nanomaterials 2020, Vol. 10, Page 496*, 2020, **10**, 496.

319 D. Prozeller, S. Morsbach and K. Landfester, *Nanoscale*, 2019, **11**, 19265–19273.

320 T. Cedervall, I. Lynch, S. Lindman, T. Berggård, E. Thulin, H. Nilsson, K. A. Dawson and S. Linse, *Proc Natl Acad Sci U S A*, 2007, **104**, 2050–5.

321 Z. Zeng, J. Patel, S.-H. Lee, M. McCallum, A. Tyagi, M. Yan and K. J. Shea, *J Am Chem Soc*, 2012, **134**, 2681–2690.

322 R. Ghosh Chaudhuri and S. Paria, *Chem Rev*, 2012, 112, 2373–2433.

323 P. A. Lovell and F. J. Schork, *Biomacromolecules*, 2020, **21**, 4396–4441.

324 R. Simič, J. Mandal, K. Zhang and N. D. Spencer, *Soft Matter*, 2021, **17**, 6394–6403.

325 J. X. Zhong, J. R. Clegg, E. W. Ander and N. A. Peppas, *J Biomed Mater Res A*, 2018, **106**, 1677.

326 A. Gharieh, S. Khoee and A. R. Mahdavian, *Adv Colloid Interface Sci*, 2019, **269**, 152–186.

327 A. M. van Herk and R. G. Gilbert, in *Chemistry and Technology of Emulsion Polymerisation: Second Edition*, ed. A. M. van Herk, John Wiley & Sons, Ltd, Second Edi., 2013, pp. 43–73.

328 I. Capek, *Polym J*, 2004, **36**, 793–803.

329 N. M. Sekerak, K. M. Hutchins, B. Luo, J. G. Kang, P. V. Braun, Q. Chen and J. S. Moore, *Eur Polym J*, 2018, **101**, 202–210.

330 L. Yang and Y. Ke, *High Perform Polym*, 2014, **26**, 900–905.

331 G. Dalwadi, H. A. E. Benson and Y. Chen, *Pharm Res*, 2005, **22**, 2152–2162.

332 F. J. Allen, C. L. Truscott, P. Gutfreund, R. J. L. Welbourn and S. M. Clarke, *Langmuir*, 2019, **35**, 5753–5761.

333 C. Liu, Y. Wang, Y. Gao, Y. Zhang, L. Zhao, B. Xu and L. S. Romsted, *Physical Chemistry Chemical Physics*, 2019, **21**, 8633–8644.

334 A. L. Chau, C. D. Pugsley, M. E. Miyamoto, Y. Tang, C. D. Eisenbach, T. E. Mates, C. J. Hawker, M. T. Valentine and A. A. Pitenis, *Tribol Lett*, 2023, **71**, 1–12.

335 N. W. Turner, C. W. Jeans, K. R. Brain, C. J. Allender, V. Hlady and D. W. Britt, *Biotechnol Prog*, 2006, **22**, 1474.

336 Y. Long, X. Huang, Y. Gao, L. Chen, F. Song and H. Zhang, *Energy & Fuels*, 2019, **33**, 3077–3088.

337 N. M. Sekerak, K. M. Hutchins, B. Luo, J. G. Kang, P. v. Braun, Q. Chen and J. S. Moore, *Eur Polym J*, 2018, **101**, 202–210.

338 N. Na, Y. Hu, J. Ouyang, W. R. G. Baeyens, J. R. Delanghe and T. De Beer, *Anal Chim Acta*, 2004, **527**, 139–147.

339 H. Fritz, M. Maier and E. Bayer, *J Colloid Interface Sci*, 1997, **195**, 272–288.

340 M. R. Battig, B. Soontornworajit and Y. Wang, *J Am Chem Soc*, 2012, **134**, 12410–12413.

341 M. Rahman, L. Y. Heng, D. Futra and T. L. Ling, *Nanoscale Res Lett*, 2017, **12**, 474.

342 O. Lunov, T. Syrovets, C. Loos, J. Beil, M. Delacher, K. Tron, G. U. Nienhaus, A. Musyanovych, V. MailäNder, K. Landfester and T. Simmet, 2011, **5**, 1657–1669.

343 V. Holzapfel, A. Musyanovych, K. Landfester, M. R. Lorenz and V. Mailänder, *Macromol Chem Phys*, 2005, **206**, 2440–2449.

344 S. Schumacher, F. Grüneberger, M. Katterle, C. Hettrich, D. G. Hall, F. W. Scheller and N. Gajovic-Eichelmann, *Polymer (Guildf)*, 2011, **52**, 2485–2491.

345 N. M. Sekerak, K. M. Hutchins, B. Luo, J. G. Kang, P. v. Braun, Q. Chen and J. S. Moore, *Eur Polym J*, 2018, **101**, 202–210.

346 J. Fang, Y. Xuan and Q. Li, *Sci China Technol Sci*, 2010, **53**, 3088–3093.

347 G. Bellisola and C. Sorio, *Am J Cancer Res*, 2012, **2**, 1.

348 V. Hermán, H. Takacs, F. Duclairoir, O. Renault, J. H. Tortai and B. Viala, *RSC Adv*, 2015, **5**, 51371–51381.

349 E. Yousif and R. Haddad, *Springerplus*, , DOI:10.1186/2193-1801-2-398.

350 O. A. Deorukhkar, B. S. Deogharkar and Y. S. Mahajan, *Chemical Engineering and Processing: Process Intensification*, 2016, **105**, 79–91.

351 Polysciences, *TECHNICAL DATA SHEET 238*, 2016.

352 K. Yang, J. Chen, Q. Fu, X. Dun and C. Yao, *E-Polymers*, 2020, **20**, 162–170.

353 K. G. Uranta, S. Rezaei-Gomari, P. Russell and F. Hamad, *Energies 2018, Vol. 11, Page 2201*, 2018, **11**, 2201.

354 L. Yang and Y. Ke, *High Perform Polym*, 2014, **26**, 900–905.

355 Y. Ji, X. Yang, Z. Ji, L. Zhu, N. Ma, D. Chen, X. Jia, J. Tang and Y. Cao, *ACS Omega*, 2020, **5**, 8572–8578.

356 L. Earnden, A. G. Marangoni, T. Laredo, J. Stobbs and E. Pensini, *J Mol Liq*, 2022, **367**, 120551.

357 C. Reichardt, in *Solvent Effects in Organic Chemistry.*, Wiley-VCH, Third., 1984, pp. 21–40.

358 L. Earnden, A. G. Marangoni, T. Laredo, J. Stobbs and E. Pensini, *J Mol Liq*, 2022, **367**, 120551.

359 G. Springsteen and B. Wang, *Chemical Communications*, 2001, 1608–1609.

360 J. W. Tomsho and S. J. Benkovic, *J Org Chem*, 2012, **77**, 2098–2106.

361 S. Schumacher, F. Grüneberger, M. Katterle, C. Hettrich, D. G. Hall, F. W. Scheller and N. Gajovic-Eichelmann, *Polymer (Guildf)*, 2011, **52**, 2485–2491.

362 J. J. Li, in *Name Reactions*, Springer Berlin Heidelberg, 2003, pp. 362–362.

363 M. Lin, G. Chen and M. Jiang, *Polym Chem*, 2014, **5**, 234–240.

364 P. J. Pandiyan, R. Appadurai and S. Ramesh, *Analytical Methods*, 2013, **5**, 3386–3394.

365 J. D. Larkin, K. L. Bhat, G. D. Markham, B. R. Brooks, H. F. Schaefer and C. W. Bock, *Journal of Physical Chemistry A*, 2006, **110**, 10633–10642.

366 X. Li, Y. Zhang, Z. Shi, D. Wang, H. Yang, Y. Zhang, H. Qin, W. Lu, J. Chen, Y. Li and G. Qing, *Nat Commun*, 2024, **15**, 1207.

367 M. A. Martínez-Aguirre, M. Flores-Alamo, F. Medrano and A. K. Yatsimirsky, *Org Biomol Chem*, 2020, **18**, 2716–2726.

368 G. Wulff and S. Schauhoff, *Journal of Organic Chemistry*, 1991, **56**, 395–400.

369 K. A. Ketuly and A. H. A. Hadi, *Molecules 2010, Vol. 15, Pages 2347-2356*, 2010, **15**, 2347–2356.

370 S. H. Walker, B. N. Papas, D. L. Comins and D. C. Muddiman, *Anal Chem*, 2010, **82**, 6636–6642.

371 N. R. Babij, E. O. McCusker, G. T. Whiteker, B. Canturk, N. Choy, L. C. Creemer, C. V. D. Amicis, N. M. Hewlett, P. L. Johnson, J. A. Knobelsdorf, F. Li, B. A. Lorsbach, B. M. Nugent, S. J. Ryan, M. R. Smith and Q. Yang, *Org Process Res Dev*, 2016, **20**, 661–667.

372 MassLynx Mass Spectrometry Software | MS Data Analysis | Waters, https://www.waters.com/nextgen/en/products/informatics-and-software/mass-spectrometry-software/masslynx-mass-spectrometry-software.html, (accessed 25 April 2024).

373 L. Xu, M. M. Coggon, C. E. Stockwell, J. B. Gilman, M. A. Robinson, M. Breitenlechner, A. Lamplugh, J. D. Crounse, P. O. Wennberg, J. A. Neuman, G. A. Novak, P. R. Veres, S. S. Brown and C. Warneke, *Atmos Meas Tech*, 2022, **15**, 7353–7373.

374 J. B. Crumpton, W. Zhang, W. L. Santos, J. B. Crumpton, W. Zhang and W. L. Santos, *Anal Chem*, 2011, **83**, 3548–3554.

375 J. P. Kamerling and J. F. G. Vliegenthart, in *Sialic acids chemistry, metabolism and function*, Springer, Vienna, 1982, pp. 95–125.

376 M. Kimani, S. Beyer, Z. El-Schich, K. Gawlitza, A. Gjörloff-Wingren and K. Rurack, *ACS Appl Polym Mater*, 2021, **3**, 2363–2373.

377 S. Shinde, Z. El-Schich, A. Malakpour, W. Wan, N. Dizeyi, R. Mohammadi, K. Rurack, A. Gjörloff Wingren and B. Sellergren, *J Am Chem Soc*, 2015, **137**, 13908–13912.

378 M. Regueiro-Figueroa, K. Djanashvili, D. Esteban-Gómez, A. de Blas, C. Platas-Iglesias and T. Rodríguez-Blas, *European J Org Chem*, 2010, **2010**, 3237–3248.

379 M. Mahani, F. Mahmoudi, J. Fassihi, Z. Hasani and F. Divsar, *Microchimica Acta*, 2021, **188**, 1–11.

380 Y. Ma, Y. Yin, L. Ni, H. Miao, Y. Wang, C. Pan, X. Tian, J. Pan, T. You, B. Li and G. Pan, *Bioact Mater*, 2021, **6**, 1308–1317.

381 L. Mavliutova, E. Verduci, S. A. Shinde and B. Sellergren, *ACS Omega*, 2021, **6**, 12229–12237.

382 H. W. Liu, W. H. T. Law, L. C. C. Lee, J. C. W. Lau and K. K. W. Lo, *Chem Asian J*, 2017, **12**, 1545–1556.

383 T. Wu, P. Bouř, R. Li and / Chemcomm, *Chemical Communications*, 2018, **54**, 1790–1792.

384 H.-W. W. Liu, W. H.-T. T. Law, L. C.-C. C. Lee, J. C.-W. W. Lau and K. K.-W. W. Lo, *Chem Asian J*, 2017, **12**, 1545–1556.

385 M. Yamamoto, M. Takeuchi and S. Shinkai, *Tetrahedron*, 1998, **54**, 3125–3140.

386 S. Nishitani, Y. Maekawa and T. Sakata, *ChemistryOpen*, 2018, **7**, 513–519.

387 K. Djanashvili, L. Frullano and J. A. Peters, *Chemistry - A European Journal*, 2005, **11**, 4010–4018.

388 C. D. Roy and H. C. Brown, *J Organomet Chem*, 2007, **692**, 784–790.

389 J. F. G. Vliegenthart, L. Dorland, H. van Halbeek and J. Haverkamp, in *sialic acids chemistry, metabolism and function*, ed. R. Schauer, Springer, Vienna, vienna, 1982, pp. 127–172.

390 N. K. Sauter, B. A. Wurzburg, J. E. Hanson, D. C. Wiley, M. D. Bednarski, G. M. Whitesides and J. J. Skehel, *Biochemistry*, 1989, **28**, 8388–8396.

391 N. Pérez, M. J. Whitcombe and E. N. Vulfson, *Macromolecules*, 2001, **34**, 830–836.

392 N. Pé Rez, M. J. Whitcombe and E. N. Vulfson, *J Appl Polym Sci*, 2000, **77**, 1851–1859.

393 G. Holdgate, in *Ligand - Macromolecular interactions in drug discovery*, Humana Press, Totowa, NJ, 2009, pp. 101–133.

394 TA instruments, Quick start: Isothermal titration calorimetry (ITC), https://www.tainstruments.com/pdf/literature/MCAPN-2016-1.pdf, (accessed 1 December 2022).

395 J. Tellinghuisen, *Biochim Biophys Acta Gen Subj*, 2016, **1860**, 861–867.

396 Y. Tamsilian, A. Ramazani, M. Shaban, S. Ayatollahi and R. Tomovska, *Colloid Polym Sci*, 2016, **294**, 513–525.

397 M. v. Sullivan, F. Allabush, D. Bunka, A. Tolley, P. M. Mendes, J. H. R. Tucker and N. W. Turner, *Polym Chem*, 2021, **12**, 4394–4405.

398 ITCRun, DSCRun, & NanoAnalyze Software - TA Instruments, https://www.tainstruments.com/itcrun-dscrun-nanoanalyze-software/, (accessed 29 April 2024).

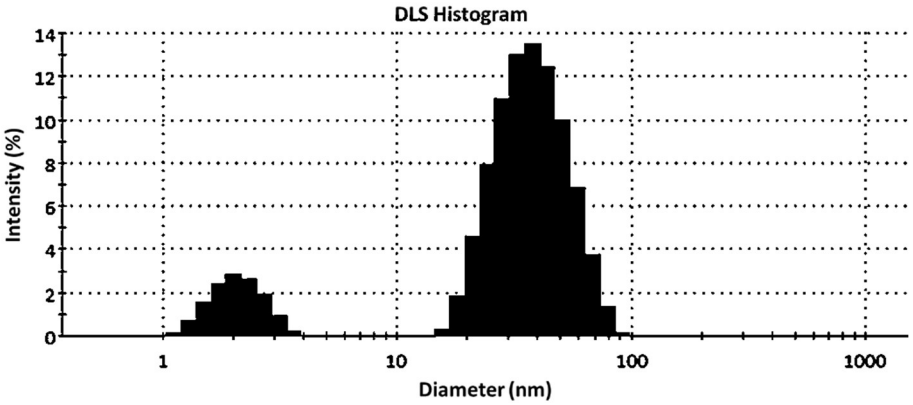
CHAPTER NINE

I. APPENDIX

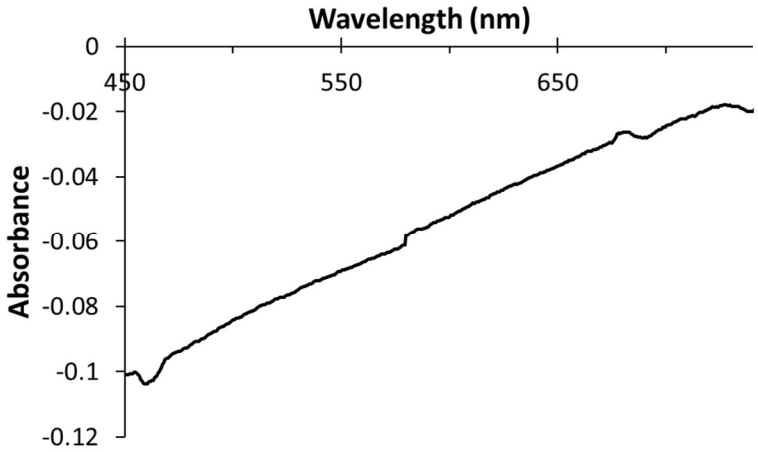
Appendix 9-1: Table to summarise the repeats of gold nanoparticle synthesis.

	N4	N5	N7
TEM diameter	17 (± 1 nm) Population size = 598	18 (± 3 nm) Population size = 545	17 (± 2 nm) Population size = 439
DLS diameter	34 (± 0.2 nm) PDI = 0.2	38 (± 1.5 nm) PDI = 0.4	21 (± 0.1 nm) PDI = 0.6

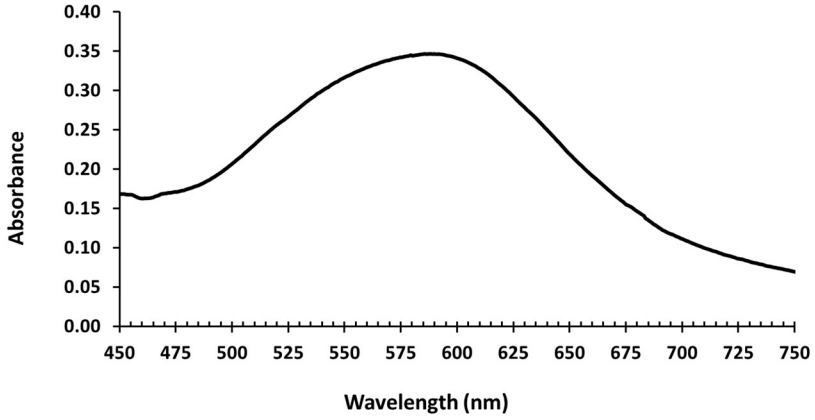
Appendix 9-2: DLS histogram depicting the flaws of using DLS to measure the diameter of nanoparticles. The presence of more than one size population causes the hydrodynamic radius value to deviate from its true average value.



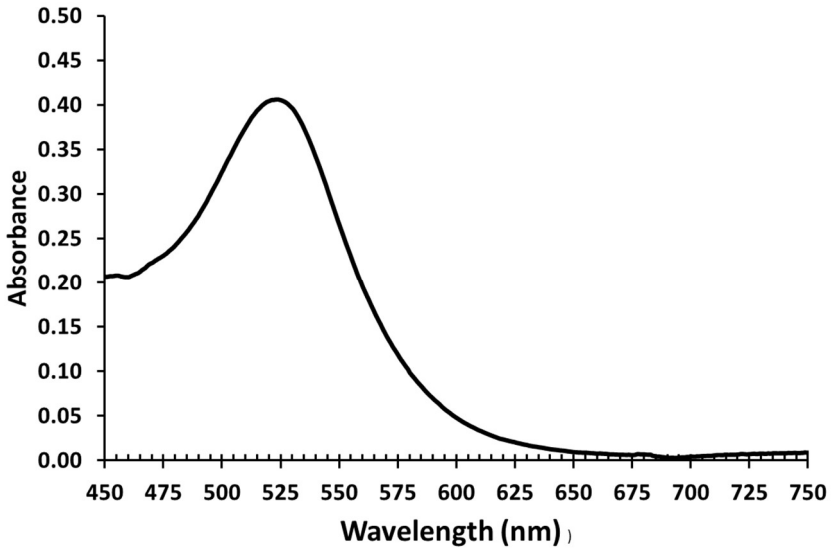
Appendix 9-3: V-Vis spectrum for citrate-capped gold nanoparticles in the presence of cysteamine hydrochloride ligand. The observed negative absorbance values indicate extensive aggregation diminishing the presence of nanoparticles.



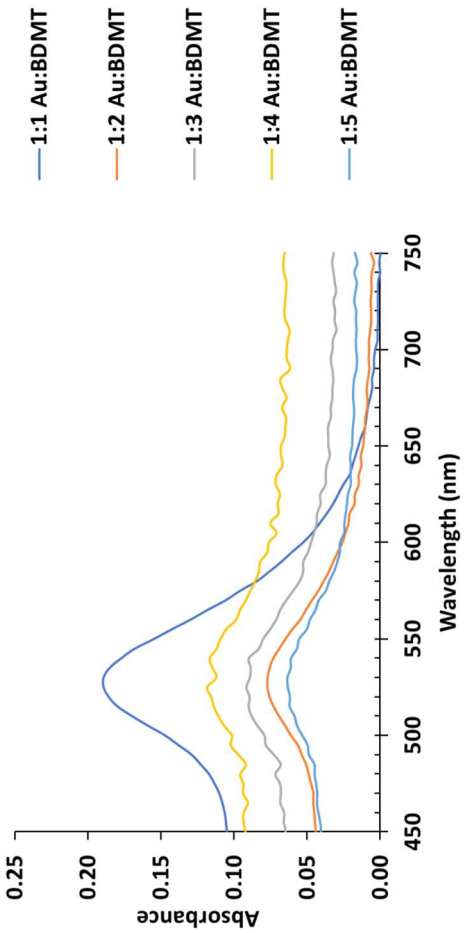
Appendix 9-4: LSPR (λ_{MAX} = 589 nm) peak of the pale blue solution of 11-MUDA functionalised gold nanoparticles (flocculation parameter = 27).



Appendix 9-5: LSPR peak of the ruby red solution of gold nanoparticles in the presence of T20 (flocculation parameter = 2).



Appendix 9-6: UV-vis spectra displaying the LSPR peaks for the series of reactions of purified citrate-capped gold nanoparticles with BDMT. The overlay of normalised LSPR peaks display a correlation between the ratio of gold to thiol (BDMT), with increasing the thiol molar ration results in a decreased in absorption and peak widening.



I. GOLD NANOPARTICLE THEORETICAL CONCENTRATION BASED ON TEM DIAMETER.

Gold nanoparticles measured via TEM = 17 nm

Average gold nanoparticle volume (nm^3) assuming spherical = $\frac{4}{3}\,\pi\,(8.5)^3 = 2572.44$

Average gold nanoparticle volume in cm^3 = 2.5 x 10^{-18}

Density of bulk Au = 19.30 g/cm^3

Average mass of a nanoparticle = $(2.5\text{ x }10-18)(19.30) = 4.9E-17$ grams

Bulk Au mass = 196.96657

Moles of Au per NP = 2.52E-19

Avogadro Number (N_A) = 6.022140857E+23

Au atoms per nanoparticle = 2.52E-19 X N_A = 151796

Bulk Au ($AuCl_4$) added into 51.7 mL reaction = 5E-3 grams

[$AuCl_4$] added into 51.7 mL reaction = 2.456 x10^{-4} mol dm^{-3}

[Colloidal Au] in reaction = $\frac{[Bulk\ Au]}{Au\ atoms\ per\ NP} = \frac{2.456\ E-4}{151796}$ = 1.65 x10^{-9} mol dm^{-3} / 1.65 nM

II. GOLD NANOPARTICLE THEORETICAL CONCENTRATION BASED ON LSPR PEAK

The concentration of gold nanoparticles may be approximated based on the Beer-Lambert law, whereby the measured absorbance value is proportional to the concentration as depicted by the equation below.

$$UV\ absorbance = \epsilon\ .C.l$$

The following equation holds when the measured solution satisfies certain conditions. Large deviations occur when the concentration is too high or too low. Provided the sample is of suitable concentration the above law holds and the concentration of the sample can be approximated providing the pathlength and molar absorption coefficient is known. The pathlength in most cases is 1 cm since most standard UV cuvettes are 1cm across. The molar absorption coefficient (ε) is a physical property of a substance. Prior literature [290] reported molar absorption coefficients (ε) for gold nanoparticles of varying sizes. Thus, assuming the nanoparticles are approximately 17 nm in size, the reported literature estimated this value to be: 5.502E^{8} dm^{3} mol^{-1} cm^{-1}.

Re-arranging "Beer Lamberts law" gives the experimental concentration value for the crude citrate-capped gold nanoparticles synthesised.

$$c = \frac{A}{\varepsilon} = \frac{0.88571}{5.502E8} = 1.6e^{-9}\ M = 1.6\ nM$$

III. THEORETICAL CONCENTRATION OF BULK GOLD IN THE SYNTHESIS OF GOLD NANOPARTICLES CALCULATED FROM REAGENT MASS.

$5x10^{-2}$ g of gold tetrachloride (MW = 393.83 g/mol) was placed into a 5 mL volumetric flask to produce a 1% stock solution. The synthesis of the gold nanoparticles used 0.5 mL of this stock solution. The total reaction volume varied depending on the amount of sodium citrate used. For reactions using 1.2 mL of the 34 mM sodium citrate stock, the total reaction volume was therefore, 51.7 mL. Therefore, the molarity (M) of the gold in the reaction may be deduced via:

$$moles\ of\ AuCl4 = {5E-2\ grams}\Big/{393.83\frac{grams}{mole}}$$

$$moles = 1.27x10 - 4$$

$$concentration\ of\ AuCl4\ stock\ solution\ = \frac{1.27e-4\ moles}{5\ mL}$$

$$concentration = 25.39\ mM$$

$$Final\ concentration\ of\ bulk\ Au\ in\ recation$$
$$= \frac{25.5.\ mM\ X\ 0.5\ mL}{51.7\ mL}$$

$$= 0.25\ \text{mM}.$$

Appendix 9-7: Tabulated summary of DLS measurements for PAM nanoparticles. Each reported diameter is an averaged value of three individual size measurements.

PAM samples		Diameter (nm)	PDI	# of peaks
A	After purification	448 (±15)	0.42	4
	After purification + sonicated	428 (±38)	0.44	2
B	After purification	1729 (±753)	0.95	4
C	After purification	1133 (±352)	0.82	4

Appendix 9-8: Tabulated DLS data for APBA functionalised PAM nanoparticles. The DLS measurements are an average of 3 individual DLS measurements of a sample.

APBA - PAM		Diameter (nm)	PDI	# of peaks
A	Sample sonicated only	306 (± 85)	0.64	3
A	Sample filtered & sonicated	296 (± 8)	0.39	2
B	Sample sonicated only	1017 (± 83)	0.62	2
C	Sample sonicated only	1951 (± 190)	0.92	1

Appendix 9-9: tabulated summary for synthesising polystyrene nanoparticles and their corresponding size analysis conducted.

ID	DLS analysis	Dilution Factor	Average Diameter	TEM analysis	Average TEM diameter
1	79 ±0.3 nm PDI: 0.012	1 in 10	**82 nm N=3**	**46 ± 12 nm Population = 291 particles**	**48 nm**
	82 ±0.6 nm PDI: 0.022	1 in 100			
	86.10 ±1.8 nm PDI: 0.01	1 in 1000			
2	77 ±1.2 nm PDI: 0.037	1 in 10	**81 nm N=3**	**50 ± 11 nm Population = 322 particles**	
	82 ±2.3 nm PDI: 0.023	1 in 100			
	84 ±3.1 nm PDI: 0.011	1 in 1000			

Appendix 9-10: Tabulated summary for size data obtained for crude DHEBA functionalised polystyrene (DHEBA-PS) nanoparticles.

ID	DLS analysis	Dilution factor	Average diameter	TEM analysis	Average TEM diameter
1	1669 ± 268 nm	1 in 100	**1989 ± 671 nm**	-	-
	2309 ± 828 nm	1 in 1000			
2	80 ± 1 nm	1 in 1000	**80 ± 1 nm**	**58 ± 8 nm Population = 322 particles**	**54 ± 3 nm**
3	No access due to COVID-19	N/A	**N/A**	**50 ± 8 Population = 128 particles**	
4	No access due to COVID-19	N/A	**N/A**	**55 ± 8 Population = 158 particles**	

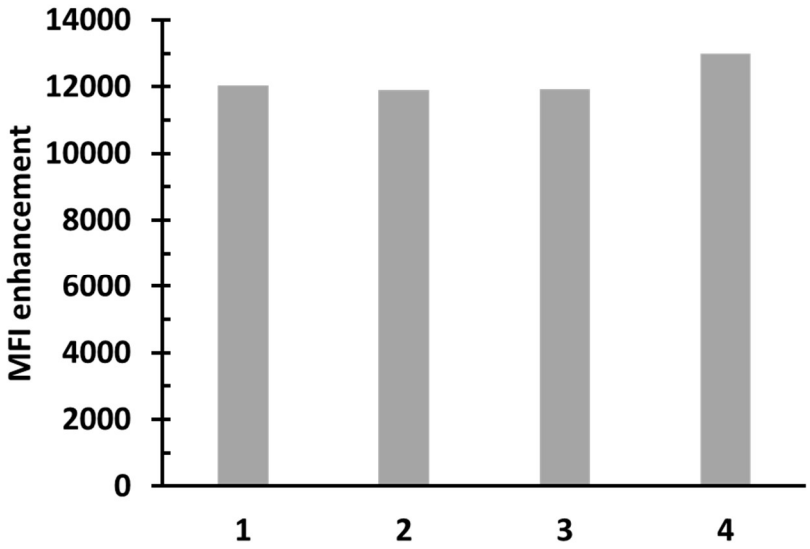
Appendix: 9-11 Tabulated summary of the change in diameter upon functionalising pure DHEBA functionalised PS nanoparticles (DHEBA-PS NPs) with DHEBA and APBA moieties.

ID	DLS diameter	PDI	Average DLS diameter
Pure DHEBA-PS NPs	65 ± 0.9 nm n = 5	0.01 ± 0.01	**65 nm**
Crude DHEBA/APBA-PS NPs	83 ± 0.2 nm n = 3	0.08 ± 0.001	**83 nm**
	82 ± 2 nm n = 5	0.078 ± 0.01	
Pure DHEBA/APBA-PS NPs	108 ± 3 nm n = 5	0.051 ± 0.02	**N/A**

Appendix 9-12: Tabulated summary for the TEM analysis carried out on polystyrene nanoparticles functionalised with both DHEBA and APBA molecules (DHEBA/APBA-PS NPs)

ID	TEM diameter	Average diameter
1	60 ± 9 nm Population = 173 particles	**67 nm** **n = 2**
2	73 ± 15 nm Population = 67 particles	

Appendix 9-13: MFI enhancement data (555 nm) replicate batches (1 – 4) of AABOB functionalised polystyrene nanoparticles interacting with ARS dye at pH 8.



IV. POLYSTYRENE NANOPARTICLES

CALCULATIONS

The nanoparticles are assumed to be 50 nm and spherical in nature, thus the surface area and volume of a single particle can be calculated as follows:

$$surface\ area\ of\ a\ single\ particle\ = 4\pi r^2$$

$$= 4\pi(25)^2 = 7853.981634\ nm^2$$

Volume of a single particle = $\frac{4}{3}\ \pi\ (25)^3 = 6.54\ E^4\ nm^3$

The ligand of interest according to literature has a footprint of around 9 nm^2. Therefore, the number of ligands per particle is:

$$number\ of\ ligands = \frac{7853}{9} = 872.66$$

Therefore, 873 molecules are required to coat a single polystyrene nanoparticle. This assumes that there are no steric and the molecule packs flat on the surface. For MI coating of an entire particle is not only not feasible but also not necessary. To coat 1/10th of a surface of a particle the number of ligands required is therefore 87. Knowing the number of ligands and Avogadro's number, the grams required may be calculated as follows:

$$moles\ of\ 1{:}4\ complex\ required\ for \frac{1}{10th} PS\ NP\ coverage =$$

$$\left[{}^{87}/_{N_A}\right] =\ 1.44\ E^{-21}$$

$$grams = moles\ X\ MW\ \ \therefore 2.038\ E^{-19}$$

Assuming ideal conditions where all starting material is converted to nanoparticles without loss or side reactions. The number of particles produced may be deduced as an approximation.

$$Number\ of\ particles = \frac{Mass\ of\ styrene\ used}{Average\ mass\ of\ a\ particle}$$

$$Average\ mass\ of\ a\ particle = density\ X\ volume$$

$$Average\ mass\ of\ a\ polystyrene\ nanoparticle = 1.06\frac{g}{cm3}\ X\ 6.54498\ E^{-17}\ cm^3\ \therefore 6.94\ E^{-17}\ g$$

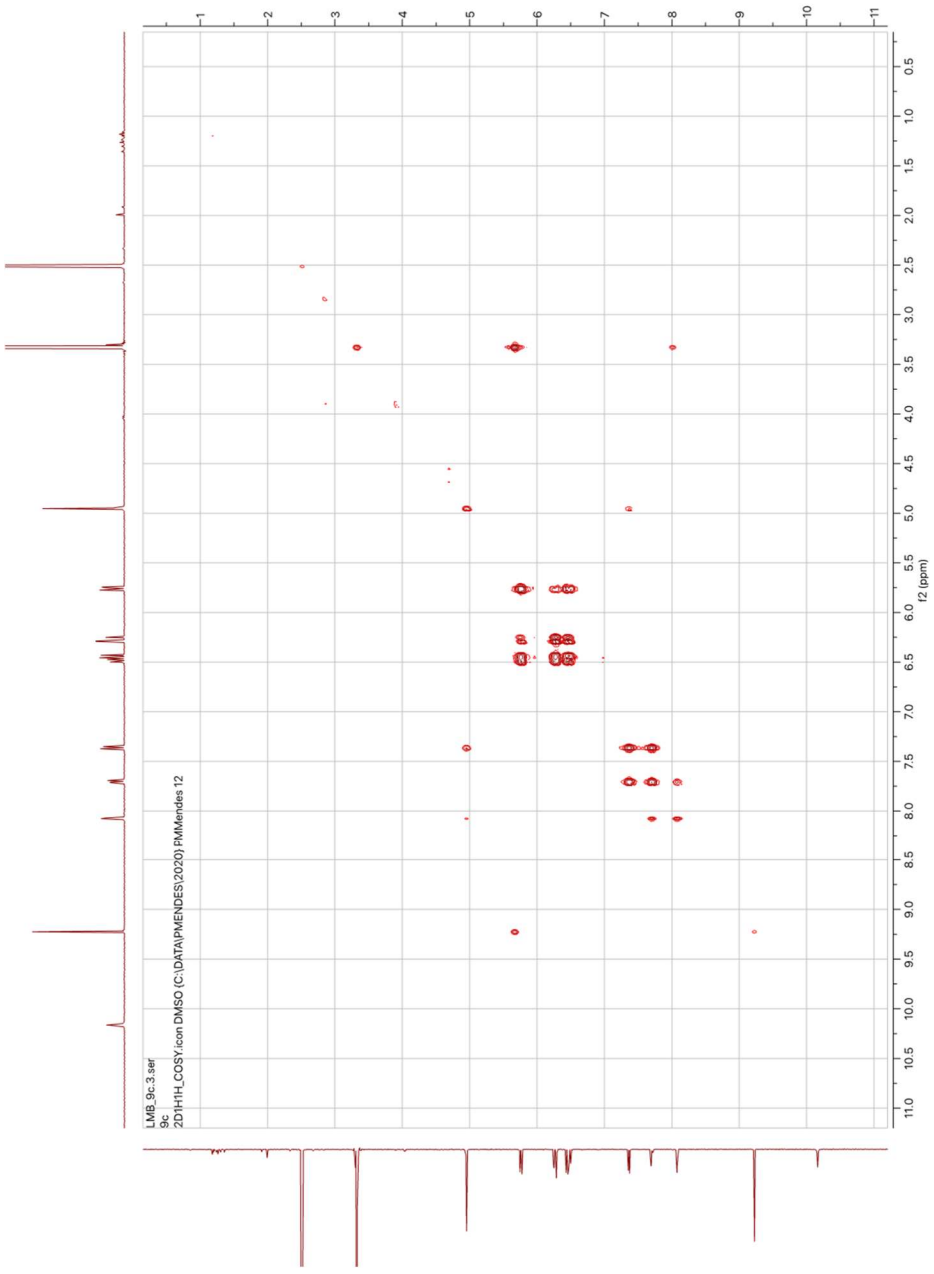
$$Number\ of\ particles = \frac{2.89\ g}{6.94E - 17\ g} = 4.416\ E^{16}$$

$$For\ a\ 31.25\ mL\ reaction\ number\ of\ particles\ present = 4.416\ E^{16}$$

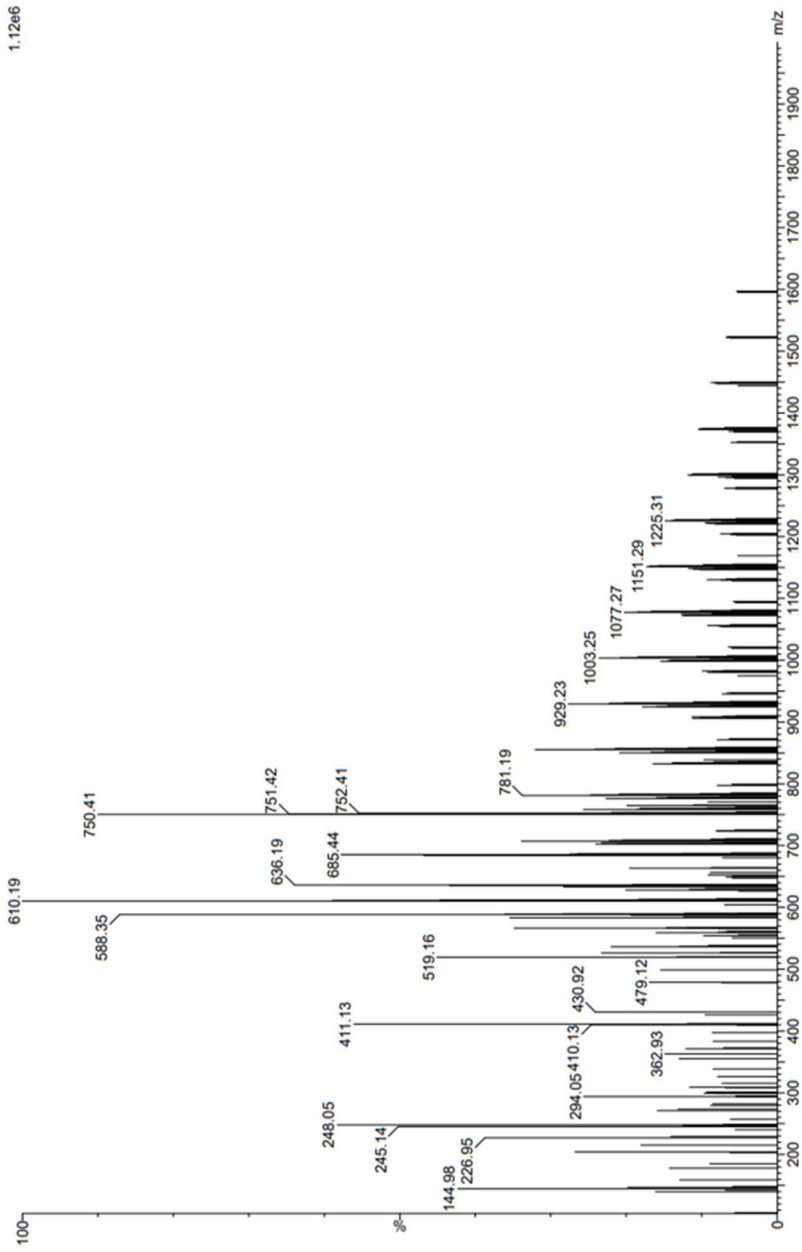
$$\therefore number\ of\ particles\ per\ mL\ \left(\frac{NP}{mL}\right) = \frac{4.416\ E^{16}\ particles}{31.25\ mL} = 1.3330\ E^{15}\ particles/mL$$

Therefore, the mass of ligand (1:4 complex of the boronate ester) required to coat 1 mL of polystyrene nanoparticles (based on 1/10th surface coverage) is approximately 0.272 mg. Thus, a mass greater than 0.272 mg of the boronate ester will be required to functionalise the DHEBA functionalised polystyrene nanoparticles.

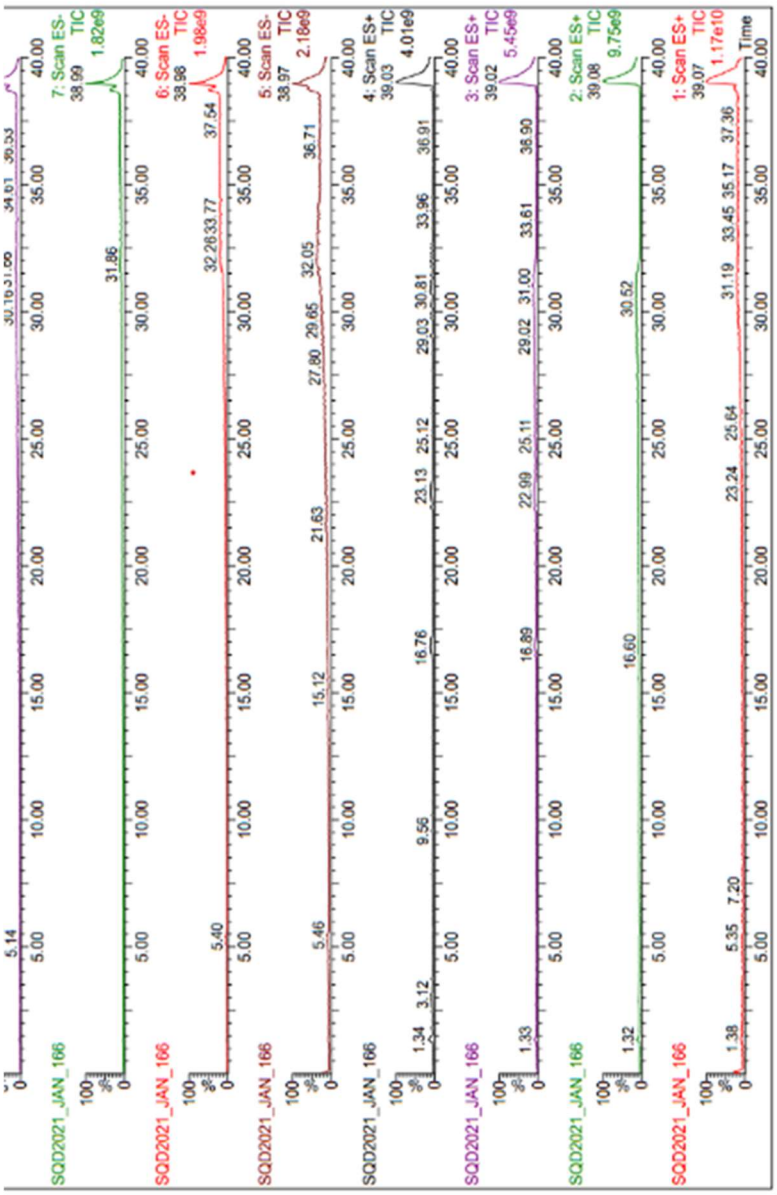
Appendix 9-14: 2D COSY ^{1}H NMR conducted to aid assignment of the 1D ^{1}H NMR spectra.



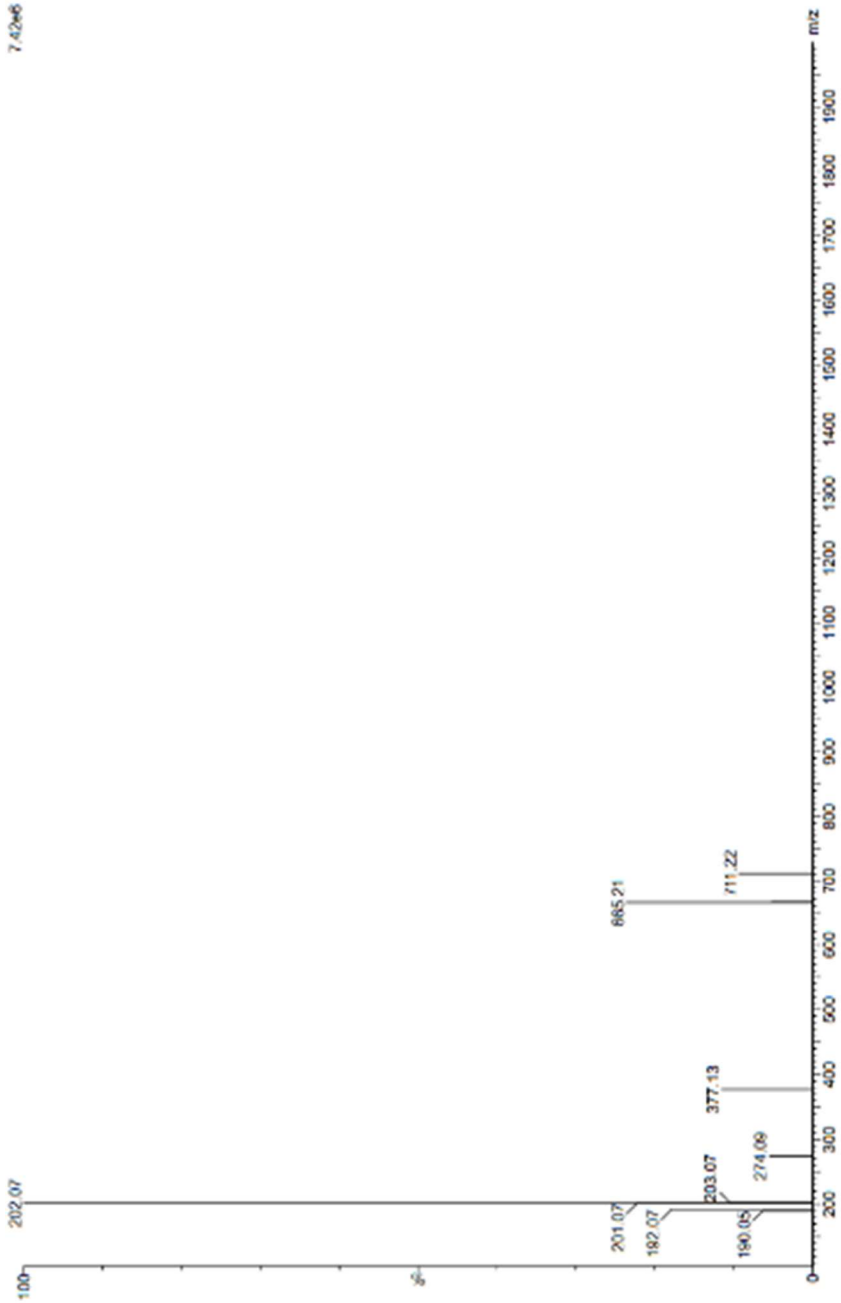
Appendix 9-15: TOF MS ES + spectrum for the AABOB receptor



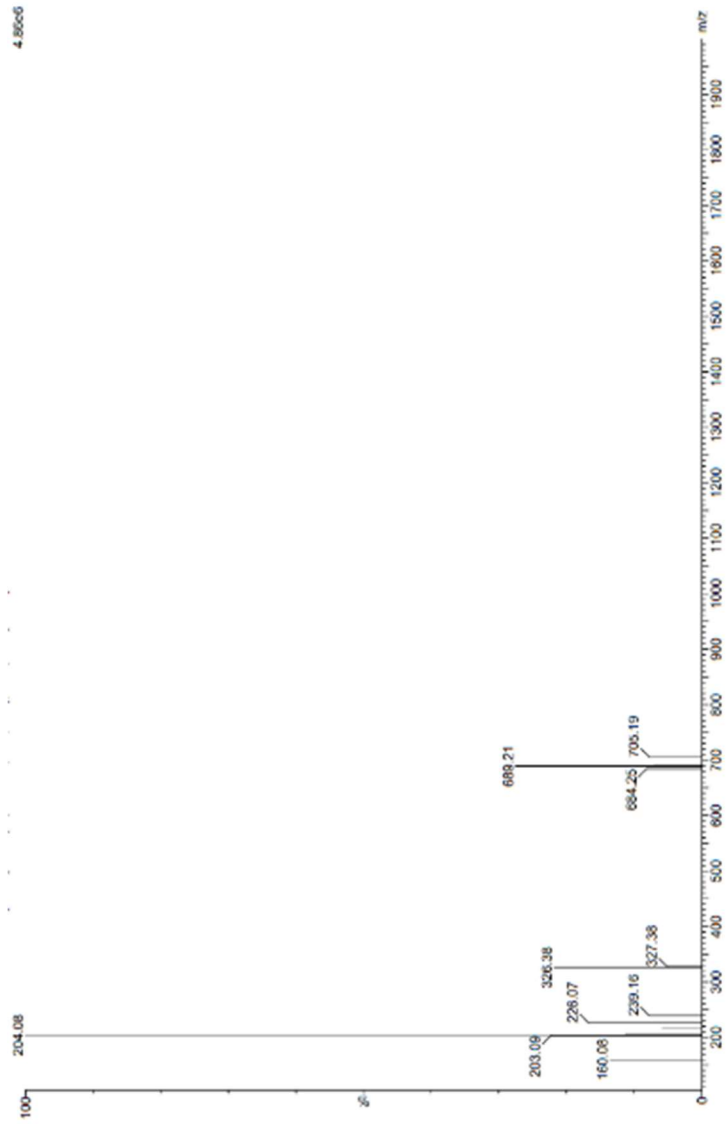
Appendix 9-16: Stacked LC-MS overlays for the boronate-ester synthesised. The spectra display the MS spectra recorded at different cone voltages to attempt to improve the ionisation of any species eluted from the C18 column. No ions were detected as displayed by the lack of peaks.



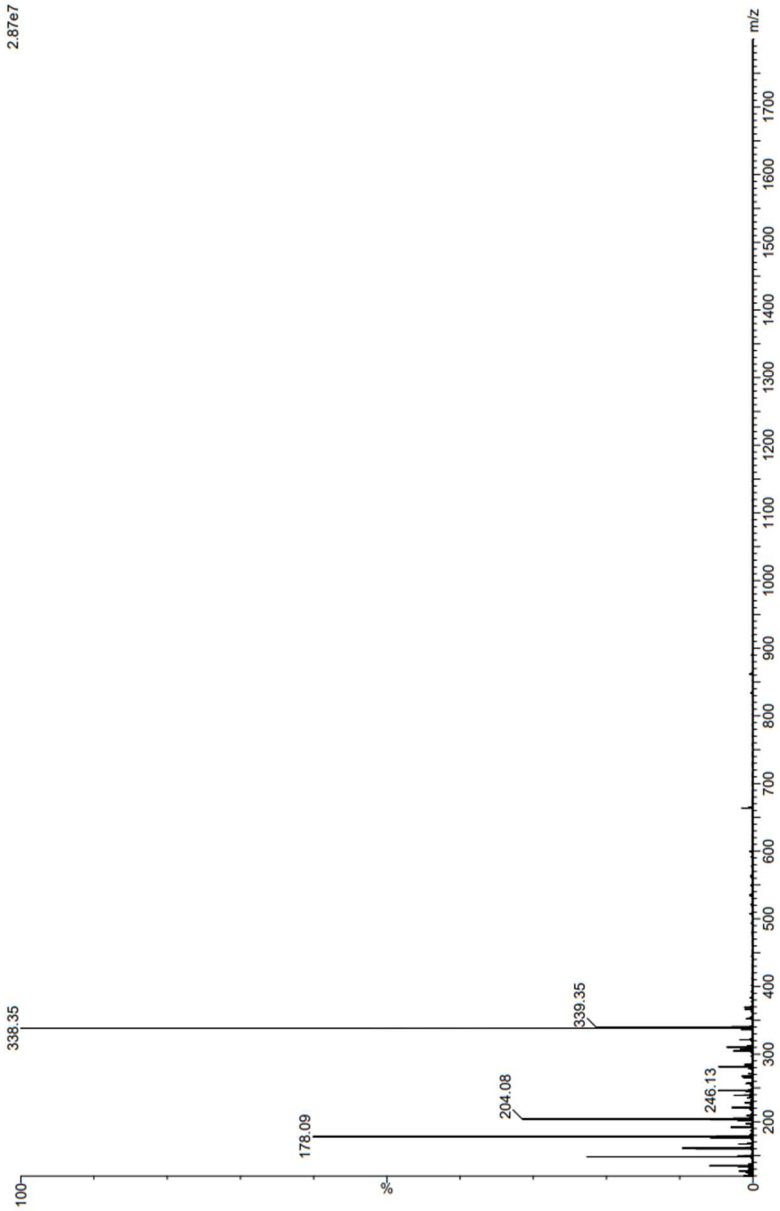
Appendix 9-17: TOF MS ES negative spectra for the crude yellow oil obtained from the boronate ester formation between AABOB and stachyose.



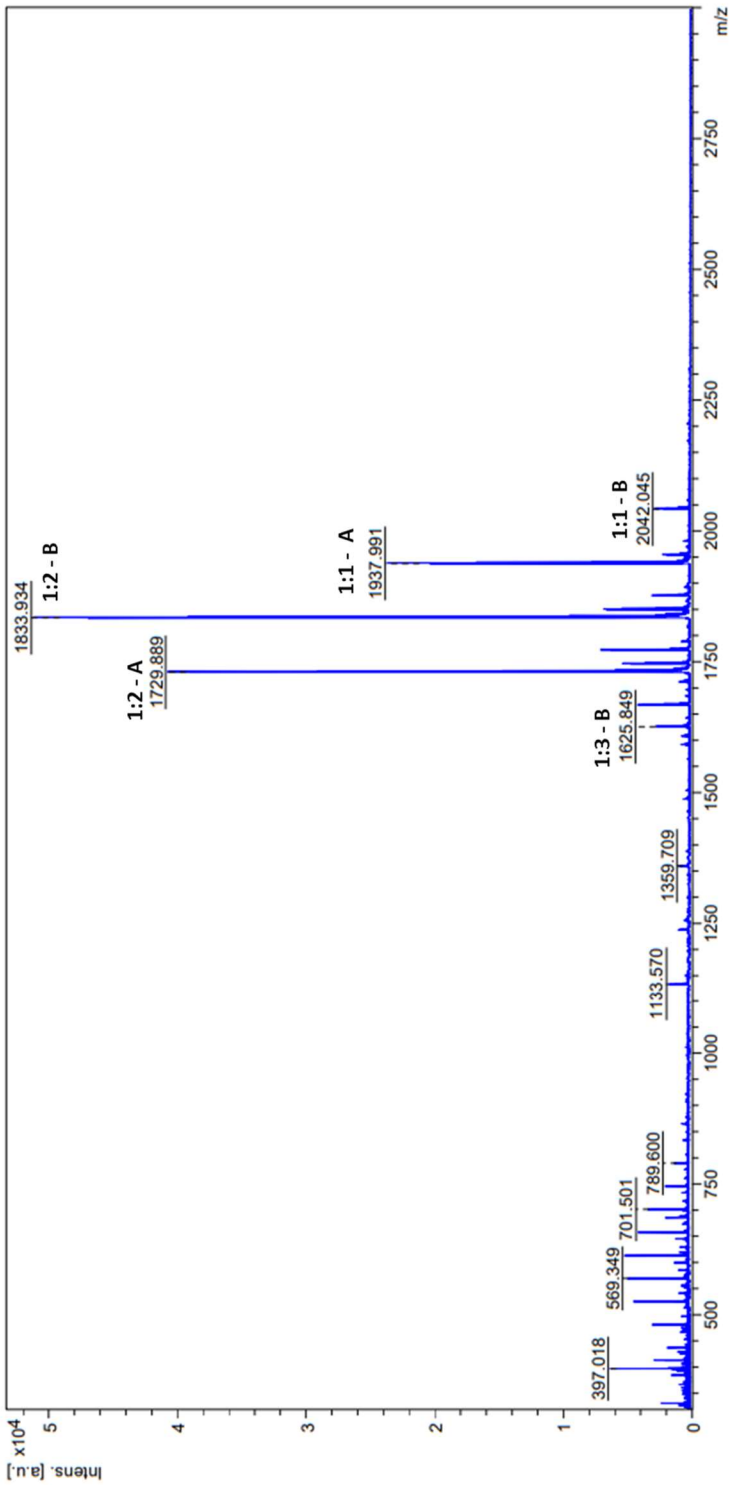
Appendix 9-18: TOF MS ES positive spectra for the crude yellow oil obtained from the boronate ester formation between AABOB and stachyose.



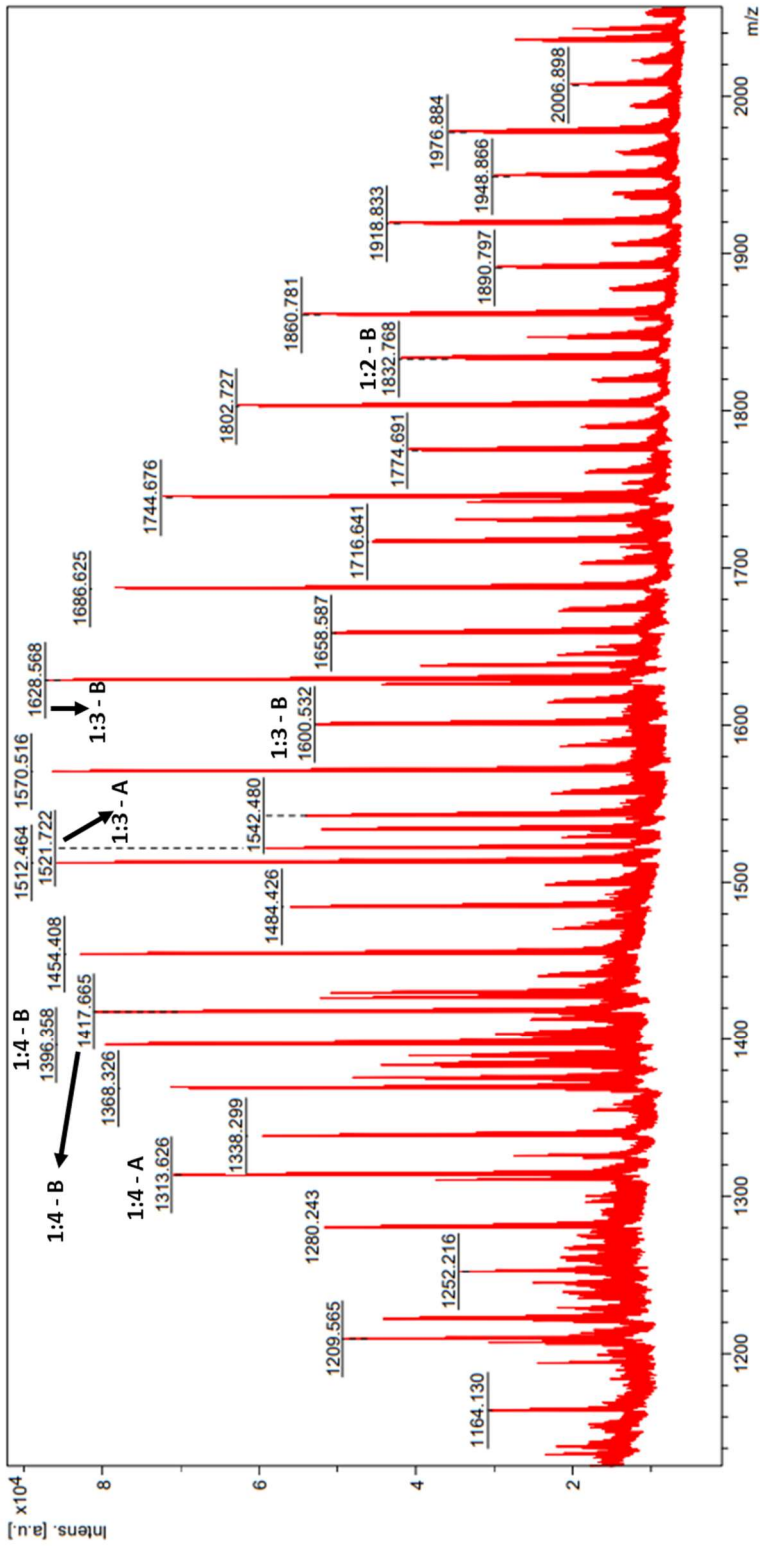
Appendix 9-19: TOF-MS ASAP + spectra for the crude yellow oil obtained from the boronate ester formation between AABOB and stachyose.



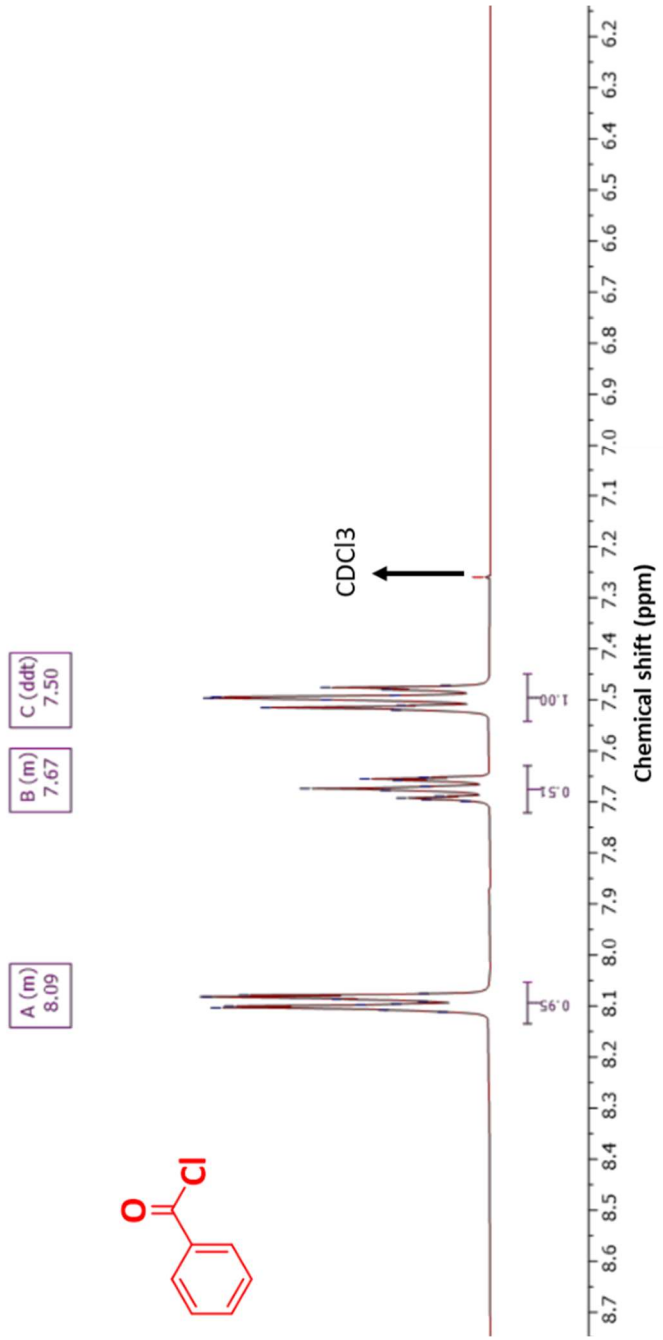
Appendix 9-20: MALDI spectra of benzoylated stachyose species displaying evidence of boronate ester formation.



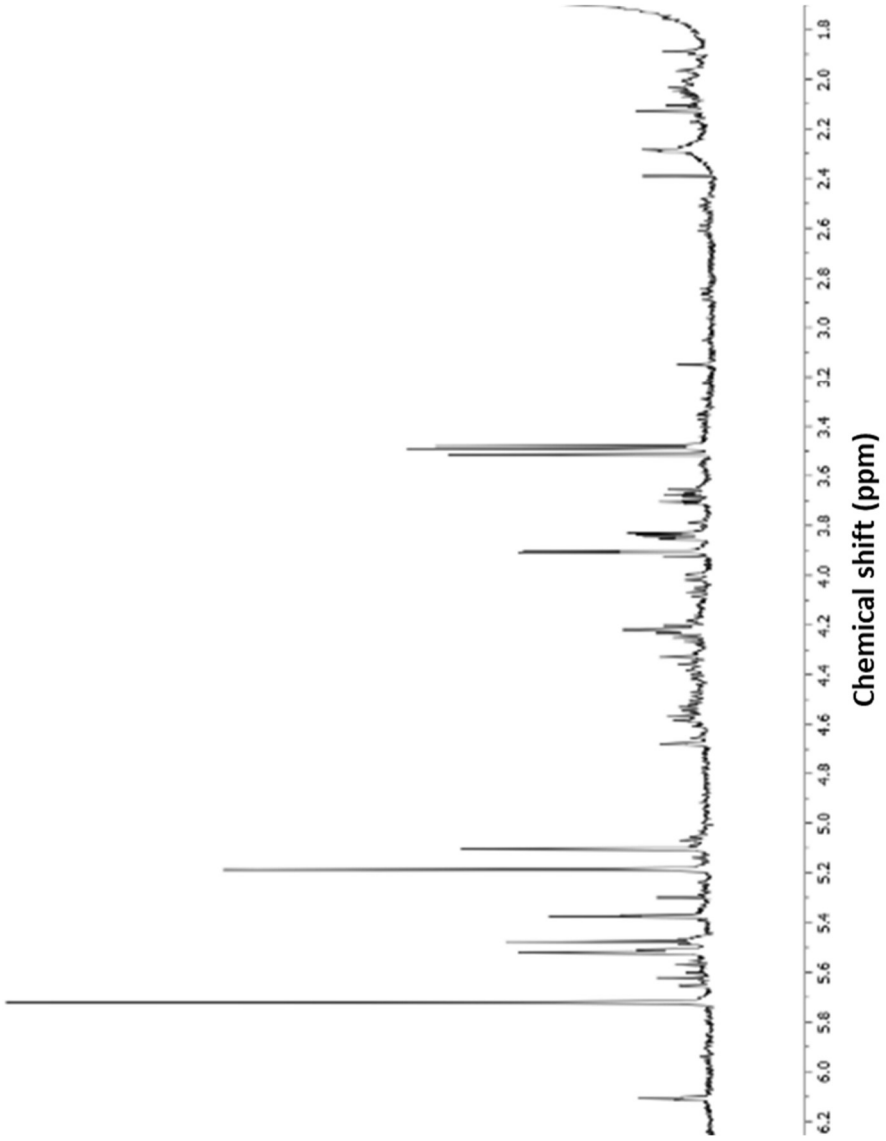
Appendix 9-21: MALDI spectra of benzoylated stachyose species displaying evidence of boronate ester formation.



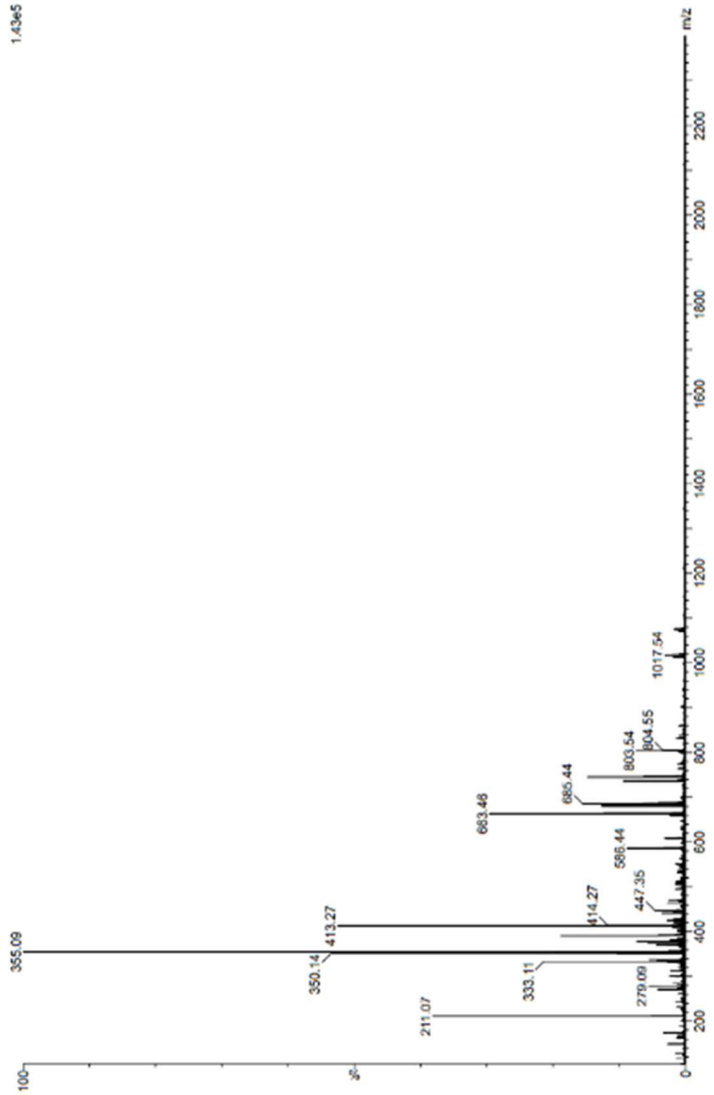
Appendix 9-22: ^{1}H NMR (400 MHz, CDCL3) of pure BzCl used for the benzoylation of stachyose and sialic acid.



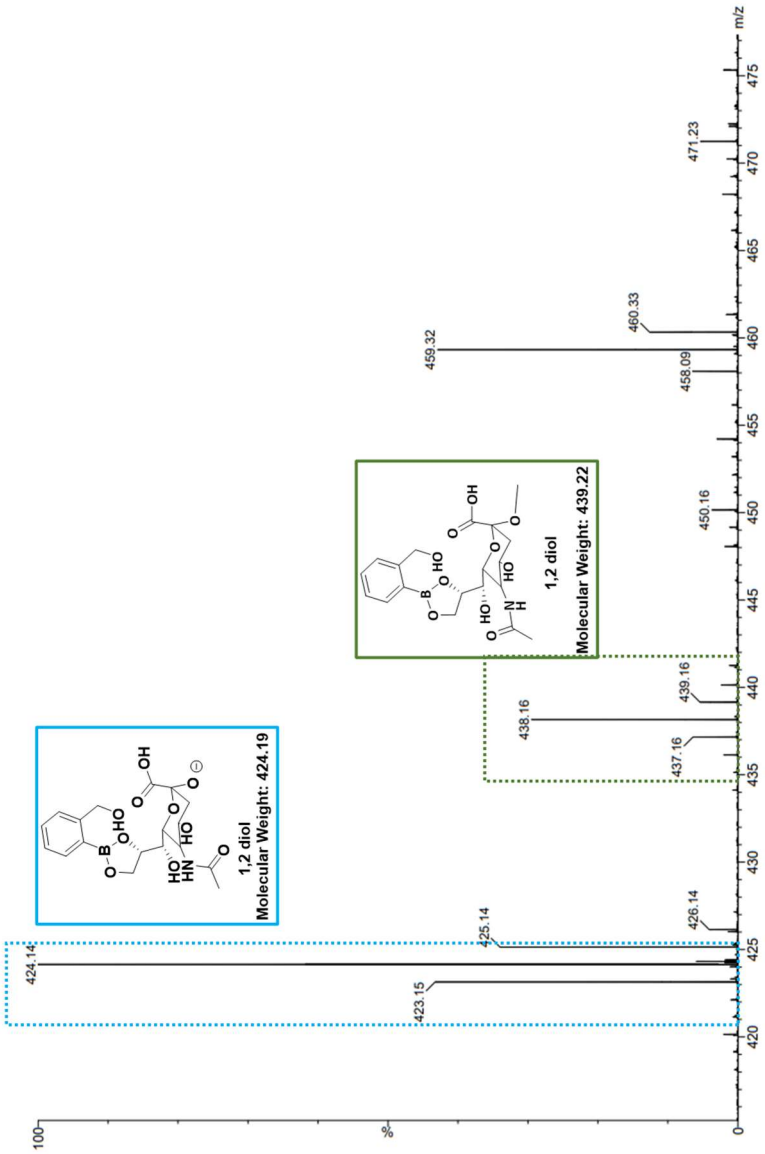
Appendix 9-23: ^{1}H NMR of the yellow oil obtained from the reaction of sialic acid, AABOB and BzCl. Due to the poor resolution because of the lack of product and the overlapping proton peaks no integration or multiplicity could be obtained. The spectra hinted the presence of sialic acid and prompter further investigation.



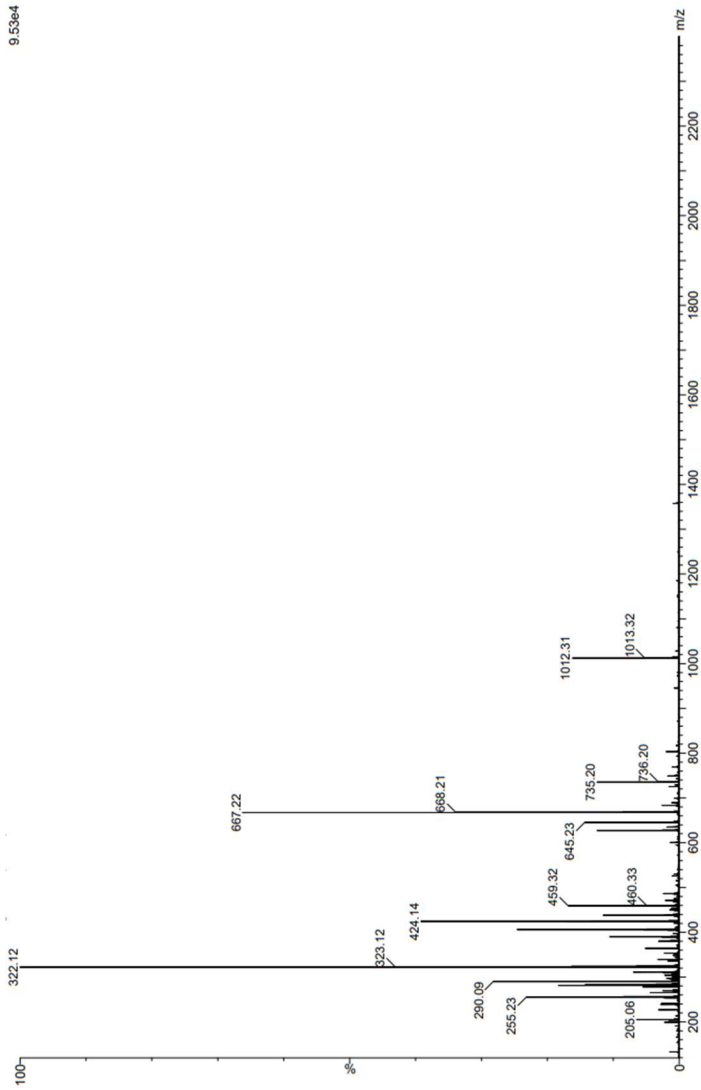
Appendix 9-24: TOF-MS ES + of the prep TLC middle band. Spectra has a dominant peak around 355 suggesting sialic acid was present, although no exact mass could be identified.



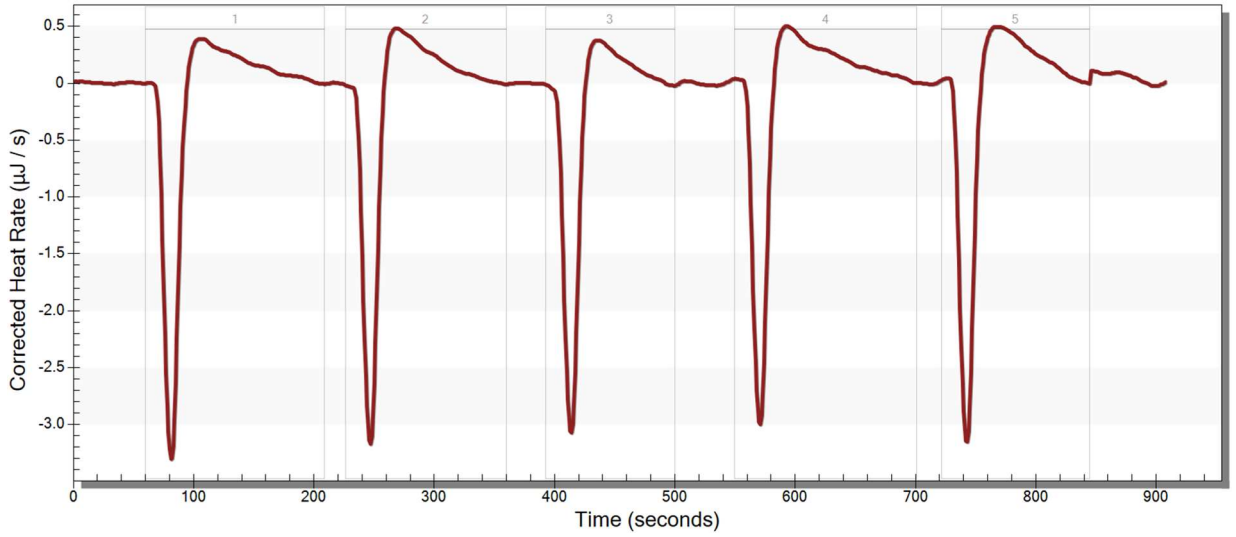
Appendix 9-25: TOF MS ES – spectra displaying the exact mass for the formation of the desired boronate ester with AABOB for methylated sialic acid.



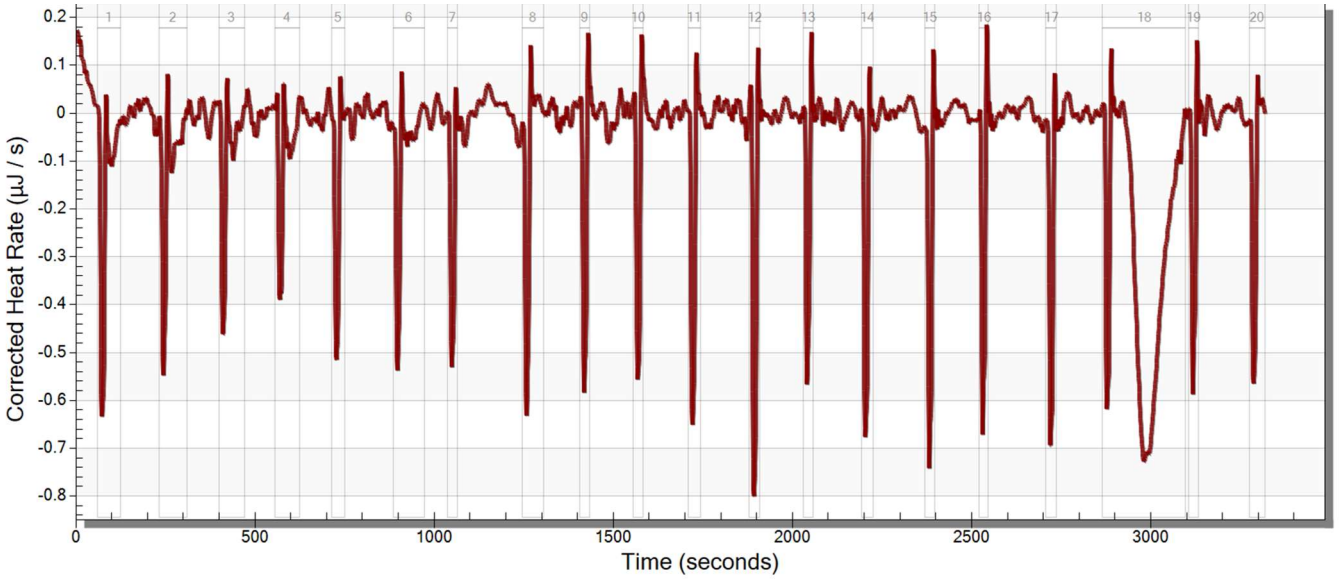
Appendix 9-26: Full MS TOF ES - spectrum obtained for the reaction mixture (DMF) for the reaction of AABOB and sialiac acid dervicates. MS spectra previously labelled with peaks of interest in main text.



Appendix 9-27: Raw heats produced for the heat of dilution control experiment of imprinted nanoparticles (2mg/mL) in the presence of 20 mM phosphate buffer (+0.5 % SDS, pH 8).



Appendix 9-28: Corrected heats produced for subsequent repeat of the reaction between lactose and the solution collected from the imprinted beads reaction at pH 5.



Appendix 9-29: Control experiment for interaction between AABOB receptor (2 mM) synthesised and Stachyose (80 mM) in Phosphate buffer pH 8.

